Development of nanostructured ceramic coatings from suspension and solution precursor thermal spraying process

Thesis submitted to the University of Nottingham for the degree of Doctor of Philosophy

Tunji Adetayo Owoseni, MSc

January 2021

Abstract

The need for high performance, low emission gas turbine engines is driving development of new coatings with bespoke compositions and microstructure to increase thermal efficiency and reduce wear of engine parts. Alumina (Al_2O_3) is suitable in wear applications while yttria stabilized zirconia (YSZ) has been the standard topcoat material for thermal barrier coatings (TBC). The shortcomings of YSZ have spurred the search for new materials and/or processing techniques. Al_2O_3 coatings are traditionally deposited using feedstock of its stable polymorph, α–Al_2O_3; despite the availability and low cost of metastable Al_2O_3 feedstock, the metastable Al_2O_3 feedstock is yet to be explored for wear applications. This thesis presents the study on coatings made of yttrium aluminium garnet (YAG) as potential alternative to YSZ for thermal barrier coating and Al_2O_3 coating produced from metastable Al_2O_3 feedstock for wear application—all the coatings investigated were produced using high-velocity oxy-fuel (HVOF) thermal spray process for coating deposition with liquid feedstock. The liquid feedstock consists of suspensions and solution precursor injected directly into the combustion chamber of the HVOF gun. The wear performance of the Al_2O_3 coating produced from metastable Al_2O_3 feedstock was two order of magnitude better than those of thermally sprayed conventional Al_2O_3 coatings. The wear rate of the as–sprayed Al_2O_3 coating was 5.53 x 10^{-9} mm^3 $(Nm)^{-1}$ and 2.94 x 10^{-9} $mm^3(Nm)^{-1}$ for the coating heat treated at 600 °C

The residual stress of Al_2O_3 and YSZ coatings studied showed that X-ray diffraction technique is useful to understand the stress state of the top surface of thermal spray coatings; this is particularly useful for contact engineering applications including wear. It was also shown that the through thickness residual stress of a thermal spray coating can be reliably obtained using incremental hole-drilling technique. The average stress

state of the Al_2O_3 coating was compressive in both the longitudinal (-162 MPa) and transverse (-104 MPa) directions as against the tensile stress state in the YSZ coating which has 149 MPa in the longitudinal direction and 102 MPa in the transverse direction. The residual stress in a thermal spray coating was also shown to scale with the building block of the coatings. Another important finding was that thermal spray coating can be made of sintered particles which only undergo thermal softening.

The YAG coatings investigated were produced from two feedstock: one from the stoichiometric solution precursor of the nitrates of aluminium and yttrium, the other from YAG suspension. The combination of thermogravimetric analysis, differential scanning calorimetry (TGA/DSC) and X-ray diffraction were used to show the mechanism of formation of YAG from the solution precursor. The YAG topcoat produced from the solution precursor was compared to a YAG coating produced from YAG suspension in terms of microstructure and thermal cycle life performance.

The results of the coating formation mechanism provided the YAG formation temperature of the solution precursor under isothermal heating condition or rapidly varied heating during thermal spray process as well as the reaction enthalpies across the formation stages. The formation temperature of YAG obtained was ~940 °C while the overall reaction enthalpy was approximately +916J/g. The microstructure of the YAG coating made from the solution precursor and the one made from YAG suspension showed they were both built from lamella, however, the defects in each of the YAG coatings were different. Compared to the YSZ topcoat, the YAG coatings had better thermal conductivity (SP-YAG had < 1.0 W/m*K while S-YAG had ~1.7 W/m*K) at the elevated temperature investigated but the YSZ coating showed improved thermal cycling life.

Journal publications

- **T. A. Owoseni,** A. Rincon Romero, Z. Pala, F. Venturi, E. H. Lester, D. M. Grant, T. Hussain, YAG thermal barrier coatings deposited by suspension and solution precursor thermal spray. Ceramics International, (accepted, May 2021).
- **T. A. Owoseni,** M. Bai, N. Curry, E. H. Lester, D. M. Grant, T. Hussain, Residual stress measurement of suspension HVOF sprayed Al_2O_3 coating via a hole drilling method. Journal of Thermal Spray Technology, 29(6), August 2020, Pages 1339–1350.
- **T. A. Owoseni,** J.W. Murray, Z. Pala, E.H. Lester, D.M. Grant, and T. Hussain, Suspension high velocity oxy-fuel (SHVOF) spray of delta-theta Al2O3 suspension: Phase transformation and tribology. Surface & Coatings Technology, Vol. 371, August 2019, Pages 97-106.

Conferences

- 10th International Charles Parsons Turbine Conference (Parsons 2019), 16-18 Sep. 2019, Cranfield University, **Cranfield, UK**

  Paper presented: Next generation thermal barrier coatings (TBC) ceramic topcoats deposited by suspension and solution precursor thermal spray

- International Thermal Spray Conference and Exhibition (ITSC 2018), 7-10 May. 2018, **Orlando, Florida, USA**

  Paper presented: Neutron Diffraction Residual Stress Measurements in Suspension HVOF Sprayed Al_2O_3 and YSZ Coatings

- Rencontre Internationales sur la Projection Thermique 2017 (8RIPT 2017), 6-8 Dec. 2017, **Limoges, France**

  Paper presented: Phase Transformations and Post-Spray Heat Treatment of a Suspension High Velocity Oxy-Fuel (SHVOF) Sprayed Delta-Theta Al2O3 Suspension

Acknowledgment

AlhamduliLlaah—all praises and exaltation are due to the Uncreated Creator of everything for His support and mercy on me. However, being grateful to Allaah includes showing gratitude to persons in whose arms one finds warmth.

‘‘*Whoever is ungrateful to people will be an ingrate to Allaah, jalla wa thanaa*’’—Abu Dawūd

This thesis is for the community; I have registered for this study alone, but I would not have completed it without the unconditional support of the many persons around me. My primary supervisor, Dr Tanvir Hussain, and my co-supervisors Prof. David M. Grant and Prof. Ed. Lester gave more than technical support and guidance, they all stood by me emotionally, no thanks to the COVID-19 occasioned pandemic.

I am grateful for the financial support from Petroleum Technology Development Fund (PTDF); I would not have been able to complete my studies without the funding. Other financial sources for the duration of my study especially in the wake of the accompanied situations to the pandemic include the Faculty of Engineering, University of Nottingham, and the management team of the Membership Benevolent Trust (MBT), a charitable arm of the Institute of Materials, Minerals and Mining (IOM^3). The support was overwhelming; it was timely—thank you, for the compassion of Peter Waugh, the Executive Secretary of the MBT.

I would not have completed the work on my PhD as well without the technical support from the many research partners to our research group. I thank the Nanoscale and Microscale Research Centre (nmRC) of the University of Nottingham for providing access to characterization instruments. I acknowledge beam time on ENGIN-X provided by STFC ISIS (experiment number RB1710193) for the TOF neutron

diffraction experiments. Mr. Rory Screaton and Mr. John Kirk helped with the spraying of the many coating samples; thank you for your time and technical inputs. Dr Nigel Neate and Dr Hannah Constantin provided support with sample characterization while Dr Zdenek Pala of GE Aviation, Czech Republic helped with crystallographic analysis of diffraction data. Members of Coatings and Surface Engineering group and the entire Wolfson Building family. Two persons from the Wolfson Building family, Dr Reda Felfel and Dr Gilbert Karimi, aided my settling in as young researcher; I had joined IOM^3 as a student member on the advice of Gilbert. Thank you, Gilbert; the IOM^3 membership offered a lifesaving grace!

I say thank you to my parents, Mr. Kamorudeen Ayinde Owoseni and Mrs. Rukayat Bukola Owoseni, for laying a good foundation on which I have built my many achievements. Your du'a and regular encouragement were worthwhile. My siblings Ismail Owoseni (Abu Mardhiyah), Aaisha Owoseni (Ummu Hameedah) and Abdul-Hakeem Owoseni (Abu al-Amin) would call very often to be sure my family and I were doing well—thank you all, I am grateful.

Someone was here through the thick or thin of it all; my dearie, Basirat Olukemi Owoseni (nee Oyeboade), wither the storm with me. When I will sneak out early or must stay away all night, even though she and our children (AmatuLlaah and Abdur-Rahmaan) needed to share time with daddy, I could not help but leave to be around for many more times—worry less, I will be here more from now on. My mentor (Dr Munirudeen Oloso) and my family support network: Dr. Nurudeen and Mrs. Fatimah Adeleke, Mr. Luqman Adesope (Abu AbdiLlaah), Mr. Bashir Adeshina (Abu Aaisha), Madam Muflihat Ayeni (Ummu Khadijah) all played significant role to ensure this journey did not get truncated despite it being stormy.

Beyond the academic circle, the Islamic Society of the University of Nottingham was awesome; I found there-in persons of similar aspirations as me, though we were of diverse background the bond we built was organic. I cannot name you all but Mubarack Ahmed (Ghana), Yassine (Morocco), Bashiru Shehu (Nigeria), Nasiru (Nigeria), Ahsen (Malawi), Muayyad (KSA), Zaid (KSA) and Lutfi (Algeria) formed a network of support through my stay. This diversity is a fascinating feature of the University of Nottingham; it is much appreciated.

To everyone who has been part of my journey at this time and from the onset, I have not taken your support for granted; JazaakumuLlaahu kulla khair in here and in the hereafter.

Table of contents

List of Figures

List of Tables

Nomenclature

Symbols	Meaning
$g(\tau)$	normalized intensity correlation function
β	Coherence factor
Re	Reynold's number
We	Weber number
Oh	Ohnesorge number
ρ	Density
u	relative speed
d	diameter
σ_l	Surface tension
η	Viscosity
θ	Diffraction angle
α_{th}	Thermal diffusivity
α_c	Thermal expansion coefficient
σ_n	Principal stress
σ_{max}	Maximum principal stress
σ_{min}	Minimum principal stress
σ_a	Directional stress
τ	Shear stress
T	Temperature
ε	Strain
$S_{1,2}$	stiffness constant
v	Poisson's ratio
E	Elastic modulus
d_{hkl}	Interplanar spacing

A_ω	Absorbance
T_ω	Transmittance
R_ω	Reflectance
I	Intensity
ω	Frequency
D	Particle size diameter
λ	Wavelength
J	Dimensionless constant
ϵ	Emissivity
R	Radius of diffraction ring
L	Detector length
σ^2	Variance
S_p	Scaling factor
A	X-ray absorption factor
P_s	Preferred orientation
L_s	Lorentz polarization
F_s	Structure factor
Φ	Reflection profile
λ_{th}	Thermal conductivity
C_p	Specific heat capacity
q	Heat flux
$t_{c,s}$	thickness
υ	Thickness fraction
R_{th}	Thermal resistance
K_{IC}	Fracture toughness
c	crack length

a	Indentation radius
H	Hardness
$L_{1,2}$	Neutron flight path
h	Planck's constant
m	Mass of neutron
Ǻ	Strain relaxation per unit depth
r_m	Mean radius
ā	Strain relaxation per unit stress
d_s	Depth of scar
r_b	ball radius
a_s	Scar radius

Introduction

1.0 Background

Gas turbine engines are used in the aviation industry to propel jet engines and in the energy industry to generate of electricity. The performance of the turbine engine is hinged on how much it is protected against environmental degradation; the degradation could result from one or all of abrasion, erosion, wear, fretting, oxidation, corrosion and creep. Two of the measures of performance of the engine include efficiency and specific fuel consumption [1]. The efficiency of the turbine is directly related to temperature of the gas at the inlet to the gas turbine engine, turbine entry temperature (TET), while wear between the turbine rotating parts affects the specific fuel consumption of the engine. Increased TET provides for higher thermal efficiency of the turbine while reduced wear will engender decrease in the specific fuel consumption of the engine [2]. Both protection against wear and improved thermal efficiency can be achieved by depositing coatings onto the surface of relevant gas turbine engine parts—the former requires wear resistant coatings while the latter needs thermal barrier coatings. Thermal barrier coatings are applied to the surfaces of turbine blades, vanes, flow path cowl, jet pipe-liner and combustor of the gas turbine to ensure increased TET necessary for higher thermal efficiency of the turbine while the wear resistant coatings are applied to compressor blades and vanes, the dovetail root of the compressor blade that comes in contact with the disc during running as well as casings and seals [1].

One of the routes for producing coatings used to protect metallic parts is thermal spray—it involves propelling melted or partially melted particles onto a surface sometime at hypersonic speed. Thermal spray coatings can be deposited from most

materials: primarily from rod, wire or powdered ceramic or cermet [3]. For instance, alumina (Al_2O_3) as a ceramic material is widely deposited as wear and chemical resistant coating [4] while yttria stabilize zirconia (YSZ) functions well as solid-oxide electrolyte in fuel cells [5] as well as in thermal barrier coatings (TBC) used in protecting turbine blades for aviation or power generation [6].

The conventional route for the fabrication of thermally sprayed ceramic coatings involves injecting ceramic powder, in the size range of ~5–100 μm, into either the plasma arc, in the case of atmospheric plasma spraying (APS), or the oxy-fuel flame in the case of high velocity oxygen fuel (HVOF) thermal spraying [7]. However, both HVOF spray technique and APS have been shown to produce thermal sprayed coatings with varied density and microstructure depending on the deposition parameters [8] and the feedstock [9].

The coatings being produced from the conventional route appears not to be providing the needed response for the future engineering applications in terms of wear and stability at high temperature [10]. Maurice Gell [10] had highlighted the potential of nanostructured materials as the needed advanced materials that may yield the coatings for the future engineering applications. In 2001, Gell et al. [11] reported the first nanostructured ceramic coatings with outstanding resistance to wear and cracking; the developed coating was thereafter endorsed by the Navy of the United State for shipboard and submarine applications. There was however further question on how to deploy nanometric size materials for thermal spray without compromising safety; this led to the research into the use of liquid media for the delivery of the nanometric materials. The outcome of the search has produced a new branch of

thermal spray—suspension and solution precursor thermal spray—though the new branch is still being developed.

The research into suspension and solution precursor based thermally sprayed coatings was aimed at producing nanostructured coatings for enhanced performance in engineering applications. In the case of the suspension thermal spray process, sub-micron to nanometric size solids is carried in aqueous or organic liquid to form the feedstock fed into plasma as in suspension plasma spray (SPS) [12] or into combustion gas in the case of suspension high velocity oxy-fuel (SHVOF) spray [13]. For solution precursor, inorganic salts containing the desired metallic and non-metallic ions are dissolved in water to form the precursor fed into either plasma as in solution precursor plasma spray [14] or combustion flame as in solution precursor HVOF spray [15].

1.1 Aim and objectives

Based the literature review and the identified research gaps, the aim of this thesis was to develop different nanostructured ceramic coatings; part of the coatings to be developed will offer protection against wear while the other will function as thermal barrier coating for improved thermal efficiency. The coatings investigated were deposited by high velocity oxy–fuel (HVOF) flame spray technique using different feedstock of ceramic suspensions in addition to solution precursor of inorganic salts. The following specific objectives were investigated:

- HVOF spraying of suspensions of Al_2O_3, YAG, YSZ, and the stoichiometric solution precursor of $Al(NO_3)_3{\cdot}9H_2O$ and $Y(NO_3)_3.6H_2O$ to produce YAG

- Microstructure of as–sprayed and heat treated Al_2O_3 coatings using electron microscopy (SEM and TEM) and X–ray diffraction.
- Wear performance of as–sprayed and heat treated Al_2O_3 coating by dry sliding wear of like–on–like in reciprocating configuration. Microhardness and indentation fracture toughness were also measured to investigate the correlation between microstructure and wear performance of the coatings.
- The residual stresses in Al_2O_3 and YSZ coatings using incremental hole-drilling technique and non-destructive techniques: X-ray and time-of-flight (TOF) neutron diffraction. The microstructure of the coatings was also studied in detail with SEM and XRD to rationalise the residual stress behaviour in terms of microstructure.
- Formation mechanism of YAG from stoichiometric solution precursor of $Al(NO_3)_3{\cdot}9H_2O$ and $Y(NO_3)_3.6H_2O$ using a combination of differential thermal analysis (TGA/DSC), Fourier transform infra-red (FTIR) and X–ray diffraction
- Life cycle performance of thermal barrier coatings (TBC) with YAG and YSZ ceramic topcoats. The failure modes of the TBCs under thermal-cyclic loading along with thermal conductivities were also investigated.

1.2 Scope of the thesis

The thesis contains seven chapters split amongst Introduction, the literature review, methodology, results, conclusion, and future work—three of the seven chapters were dedicated to the results of the experimental procedures presented in the methodology chapter. Overview of the details in each of the chapters is presented below.

The details of relevant literature reviewed to identify knowledge gap was presented in chapter two; the literature review was concluded with identified knowledge gap. Aim and specific objectives was formulated to provide insight into some of the questions raised by the knowledge gap. Chapter three described the methodology employed to achieve the set aims of the thesis; succinct description of the equipment used for all experiments were provide together with the associated theory behind each of the methods.

Chapters four through to six contained the results of the experimental details provided in chapter three to address the aim and outlined specific objectives given at the end of chapter one. Each of the result chapter contains detailed discussion of the results; summary of the findings was provided to conclude each of the chapters. The first result chapter, chapter four, provided the background to understanding the capability of HVOF spray technique to produce coatings from suspension feedstock. As such, chapter four was based on the study of the microstructure and wear performance of Al_2O_3 coating produced from the suspension of metastable Al_2O_3. In chapter five, the result of the study of the residual stress in suspension thermal sprayed coatings of Al_2O_3 and YSZ were presented. The work presented in chapter five was to provide the understanding for the mechanism of failure that would accompany the application of coatings produced based on the concepts in chapter four. Further use of the HVOF spray techniques was explored in chapter six. In chapter six the results of ceramic topcoats of YAG deposited from solution precursor and suspension compared with YSZ topcoat. A general conclusion and proposed future work were presented in a separate chapter in the end as chapter seven.

Literature review

2.0 Introduction

Surface engineering (SE) entails integrated techniques that offers specific treatment to the top or near surface of a component for improved surface-dependent performance and prolonged service life. Engineering the surface of a component may involve one or both of changing the microstructure and changing the composition of the near surface of the component. The success of a surface engineering process lies in effective use of the initial bulk materials surface characteristic details—the main classification for surface engineering processes is show in Figure 2-1. Engineered surfaces are tailored to resist corrosion, wear, chemical attack, ice formation, thermal degradation, enhance biocompatibility, electrical conductance, and charge storage better than their underlying bulk materials. Engineered surfaces thus finds applications in homes (kitchen wares, bathtubs, etc.) and industry (transportation, power, electronics, etc.) where enhanced functionality and reduced degradation effects are sought.

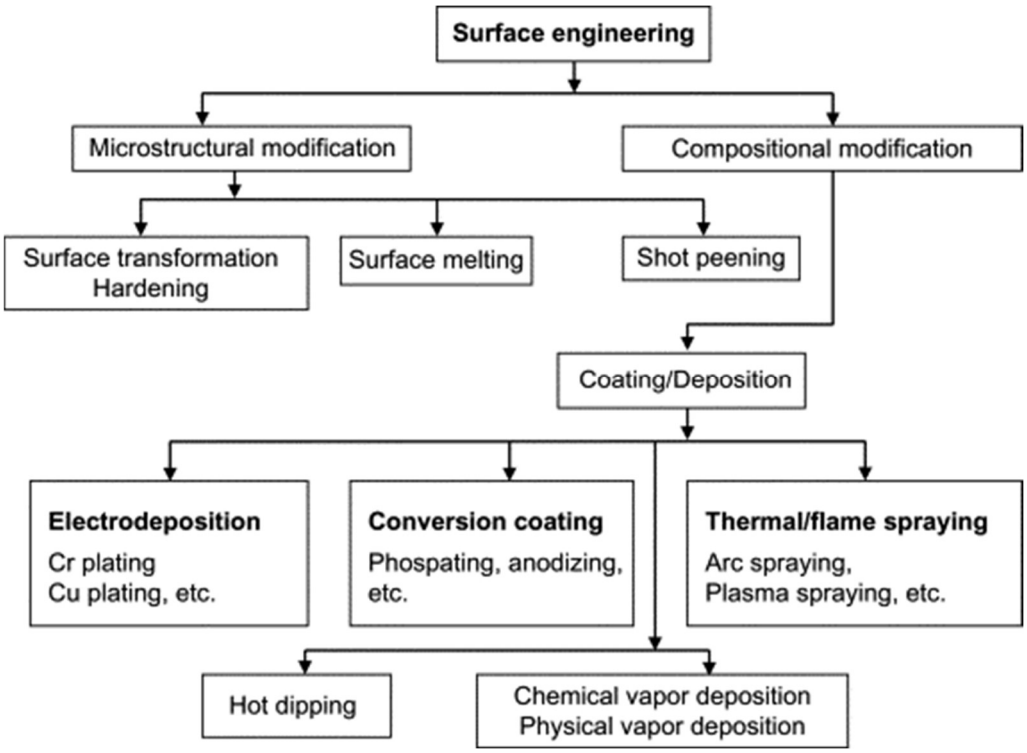

Figure 2-1: Main classification processes in surface engineering [16]

Surface engineering through the modification of the composition of the surface is of interest here; it is this route that involves the melting and deposition of materials to protect a surface. This route consists of many other sub-techniques like dipping, electroplating, vapour deposition and thermal spray [16, 17]. Desirable features of thermal spray coatings relate to the intended functional applications. Leading industrial users of thermal spray coatings is the aerospace, while other existing market include automobile, maritime and biomedical engineering. The generation of the coatings has been from the spraying of metal, cermet and/or ceramics—almost any material could be deposited by thermal spray processes [18]. Most of the materials deposited are in of the form of a rod, wire or powder fed into a plasma or a combustion gas as in a flame spray of a high velocity oxy-fuel (HVOF) thermal spray [3]. Thermally generated coatings are expected to have functional characteristics that matches with structural and microstructural features discernible through established techniques. Such

function–property relationship is essential for the fundamental understanding behind coating performance [19].

Recent efforts towards the enhancement of coating performance are potentially being sought in nanostructured coatings. deposited from solution precursor and sub-micron to nano sized materials carried in liquid media [10] or agglomerated powder particles [20]. For instance, nano-structured Al_2O_3 based ceramic coatings have benefits over their conventional counterparts including enhanced adhesive strength (65–70 MPa) [21], resistance to crack growth [11, 22], and excellent wear performance [11, 23]. The improved wear performance of nanostructured coatings is linked to the improved hardness and fracture toughness of the coatings [24]—this is because the fracture toughness and hardness have inverse relation with the square root of the particle size of the feedstock due to Hall–Petch effect [25].

Industries rely on the advances in surface engineering for some of the required innovation to drive performance. The aviation sector specifically looks forward to progresses made in thermally sprayed coatings to ensure higher inlet turbine temperature for improved thermal efficiency and reduced wear between contacting rotating surfaces to cut-down specific fuel consumption. For this purpose, thermal barrier coatings are applied to the surfaces of turbine blades, vanes, flow path cowl, jet pipe-liner and combustion chamber. Similarly, parts of the turbine engine which rotates in contact with other parts are protected against wear using wear resistant coatings. Common parts of the turbine engine with wear resistant coatings include the joints of the variable stator vanes, compressor blades, the dovetail root of the compressor blade that comes in contact with the disc during engine operations as well as casings and seals [1].

In many of the cases where thermal spray coatings are applied for protection against wear, a like-on-like procedure is implemented—i.e., the contacting surfaces will have coatings of the same type materials deposited onto the individual component surfaces. Combustor spring clips, often used between the combustor liner and the transition duct, is subjected to sliding motion resulting in local component wear which can be forestalled by the use of wear-resistant coatings. The choice of wear resistant materials is often governed by the operating temperature of the components. For instance, tungsten carbide (WC-x) based coatings are used at temperatures under 540 °C [24], chromium carbides (CrC-y) are used for temperatures of up to 815 °C while alumina (Al_2O_3) based coatings can go up to 1100 °C [1].

2.1 Thermal spray processes with liquid feedstock

Thermal spray process with liquid feedstock describes a family of surface modification processes (Figure 2-2) where submicron to nano size materials of metal and/or non-metal get heated and propelled on to a substrate forming layers of stacked lamellae (Figure 2-3) [21, 26]. The microstructural and other salient properties of the formed coating would be significantly influenced by the starting materials and spray parameters which are numerous and could be complex [21]. The obtained coating is aimed at improving the performance of a component functionalizing its surfaces for varying applications [18]. The surface modification of manufactured components that now have enhanced resistance to corrosion, wear, fatigue, amidst other such surface degradation has engendered novelty in materials applications [21]. Stringent design specifications could be met using thermal spray coatings while keeping the budget low yet maintaining quality [21]. Thermal-spray techniques has grown from yielding coatings of tens of micron-meter (μm) [27] to few millimeters (Figure 2-4) [18].

Thermal spray developed from the emergence of powder metallurgy, a consolidation manufacturing route and paint production, though incongruent fields, both use particles as starting material. The ineffectiveness and high cost of production of powder required for the powder metallurgy processing led to the introduction of melt spraying in the late 19th century [27]. Dr Max Ulrich Schoop (Zurich, Switzerland) and co. built on these principles to make coatings on substrates by developing equipment that melt and propel powdered metals. The effort yielded patents besides adding to the knowledge of surface engineering that now includes processing techniques involving the spraying of melted materials (Figure 2-2) as protective coatings and repair of components [18, 27]

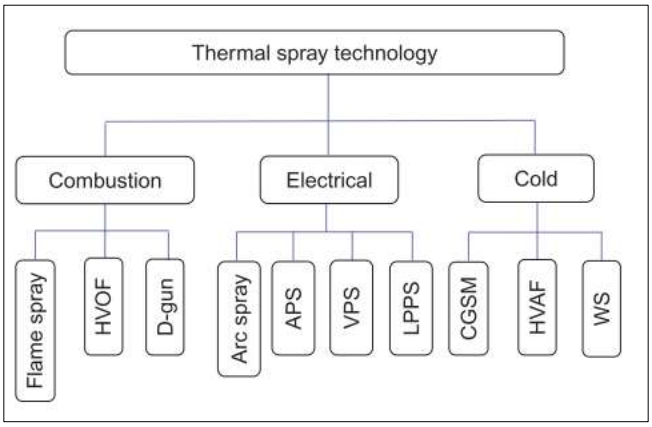

Figure 2-2: Classification of thermal spray techniques, with the acronyms meaning: HVOF (high-velocity oxygen fuel), D-gun (detonation gun), APS (atmospheric plasma spray), VPS (vacuum plasma spray), LPPS (low-pressure plasma spray), CGSM (cold gas spraying method), HVAF (high-velocity air fuel) and WS (warm spray) [18]

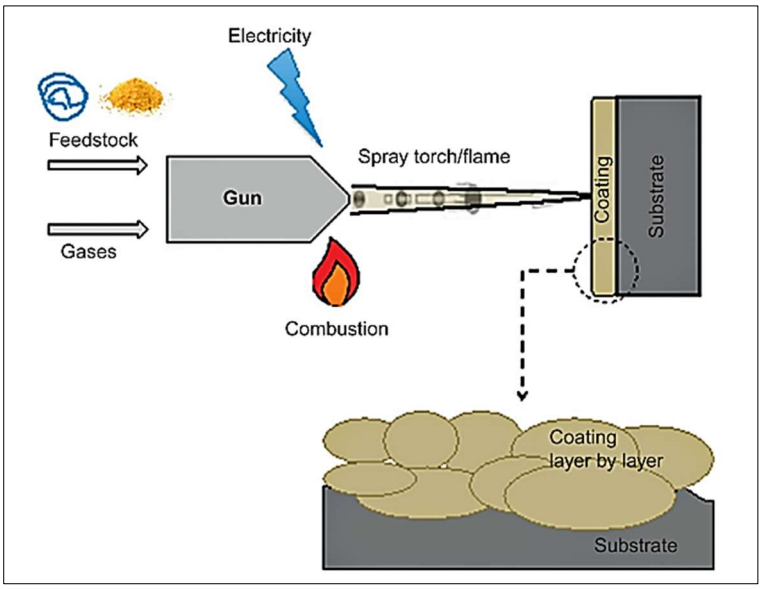

Figure 2-3: Schematic representation of thermal spray process [18]

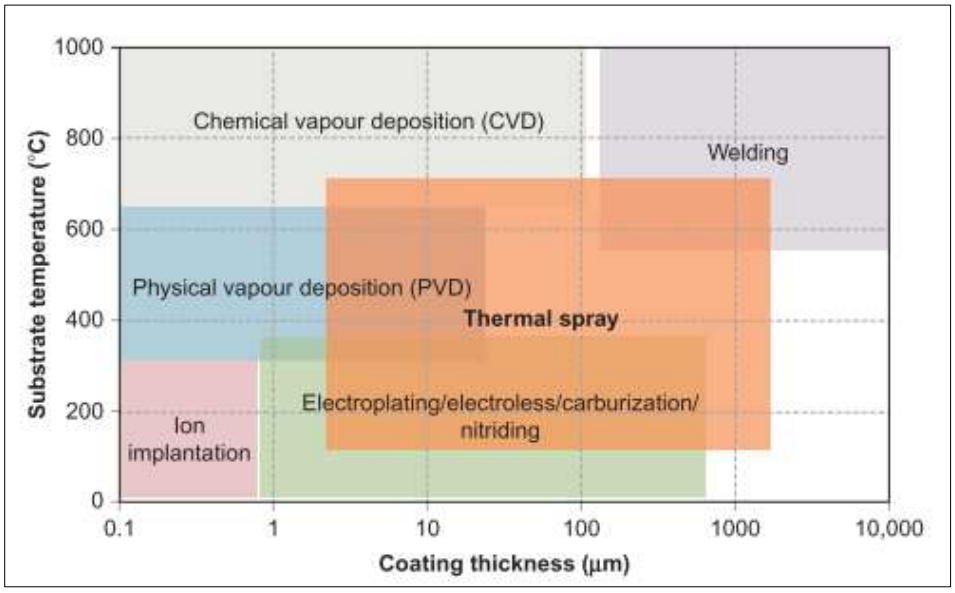

Figure 2-4: Comparison of coating techniques using deposit thickness and substrate temperature [18]

Thermal spray techniques/coating systems could be classified based on the deposition mode/heating source. This would put the techniques into three sub-families of coating systems. [7, 18]. The first category would generate heating energy via combustion of fuel (hydrogen-H_2, ethyne-C_2H_2, ethane-C_2H_4 and propane-C_3H_8) [28] and it is the

oldest since 1910s, now referred to as flame spray techniques. The second group uses electric arc of direct current type or pulsating in melting even metals of higher melting point. The most recent approach developed since 1980s use no electric energy nor flame or uses low-temperature combustion. It sought to deposit materials with their original features intact. It does so at low degree of oxidation (warm spray and air-fuel system) or without melting (solid-state spraying) [7, 18].

Classifications could also result from spray techniques meeting unique technical and/or economical needs such as productivity, controlled environment, sprayed particles' mobility and coating characteristics [7]. That needs birth invention is further buttressed by the advancement in thermal spray feedstock and equipment. After World War II, aerospace industry did require more robust and durable engine component parts [18] to meet yet increasing civic and security demands. This progress is in part due to enhanced testing methods/diagnostic tools [19, 29], process optimization, modelling, nanotechnologies and environmental requirements [18].

The choice of coating technique by clients and coating makers is often influenced by any or all of coating thickness, in-situ substrate temperature, and feedstock. These key parameters vary among the coating techniques currently in use in the industry (Figure 2-4) and would influence the robustness of coatings based on oxide contents, porosity and bond strength [18, 28]. Similarly, the industrial adoption of a coating technology is influenced by the availability of necessary equipment with guaranteed operational safety [30].

So far, two of the many thermal spray techniques have been used to spray liquid precursor feedstock. Succinct descriptions of the two techniques are presented in the following subsections.

2.1.1 High-velocity oxygen fuel (HVOF)

High velocity oxy-fuel as it is otherwise called makes coatings by melting feedstock delivered by a carrier gas (N_2 or Ar) radially or axially. The heat source is from a pressurized chamber where continuous combustion of oxy-fuel mixture occurs. This fuel could be gas or liquid (kerosene). HVOF has been recognized as an efficient, cost effective technique to make coatings of significant bond strength [18, 31]. It is thus becoming a standard for depositing ceramic-metallic coatings (cermet) materials like WC–Co. Its stand-off distance is in the range of 150–300 mm [7, 18]. No protective atmosphere is required, and powder feedstock sizes typically are in the range of 5–45 μm.

2.1.2 Plasma Spray (PS)

Plasma spraying constitutes a family of thermal spray techniques operated in the open or in a controlled space—a low pressure or vacuum chamber. A non-transferred electric arc generates heat to ionize a stream of gas to achieve in-flight melting of radially supplied feedstock (20–90 μm size range) and propel the melts to coat a substrate [32]. The ionizing temperature at which plasma is generated could be above 7000–8000 °C and at atmospheric pressure. Where two gases are used, one stabilizes the plasma (usually Ar or N_2) and ensures accelerated flow of gases and feedstock and the other (H_2 and He) improves heat transfer to the particles. The following gas mix has been reported: Ar–H_2, Ar–He, Ar–He–H_2, N_2, and N_2–H_2 [32].

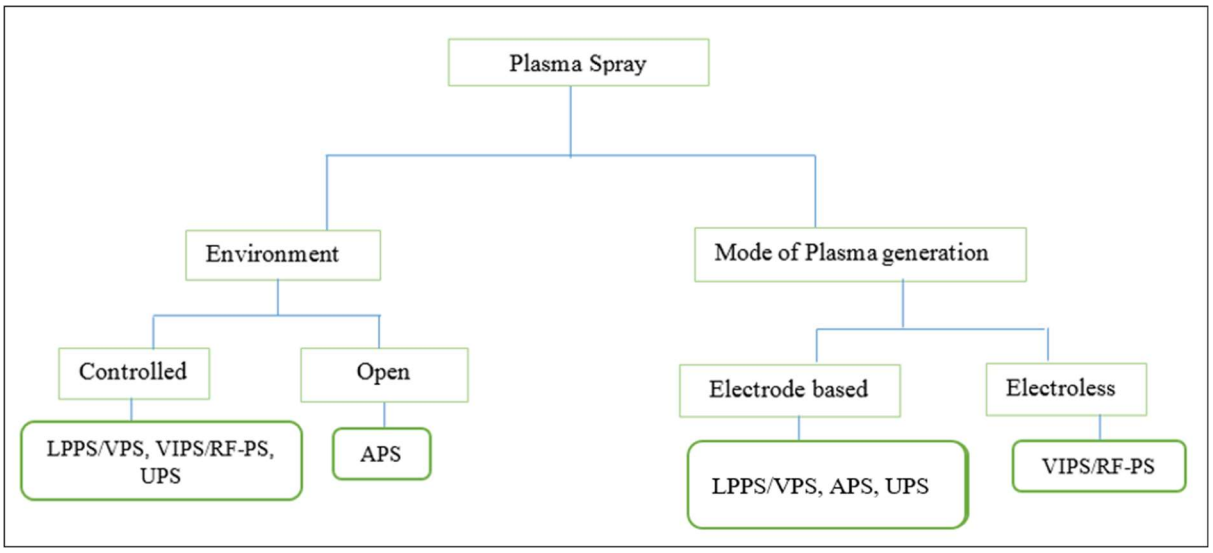

Figure 2-5: Class of Plasma Spray

The classification of the plasma spray processes (Figure 2-5) is based on the operating environment or mode of plasma generation [33]. If done in the open it is referred to has atmospheric plasma spray (APS) and if in controlled space, low pressure plasma spray (LPPS) or vacuum pressure plasma spray (VPS). When deposition is done underwater, it is referred to as under water plasma spray (UPS) which may be dry or wet method depending on how the processing space is covered [7]. APS, UPS and LPPS/VPS uses electrodes in generating plasma while vacuum induction plasma spray (VIPS) otherwise called radio frequency induction plasma spray (RF-PS) is an electroless process [32, 33]. In the electroless plasma process, electromagnetic coupling of energy into the discharge cavity occurs producing high volume, low-energy density, and low velocity (10-100 m/s) plasma with bulk temperatures in a typical range of 6,000–9,000 K. This process also allows internal axial injection of powder or suspension into the discharge cavity [33]. By implication, it could be used to spray submicron to Nano metric sized feedstock.

The quality of the coatings obtained using any of these techniques would be influenced by characteristics of the feedstock and spraying device. [33] Typically, APS though

offers up to 50 % deposition efficiency [32]. APS coatings could have oxide contaminations from reactions of melts and entrained atomic oxygen from surrounding air while VPS plasma jet yields very dense and oxide-free coatings [32, 33]. Plasma coatings could undergo post deposition treatment using any of the following: furnace annealing, laser treatment, sealing with organic and inorganic sealants, spark-plasma treatment [7].

2.2 Solution precursor and suspension for thermal spray

2.2.1 Essential characteristics of solution precursor and suspension for thermal spray

2.2.1.1 Solution precursor

The solution precursors used in the thermal spray of coatings consist of the salt of metals—it often contains the trioxonitrate ($_{-}NO_3$) or the carboxylate salts with general formula $M(RCOO)_n$–M is a metal, R is an organic compound and n is the number carboxylate group in the compound [34]. The salts selected contains the metal whose oxide is desired for a coating; aluminium triacetate ($Al(CH_3COO)_3$) has been sprayed to produce Al_2O_3 coating [35] while both zirconium tetraacetate ($Zr(CH_3COO)_4$)/yttrium trinitrate ($Y(NO_3)_3$) [36] and zirconium oxynitrate ($ZrO(NO_3)_2$)/yttrium trinitrate ($Y(NO_3)_3$)[37, 38] have been sprayed to produce both 7YSZ (ZrO_2+ 7 wt. % Y_2O_3) and 8YSZ (ZrO_2+ 8 wt. % Y_2O_3). The solution precursors contain additives—ethanoic acid has been used in precursors for Al_2O_3 [35] and YSZ [36] coatings.

2.2.1.2 Suspension

A mono or multiphase system of dispersed materials usually in a continuous medium is termed colloid. The dispersed phase would be in a size range of nanometer to the micrometer scale. Suspension is a colloidal system of solid particles dispersed in

aqueous or organic liquid. The size scale of materials in suspension implies high surface/volume ratio; this can affect the stability of the suspension if the particles agglomerate. Instability would mean coagulation or agglomeration of particles, while the former would not be spray able the latter would yield coatings with defects [39]. A stable suspension is required for coating deposition.

The obvious advantages of spraying nano- to submicron sized particles in stable suspensions should spur widespread use in the industry but their commercial supply is limited. Besides, available suspensions have limited compositions and size distribution, where however multimodal mixture exists stability is an issue [39-41]. Custom made suspensions can be prepared to achieve bimodal or multimodal size distribution in which nano sized powders are mixed with submicron- or micron-sized particles.

Suspension feedstock is prepared by mixing solid particles of the material to be deposited with or aqueous or organic liquid in a predetermined proportion—with or without additives. The main role of the additives is to ensure stability either electrostatically or sterically. The former is achieved using inorganic agents (usually acid or alkaline, depending on the pH of the medium) while the latter would require polymeric additives, otherwise called dispersants [42].

The required features of suspension for effective spray run include such characteristics as would allow:

- It to remain stable for the time of processing.
- Uninterrupted delivery to spray torch
- Effective injection with or without atomizer into flame/jet
- Non-intense cooling of jet/flame. [39, 42]

A crucial step in the spraying process is the feedstock injection/atomization and it has been shown to influence coating properties significantly [43, 44]. Its influence is however connected to the suspension properties [44] as discussed in the next subsection.

2.2.2 Spray requirements and properties of liquid feedstock: solution and suspension

Essential properties usually measured for spray suspension could include particle loading (volume or weight % concentration), pH, zeta potential/iso-electric-point (*iep)*, viscosity, surface tension, density, and stability, particle size distribution (PSD) and specific surface area (S_s). These properties are influenced by the quantity and type of materials in use. Researchers have demonstrated the interdependence of some or all these properties. While solid particle loading would impact on the viscosity and surface tension of the suspension the remaining properties would affect its stability in storage or during processing [39, 45, 46]. These properties are rarely measured for solution precursors [34].

The overall effect of suspension formulation vis-à-vis its properties connects with the coating properties through the atomization process. The atomization step impact on the suspension droplets that mix with the flame/jets determining the molten droplet size. The size of the molten droplets could correlate with grain/splat sizes which could further influence measurable properties of the coating. [43, 44] The behaviour of liquid feedstock during atomization is often characterized by some dimensionless numbers viz: Weber number (We) [47], Reynolds number (Re) [44] and Ohnesorge number (Oh) [48, 49]. Equations 2-1 to 2-3 describe the three dimensionless numbers.

$$Re = \frac{\rho_l u_l d}{\eta_l}$$ ---------- Equation 2.1

$We = \frac{\rho_l {u_l}^2 d}{\sigma_l}$ ---------- Equation 2.2

$Oh = \frac{We}{Re} = \frac{\eta_l}{\sqrt{\rho_l d \sigma_l}}$ ---------- Equation 2.3

Where ρ_l and u_l is the density of the fluid and relative speed of the suspension to the surrounding medium, respectively. The viscosity of the suspension and the surface tension are also denoted by η_l and σ_l accordingly. The internal diameter of the injector nozzle represents the diameter of first-order suspension drop corresponding the characteristic length d in the equations. Essentially, Re relates fluid inertia to viscosity and We gives the relation of inertia to surface tension (σ) which describes the resistance of suspension drops to increased surface area accompanying atomization process [44]. The atomization of the injected suspension has two breakup stages viz deformation and flattening (first stage, *We* < 12) and the second stage could have three different regimes depending on the prevailing We: bag breakup (12 < *We* < 80), stretching and thinning breakup (80 < *We* < 350) as well as catastrophic breakup respectively We ≥ 350 [50]. While it is important to understand the atomization regime of the injected liquidised feedstock, as caused by the spray parameters of a coating deposition process; atomization will not be investigated as part of the scope of this thesis.

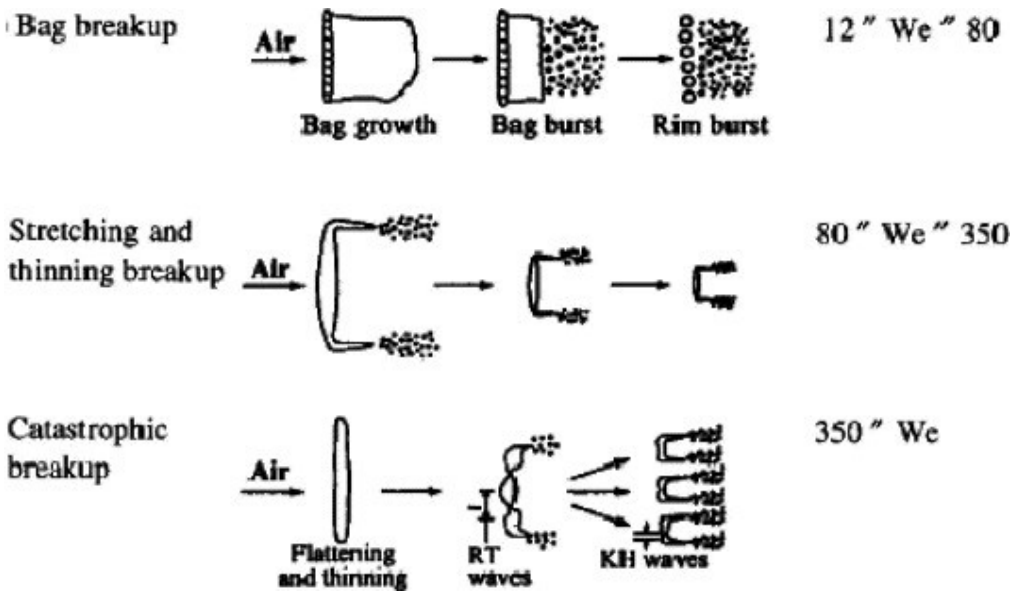

Figure 2-6: Droplet break up and atomization with the hydrodynamic criteria [51]

2.2.3 Properties of Sub-Microns and Nanostructured Al_2O_3 Suspension

Al_2O_3 like other materials could be dispersed in aqueous and/or organic medium to form suspension [42, 52]. Al_2O_3 suspension properties viz PSD, stability, viscosity, zeta potential, surface tension cum spray-ability is governed by colloidal principles. These properties could be affected by one or all of pH, particle loading and the action of dispersants [53, 54]. Submicron sized and nano Al_2O_3 suspension properties has been studied in relation to the suspension constituents by various groups and some of their findings would be presented following paragraphs.

Singh et al. [53, 54] studied submicron sized aqueous alpha Al_2O_3 suspension. The effect of pH on PSD, viscosity, zeta potential and stability of the suspension was investigated. Changes in the suspension pH from acidic towards alkalinity while maintaining 5 volume % concentration caused decreased stability as particles flocculates and viscosity increased. These results obtained without dispersants suggests suspension with low particle loading (volume %) could have optimum stability in the acidic pH range (Figure 2-7a and 2-7b). However, higher particle loading up to

20-50 volume % would require dispersants without which stability may not be optimum though Singh et al. [54] shows that it is possible to have a stable suspension with particle loading up to 25 volume % without any dispersant.

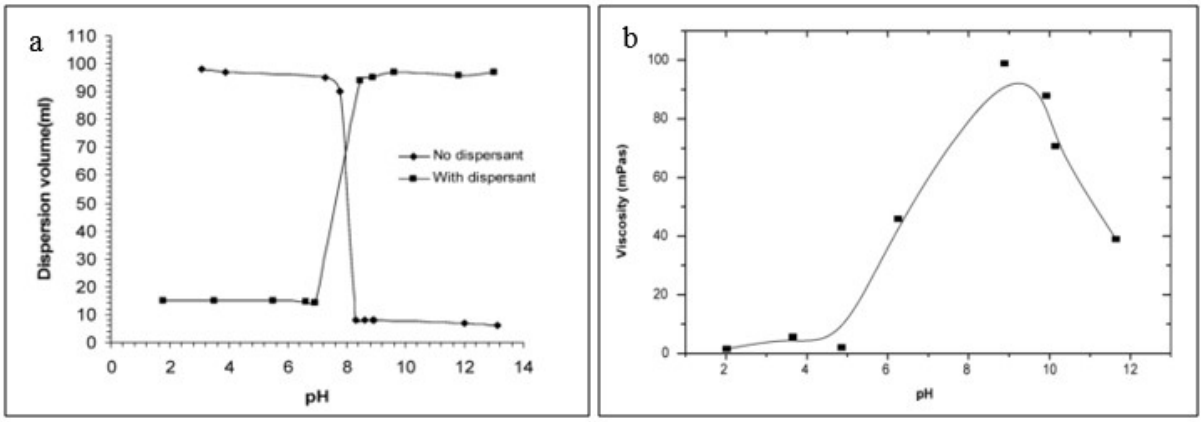

Figure 2-7: Variation of dispersion volume and viscosity with pH [53]

Similarly, the zeta potential of the suspension is influenced by pH variation with or without dispersants. Zeta potential being electrical potential gradient due to shear as particles move through a liquid medium [39] depends on the particle surface charges. The pH at which the zeta potential is zero is known as the isoelectric point (*iep*). Zeta potential values above or below *iep* would imply mobility of charged particles and a measure of the stability of the suspension. A suspension of Al_2O_3 could be stable having a non-zero zeta potential without pH modification or addition of dispersants just due to the surface charges of the suspension particles. The charge density on hydrated Al_2O_3 particles in suspension is however due to adsorption or desorption of H^+ or OH^- ions being an amphoteric oxide, where surface concentration of H^+ and OH^- equates electrostatic equilibrium is established and particle mobility is stalled the isoelectric point is reached and zeta potential goes to null (Figure 8). [54]

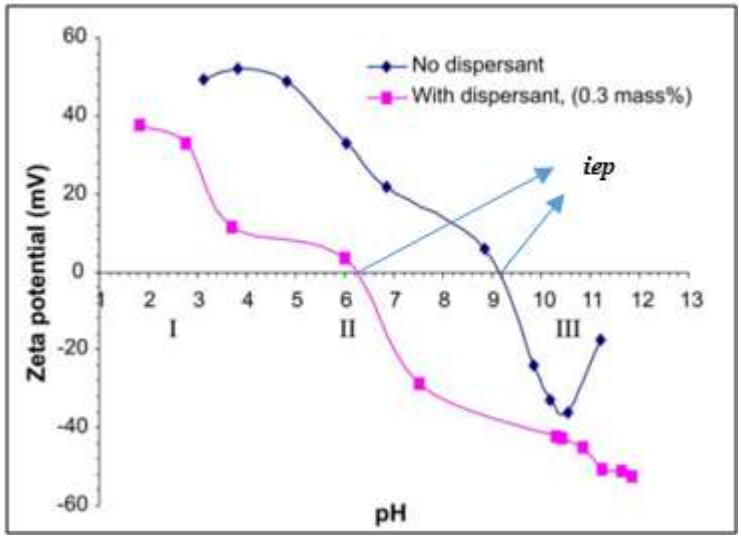

Figure 2-8: Variation of zeta potential with pH [54]

Sarama et al. [55] shows the effect of particle loading on specific surface charge and pH of Al_2O_3 particles in suspension. Increasing particle loading resulted in reversal in surface charge from positive to negative and the point of inflexion was 16.5 wt. %. This in turn led to increasing pH value making the medium alkaline remaining constant at a pH of ~ 9 (Figure 2-8).

The scenario was attributed to reduced ionic strength of the medium as H^+ get consumed as the added solids get hydrated (Equation 2.4).

$AlOH + H^+ \rightleftarrows AlO^+ + OH^-$---------- *Equation 2.4 [54]*

The implication of this includes tendency for agglomeration as the pH approaches the iep in agreement with the findings of Singh et al. [54]. Under such conditions, the addition of dispersants would increase surface charges of the suspension particles in this case making it more negative so much that the iep shifts to the left (Figure 2-9). The mutual repulsion among the particles now increases due to further adsorption of

negatively charged dispersant ions on to Al_2O_3 particles there by enhancing dispersion. [53, 54].

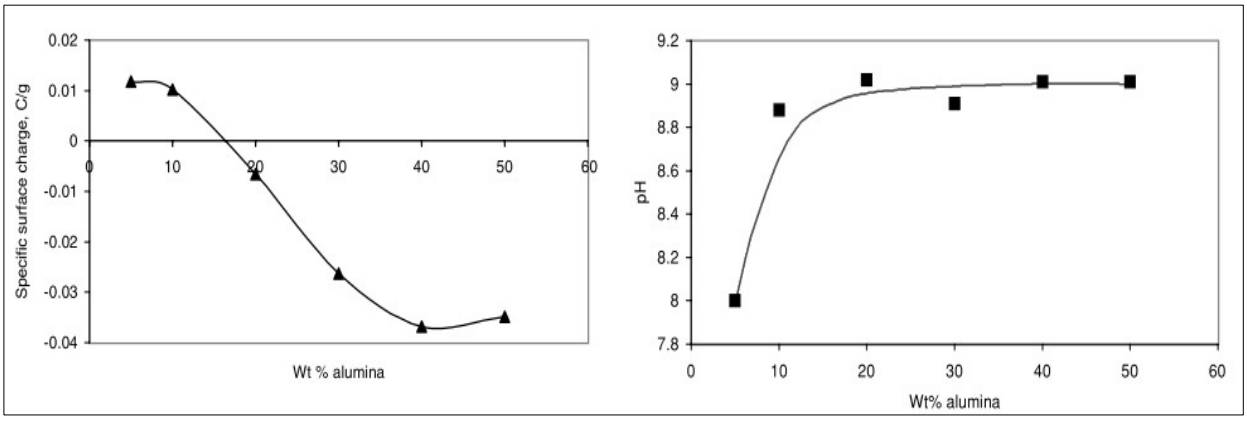

Figure 2-9: Variation of specific surface charge and pH of Al_2O_3 with particle loading [55]

However, for effective injection/atomization of suspension into flames/plasma jet it must satisfy some flow requirements. Where increased particle loading is desired, the corresponding viscosity increment may impact on spraying process. Another important point to take into consideration is that for an easier liquid injection, the viscosity of the suspension or the solution must remain as close as possible as that of the solvent.

2.2.4 Coating formation mechanisms in liquid precursor thermally sprayed coatings

Conventional thermal spray uses solid feedstock to produce coatings for different applications and specific functionality. The feedstock materials are such as stable for thermal spray conditions [18]; they have been majorly powders, rods, wires [7]. However, the need for safe and effective methods in producing nanostructured coatings engendered the use of suspensions and solutions. This idea to spray liquid feedstock came from spray pyrolysis—a technique used in ceramic powders production [42]. The use of liquid carriers in spray coatings allows varying thickness

of depositions as may be desired for different applications [56]. Both plasma spray and HVOF spray processes have been tried for suspension and solution feedstock. Electroless radio frequency induction plasma spray (RF-PS) set-up has been used to spray suspension—otherwise called suspension plasma spray (SPS) [57]. Electrode based plasma processes have been used to spray solution precursors; the process has been named solution precursor plasma spray (SPPS) [34]. SPS coatings have reduced chances of contaminations from electrodes as against SPPS which is electrode based. mainly for thermal barrier coatings (TBC) solid oxide fuel cell (SOFC). While the choice of suspension or solution precursor depends on the material to be processed, the following subsections focus on preparation and salient features of suspension-based feedstock.

2.3 Thermally sprayed Al_2O_3 coatings

2.3.1 Microstructure of thermally sprayed Al_2O_3 coatings

The microstructure of coatings evinces the extrinsic properties such as the build-up (splat layers), inclusion (partially melted, unmelted, re-solidified particles) and defect features like cracks (intra- and inter- splat), pores (of globular, interlamellar and interlayer types) and voids—see Figure 2-10. Splats are usually attributed to molten particles; however, the contact forms in-between the overlaid splats with or without inclusions would define the nature of a particular coating. The extent to which all or some of the listed features are present in a coating often influence its overall characteristics and functionality [58-60].

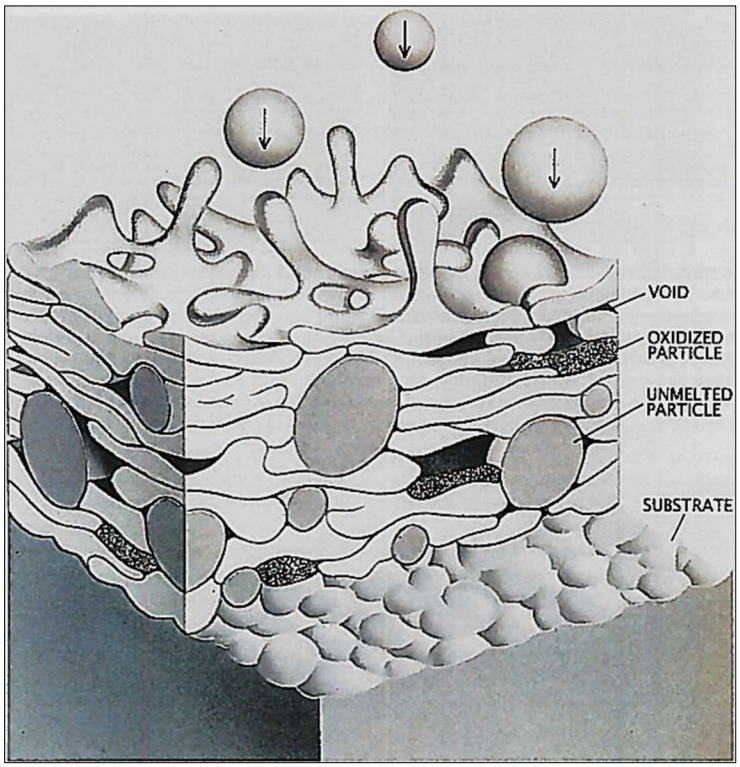

Figure 2-10: schematic showing the build-up of typical thermal sprayed coating [61]

Apart from cracks which often result due to the thermal mismatch between the coating and the substrate during cooling, the contact formed amongst the overlaid splats would also create defects like pores and voids. Pores of interlamellar and globular types are presumed to result from one or all defective contacts between overlaid splats and entrapped partially molten particles or gas [61-66]. Differently, the aforementioned coating features are not unconnected to the processing technique or the processing parameters used in the deposition of the coating [20, 47, 63, 67, 68]. More so, the characteristics of the feedstock employed in the coating deposition also influences the coating microstructure features [44, 69-71].

Coatings produced using suspension have reduced surface roughness compare to coatings from conventional processes of HVOF or APS; the Ra value for the coatings

made from suspension are in the range of 1–3 μm [30]. This is true when the suspension so sprayed is water based; the Ra value of 8–9 μm was obtained when a suspension with organic medium was used [72]. Al_2O_3 coatings produced from suspension also have denser microstructure; the porosity can be as low as ~2 % compare to ~5 % in HVOF Al_2O_3 or ~9 % in APS Al_2O_3 [73]. It should, however, be mentioned that when the suspension was isopropanol based, the porosity was above 30 %.

2.3.2 Phase stability in thermally sprayed Al_2O_3 based coatings

The structure of thermal spray coatings refers to the crystalline forms, phases or polymorphs of sprayed materials obtainable when materials undergo thermal spray processing [74]. Some of the polymorphs of Al_2O_3 reported in the literature including corundum, its stable phases are listed in Table 2-1. The polymorphism in Al_2O_3 has been attributed to varying stacking sequence of ionic oxygen layer (FCC or HCP) and the distribution cum ordering of aluminium ions on its tetrahedral and octahedral sites.

Table 2-1: Description of Al_2O_3 polymorphs [75]

S/N	Polymorphs	Crystal structure		Lattice parameters		
		FCC	HCP	a (Å)	b (Å)	c (Å)
1.	α-Al_2O_3		trigonal	4.75		12.97
2.	η-Al_2O_3		cubic	7.9	7.9	7.9
3.	κ-Al_2O_3		orthorhombic	4.69	8.18	8.87
4.	χ-Al_2O_3	hexagonal		5.56		13.44
5.	γ-Al_2O_3	cubic		7.9	7.9	7.9

6.	θ-Al_2O_3	monoclinic	1.5 a_γ	$a_\gamma \frac{\sqrt{2}}{4}$	$a_\gamma \frac{\sqrt{2}}{2}, \beta = 104°$
7.	δ-Al_2O_3	Tetragonal	a_γ	a_γ	$3a_\gamma$
8.	δ^*-Al_2O_3	Orthorhombic	a_γ	$1.5a_\gamma$	$2a_\gamma$

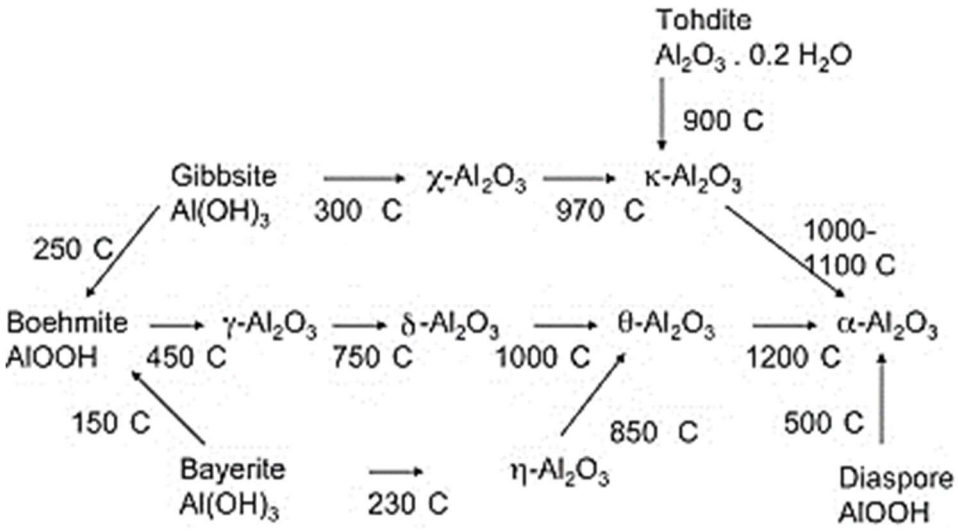

Figure 2-11: Schematic representation of the transformation amongst Al2O3 polymorphs [76]

The metastable polymorphs are often referred to as transition phases and the commonest of them are γ–, δ–, and θ– Al_2O_3 [77-80]. Thermal spray is one of the routes for obtaining transitional polymorphs of Al_2O_3 [79, 80] other than thermal oxidation of aluminium salts [75], rapid quenching of melts, dehydration of oxide and hydroxide of aluminium (see Figure 2-13), vapour deposition and heat treatment of amorphous Al_2O_3 [75, 77, 79, 80]. Structural characterization in thermal spray coatings has been through one or combination selected area electron diffraction (SAD/SAED), x-ray diffractometry (XRD) and thermal analysis (differential thermal analysis-DTA, differential scanning calorimetry-DSC, and thermal gravimetric analysis-TGA) [77].

The microstructure of coatings consists of regions of overlaid splats and those of adjoining splats, respectively; adjoining splats can be separated by inter-splat microcrack(s). Each of the regions can differ even in crystal structure as they appear to have cooled at different rates. C-J Li et al. [81] demonstrated these with plasma sprayed Al_2O_3 coating using SAD; coatings areas in the region dominated by adjoining splats contains crystalline γ–Al_2O_3 (see Figure 2–12) as against the region of overlaid splats which are amorphous (see Figure 2–13).

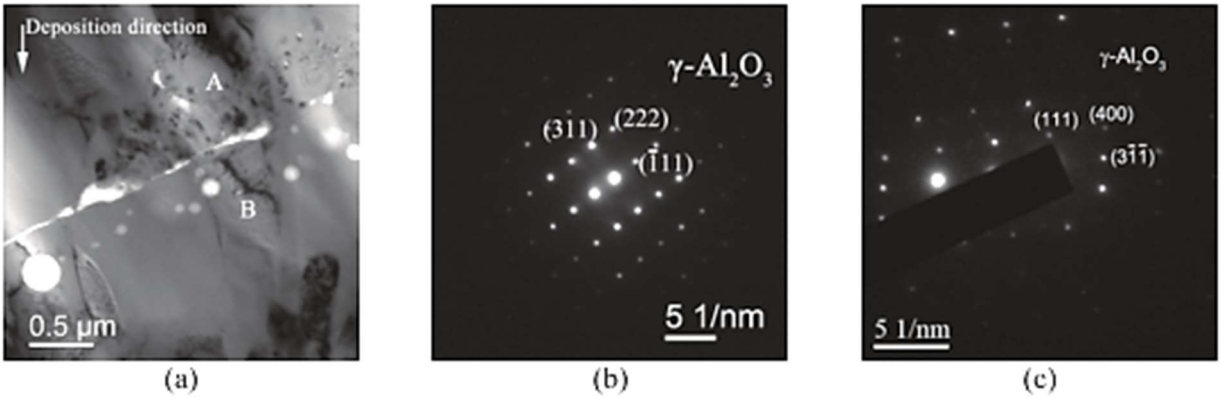

Figure 2-12: (a) Bright-field TEM image of APS-sprayed alumina coating showing region of adjoining splats; (b) SAD pattern of the region marked "A" in (a); and (c) SAD pattern of the region marked "B" in (a). [81]

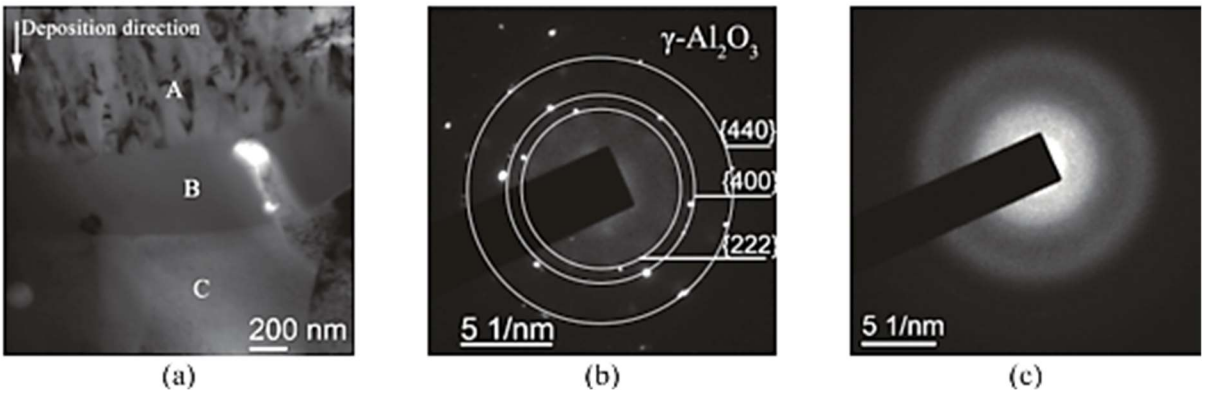

Figure 2-13: (a) Bright-field TEM image of APS-sprayed alumina coating showing region of overlaid splats; (b) SAD pattern of the region marked "A" in (a); and (c) SAD pattern of the region marked "B" in (a). [81]

2.3.3 Wear performance of thermally sprayed Al_2O_3 based coatings

Surfaces rubbing against each other often experience wear in one or both of the surfaces [82]. In turbine engines, wear manifests as erosive, sliding, and fretting wear; wear of the fan and compressor in the turbine engine often leads to increased specific fuel consumption [2]. Protection against wear has been studied for thermally sprayed powder of the carbides of transition metals (WC, Mo_2C, TiC, Cr_3C_2, TaC, NbC) and three oxides of the transition metals—Al_2O_3, TiO_2, and Cr_2O_3 [83]. Al_2O_3 suspension has been successfully processed for nanostructured coatings studied for wear applications. The average sliding wear rate of Al_2O_3 coating deposited from suspension with HVOF is in the order of 10^{-6}–10^{-5} $mm^3(Nm)^{-1}$ [21, 84, 85]. Such coating contains mostly γ–Al_2O_3 phase in the as-sprayed form whilst coatings containing mostly α–Al_2O_3 exhibit sliding wear rates up to two orders of magnitude lower at 10^{-7} $mm^3(Nm)^{-1}$, despite typically having lower porosity [85]. The wear resistance of coatings is known to increase with higher fracture toughness—the fracture toughness of a material represents it resistance to crack growth [86]. It is generally accepted that thermal sprayed coatings containing α–Al_2O_3 typically have a

higher indentation fracture toughness (~1–5.5 $MPam^{0.5}$) compare to a coating with more γ–Al_2O_3 which have fracture toughness between 0.5–2.0 $MPam^{1/2}$; the high fracture toughness engenders improved wear performance in the coating [85]. The fracture toughness is such relevant to wear performance because the pull-out failure mode in ceramic coatings will be preceded by crack initiation and propagation withing the microstructure of the coating. However, in most cases it is challenging to retain the α–Al_2O_3 phase whilst achieving a low porosity content in the coating (~2–4 %) [9, 84, 87]. Low porosity can be achieved by increasing the temperature or velocity of the in-flight powder particles, but this can also induce melting. Melting of the feedstock in thermal sprayed Al_2O_3 coatings will nucleate γ–Al_2O_3 from α–Al_2O_3 melt at the substrate surface [21, 88]—as γ–Al_2O_3 is the most energetically favourable crystalline phase [89]. When depositing thermally sprayed Al2O3 coatings, there exists a trade-off between retaining the more desired α–Al_2O_3 phase and reducing porosity in the coating.

The mechanism of wear exhibited by Al_2O_3 coatings has been related to the coating porosity, the quantity of the α–Al_2O_3 phase retained in the coating as well as the coating fracture toughness. Porous coatings have been shown to have reduced wear performance compare to dense coatings; this the superiority HVOF based Al_2O_3 coatings have over APS based Al_2O_3 coatings [90]. The porosity in coatings engenders the wear mechanism such as grain pull–out which often accompanies brittle fracture; this puts the wear in such coatings in the severe wear regime. The predominant wear mechanism in coatings with retained α–Al_2O_3 phase is the plastic flow where the wear trach shows smooth surfaces characteristic of a mild wear as against the rough surface in a severely worn surface [85, 88, 90]. Figure 2–14 shows examples worn

surfaces with evidence of pull–out and plastic flow for severe and mild wear regimes, respectively.

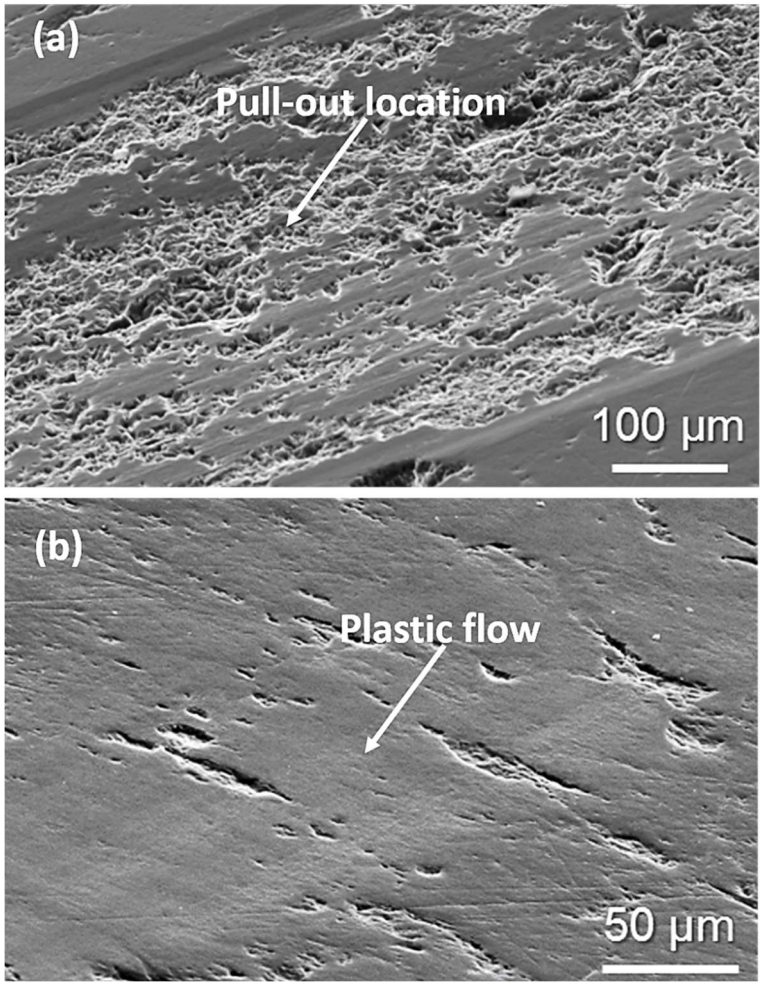

Figure 2-14: Scanning electron micrographs of wear track top surfaces showing (a) pull-out (b) plastic flow region [88]

2.4 Residual Stress in Thermally Sprayed Ceramic Coatings

Stresses are generated in coatings deposited by thermal spray processes due to the processing technique. Residual stress is the inherent stress in a material keeping it at equilibrium when unloaded [91]. The overall performance and lifetime of coatings are subject to the magnitude and nature of their residual stresses [92]. The nature of the residual stresses found in thermally sprayed coatings are primarily due to either the

deposition process or property mismatch between the coating and the substrate. The deposition process builds quenching and the peening stress in case of HVOF thermal spray; the property mismatch yields the thermal stresses. The peening stress developed due to the impact velocity of unmolten or partially molten particles impinging overlaid splats. The quenching stress developed as splats reach thermal equilibrium with underlying splats or substrate while the thermal stress formed from the cooling of the coating and the substrate—this may preclude thermal gradients [93]. The quenching stress is tensile and process specific—its magnitude increases with inter-pass coating thickness and inter-lamellae bond strength [21]. The magnitude of quenching stress reduces by through thickness yielding as splats spread, intra- and inter- splat micro cracking and interfacial sliding [93]. The peening stress is compressive giving its mode of development—its magnitude can also be reduced by the formation of micro-cracks [94]. The thermal stress, however, can be tensile or compressive depending on the thermal expansion coefficients (CTE) of the coating and the substrate. The contribution of the thermal stress can be minimized if the substrate/coating CTE ratio is approximately unity—this will reduce the mismatch strain (see Equation 2-5).

$$\varepsilon = \left(\frac{\alpha_s}{\alpha_c} - 1\right) \alpha_c \Delta T$$ ---------- *Equation 2.5*

ε is the mismatch strain; ΔT (°C) is the temperature change across the coating thickness; α_c and α_s are the thermal expansion coefficient of the coating and the substrate, respectively.

Residual stress measurement techniques vary in their accessibility and precision they include diffraction techniques (neutron and X-ray), curvature method, focus ion beam milling, hole-drilling and digital image correlation—neutron diffraction technique

offered the deepest non-destructive penetration measurement. These techniques measure residual stress in bulk materials and coatings [95]. Thermal spray coatings consist of splats and defects of different types and can have different degree of crystallinity and amorphous contents. None of the residual stress measuring techniques provides enough information on the contribution of each of the thermal spray coating constituents.

The X-ray based non-destructive diffraction technique rely on the dominant crystalline phase in a coating, to calculate its residual strain or stress [96, 97]. The residual stress measurement relies on the relationship between a measured diffraction angle θ and the lattice spacing of the identified crystalline contents of the coating. The residual stress is analysed from the shifts in the peaks of a strained sample based on the $\sin^2\psi$ method—the lattice strain ($\varepsilon_{\varphi,\psi}$) for a biaxial stress state is given in Equation 2-6 [98, 99].

$$\varepsilon_{\varphi,\psi} = \frac{1}{2} s_2^{\{hkl\}} \sigma_\varphi sin^2\psi + s_1^{\{hkl\}} [\sigma_{xx} + \sigma_{yy}] \quad \text{---------- Equation 2.6}$$

$$\varepsilon_{\varphi,\psi} = \frac{\Delta d_{\varphi,\psi}}{d_0}, \qquad s_1^{\{hkl\}} = \frac{-\upsilon}{E}, \qquad \frac{1}{2} s_2^{\{hkl\}} = \frac{1+\upsilon}{E} \quad \text{---------- Equation 2.7}$$

Equation 2-5 is based on the coordinate system shown in Figure 2-15; for a thin sample, the components normal to the plane of the sample are negligible. The share stress terms were also neglected as the sample is oriented to obtain zero share stress so that the directional stress components σ_{xx} and σ_{yy} are obtained as the principal stresses. $S_{1,2}^{\{hkl\}}$ represents the X-ray elastic constant of the sample; the equivalent equations which relates the elastic constant to the Poisson's ratio and the elastic modulus for an isotropic material are given in Equation 2-6. Combining Equation 2-6 and 2-7, it can be shown that:

$$\sigma_{\varphi} = \frac{E}{1+\upsilon} * \left(\frac{\Delta d_{\varphi,\psi}}{sin^2\psi}\right) x \frac{1}{d_0}$$ ---------- *Equation 2.8*

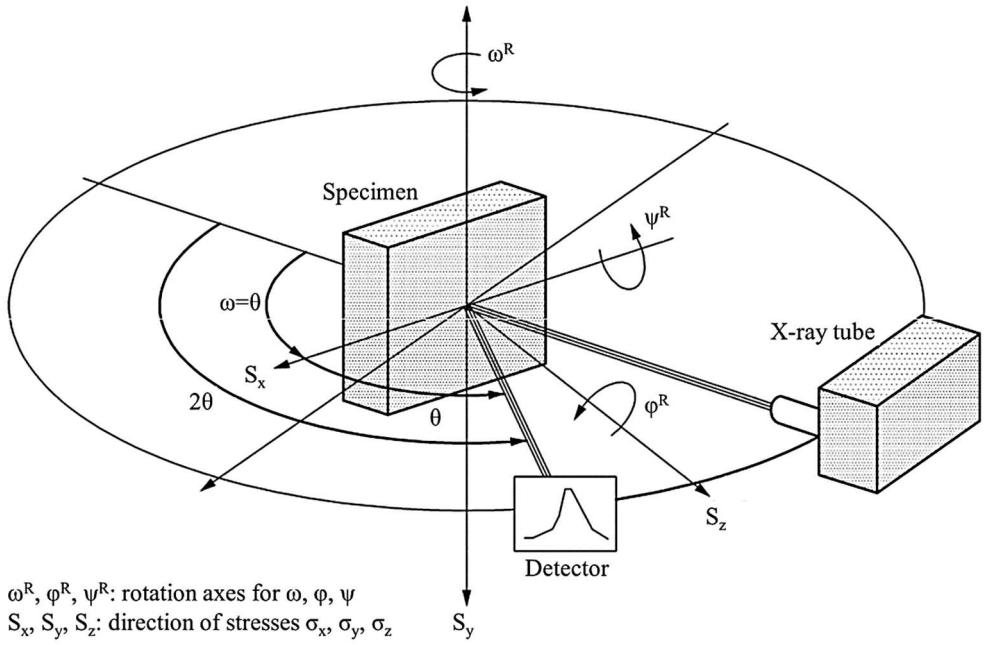

Figure 2-15: Schematic for the coordinate system of the sin^{2}ψ method [100]

Equation 2-8 gives an approximate solution for the sin^{2}ψ method; the term in the bracket represents the slope of a plot of interplanar spacing ($d_{\varphi,\psi}$) against sin^{2}ψ, d_0 denotes the intercept on the vertical axis while σ_{φ} is the stress in a direction on the surface of the sample. Other non-diffraction based residual stress measuring techniques rather provide the stress in the coatings as a bulk contribution of its constituents [101, 102]. Incremental hole-drilling—a quasi-non-destructive technique—can profile the residual stress of a coating. The incremental hole-drilling method measures residual stress through the elastic material relaxation in a sample as it undergoes stepwise drilling; the set-up of a typical incremental hold drilling is shown in Figure 2-16.

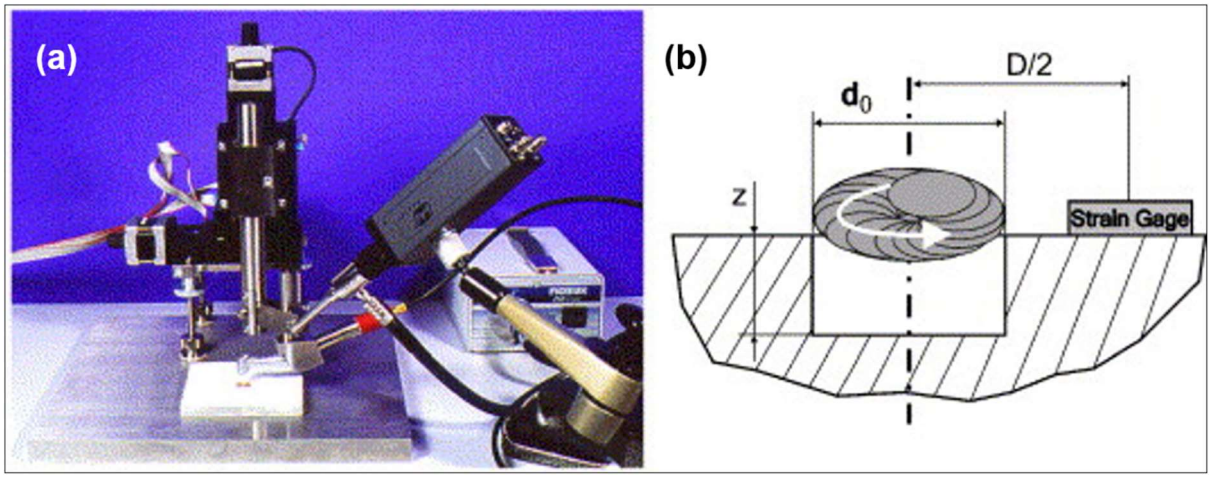

Figure 2-16: (a) Incremental hole-drilling set-up (b) schematic of the step wise cutting through a sample [103]

The stepwise drilling distorts the stress field as materials get removed the remaining material deforms elastically to rearrange the residual stress field to achieve a new equilibrium. The measurement of the deformation around the drilled hole is used in the calculation of the underlying stresses before the removal of the material [104]. A major advantage of this technique is its commercial availability, and it has been used by industry practitioners for quality assurance.

The residual stress in coatings can also be measured using the combine curvature of the coating and the underlying substrate as a composite. The curvature method can be based on the elastic or plastic deformation of the composite specimen as well as the elastic-plastic response of the composite specimen [105]. The curvature of the sample can be monitored using either laser beam or full-field optical technique. 3D digital image correlation (DIC) technique is an advanced full-field optical technique; it uses dual camera to make images of the top surface of an object before and after deformation. The process of taking the image of an object simultaneously with two cameras is called binocular stereovision (Figure 2-17(a)); the images taken are used for 3D reconstruction of the object to be studied. Triangular meshes are then

generated from the images of the deformed and the undeformed states of the object for finite element analysis (Figure 2-17(b)). The finite element analysis yields the strain in the object based on the triangular elements obtained from the mesh.

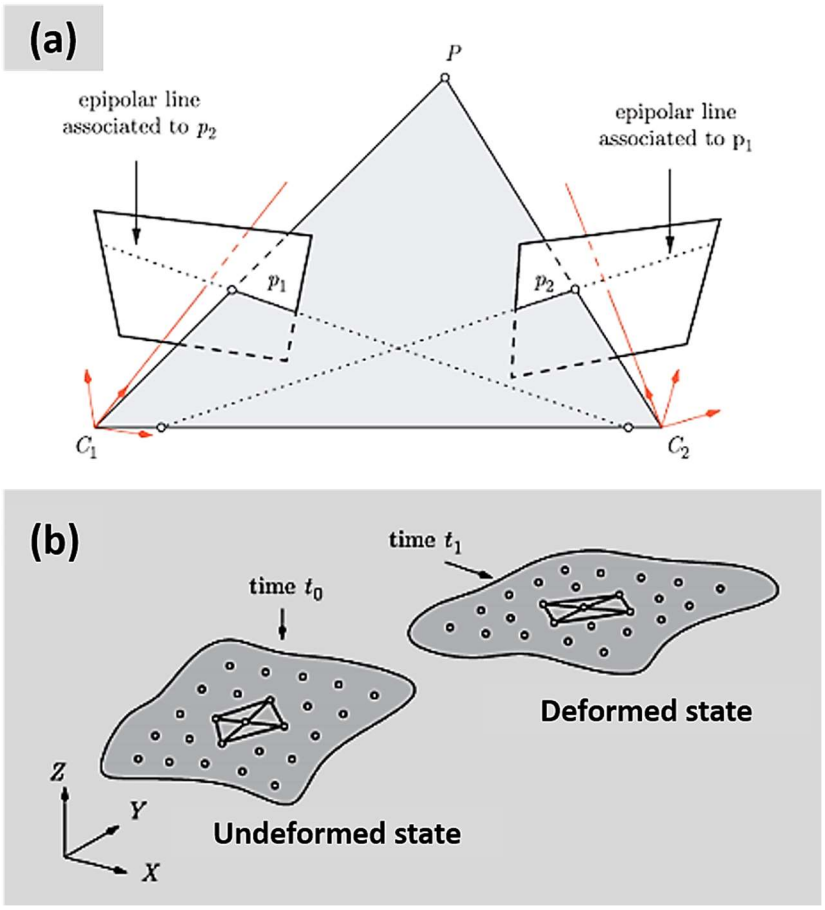

Figure 2-17: Schematic representation of a typical 3D digital image correlation (DIC) method for residual stress measurement showing (a) typical point P on a surface and its images P1 and P2 through the optical centres C1 and C2 of the two cameras respectively (b) 3D strain field showing mesh elements of the deformed and the undeformed state of the object [106]

HVOF thermal sprayed Al_2O_3 coating from micron size powder and spray dried nano powder was reported by Bolelli et al. [97]. The magnitude of the X-ray diffraction residual stress in the coating from the nanostructured powder was higher (136 MPa) as opposed to 116.5 MPa from the micron size powder—although both coatings remained tensile. In a different work, Bolelli et al. [9, 21] measured the residual stress

of HVOF sprayed Al_2O_3 coatings deposited from alcohol-based suspension using incremental hole-drilling technique—the coatings show tensile and compressive stresses. In the first work [9], the author linked the nature of the stress in the Al_2O_3 coating to deposition efficiency. Coating deposited from suspension with large agglomerates (D_{50} = 18.3 μm) has the least deposition efficiency with compressive stress profile averaging (–184 MPa). Two other coatings from suspension of smaller agglomerates (D_{50} = 1.52 μm and 2.89 μm) are thicker due to increased deposition efficiency; the residual stress profile was tensile with average of 18 MPa and 60 MPa, respectively. In the second work [21], the residual stress profile of Al_2O_3 coatings deposited from Al_2O_3 suspension of micron size particles (D_{50} = 1.26 μm) and another of sub-micron size particles (D_{50} = 0.55 μm) using different spray conditions specified by combustion chamber length and suspension injection mode (gas atomized and mechanical injection) were compressive. Even so, with the same combustion chamber length (22 mm) and the same suspension, a change in suspension injection mode changed the coating microstructure with accompanied increase in the compressive stress in the coating—the coating made with mechanical injection has –132 MPa while the other made with gas atomized injections has –238 MPa.

The residual stress in YSZ coatings varies in nature and magnitude depending on the processing route viz–a–viz deposition process, feedstock, whether powder or liquid, as well as the nature of the deposition surface. The nature and magnitude of residual stress in atmospheric plasma spray (APS) YSZ coating measured by X-ray diffraction was tensile with magnitude of 5–25 MPa [98] as opposed to 35–91 MPa of SPS coatings reported by Macwan et al. [107]. The variation in the magnitude of the stress state of APS and SPS YSZ coating might be down to the particle size distribution of

the feedstock. APS uses larger particle sizes than SPS which uses submicron– to nano size materials. Reduced particle size enhances particle heating and melting; the extent of heating of the particles is the source of the quenching stress (tensile) in the resulting coating from the particles. Based on the reduced size of the particles use in SPS, it is expected that the SPS coatings should have higher tensile stress state than the APS of the same material. On the other hand, the nature of the residual stress in SPS coatings are further influenced by the surface morphology of the substrate [108]. Zou et al. [108] measured the residual stress in the YSZ coating deposited by SPS using Raman Spectroscopy. The YSZ on APS sprayed bond coat had tensile residual stress of 7 MPa contrary to the compressive –7 MPa in the YSZ on HVOF sprayed bond coat. This disparity in the nature of the stress state of the two coatings may have stemmed from the interfacial condition between the coatings and the underlying substrate. HVOF deposited bond coats would have higher peening stress that leaves it in the compressive state compared to the APS bond coat.

It is also possible to obtain the contribution of the named sources of the residual stresses to the overall stress state of a coating. Zhu et al. [102] showed that the overall stress state of YSZ topcoat deposited by APS was compressive with tensile quenching stress (55.7 MPa) in addition to compressive thermal stress (–229.1 MPa). The dominant of the two stress sources was the thermal stress to make the overall stress state of the YSZ topcoat to be compressive with a magnitude of –173.4 MPa.

2.5 Thermal barriers coating system

Gas-turbine engines use hot gas streams to propel jets and to generate electricity. The metallic components in the gas-turbine engines are protected against the high temperature impact of the hot gas streams by thermal barrier coating (TBC) system.

TBC system consists in successive order a refractory oxide topcoat, thermally grown oxide (TGO) and a bond coat [109]. The TBC system earned its name from its refractory oxide topcoat with the main function of thermal insulation. The effectiveness of the TBC systems relies on the integrity of the topcoat specified by phase stability, thermal conductivity, low weight, high strain tolerance, coefficient of thermal expansion (CTE) at the interface with the bond coat, resistance to ambient and high temperature oxidation, chemical compatibility with the underlying bond coat and the TGO—a protective oxide [110]. The bond coat, an alloy coating, shields the base metal in the TBC system against high temperature corrosion and oxidation; it is formulated to ensure slow and sustained production of the TGO, when hot air reaches its surface through the topcoat [111]. The bond coat contains cobalt (Co) and/or nickel (Ni) as its base elements in addition to aluminium, chromium, and yttrium—this is the MCrAlY bond coat where M represents one or both of Co and Ni. Aluminide of Ni or platinum (Pt) could also be used in place of MCrAlY [112, 113].

Although the bond coat would form the TGO in response to the oxygen ingression reaching it, its constituent elements could get used up. The consumption of the alloying elements depends on the affinity of each of them to react with oxygen; aluminium has the highest oxygen affinity to form the initial protective oxide of alpha Al_2O_3 (α-Al_2O_3). Further growth of the TGO is controlled by the rate of oxygen ionic diffusivity pass the TGO or the rate of outward diffusion of aluminium from the bond coat—the thickness of the TGO could reach 1-10 μm. Unchecked degradation of the bond coat will compromise the protection provided by the TBC system; this means the microstructure of the topcoat must be engineered without compromising its desirable features to support the durability of the bond coat.

2.5.1 TBC system topcoats: microstructure, materials, and processing technique

TBC topcoat is characterized by important properties like thermal conductivity, density and strain tolerance; these properties are determined by the microstructure which is in turn influenced by material and processing conditions [114]. The standard topcoat material has been yttria stabilized zirconia (YSZ) for its desirable characteristics like a CTE of ~ 11 x 10^{-6} K^{-1} relative to the underlying bond coat, high melting point of 2700 °C and a relatively low thermal conductivity of ~2.3 WmK^{-1} at 1000 °C for a bulk sample [6]. YSZ shows ferroelastic toughening (switching between tetragonal phases t' and t'') at elevated temperatures; this makes it resist impact and erosion wear [110]. However, the ferroelastic switching compromises the integrity of YSZ at temperatures from 1200 °C; it shows eutectic composition of cubic and monoclinic phases. This is a detrimental transformation often accompanied with 3-5 % volumetric change that contributes to the topcoat failure [115]. For these reasons, YSZ has been processed with different deposition techniques in addition to a search for new topcoat materials.

APS deposited YSZ topcoat built from overlaid lamellar could reach 300 μm in thickness with arrays of microstructural defects: inter-splat boundaries, pores, and cracks (Figure 2-18). The microstructure of APS YSZ gives a porosity of 15-25 % [116, 117]; the distribution and orientation of the defects could lower its thermal conductivity to 0.7-1.0 WmK^{-1} [116]. APS YSZ topcoat could undergo 800-1000 1-hour cycles before failing due to its high residual stress state and reduced strain tolerance. The strain tolerance improves with alteration to the plasma spray conditions which ensures the formation of dense vertically cracked otherwise called segmented coating (Figure 2-19); the vertical cracks could reach 3-10 per millimeter depending on the temperature of the substrate and the impinging particles. A typical segmented coating

with ~ 3.6 mm^{-1} segmented crack density shows a thermal shock cycling life that exceeds 1700 [118]. However, the increased density of the segmented coating raises the thermal conductivity to 1.3-1.8 WmK^{-1} [109].

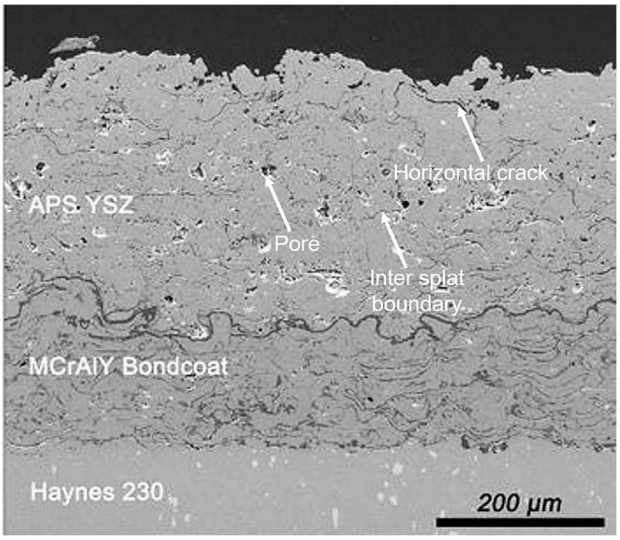

Figure 2-18: Cross-sectional SEM image of a TBC system showing typical APS YSZ topcoat microstrutural features [116]

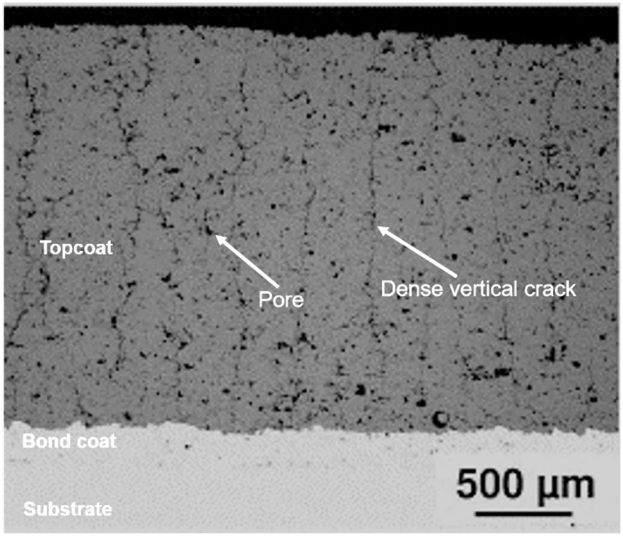

Figure 2-19: Cross-sectional SEM image of segmented APS YSZ topcoat showing pores and dense vertical cracks [118]

Even more compliant topcoats has been produced with another processing technique, electron beam physical vapour deposition (EB-PVD) [119]. The deposition rate of EB-PVD is controlled by the deposition parameters, chamber pressure and substrate temperature [120]. The deposition rate reaches 2 μm/min if the chamber pressure is maintained at 10^{-2} Pa and the substrate temperature kept at 800–900 °C [121]. EB-PVD deposited YSZ presents feathery microstructure of columnar YSZ grains (2-10 μm in diameter); it has globular and spheroid pores though not enough to lower its thermal conductivity (~1.5-2.0 WmK^{-1}) compare to the segmented coatings [6, 122, 123].

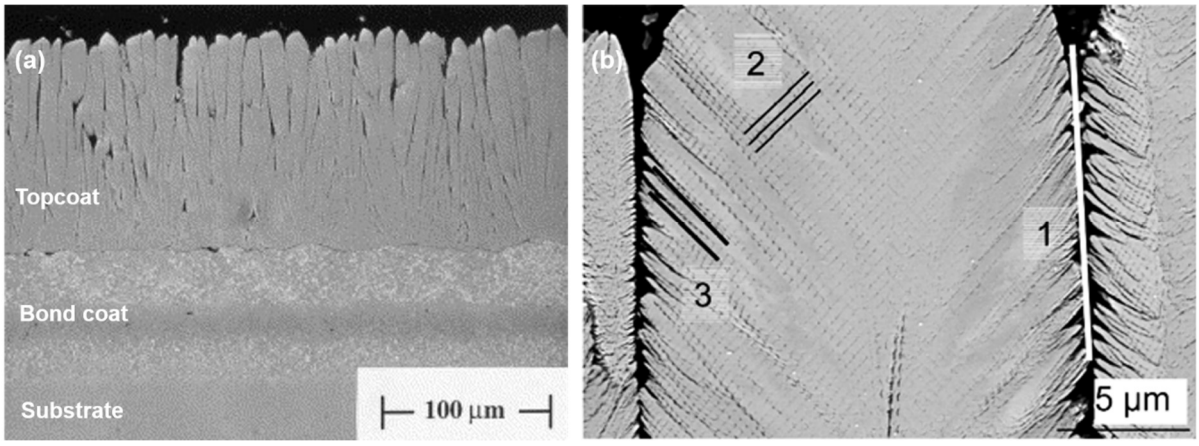

Figure 2-20: SEM image of columnar YSZ deposited by EB-PVD (a) Cross-section showing the columnar topcoat, the bond coat and the substrate [123] (b) magnified columnar grain showing columns and inter-columnar gaps marked (1), globular and spheroid pores marked (2) and the feather arm marked (3) [122]

Although EB-PVD produced topcoats with improved life cycle because of its columnar microstructure (Figure 2-20)—a reason for its use in the industry. The mechanism of formation of the columnar microstructure is governed by either the 3D island growth (Volmer–Weber model, VW model) or the 3D islands on the top of one or a few epitaxial layers (Stranski–Krastanov model, SK model). The dominant of the two models is dependent on the material parameters of the substrate and the deposit as

well as the supersaturation of the vapour. The formation of island structure is preceded by the condensation of vapour to form clusters. As the deposition and surface diffusion of the vapour cluster go on, the island grows to unite with nearby islands. The joint island structure would thus grow perpendicular to the substrates to form the columnar structure [124]. However, the deposition rate in EB-PVD is slow and expensive to run [6, 125, 126]. Plasma spray physical vapour deposition (PS-PVD) a modified vacuum plasma spray (VPS) process seems to resolve the challenges found with EB-PVD; it can be operated cheaper yet with higher deposition efficiency.

PS-PVD operates at higher electrical input power (150-180 kW) which ensures melting and evaporation of the feedstock. It uses consolidated nano-sized [124] and/or submicron-sized YSZ powder [127, 128] to facilitate the melting and evaporation of the powder. PS-PVD offers columnar microstructure, dense microstructure with distributed pores and mixed microstructure of columnar and dense layers [124, 129]. Figure 2-21 shows PS-PVD YSZ columnar structure similar to those found in EB-PVD; this microstructure formed from evaporated particles usually at a spray distance of 1000 mm [124, 125]. However, the process was tailored by sequence of low deposition rate steps and extended pre-oxidation of the bond coat surface to achieve double the life cycle of an APS topcoat in a burner rig test [126]. The PS-PVD topcoat combines the strain tolerance of the EB-PVD YSZ and the low thermal conductivity of APS YSZ topcoats; the thermal cycling life of the PS-PVD topcoat reached 1000 cycles in a burner rig test while its thermal conductivity was 0.8 W/mK [125].

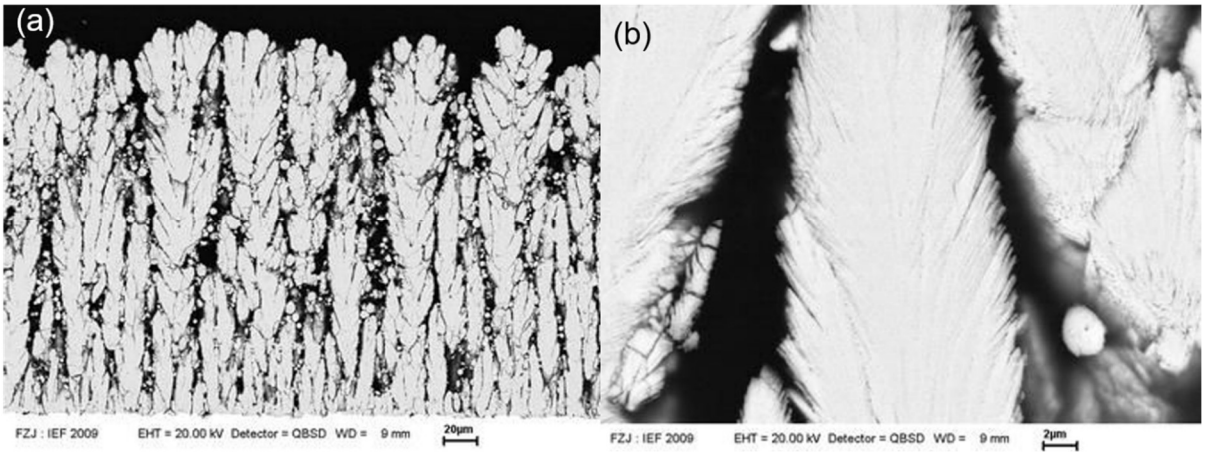

Figure 2-21: : SEM image of columnar YSZ deposited by PS-PVD (a) Cross-section showing the columnar grains and the inter-columnar gaps in the topcoat (b) magnified columnar grain showing the columns and inter-columnar gaps and the feathery arms [125]

Existing TBC works seems to demonstrate that improved TBC life cycle can be achieved in either or both of columnar coatings and segmented coatings, further search had gone into reducing the thermal conductivity of the two types of topcoats. Reduction in thermal conductivity comes with increased porosity; the new topcoat would be a coating that will combine higher porosity with segmented cracks or columnar grains. This new topcoat was further sought in submicron-sized feedstock and solution precursor. Submicron-sized YSZ can be sprayed as consolidated powder as has been used in PS-PVD [127, 128] or in liquid carrier as in suspension plasma spray (SPS) process [130-132]. SPS produces segmented coating [133, 134], APS overlaid lamellar built microstructure and columnar coatings [130]. SPS would produce the APS kind of microstructure (Figure 2-22) if the topcoat is sprayed using suspension with micron size powder (D_{50} = 15 ± 6µm); it produces segmented coating with nanometric powder (D_{50} = 25 nm) in suspension (Figure 2-23 (a)) [133] or submicron sized powder (D_{50} = 320 nm) in suspension (Figure 2-23 (b)) [134].

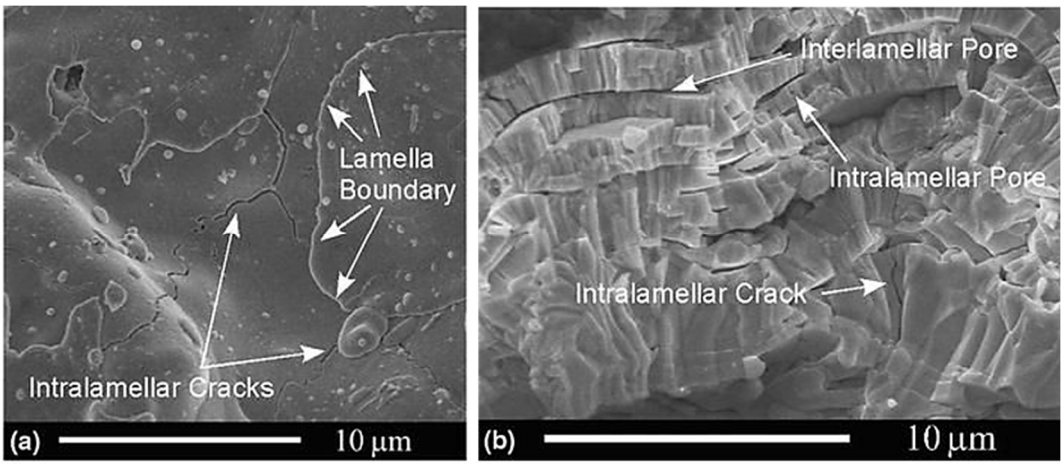

Figure 2-22: SEM images showing the standard APS microstructure obtained from SPS of micro sized powder in suspension (a) a high magnification of the top surface and (b) a fractured cross section normal to the substrate [130]

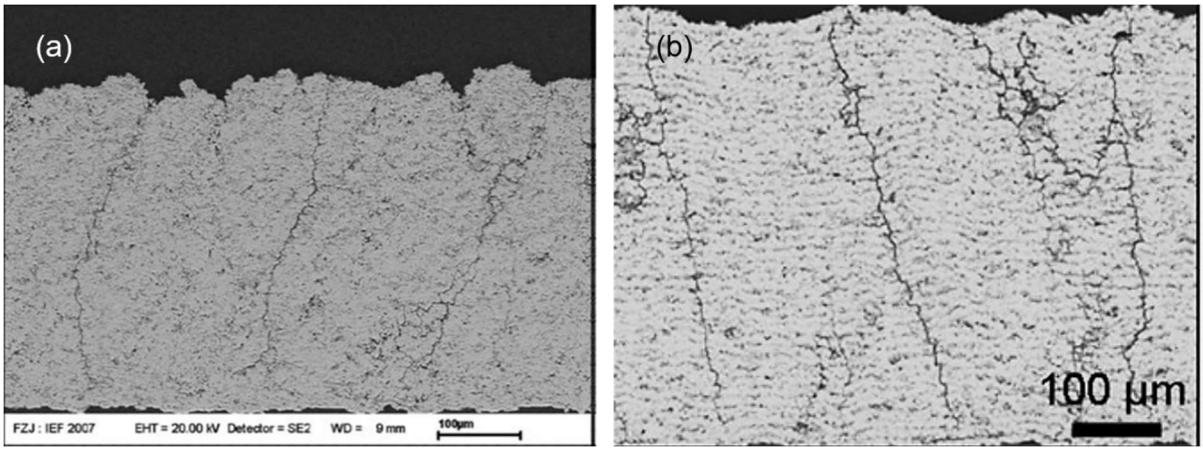

Figure 2-23: SEM cross sectional images of segmented coating microstructure obtained from SPS (a) nanometric sized powder in [133] (b) submicron sized powder in suspension [134]

Kassner et al. [133] suggested segmented coating produced by SPS could have high porosity and high strain tolerance due to his high segmentation crack density (7 cracks/mm) compare to 5 cracks/mm in APS coatings. The segmentation crack density in SPS coatings seems to be controlled by spray parameters (stand-off distance and plasma torch power) and suspension particle loading [12]. The segmentation crack density increases with the spray parameters (40-60 mm stand-off

distance and 50-70 kW torch power); ~ 7/mm at the minimum and could reach 13/mm as the parameter increased. However, when the particle loading is fixed at 20 wt. %, the stand-off distance kept at 50 mm and torch was operated at 65 kW, the coating obtained showed combined microstructure with columnar grains and vertical cracks [12]. Differently, Ganvir et al. [135] produced SPS topcoats with varying microstructure using a 30 wt. % load suspension with micrometric particle size (D_{50}: < 3 μm and < 10 μm). The SPS topcoats deposited under this condition produced a microstructure intermediate between the columnar based and the lamellae-based microstructure. This intermediate microstructure presents with the vertical cracks like the ones in the columnar microstructure of EB-PVD topcoats and the inter-pass boundaries as in lamellae microstructure of APS topcoats.

The columnar grains formed in SPS coatings (Figure 2-24) results from the droplet size formed from the atomization of the suspension entering the plasma plume [130] and the roughness of the deposition surface [136]. The reduced droplet size from the atomization of the suspension caused the droplets to take a divergent trajectory from the direction spray; the droplets then travelled parallel to the deposition surface to get caught by surface asperities causing lateral and vertical growth of the deposits. The lateral growth defines the columnar grains width while the vertical growth defines the eventual coating thickness [130].

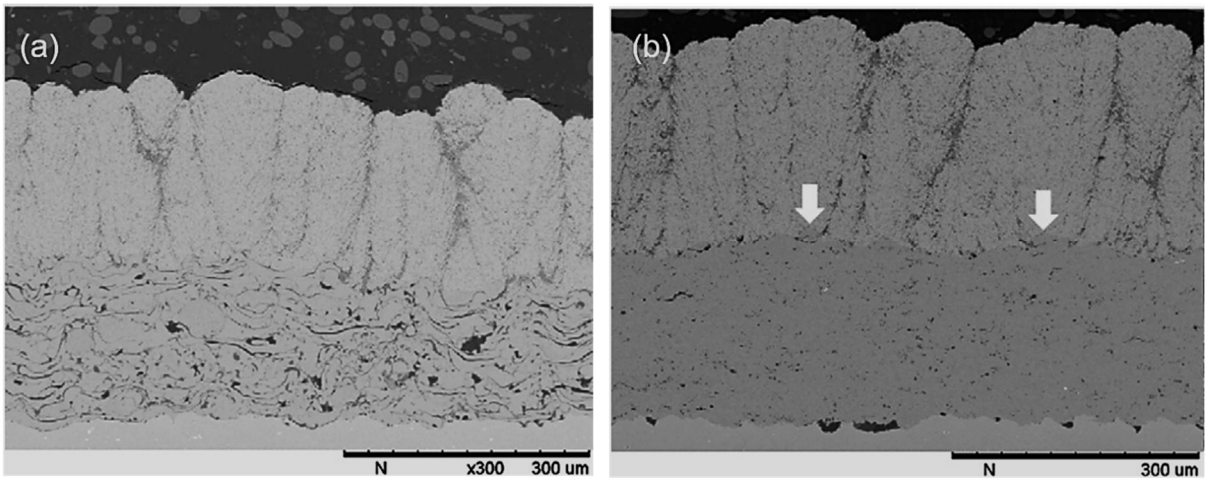

Figure 2-24: SEM cross sectional images of columnar coating microstructure obtained from SPS (a) deposited on as-sprayed APS bond coat (b) deposited on as-sprayed HVAF bond coat [136]

Other than the size of the droplets obtained from atomization of the suspension, VanEvery et al. [130] showed that the particle loading in the individual droplet of suspension interacting with the plasma plume controls the size of the lamellar formed in the SPS columnar microstructure—the lamellar size increases with suspension particle loading. Differently, the amount of suspension (particles and carrier medium) interacting with the plasma plume could be specified by the suspension feed rate. Bernard et al. [137] showed that increased suspension feed rate (25 g/min to 44 g/min) caused reduced deposition efficiency of up to 14 %; the loss in deposition efficiency was attributed to reduced heat treatment of the injected particles which resulted in overspray. Overspray means molten particles got shrouded in partly molten or unmolten particles with poor or no adhesion; the poor adhesion caused these particles to fall off during the spray there by creating inter pass porosity [138]. Inter pass boundaries are great for reduced thermal conductivity in topcoats [138, 139] but they could be lateral crack initiation point; the growth of lateral cracks would compromise the structural integrity and life cycle performance of the topcoat [108].

The surface roughness on the other hand seems to dictate the number and morphology of the columnar grains that form the coating. Curry et al. [136] and Zou et al. [108] deposited columnar SPS topcoats on different bond coat surfaces. Curry et al. made APS and high velocity air fuel (HVAF) deposited bond coat surfaces to varying roughness finish: polished, grit blasted, polished then grit blasted and as-sprayed—only the as-sprayed cases are presented here (Figure 2-24) while Zou et al. [108] used as-sprayed APS and HVOF deposited bond coats (Figure 2-25). The number and the width of the columnar grains decreased with increasing surface roughness. The as-sprayed APS bond coat presented rougher surface (R_a = 11-12 μm) in both studies compare to the as-sprayed HVAF bond coat (R_a = 8-9 μm) and HVOF (R_a = 5-6 μm). The SPS topcoats on HVOF bond coat have the narrowest and the highest number of columns amongst the three samples. However, the morphology of the columns presents with broad top tapering down towards the deposition surface. The SPS topcoats produced by Curry et al. [138] varies significantly from those produced by Zou et al. [108] Those from the latter has inter pass boundaries, clearer inter columnar gaps with broader column tops. The variation could be from the particle loading and the size distribution of the 8 wt. % YSZ suspension used in the topcoat deposition; the former used 10 wt. % loaded suspension containing 500 nm D_{50} particles while the latter used 25 wt. % loaded suspension containing 50 nm D_{50} particles. The high inter pass boundaries in the SPS topcoats from Zou et al. could have been due to the increased feed rate of 45 ml/min as presented earlier.

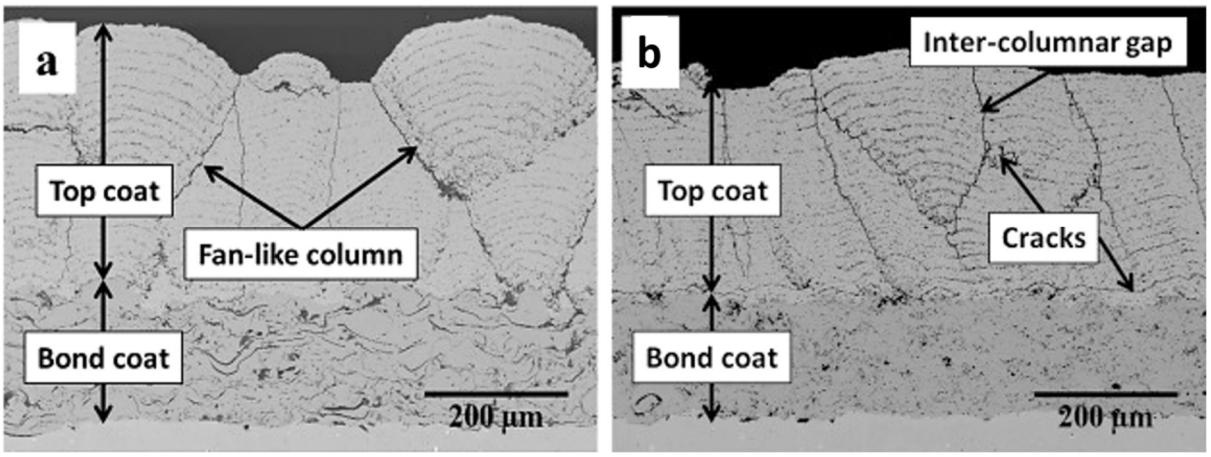

Figure 2-25: SEM cross sectional images of columnar coating microstructure obtained from SPS (a) deposited on as-sprayed APS bond coat (b) deposited on as-sprayed HVOF bond coat [108]

From the foregoing, topcoats with varying microstructure could be produced with YSZ based on the processing technique and the deposition parameters on the one hand and the deposition surface on the other. However, the varying microstructure (layered with inter-lamella pores, segmented and columnar) allows for the control of thermal conductivity and strain tolerance; it does not address the question of phase stability at elevated temperature nor the chemical resistance against CMAS (calcium-magnesium-alumino-silicate) attack. Open microstructure such as produced by APS, SPS and EB-PVD would not prevent CMAS incursion nor direct oxygen conduction to the underlying bond coat. Both the oxygen infiltration and CMAS incursion could be addressed by the change of material or processing technique. Even for the implementation of either of these two solutions, a new topcoat material other than YSZ would be necessary. This is because oxygen can also reach the bond coat by the ionic conduction through the lattice structure of YSZ [140]. The ionic oxygen conductivity of YSZ increases with temperature and its yttria (Y_2O_3) content [141].

Phase stability in YSZ topcoats

Besides the issue of oxygen conduction through the microstructure and the lattice structure of YSZ, it undergoes undesirable phase transitions between its metastable phases of t', yttrium lean tetragonal and yttrium rich cubic phase at temperatures around 1200 °C [142]. The undesirable phase transition could also occur due to calcium magnesium-alumino-silicate (CMAS) attack. Molten CMAS dissolves YSZ through selective removal of yttrium ions in the YSZ structure: this destabilizes the metastable tetragonal phase and results in its transformation to monoclinic with an accompanied 2–5 % volumetric expansion [143]. CMAS is found in volcanic ash, sand and runway rubbles; it infiltrates the topcoat from the air carried into the turbine engine [110]. Again, YSZ coatings sinter at temperatures from 1000 °C: this causes densification in nano structured YSZ coatings [144] and necking in the atmospheric plasma (APS) sprayed YSZ coatings [115]. The necking reduces the strain tolerance of the APS YSZ coating leading to increased stiffness and internal stress—a phenomenon that compromises the thermal cyclic life of the coating.

Alternative topcoat materials

Four categories of alternate topcoat materials (defect clusters, perovskites, hexa-aluminates and pyrochlores) to YSZ are being investigated in the development of the next generation TBCs due to one or more properties between lower thermal conductivity, high melting point, increased thermal cycling life, high temperature phase stability, and resistance to CMAS attack. Pyrochlores ($A_2B_2O_7$ structure with A being +3 or +2 cations and B +4 or +5 cations) are the most studied alternate materials of the four categories because of the combined properties of low thermal conductivity, high temperature phase stability, and resistance to CMAS attack [109]. A

representative pyrochlore ($Gd_2Zr_2O_7$) resists CMAS infiltration and can be deposited without any stoichiometry loss as is the case with plasma sprayed $La_2Zr_2O_7$—it loses La_2O_3. $Gd_2Zr_2O_7$ reacts with calcium and silicon in the CMAS to form gadolinium apatite. However, its major drawback remains instability with the TGO layer; it reacts with the TGO to form a porous perovskite ($GdAlO_3$) which will further compromise the integrity of the bond coat [145]. Differently, Padture and Klemens [146] proposed yttrium aluminium garnet (YAG) as TBC topcoat material because of its lower grain boundary oxygen diffusivity (10^{-20} m^2/s) compared to YSZ (10^{-10} m^2/s); it has high temperature phase stability [140, 147], resistance to sintering, CMAS attack and it does not react with the TGO layer [116, 145]. These considerations have put YAG as a material of choice in the development of the next generation TBC topcoat. However, the microstructure of YAG coating must be carefully engineered to resist oxygen conduction [148] and CMAS attack [143] without compromising durability—since a porous coating allows influx of oxygen and CMAS materials.

Thermally sprayed YAG topcoat

YAG coatings have been deposited using radio frequency precursor plasma spray process [149]. The as-sprayed coating was fully crystalline, porous, and nanostructured; its main phase was hexagonal yttrium aluminium perovskite (YAP) with some yttrium aluminium monoclinic (YAM). Post spray plasma treatment of the as-sprayed coating in 10 s transformed it to mainly YAG and some orthorhombic YAP. The first TBC work to incorporate YAG was a multilayer TBC produced by small particle plasma spray process—a variant of APS [140]. A porous YAG coating (10 μm) was sandwiched between layers of YSZ coating (30 and 200 μm) for phase stability and in another architecture, the 10 μm porous YAG coating was deposited on an 80

μm thick YSZ coating for oxidation protection. The YAG layer, although porous, prevents Y_2O_3 depletion at the YSZ/YAG interface to ensure phase stability for the YSZ in the sandwich architecture; it also slows down TGO growth rate in the latter architecture by a factor of about three. A fully dense YAG has oxygen diffusivity 10 orders below that of a dense YSZ. A columnar YAG coating with some YAP, YAM and Y_2O_3 was produced by electrostatic spray-assisted vapour deposition (ESAVD) using solution precursor [150]. The coating has uniformly distributed inter-columnar spacing of 2 μm which would aid oxygen influx to the bond coat. The ESAVD technique could be a means to produce strain compliant YAG coating but it has low deposition efficiency, besides the coating needs post deposition heat treatment at temperatures of 700-900 °C to form pure YAG.

Weyant and Faber [148] studied APS deposited YAG to provide a model through the design of experiment that links microstructure features with plasma spray process deposition parameters. The flame power and the standoff distance was found to control the porosity and the crystallinity of the YAG coating, using powder with the standard particle size range—they found that coatings with low porosity are mostly amorphous and vice versa. However, the amorphous coatings would crystalize to YAG in ~ 18 min at 900 °C without sintering. Gu et al. [151] sprayed composite YAG/YSZ coating using APS with varying mix of the YAG and YSZ powders. The composite coating is dense with amorphous YAG, crystalline YAG and YAP phases in crystalline YSZ coating. The crystallization of the amorphous YAG is suppressed by YSZ, even at 1200 °C it takes 12 h to achieve full crystallinity as against pure amorphous YAG coating, which crystalizes in 30 min at 920 °C. The crystallization process of the amorphous YAG in the composite coating also initiates and propagates micro cracks

that would form oxygen pathway to the bond coat. Kumar et al. [145, 152] reported YAG TBC deposited by solution precursor plasma spray (SPPS). The YAG TBC was engineered to possess a stack of horizontal micro pores which they termed inter-pass boundaries. The inter-pass boundaries were shown to support the low thermal conductivity and strain compliance of the coating that ensures its durability supersedes APS YSZ with or without CMAS presence. However, with the continued interest in YAG based TBC topcoats, high velocity oxy-fuel (HVOF) thermal spray could provide variant microstructures based on effective combination of materials and processing technique.

2.5.2 Thermal conductivity in TBC topcoats

The determination of the thermal conductivity of the topcoat in a TBC is however not straight forward. Often times, the measurement is done in a layered configuration while the topcoat is bonded to a substrate [135, 153, 154] at other times, the topcoat is obtained as a free-standing coating. Available literatures suggest there is little or no consideration for what the standard configuration should be for obtaining the thermal conductivity of the TBC topcoats. The desired thermal conductivity value of ~1.0 $Wm^{-1}K^{-1}$ [155] for as–sprayed TBC topcoat has been consistently sought through the modification of the topcoat microstructure by trying different materials and/or deposition process/parameters. It has not mattered whether the thermal conductivity is obtained using the layered configuration approach consisting of topcoat plus substrate or using free-standing coatings.

Depending on the processing technology and conditions, the thermal conductivity of as-sprayed 7–8 YSZ measured at room temperature lies in the range of 0.5–1.6 $Wm^{-1}K^{-1}$ (see Table 2-2). Specifically, the quantitative contribution of a YAG topcoat to

the thermal conductivity of a combined layered architecture of YAG/YSZ was not presented by Su et al. [140]. In the configuration, a lamella based YAG deposited by APS laid on APS deposited YSZ; the combined architecture has as-sprayed conductivity of 1.05 $Wm^{-1}K^{-1}$. This value suggests the combine configuration could have some merit in utilizing the properties of its constituent layer materials; especially when the value is just 5% above the desired value of 1.0 $Wm^{-1}K^{-1}$ and ~ 33 % less than the value of a single layer EB–PVD deposited YSZ. More so, at elevated temperature above 1000 °C single layer YAG with engineered porosity layers showed reduced thermal conductivity as the coating resisted sintering. The distribution of the porous layers within the coating thickness to be perpendicular to the direction of the heat flow prolonged the heat conduction path. Differently, where the as-sprayed coating has amorphous contents, the thermal conductivity of the coating will increase when amorphous to crystalline phase transition occurs at the elevated temperature [156].

Table 2-2: Thermal conductivity of TBC topcoats from powder compared to those from suspension and solution precursor based on microstructure and measurement configuration.

S/N	Materials	Process	Microstructure	Measurement configuration	Thermal conductivity (λ) $W.m.K^{-1}$		Ref.
					25 °C	≥ 1000 °C	
1.	7 wt. % YSZ	APS	Lamellae based	Topcoat +substrate	0.90	–	[157]
2.		EB-PVD	Columnar		1.50	–	
3.		SPS (D_{50} = 0.5 µm)	Columnar		1.25	–	
4.	7 wt. % YSZ	SPS (D_{50} ≤ 3 µm)	Intermediate	Topcoat +substrate	0.56	1.30	[135]
5.		SPS (D_{50} ≤ 10 µm)	Intermediate		0.90	1.80	
6.		SHVOF (D_{50} ≤ 3 µm)	Dense with vertical and horizontal cracks		0.86	1.13	
7.		SHVOF (D_{50} ≤ 10 µm)	Dense with vertical cracks		1.29	2.09	
8.	7 wt. % YSZ	EB-PVD	Columnar	Topcoat +substrate	1.58	1.40	[158]
9.		SPS (D_{50} = 0.5 µm)	Columnar		0.80	0.86	
10.		SPS (D_{50} = 0.5 µm)	Columnar with reduced inter-columnar gaps		0.71	0.70	
11.	7-9 wt. % YSZ	APS	Lamellae based	Topcoat +substrate	0.69	1.31	[159]
12.	8 wt. % YSZ	SPS/APS bond coat	Columnar	Topcoat +substrate	0.58	–	[136]
13.		SPS/HVAF bond coat			0.82	–	
14.	YAG	APS: as-sprayed YAG/YSZ	Lamellae based		1.05	1.25	[140]

15.		50–HT YAG/YSZ		Free standing multi-layer topcoat	2.15	1.85	
16.		100–HT YAG/YSZ			2.25	1.85	
17.	SPPS YAG	L–IPB	Lamellae with engineered porosity	Free standing single layer	1.68	0.95	[145]
		M–IPB			1.53	0.95	
		H–IPB			0.70	0.58	

2.5.3 Lifetime performance of TBC

Thermal barrier coatings operate under extremely harsh conditions of combined high temperatures, steep temperature gradients, fast temperature transients, high pressures, and additional mechanical loading, as well as oxidative and corrosive environments—these are difficult conditions to reproduce in the laboratory, all at once. Prominent life performance evaluation tests that have been implemented for TBC in the laboratory include but not limited to thermomechanical fatigue or thermal cyclic fatigue (TCF) and thermal gradient/shock (TG) test. These test conditions as mentioned are less suitable for testing the complex shaped blades and vanes of the gas turbine; however, the testing procedures provide means to evaluate fundamental coating properties such as rates of sintering, thermal cycle lifetimes, thermal conductivities, and to investigate the damage evolution of the planar TBC systems under high-flux conditions. The representative sample used in the testing and evaluation process is usually a button cut out of a superalloy [160]. Often the button samples are cut from the superalloy before coating it with a bond coat layer and another layer of topcoat. It may also be that a rectangular coupon is bond coated and then with the topcoat before the button samples are cut out using electro–discharge machining (EDM) or using waterjet.

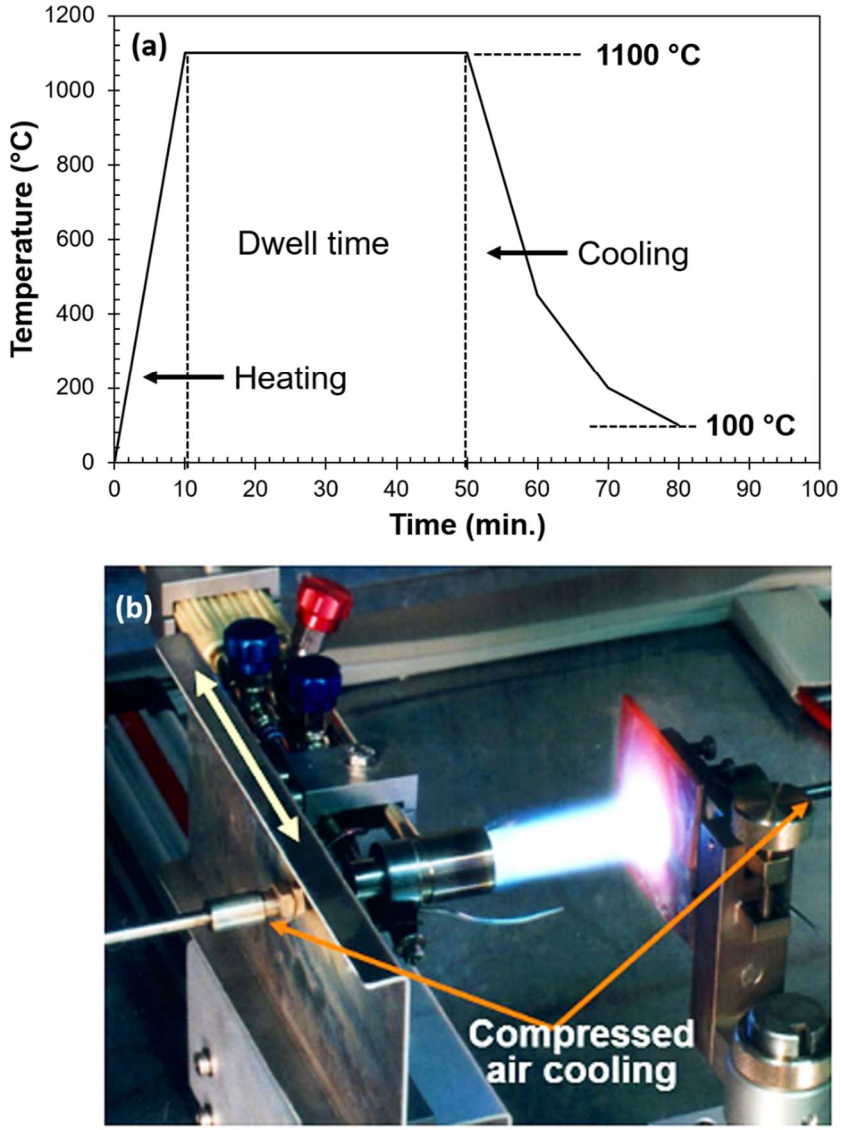

Figure 2-26: (a) Typical thermal cyclic fatigue test cycle showing the heating, dwell and cooling stage (b) a disk-shaped thermal-barrier coating sample being heated with oxy–fuel flame and the back-side being cooled with compressed [134].

In a TCF test, the samples get heated to an elevated temperature, held at the elevated for a specified dwell time before being rapidly cooled outside of the furnace for a specified time or to a specified temperature. Thermal gradient on the other hand, involves heating the topcoat face of a sample with simultaneous cooling of the back side of the substrate with compressed air. The heating of the front face can be either with high–power CO_2 laser or oxy–fuel flame directed towards the sample surface

[160]—Figure 2–18 shows the description of the two tests procedures. The thermal shock test involves inserting the TBC sample into a furnace already heated up to a temperature above 1000 °C. The sample is then held in the furnace for a specified duration before it gets quenched in water at room temperature [161]. The implementation of TCF tests varies depending on whether the TBC is meant for land–based turbines or to be used in aviation engines; usually TBCs meant for use in aviation engines are tested under repeated one–hour cycles while those for land–based turbines are subjected to repeated eight–hour cycles [116].

Table 2-3: Life performance evaluation of TBC topcoats showing test methods and the topcoat microstructure

S/N	Materials/Process		Microstructure	Test temp. (°C)	Test			Cycles to failure	
					TCF	TG	Failure criterion	TCF	TG
1.	SPS YSZ/LPS bond coat	[134]	Segmented	1400	–	7 min	≥ 30 %	–	660
2.	APS YSZ/Cold spray bond coat	[162]	Lamellae based	1150	–	4 min	–	–	3000
				1200					2500
				1250					2000
3.	SPS (D_{50} ≤ 3 µm)	[135]	Intermediate	1100	1–hour 10 min	–	≥ 20 %	263	–
	SPS (D_{50} ≤ 10 µm)		Intermediate					323	
	SHVOF (D_{50} ≤ 3 µm)		Dense with vertical and horizontal cracks					226	
	SHVOF (D_{50} ≤ 10 µm)		DVC					230	
4.	SPS YSZ/Pt–γ/γ’ bond coat	[158]	Columnar	1100	1–hour 15 min	–	20 %	1000	
	SPS YSZ/β-(Ni,Pt)Al bond coat		Columnar					2145	
5.	APS YSZ/APS bond coat	[159, 163]	Lamellae based	1100	1–hour 10 min	–	20 %	700	–
6.	SPS YSZ/ APS bond coat	[136]	Columnar	1100	1–hour 10 min	–	20 %	295	–
	SPS YSZ/ HVAF bond coat							290	
	APS YSZ/ APS bond coat		Lamellae based	1200	–	75 sec	20 %	–	1800
	SPS YSZ/ HVAF bond coat		Columnar						9903

7.	SPS YSZ/ APS bond coat	[138]	Columnar with vertical cracks	1100	1–hour 10 min	–	20 %	275	–
	SPS YSZ/ HVOF bond coat							120	
	APS YSZ/ APS bond coat		Lamellae based					295	
8.	SPS YSZ/ APS bond coat		Columnar with vertical cracks	1200	–	75 sec	20 %	–	7000
	SPS YSZ/ HVOF bond coat								7000
	APS YSZ/ APS bond coat		Lamellae based						3000
9.	SPPS YAG (L–IPB)	[116]	DVC with engineered porosity	1121	1–hour	–	≥ 50 %	~1200	–
				1150				~600	
	APS YSZ		Lamellae based	1121	1–hour		≥ 50 %	~900	
				1150				~450	

A summary of some of the life cycle tests on TBC samples (see Table 2–3) have not shown specific preference for any of the three methods described above. The TBCs generally appears to survive more cycles when subjected to thermal gradient tests compare to thermal cyclic fatigue tests. On which of the tests better represents the condition of the turbine parts in service, the thermal gradient test procedure can be considered to give a closer representation. The turbine parts in service would receive heating on the coated sides while being cooled on the uncoated face simultaneously. This matches the test condition as implemented in thermal gradient tests. The thermal fatigue cycle test rather heats the coated and the bare face of the test samples altogether before they are cooled ahead of a new cycle. Despite this seeming inadequacy, the thermal cyclic fatigue appears to be the mostly used test procedure in the life performance study of TBCs.

2.6 Summary

The following points summarized the relevant information on the literature reviewed for feedstock, processes, characterization and performance evaluation of thermally sprayed ceramic materials studied for wear and thermal barrier coating application.

- The particle size distribution of the feedstock and the processing technique dictates the microstructure of coatings. The variation in the microstructure of the coatings has been linked to the measurable properties of the coatings viz fracture toughness, thermal conductivity, residual stress, and thermal cyclic life span.
- The predominant crystallographic phases in thermally sprayed Al_2O_3 coatings with molten particles are the amorphous and γ–Al_2O_3. The amorphous phase in such coatings can be transformed to α–Al_2O_3 when heat treated at temperatures above 1000 °C.
- Phase stability in thermal sprayed YSZ topcoat still remain a concern for which potential alternative materials are being sought in defect clusters, perovskites, hexa-aluminates and pyrochlores. However, no single material appears to be sufficient to meet the combined concerns of phase stability and CMAS attack.
- Thermal conductivity measurements of TBCs have been done using coating on substrate or free-standing coating. The procedure with coating on substrate requires the separation of the coating contribution to the overall measured thermal conductivity.
- The thermal conductivity of dense YAG coatings deposited by APS has only been measured at room temperature.
- YAG coatings with engineered porosity deposited from solution precursor

showed reduced thermal conductivity at elevated temperature. The mechanism was linked to the inter-pass boundaries introduced into the coating microstructure through optimized processing parameters.

- The thermal cyclic fatigue test is the most used life performance test for TBCs even when the thermal gradient test for life performance of TBCs mostly represent the in–service condition of turbine parts with TBC.

2.6.1 Gaps in literature

Most studies on thermally sprayed Al_2O_3 coatings, however, used a thermodynamically stable alpha phase powder that resulted in γ-Al_2O_3 in the coating. The manufacturing of α-Al_2O_3 begins from its ores by Bayer process and finishes by heat treatment. The process yields the desired alpha phase at a temperature above 1000 °C; however, many of the transitional Al_2O_3 phases can be produced at lower temperature. The energy and resources consumed in producing α-Al_2O_3 powder from Al_2O_3 salts is intensive and it is subsequently wasted when thermal spraying of this valuable feedstock results in the formation of γ-Al_2O_3. An alternative and sustainable approach is to use a metastable feedstock (such as delta-theta Al_2O_3) being easier to obtain and it can transform to γ-Al_2O_3 during thermal spraying. Despite the low cost and availability of the suspension of the metastable phases these have received little or no attention as feedstock materials for thermal spray.

Despite Al_2O_3 and YSZ being widely used and studied engineering ceramics, limited work has been reported on the through-thickness residual stress behaviour of SHVOF thermal sprayed Al_2O_3 and YSZ. A detailed understanding of residual stress of the coatings will provide further insight into the performance evaluation of the coatings vis-à-vis the role of residual stress.

The studies on the deposition of YAG, a non–oxygen conducting ceramic, for TBC applications were yet to be investigated with HVOF deposition process—a processing technique capable of producing dense coatings needed to forestall the challenge of fly ash and calcium–magnesium–alumino–silicate (CMAS).

Experimental methodology

3.0 Introduction

This chapter presents the materials, the coating deposition procedures and the characterization methods employed in the study of the coatings produced to justify the stated objectives of this thesis.

3.1 Materials

Commercially available ceramic suspensions and inorganic salts for solution precursor have been used in the deposition of coatings studied in this work (see Table 3–1). The materials include two inorganic salts [164], two alumina (Al_2O_3) suspensions, one yttria stabilized zirconia (YSZ) suspension and one yttrium aluminium garnet (YAG) suspension. The as–supplied particle loading for the YAG was ~ 50 wt. %; the suspension was made into a 20 wt. % suspension to ensure free flow during the spray process. The solution precursor was made from stoichiometry solution of aluminium trioxonitrate (V) nonahydrate and yttrium trioxonitrate (V) hexahydrate. Fractional part of each suspension to be sprayed was heated separately in a box furnace at 100 °C for 8 h to obtain dried powder for secondary electron (SE) images on the Scanning Electron Microscope (SEM) and for X–ray diffraction analysis.

Table 3-1: List of materials with their description and suppliers

S/N	Materials	Supplier	Particle loading (wt. %)	PSD, D_{50} (μm)	Medium
1.	CR1 Al_2O_3 suspension	Baikowski (Poisy, France)	~ 21	1	Water
2	GTV Al_2O_3 suspension	GTV Verschleißschutz GmbH (Luckenbach, Germany)	~ 14	–	Water
3.	YSZ suspension	Treibacher Industrie AG (Althofen, Austria)	~ 25	0.6	Ethanol
4.	YAG suspension	Baikowski (Sillingy Cedex, France)	~ 50	0.09	Water
5.	Aluminium trioxonitrate (V) nonahydrate, $Al(NO_3)_3.9H_2O$	Fisher Scientific (Loughborough, England)	–	–	–
6.	Yttrium trioxonitrate (V) hexahydrate, $Y(NO_3)_3.6H_2O$	Fisher Scientific (Loughborough, England)	–	–	–

Two substrates were used in the deposition of coatings—stainless steel and Ni–alloy. The stainless steel, AISI 304 cold rolled stainless steel supplied by Unicorn (Derby, England), was used as the primary substrate for all sprayed coatings. It has a nominal composition of 19.0–Cr, 9.3–Ni, 0.05–C, and the balance is Fe (in wt. %). Each stainless–steel substrate has a dimension of 60 x 25 x 2 mm. The Ni–alloy used was the Hastelloy C–263 grade provided by Rolls Royce (Derby, England). The Ni–alloy has nominal compositions in wt. % of 0.5–Al, 2.2–Ti, 20.4–Cr, 0.5–Fe, 20.2–Co, 6.0–Mo; the balance is Ni. The dimension of the Ni–alloy has used during the deposition was 60 x 15 x 2 mm.

3.2 Feedstock characterization and analysis

3.2.1 Particle size distribution (PSD) in the suspension

PSD can be obtained based on the concept of dynamic light scattering (DLS). DLS refers to measurement and interpretation of light scattering data on a microsecond timescale to obtain particle size and shape. When a monochromatic light is beamed on particles undergoing Brownian motion in a liquid medium, the interaction of light with the electric charges on the particle surface causes scattering of light. The monochromatic incident light undergoes Doppler broadening due to the continuous motion of the particles in the liquid medium. Constructive interference from the scattered lights generates detectable signals as fluctuating intensities with respect to time (ns–μs) to determine the rate at which the intensities fluctuate—micron size particles move slowly as against nano to submicron size particles which move very fast to give higher intensity fluctuations. The rate of the fluctuation of the intensities is related to the diffusion behaviour of the particles quantified as the diffusion coefficient (D_T). The diffusion coefficient relates to the hydrodynamic size of the particles of

particles. Equation (3.1) connects the normalized scattered light intensity to the diffusion coefficient [165].

$$g(\tau) = 1 + \beta exp(-2D_{\tau}q^{2}\tau)$$ ---------- Equation 3.1

$$\vec{q} = \frac{4\pi\eta}{\lambda} sin\left(\theta/_{2}\right)$$ ---------- Equation 3.2

g(τ) represents normalized intensity correlation function, β coherence factor (scattering properties of particle), D_{τ} is the diffusion coefficient, τ is the lag time between two time–points. The parameter q in Equation (3.1) represents a Bragg wave vector (see Equation 3.2) which connects the incident light wavelength (λ), refractive index (η) of the liquid medium carrying the particles and θ, the signal detection angle—π is a mathematical constant (3.142).

One of the Al_2O_3 suspensions and the YAG suspension used in coating disposition were characterized to obtain the PSD in the feedstock—the setup is shown in Figure 3–1. The PSD in the G–Al_2O_3 suspension was measured with a Malvern Zetasizer Nano–ZS (Malvern, England). The YAG suspension was analysed using the Coulter LS230 (High Wycombe, England). Each measurement was done using 20 µl of the respective suspensions.

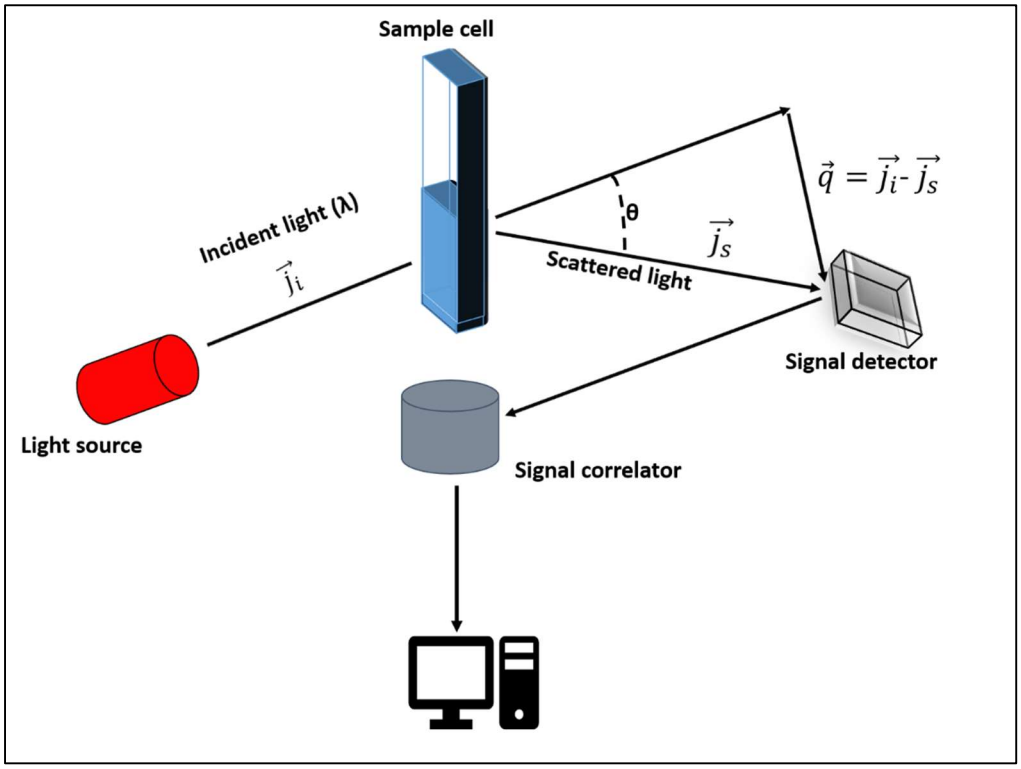

Figure 3-1: Schematic representation of the particle size measurement based on dynamic light scattering

3.2.2 Solution precursor preparation (YAG) and constituent analysis

187.56 g of the aluminium salt and 114.90 g of the yttrium salt were dissolved in deionized water, each in 500 dm^3 at normal atmospheric temperature and pressure. Each solution was then mixed together to have a 1000 dm^3 solution precursor with a molarity ratio 5:3. Fractional part of the solution precursor was heated in furnace at 80 °C for 24 hours to make a sol. One of the obtained sols was calcined in a box furnace at 900 °C for 3 hours. Part of the globule obtained from the calcined sol was grounded into powder for SE images on the SEM and for X–ray diffraction analysis. The other sol was used for differential thermal analysis.

3.2.2.1 Differential thermal analysis of the precursor

Thermal analysis of the sol obtained from the heating of the solution precursor presented in subsection 3.2.2 above were performed using simultaneous TGA/DSC (SDT Q600, TA Instruments, USA). Two empty Al_2O_3 pans were scanned from ambient temperature to 1000 °C at a ramp rate of 10 °C/min in flowing air. This scan forms the baseline to quantify the weight loss and the change in heat flow between the sample and the reference material. ~ 9 mg of the sol (prepared in subsection 3.2.2 above) was then weighed into one of the Al_2O_3 sample pans leaving the other as the reference sample. The scan was then repeated using the same conditions as the baseline. Graphs of % weight loss and heat flow as a function of temperature were plotted to show the exothermic and endothermic reactions associated with the weight loss of the sol.

3.2.2.2 FTIR analysis of calcined sols

Fourier transform infrared (FTIR) uses infrared beam of light to probe an unknown sample for the identification of its constituent compounds. FTIR measurements determine the intensity of an incident beam of infrared radiation as a function of wavelength (4000–200 cm^{-1}) or frequency (2.5–50 μm) after it interacts with the sample. During an FTIR measurement the infrared spectrophotometer disperses the light from a broadband infrared source and measures its intensity at each frequency/wavelength. The ratio of the intensity before and after the light interacts with the sample is determined. The plot of the intensity ratio against frequency/wavelength makes the infrared spectrum. Peak position on the spectrum provides qualitative sample identification; this is because each chemical functional group displays peaks at a unique set of characteristic frequencies/wavelength. The intensity ratio axis on the

infrared spectrum can be presented as transmittance, reflectance, or absorbance. If one is measuring the fraction of light transmitted through the sample or reflected off the sample surface, the intensity ratio reads as in Equation (3-3). The absorbance (A_w) is related to the transmittance using Beer–lambert equation given in Equation (3-4) [166].

$$T_\omega = \left(\frac{I_T}{I_0}\right)_\omega \; or \; R_\omega \left(\frac{I_R}{I_0}\right)_\omega \qquad \text{---------- Equation 3.3}$$

$$A_\omega = -log\, T_\omega \qquad \text{---------- Equation 3.4}$$

I_0 is the incident beam intensity, I_T and I_R are the transmitted and the reflected light intensity, respectively. T_ω and R_ω are the respective transmittance and reflectance of the sample at frequency ω.

FTIR spectra were recorded for pulverized samples of each of the solution precursor calcined at three temperatures: 450 °C, 750 °C and 900 °C using spectrophotometer (Tensor 27) supplied by Bruker (Coventry, UK). The spectrophotometer has a liquid nitrogen cooled detector—this ensures well resolved spectra of relatively intense signals were collected before each spectrum was recorded. The spectrophotometer was set to an average of 64 scans per spectrum. The spectra were collected over the wavenumber range of 400–4000 cm^{-1} at a resolution of 4 cm^{-1} specified for solid samples.

3.3 Deposition of coatings

Prior to coating depositions, substrates were grit blasted with fine Al_2O_3 particles (0.125–0.149 mm) using a grit blaster from Guyson (Dudley, England). Blasting pressure was 3 bar for substrates used directly in the spraying of suspension and solution precursor while a blast pressure of 6 bar was used for substrates meant for the deposition of bond coats. Distance of 50–100 mm was maintained from the nozzle of the grit blaster in all cases. Following grit blasting, the substrates were cleaned in industrial methylated spirit (IMS) in an ultrasonic bath for 10 minutes and blown dry with compressed air.

All coatings deposited from suspension and solution precursor were sprayed using a modified UTP TopGun SHVOF thermal spray unit from Miller Thermal Inc. (Wisconsin, USA) with axial injection of suspension or solution precursor directly into the combustion chamber with a nozzle of 0.3 mm exit diameter (see Figure 3–1). The substrates were mounted onto a rotating carousel with a vertical axis of rotation of 73 rpm with the spray gun traversing vertically at a speed of 5 mms^{-1} during spraying [85].

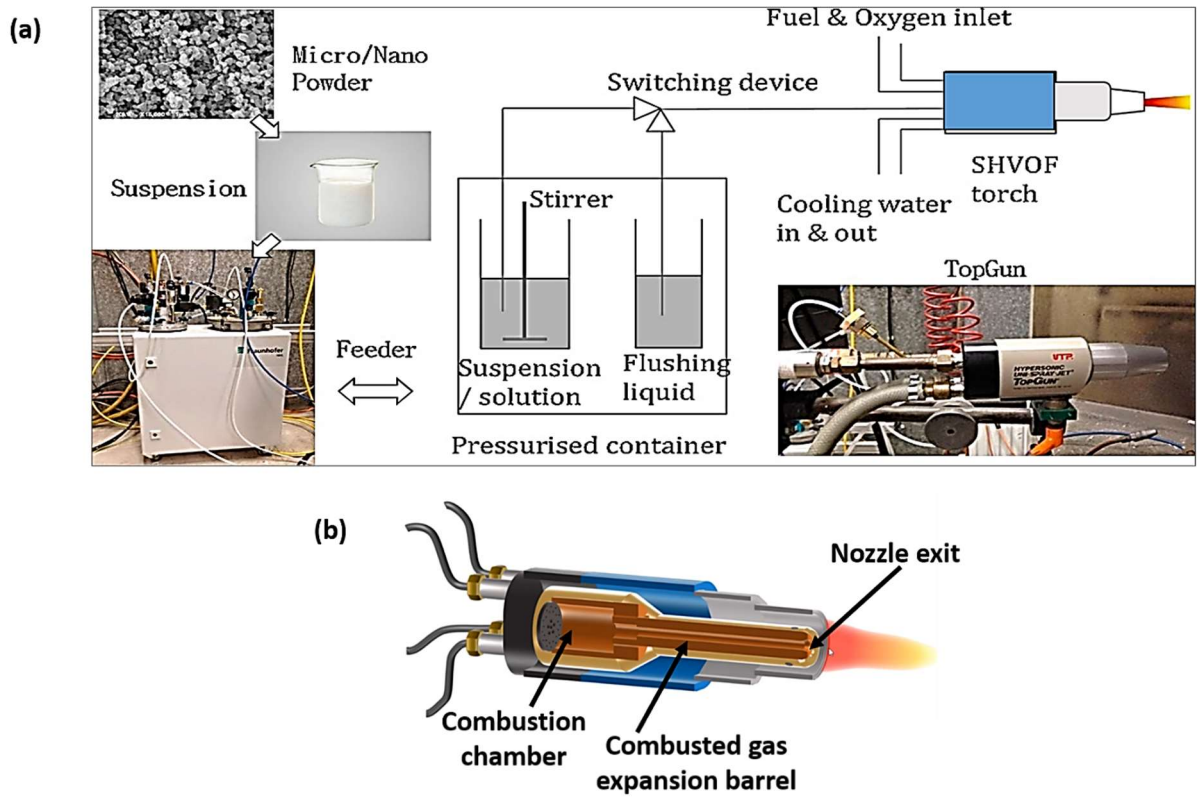

Figure 3-2: (a) Schematic a pictorial representation of the suspension/solution precursor HVOF spray set up [144] (b) schematic of the cross section of the TopGun showing its internal features .

Five coatings were deposited from suspension and one from solution precursor to complete the work presented in this thesis. The spray parameters used for the coating depositions as shown in Table 3–2 are the optimized parameters obtained by a member our research group—Sunil Chadha. The suspension or solution precursor was delivered from a pressurized vessel maintained at 3–5 bar. The C–Al_2O_3[1] and the G–Al_2O_3[2] were sprayed onto AISI 304 alone while the YSZ and YAG coatings were sprayed onto both AISI 304 and Ni–alloy. The coatings deposited onto bond coated Ni–alloy was later used for thermal cycling durability tests. The YSZ coating deposited at 110 kW flame power is referred to as the T1–YSZ while the one deposited at 99 kW

[1] Al_2O_3 coating deposited from CR1 Al_2O_3 suspension
[2] Al_2O_3 coating deposited from GTV Al_2O_3 suspension

is referred to as the T2–YSZ. Single splats of were collected onto 1 µm–polished AISI 304 substrates. In the case of the single splat collection, the rotating carousel was maintained at a vertical axis of rotation of 100 rpm with the spray gun traversing vertically at a speed of 30 mms^{-1} during the spray to ensure only few splats were collected.

Table 3-2: Spray parameters for SHVOF thermal sprayed Al_2O_3, YSZ, suspension YAG (S–YAG), and solution precursor YAG (SP–YAG) coatings deposited onto AISI 304 and Ni–alloy substrates.

	C–Al_2O_3	G–Al_2O_3	T1–YSZ	T2–YSZ	S–YAG	SP–YAG
Fuel (hydrogen) flow rate, l/min.	612	612	788	700	612	612
Oxygen flow rate, l/min.	306	306	337	300	306	306
Flame power, kW	101	101	110	99	101	101
Suspension flow rate, ml/min.	90	90	100	50	50	50
Spray distance, mm	85	85	85	85	85	85
Number of passes	41	8	26	26	40	20

Commercial CoNiCrAlY powder (Table 3–3) supplied by Praxair Surface Technologies (Indianapolis, USA) was sprayed to form a bond coat onto the Ni–alloy using a commercial MetJet II HVOF spray system (Metallisation Ltd, Dudley, UK). The HVOF system (see Figure 3–3) was operated with kerosene fuel and a nitrogen carrier gas—see the deposition parameter in Table 3–4. Powder was injected radially downstream of the throat—the nozzle exit. Compressed air cooling was maintained for the samples during and after spraying.

Table 3-3: Nominal chemical composition of the CoNiCrAlY powder (CO–210–24)

	Co	Ni	Cr	Al	Y
Wt. %	38.5	32.0	21.0	8.0	0.5
At. %	34.3	28.6	21.2	15.6	0.3

Table 3-4: Bond coat spray parameters

Parameters	Values
Stand–off distance, mm	356
Traverse speed, m/s	1
Carrier gas (N_2) flow rate, l/min	5.5
Oxygen (O_2) flow rate, l/min	890
Fuel (kerosene) flow rate, ml/min	470
Nozzle length, mm	100

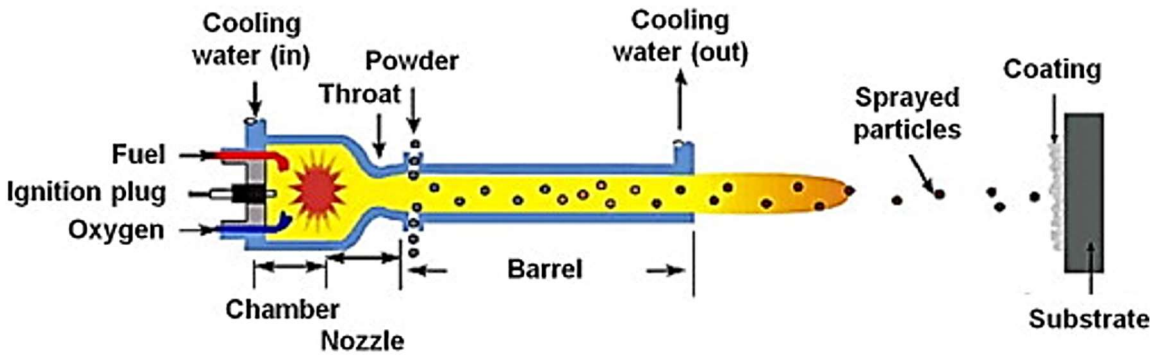

Figure 3-3: Schematic of the HVOF spray process used for bond coat deposition [167]

3.3.1 Diagnostic characteristics of in–flight particles

The inflight velocity and temperature of the ceramic particles sprayed from suspensions and solution precursor was obtained using Accuraspray 4.0 kit supplied by Tecnar (St. Bruno, Canada). The kit consists of optoelectronics sensor system with attached coupled–charged–device (CCD) camera and a two–colour pyrometer. The CCD camera enables the analysis of the flame appearance vis–a–vis position, width, distribution, and intensity—the plume density. The pyrometer evaluates the intensity of the radiation emission of the particles (travelling through the combusted gas exiting the nozzle of the spray torch) at two wavelengths, λ_1 and λ_2. The intensity of the radiation emitted from the particles are analysed based on the equation described by Planck (Equation (3.5)) [168].

$$I_{em}(\lambda,T) = \varepsilon \frac{C_1}{\lambda^5} * d^2 \left[exp\left({}^{C_2}/_{\lambda T}\right) - 1\right]^{-1} d\lambda$$ ---------- Equation 3.5

I_{em} represents the radiation intensity (in W/sr) at a wavelength, λ (in m), for a body at surface temperature, T (in K), dλ is the interval between the two wavelengths at which measurements were taken while ε is the emissivity, a dimensionless constant described as the ratio of a gray body's thermal radiation to a black body's thermal

radiation at the same temperature. Particle diameter is denoted with d while C_1 and C_2 are dimensioned constants taken as 9.352 x10^–17 ($W.m^2$) and 1.439 x10^–2 (m.K) respectively. The temperature (T) of the particles is then obtained from the ratio of the radiation intensity signal ($I_{\lambda 1}$ at λ_1 and $I_{\lambda 2}$ at λ_2) collected from the sensors following the Planck's law and assuming the gray body hypothesis such that the temperature, T is written as in Equation (3-6) [169]:

$$T = \frac{C_2(\lambda_1 - \lambda_2)}{\lambda_1 \lambda_2} * \left[ln \frac{I_{\lambda 1}}{I_{\lambda 2}} + 5\, ln \frac{\lambda_1}{\lambda_2} \right]^{-1}$$ ---------- Equation 3.6

The velocity of the particles is obtained based on the concept of a time–of–flight measurement using cross–correlation calculation. Each particle in the measurement volume radiates a signal that passes through two adjacent measurement points; the velocity is then calculated from the location of the maximum of the cross–correlation factor as a function of time difference between the two adjacent measurement points [170]..

The data acquired for each suspension/solution precursor sprayed was obtained using a stand-off distance of 85 mm as in the spray conditions in Table 3-2. The Accuraspray device was positioned 200 mm radially to the axis of the combusted gas jet exiting the spray torch (see Figure 3–4).The kit provides ensemble measurement of particles in a control volume in a spray jet rather than a single particle [21]. In this case, the control volume was 3.2 mm x 10 mm x 25 mm. Multiple measurements (~60) is taken at a reaction time of 5s with a signal amplification of 24–27 times and camera exposure time of 41 ms. The velocity and temperature values recorded represents the average for the particles in the control volume. Each temperature and velocity measurement taken will have an associated measurement error ±3 % to account for the uncertainties in the coating deposition process.

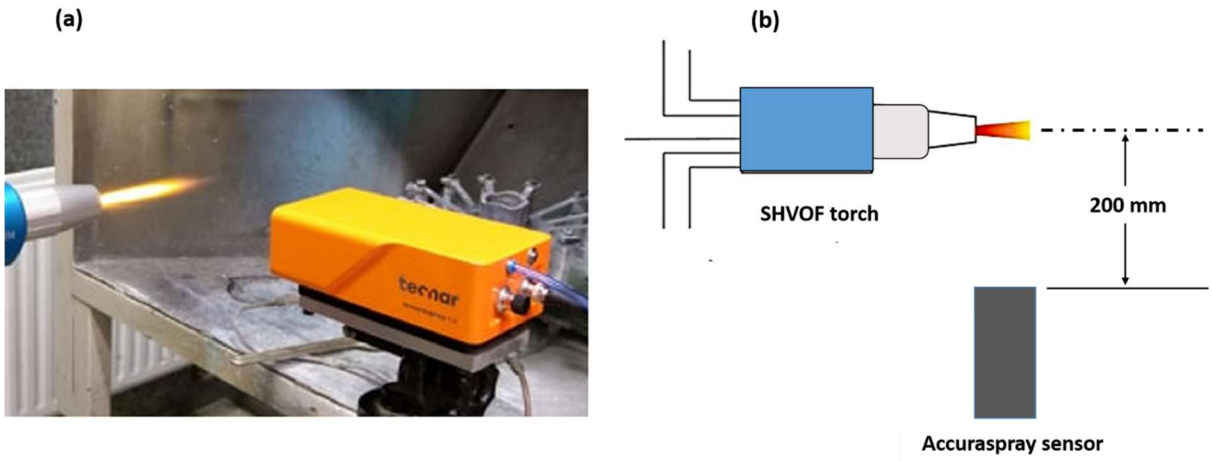

Figure 3-4: Diagnostic characterization experimental setup (a) Pictorial view (b) Schematic representation

3.4 Microstructural characterization of materials and coatings

3.4.1 SEM imaging of ceramic particles, coatings and EDX analysis

Scanning electron microscopy involves the use of focused electron beam to probe the surface of a material to obtain topographical and elemental composition–based information. The impinging electron beam (the primary electron) interacts with the material to cause the emission of electrons and X–ray photons characteristic of the material. The impinging electron undergoes either inelastic or elastic collision with the atoms of the sample material; inelastic collision produces secondary electrons with energy less than 50 eV while the elastic collision produces backscattered electrons with energy more than 50 eV or comparable to the energy of the primary electron depending on the atomic number (Z) of the atoms involved. High atomic number elements are more likely to yield backscattered electrons. The secondary electrons therefore provide surface topography information of the sample, whilst the backscattered electrons provide information about the atomic weight of the sample, which creates Z–contrast.

Additionally, the primary electron energy reaches between few hundred eV to 30 keV; this makes it capable of ejecting a core electron from an atom to cause excitation of the atom. The excited atom then decays to its ground state to produce X–ray photons or Auger electrons. The X–ray emission signals are characteristic of the element that produced them; the signals can be sorted by energy in an energy dispersive X–ray detector to present the elemental composition of the sample material. This elemental composition analysis technique is called energy dispersive X–ray spectroscopy (EDX or EDS) [166].

Cross–sections of the coatings were prepared by standard metallographic procedures. For each coating sample a small piece (10 x 25 x 2 mm) is cut from a representative sample using a precision cutter cooled with water before the cut piece is hot mounted in conductive resins (Bakelite) for grinding and polishing to 1 μm diamond finish. The initial plane grinding step was performed for approximately 3 minutes using abrasive papers (P240, P400, P800 and P1200) fixed on a grinding and polishing wheel with water sprayed continuously. The sample is washed off with liquid soap and water and sprayed with industrial methylated spirit (IMS) before it was dried in a stream of warm air. The sample was then polished for another 3 minutes on 6 μm diamond wheel with sparing spray of polishing spirit. The sample is then washed first with acetone to dissolve any adhering film before the sample is washed off with soap and water, sprayed with IMS and dried in a stream of warm air. The polishing step is repeated on 1 μm diamond to achieve a shining surface finish.

Fractured surfaces of the coatings were prepared from notched pieces (see Figure 3–5) cut from representative samples; each one of the pieces has a dimension of 5 x 25 x 2 mm. The notch on each piece was created by holding the coated side of the piece

face down on a bench vice to cut the uncoated side of the substrate to a depth of ~ 1.90 mm using a mini hack saw. The notched piece is then submerged in ~ 0.5 litre of liquid nitrogen for 5 to 10 minutes before it was transferred onto a bench vice to be fractured at the notch.

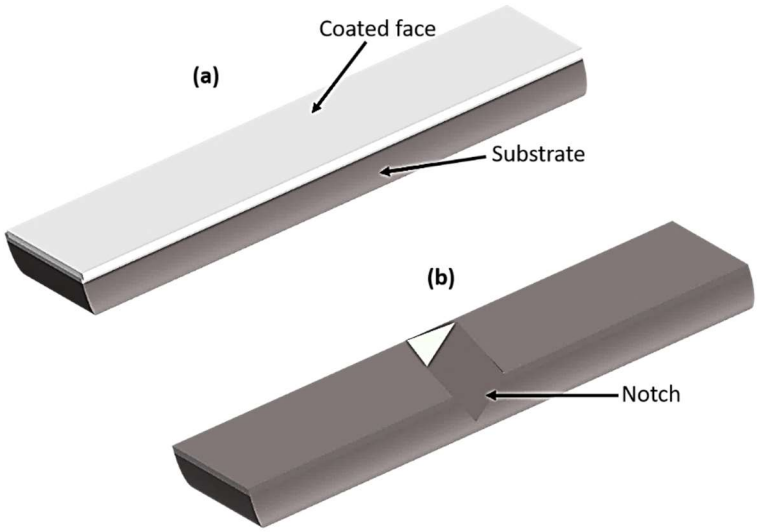

Figure 3-5: schematic of notched samples (a) without notch (b) with notch

Powdered samples from the suspensions and the calcined sols of the solution precursor were lightly spread on a polymer adhesive tape stuck to a tub. Each imaging sample was coated with carbon to a thickness of 10–20 nm before examination on the SEM. The secondary electron (SE) images of powder from the suspensions, the calcined sols of the solution precursor, the fractured surfaces, the single splats and the BSE images of the coatings cross section were obtained using JEOL 6490 SEM from JEOL Ltd. (Tokyo, Japan). The SEM was operated at an accelerating voltage of 20 kV and a working distance of 10 mm. The porosity of as–sprayed coatings (C–Al_2O_3, G–Al_2O_3, T1–YSZ and the T2–YSZ) and the heat–treated G–Al_2O_3 coatings (HT–750–6h and HT–750–48h) were analysed using image analysis software—Image–J (NIH, USA). The porosity was based on the volumetric ratio of pores to solids.

The crack densities on the top surface of HT–750–6h and HT–750–48h coatings were also obtained by image.

Compositional analyses of YAG and the MCrAlY bond coat were performed using an Oxford Instruments EDX with INCA X–ray microanalysis software. The YAG sprayed from suspension and that prepared from the solution precursor were analysed for comparison. Similarly, the as–received bond coat and the thermally cycled bond coat were analysed to show compositional variations resulting from the thermal cycling experiment.

3.4.2 Focus ion beam (FIB)–SEM milling

A FIB–SEM uses the combination of focused ion and focused electron in the production of electron transparent specimen for transmission electron microscopy (TEM) observation. The focused ion provides for the milling of the specimen while the focused electron allows for immediate visualization of the milled surface. FIB mills a surface with gallium ion (Ga^+) probe focused to ~ 5 nm to ~ 0.5 μm in diameter. The focusing of the probe is achieved by adjusting the probe current density from tens of pico–Amperes (pA) to several nano–Amperes (nA) to mill a surface, Ga^+ are accelerated onto the surface to generate secondary ions or atoms. The generated secondary ions can also be used to construct images of the surface. A typical acceleration voltage for FIB operation lies between 5 and 50 keV—the incident ion penetration depth is ~ 20 nm for 25 keV Ga^+. However, before a FIB milling is completed on a surface, a metal layer (typically 1 μm wide 2 μm high 30 μm long) is deposited using ion assisted chemical vapour deposition to avert surface damage. Common metals used for the surface protection include tungsten (W), platinum (Pt), aluminium (Al), copper (Cu). A trench is milled out with the FIB probe on the two sides

of the deposited metal before the sides connecting the strip to the wafer will be cut through. The strip will then be tilted for thinning to electron transparency (~ 100 nm). The strip is returned to its initial orientation before it will be cut at the bottom and deposited on a TEM grid—this is the lift out technique [171]. See Figure 3–6 for the schematic of the process.

Focused ion beam (FIB) milling of some sections of the as–sprayed G–Al_2O_3 coating was done using FEI Quanta 3D FIB–SEM (Tokyo, Japan). The milling was done parallel to the plane of the sample surface to ensure the regions of interest were covered. A strip of platinum (20 µm x 1.5 µm x 1.0 µm) was deposited onto the surface as a protective cover on the region to be milled. A trench is milled out with the FIB probe on the two sides of the strip before the sides connecting the strip to the wafer were cut through. The strip was tilted, cut at the bottom, and deposited on a TEM grid. The FIB milling produced a thin foil of ~ 5 µm x 3 µm thinned to a thickness of ~ 100 nm. The thin foil lift–out was then transferred to JEOL 2000FX TEM for selected area electron diffraction analysis (SAED).

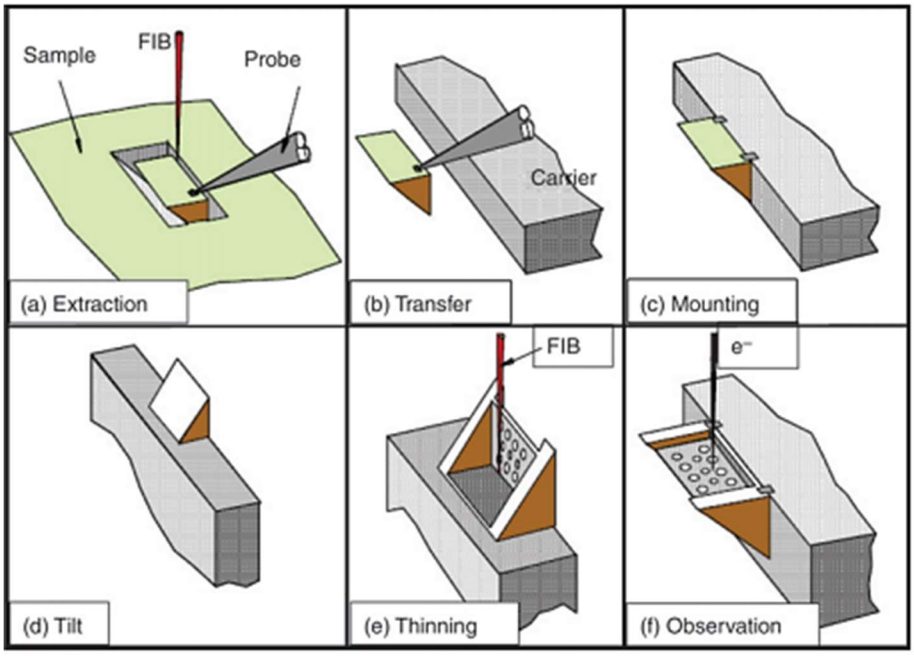

Figure 3-6: Sequence of TEM sample preparation [172]

3.4.3 Transmission electron microscopy (TEM)

Transmission electron microscope (TEM) illuminates an electron transparent specimen with a static beam of electrons operating at 100–400kV accelerating voltage. The incident electron beam is used as transmitted or diffracted electrons from the sample at the objective lens of the microscope are recombined by the objective lens to form a diffraction pattern in the back focal plane of that lens and a magnified image of the sample in its image plane. A series of intermediate magnetic lenses projects the obtained signal (an image or a diffraction pattern) onto a detector which could be a fluorescent screen, a film plate or a video camera (See Figure 3–7) [166]. In the transmitted electron–based imaging, part of the electron beam transmitted through the sample is scattered based on the crystallinity of the sample to create what is known as the bright field image—a crystalline sample will show as dark diffraction contrast while an amorphous sample will appear bright.

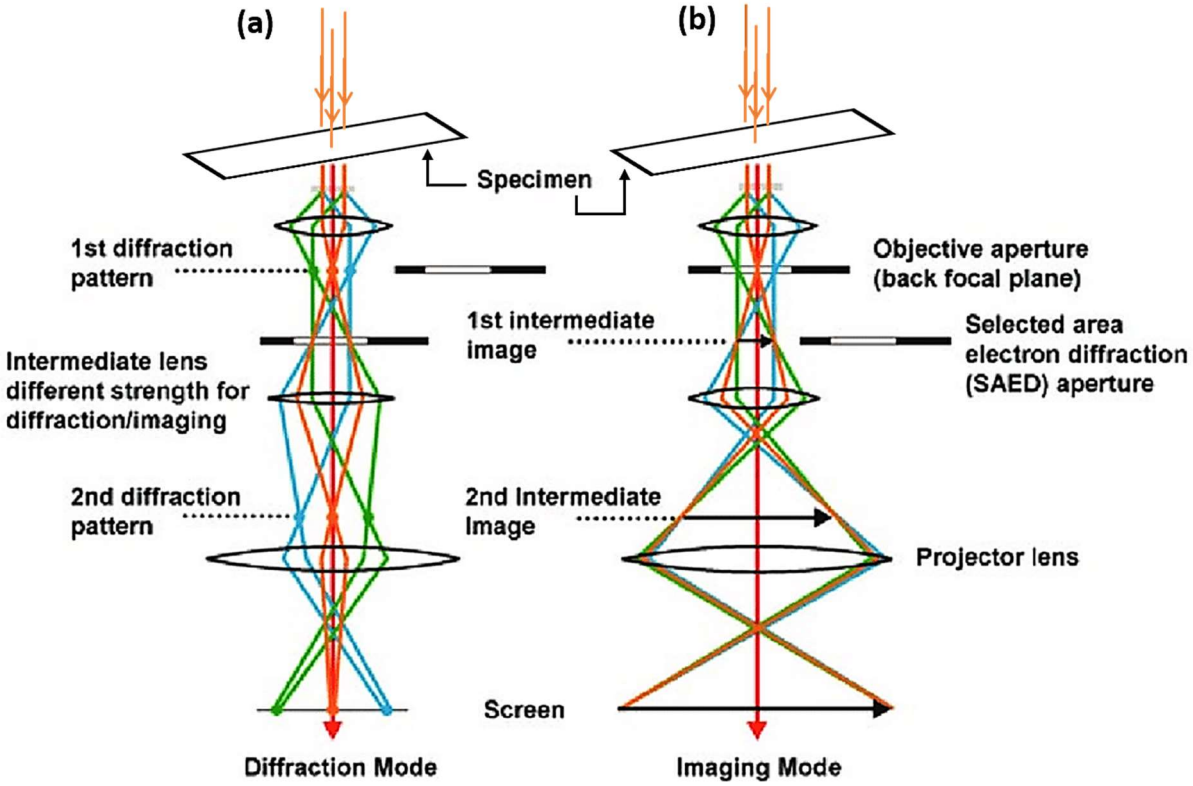

Figure 3-7: Schematic of ray diagrams in a TEM column showing (a) diffraction pattern acquisition mode (b) imaging mode [173]

The diffracted electron beam produces dark field image which gives information about the crystal structure of a sample based on selected area electron diffraction (SAED) patterns. The diffraction pattern consists of bright ring spots representing randomly oriented crystallites. The radius of the diffraction ring (R), the distance between the sample and the detector (L) and the diffraction angle are connected as in Equation (3-7).

$tan\,2\theta = R/L$ ---------- Equation 3.7

Bragg's law is applied to the diffraction rings to determine an unknown crystal structure in a sample such that the wavelength (λ), the interplanar spacing (d) and the diffraction angle (θ) are connected as shown in Equation (3-8)— n is the order of diffraction.

$n\lambda = 2dsin\theta$ ---------- Equation 3.8

The diffraction (θ) angle in SAED is small when compared to the diffraction angle in X–ray diffraction; the difference stemmed from the difference in the wavelength between the high energy electrons and the X–rays. High energy electrons (100 keV) have very small wavelengths of 0.0037 nm as against 0.154 nm in X–rays. Given that the magnitude of the SAED diffraction angle θ is very small, sin θ is taken to be θ so that the Bragg equation becomes simplified to:

$n\lambda = 2d\theta$ ---------- Equation 3.9

Similarly, it follows that tan 2θ ≈ 2θ for a small angle; so, combining Equation (3-7) through to Equation (3.9) yields d, the interplanar spacing of the unknown crystal structure, as in Equation (3.10).

$d = \frac{n}{R}(\lambda L)$ ---------- Equation 3.10

Where λL is the camera constant and is obtained using a reference aluminium sample of known lattice parameters under the same electron–optic conditions and R is the radius of the diffraction ring [174].

A JEOL 2000FX TEM (Tokyo, Japan) with a camera constant of 1.0 m operating at 200 kV accelerating voltage with a wavelength of 0.0025 nm was used to obtain bright field TEM images and diffraction patterns on a fluorescent screen for the as–sprayed G–Al_2O_3 coating.

3.4.4 X–ray diffraction analysis

X–ray diffraction (XRD) is a non–destructive technique used to identify the crystalline phases present in materials in addition to measuring the structural properties of the phases as in strain state, grain size, epitaxy, phase composition, preferred orientation, and defect structure. XRD technique uses monochromatic X–ray radiation (λ = 0.7–2.0 Å) to cause coherent elastic scattering when incident on crystallites. The coherent elastic scattering would be either a Bragg scattering or an elastic diffuse elastic scattering; the former being for crystalline samples and the latter for amorphous samples. When Bragg scattering occurs, it is either of constructive or destructive interference; a constructive interference produces a peak. The intensity of the peaks depends on the atomic number (Z) of the elements involved—high–Z elements, show higher diffracted intensity compared to low–Z elements. Bragg scattering is represented mathematically as in Equation (3-9)—Figure 3–8 shows the schematic of Bragg scattering in an X–ray diffraction experiment [166, 175].

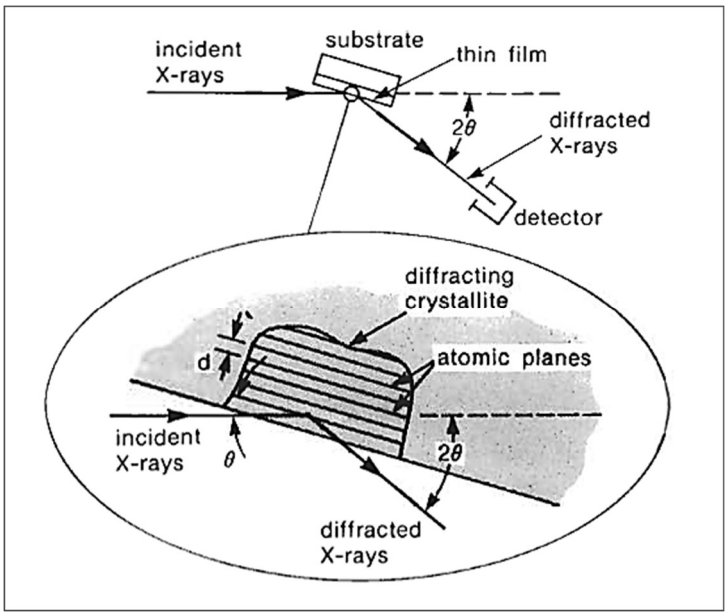

Figure 3-8: Schematic representing Bragg scattering from X–ray diffraction experiment [176]

Data collected from diffraction experiments are often matched against database of diffraction patterns for the different phases that were examined. The matching of the collected data against the database of known patterns would aid phase identification—a qualitative process. However, to quantify the phases as well as obtaining other microstructural details (crystallite size and degree of crystallinity) of the investigated material, requires that the accidental and systemic peak overlap characteristic of powder diffraction data be resolved. The peak overlap results from the projection of 3–D reciprocal lattice data onto 1–D 2θ axis as is always the case in diffraction data. Rietveld method solves this problem through the least squares fit procedure where in the weighted sum (S_y) of the squared difference (residual, r) between the entire information contents of a sample diffraction pattern fitted to a calculated diffraction pattern model for the sample is minimized as in Equation (3.11). The least–square refinements is then iterated to obtain the best fit of the whole data of the observed powder diffraction pattern to a calculated pattern determined from simultaneously

refined models for the crystal structure(s), diffraction optic effects, instrumental errors, and other specimen characteristics like lattice parameters.

$$S_y \xrightarrow{min} \sum_{i=1}^{n} w_i {r_i}^2 \ni \frac{\partial S_y}{\partial y_i} = 0;\ w_i = {1}\Big/{\sigma^2\left(y_{obs,i}\right)}$$ ---------- Equation 3.11

$$r = y_{obs,i} - y_{cal,i}$$ ---------- Equation 3.12

$$y_{cal,i} = \sum_p \left(S_p \sum_{s(p)} \left(L_s M_s \left|F_{s,p}\right|^2 \emptyset(X) P_s A\right)\right) + B_i$$ ---------- Equation 3.13

$$L_s = \frac{1}{cos\,\theta sin^2\theta} \propto \frac{1}{sin\,\theta\, sin(2\theta)}$$ ---------- Equation 3.14

Where i = 1,2,3…n signifies a counter, y_{obs} is the observed intensity from the specimen, y_{cal} is the calculated intensity (Equation 3.13), w_i is the applied weight obtained as the inverse of the variance (σ^2) of the observed intensity. In Equation (3.13), the outer summation runs over all crystalline phases (p) with Bragg reflections in the diffraction pattern of the specimen, the inner summation runs over all Bragg reflections s(hkl) of a phase p, which contribute to the position i in the diffraction pattern of the specimen, S_p is the scaling factor applied to the reflection intensities of each phase in the specimen in proportion to the weight fraction of the phase, Φ is the reflection profile function for a small peak shift with respect to a $2\theta_p$, P_s is the preferred orientation function, A is the X–ray absorption factor of the specimen. L_s is the Lorentz polarization (Equation 3.14), F_s is the structure factor for ith Bragg reflection and M_s is the multiplicity factor for peak overlap—its value ranges between 2 and 48. The B term in in Equation (3.13) represents other non–crystalline contents of the specimen diffraction data such as the background coming from thermal diffuse scattering, incoherent scattering, inelastic scattering and sample environment at position i in the diffraction pattern [175, 177].

The powders dried from the Al_2O_3 and YSZ suspensions were scanned on a Bruker D500 diffractometer (Siemens. AB, Germany) with a Cu Kα radiation source (1.54 Å) and a point detector for phase identification. The scans were completed within 10º–120º 2θ, step of 0.05° and dwell of 4 s for phase analysis. The as–sprayed coatings and the heat–treated G–Al_2O_3 were scanned for phase analysis with 10º–140º 2θ, step of 0.04° and dwell of 16 s. A more detailed scan was executed for the coatings to reduce noise in the acquired signals. However, the powders from the YAG suspension, the calcined sols of the precursor, YAG coatings and thermal cycled coatings were scanned on Bruker D8 Advance with DaVinci X–ray diffractometer (Coventry, England) with a Cu Kα radiation source (1.54 Å). It however has a LYNXEYE XE–T high energy resolution 1D x–ray detector which allows it collect data rapidly. The scans on this instrument were completed within 10º–80º 2θ, step of 0.02° and dwell of 1s/step.

Quantitative Rietveld refinement of the XRD data was performed with TOPAS (Coelho Software, Australia) to quantify the phases [178]. Structure model of gamma and theta Al_2O_3 used in the Rietveld refinement of the Al_2O_3 samples were taken from Zhou and Snyder [179] while for delta Al_2O_3 Repelin and Husson [180] structure was used. The degree of crystallinity and the crystallite size in the powder and the coatings were obtained. The whole powder pattern fitting (WPPM) method [175] was used in the analysis for the crystallite size—only broadening due to coherently scattering domain size modelled by Lorentzian function was considered in the estimation of the crystallite size.

3.5 Thermal analysis and post spray heat treatment

3.5.1 Thermal Analysis: specific heat, thermal diffusivity, and thermal conductivity

Pellets of YAG and YSZ were produced from powder dried from the as–received suspensions of the two materials using by spark plasma sintering technique. Each pellet was produced using the DR.SINTER LAB. Jr model 632Lx (Fuji Electric, Osaka Japan) with the pressure set to 40 MPa and maintaining a dwell time of 15 minutes. The YSZ pellet was produced to ~ 13 mm diameter and a thickness of 2.14 mm with a ~ 1 g of powder at a temperature of 1000 °C and a heating and cooling rate of 100°C min^{-1}— the temperature was controlled by a K–type thermocouple. The YAG pellet on the other hand was produced to ~ 13 mm diameter and a thickness of 1.4 mm with a powder of ~ 0.62 g at a temperature of 1200 °C and a heating and cooling rate of 100°C min^{-1}—the temperature was controlled by a portable IR–AH radiation thermometer of Chino Corporation (Tokyo Japan). The produced pellets were used to measure the specific heat of the YAG and YSZ samples on a LFA 467 HT equipment supplied by NETZSCH Instruments (Selb, Germany). The specific heat measurement was done in a range of 25 °C –1100 °C with interval of 100 °C and heating rate of 10 °C/min. The Pyroceram standard supplied by the manufacturer was used a reference.

Thermal conductivity (λ) of TBC topcoats is not measured directly being a derived quantity [154]; it can be calculated from an equation relating it to the thermal diffusivity, specific heat at constant pressure (C_p) and density (ρ)—$\lambda = \alpha C \rho$. The thermal diffusivity (α) of the coating is determined based on temperature phase measurement techniques while the specific heat of the coating is obtained from differential scanning calorimetry and the density of the coating could be calculated based on the sample geometry and mass. The temperature phase measurement techniques that provide

thermal diffusivity (α) varies. The distinguishing features of the measurement techniques relies on the heating and temperature sensing methods involved.

A measurement technique with heating and temperature sensing done on opposite sides of the sample is termed 2-sided; this method is destructive to the sample. When the measurement involves heating and temperature sensing on the same side of the sample, it is 1-sided and considered non-destructive [181]—see Figure 3-9. The laser flash technique is a variant of the two-sided photothermal technique; it uses pulsed laser to heat up the sample face and a single infrared detector to measure the temperature rise on the rear face—this makes it a destructive technique and may not be used on an actual component coated with TBC [182].

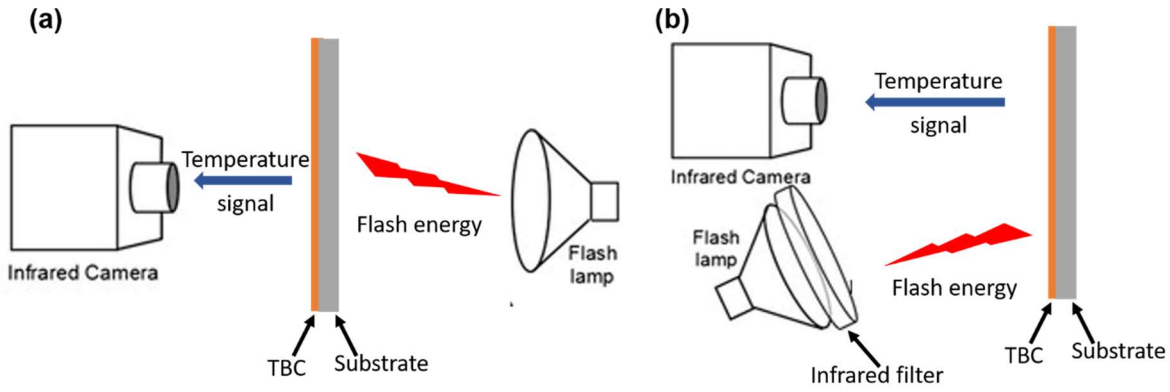

Figure 3-9: schematic representation of (a) 2-sided and (b) 1-sided photothermal imaging technique of diffusivity measurement [182]

The laser flash technique allows fast measurement and the use of small size samples with simple geometry. The front face of the sample heats up from pulse of energy delivered by laser flash causing the back-face temperature to rise by one or two degree. The sample is maintained at the desired temperature for a short duration measurement to alleviate possible cooling effect. The flash technique of measuring

thermal diffusivity was first presented by Parker et al. [183] for near ambient temperature measurement. It has however been used extensively thereafter for high temperature measurement suitable for TBCs [153, 154, 184]. The analysis of the measurement data is based on the solution of the 1-D heat equation [183] expressed as:

$T(x,t) = \frac{1}{L}\int_0^L T(x,0)\,dx + \frac{2}{L}\sum_{n=1}^{\infty} exp\left(\frac{-n^2\pi^2\alpha t}{L^2}\right) * cos\frac{n\pi x}{L}\int_0^L T(x,0)\,cos\frac{n\pi x}{L}\,dx$ ---- *Equation 3.15*

With the initial conditions of:

$T(x,0) = \frac{q}{\rho C\beta}, 0 < x < \beta$ ---------- *Equation 3.16*

and

$T(x,0) = 0, \beta < x < L$ ---------- *Equation 3.17*

Where T is temperature (°C), x is small thickness (mm), t is time (s), L is total sample thickness (mm), β is small depth from the sample front side, α is the thermal diffusivity (m^2/s) and q is heat flux (J/m^2). At the back face of the sample where x = L, the temperature distribution is expressed as:

$$T(L,t) = \frac{q}{\rho CL}\left[1 + 2\sum_{n=1}^{\infty}(-1)^n exp\left(\frac{-n^2\pi^2\alpha t}{L^2}\right)\right]$$ ---------- Equation 3.18

Two dimensionless parameters J and τ are defined to normalize the response on the back face of the sample.

$J(L,t) = \frac{T(L,t)}{T_{Max}}$ ---------- *Equation 3.19*

$\tau = \frac{\pi^2\alpha t}{L^2}$ ---------- *Equation 3.20*

Combining (3.18), (3.19) and (3.20) gives:

$J = [1 + 2\sum_{n=1}^{\infty}(-1)^n exp(-n^2\tau)]$ ---------- *Equation 3.21*

The thermal diffusivity obtained from laser flash measurement is deduced from a plot of J against τ in which case the value of τ for when J is 0.5 is taken as 1.38 corresponding to 50 % rise in temperature at the back face of the sample. The thermal diffusivity is thus written as:

$$\alpha_{th} = \frac{1.38L^2}{\pi^2 t_{0.5}} \quad \text{---------- Equation 3.22}$$

Where $t_{0.5}$ is the time for the 50% rise in the temperature of the sample back face.

The determination of the thermal conductivity of the topcoat in a TBC is however not straight forward. Often times, the measurement is done in a layered configuration while the topcoat is bonded to a substrate [135, 153, 154] at other times, the topcoat is obtained as a free-standing coating. The former case requires knowing the density of the substrate and its thermal properties (diffusivity, heat capacity and conductivity) for the entire desired temperature measurement range. This will then allow the determination of the unknown thermal conductivity of the topcoat using the rule of mixture [140] given in Equation (3-23).

$$\lambda = \frac{\lambda_1 \lambda_2}{\nu_1 \lambda_2 + \nu_2 \lambda_1} \quad \text{---------- Equation 3.23}$$

υ represents thickness fraction while subscripts 1 and 2 are for coating and the substrate, respectively. Equation (3.23) was obtained based on the series heat conduction model proposed by Ravichandran and An [153] for multilayer coating architecture with basic assumptions of well bonded coating/substrate interface. The effect of porosity and splat interfaces are not considered in Equation (3.23).

Thermal diffusivity measurement of the T2–YSZ coating, the S–YAG and the SP–YAG deposited onto AISI 304 was performed using a double layer measurement—for composite samples [185, 186] on the LFA 467 HT equipment. Another sample of

uncoated stainless steel was also measured. The measurement range for the thermal diffusivity was 25 °C–1000 °C for each of the samples. The samples were on 10 mm x10 mm in dimension as cut on a precision cutter from the as–sprayed coupons. Both the plain and coated sides of each composite sample was sprayed with a thin layer of graphite to prevent transmissibility of the laser pulse through the YAG layer. Data acquisition and evaluation was done using the Proteus–Windows software package provided by the equipment manufacturer. The thermal diffusivity values acquired from the equipment was based on Equation (3.22) for thermal diffusivity described by Parker et al. [183].

The thermal conductivity of the uncoated substrate and the composite samples were obtained from the Proteus–Windows software package based on the one–dimensional heat flow equation described by Taylor [154]:

$\lambda = \alpha(T)C_p(T)\rho$ ---------- Equation 3.24

In Equation (3-24), λ is the thermal conductivity, α is the thermal diffusivity (as obtained from Equation (3-22) and ρ is density. The thermal conductivity of the coating layer was then obtained from Equation (3-23) based on the rule of mixture and the series heat–transfer model of multilayers [140, 187].

3.5.2 Post spray heat treatment of G–Al_2O_3 coatings

Post–spray heat treatment of the as–sprayed G–Al_2O_3 coatings deposited using the G–Al_2O_3 suspension supplied by G was performed at 600 °C for 6 h and 750 °C for 6 h and 48 h at ~15 °C min^{-1} heating rate. The coatings were furnace cooled to room temperature at the end of the heat treatment cycle. Heat treatment performed at 600

ºC for 6 hours, 750 ºC for 6 h, and 750 ºC for 48 h yielded samples later referred to as HT–600–6h, HT–750–6h and HT–750–48h, respectively.

3.5.3 Thermal cycling

The performance evaluation of the TBC topcoats was completed by thermal cyclic durability tests. Here only the coatings on bond coated Ni–alloy was used—the S–YAG, the SP–YAG and the T1–YSZ. The tests were carried out in 80–minute cycles using a programmable bottom–loading isothermal furnace (CM Furnaces Inc., Bloomfield, NJ) shown in Figure 3–9. Each cycle consists of 10–mins heat–up to 1100 °C, 40–mins dwelling at the maximum temperature and 30–minutes forced air–cooling; the cooling ensured the samples reached ~ 100 °C before a reheating. Each sample was subjected to 100 cycles of ~ 133 hours. Samples were taken off the furnace after the set number of cycles for further analysis by XRD, SEM and EDX—these analysis would provide insight into the mechanism driving the topcoats failure in the TBC architecture.

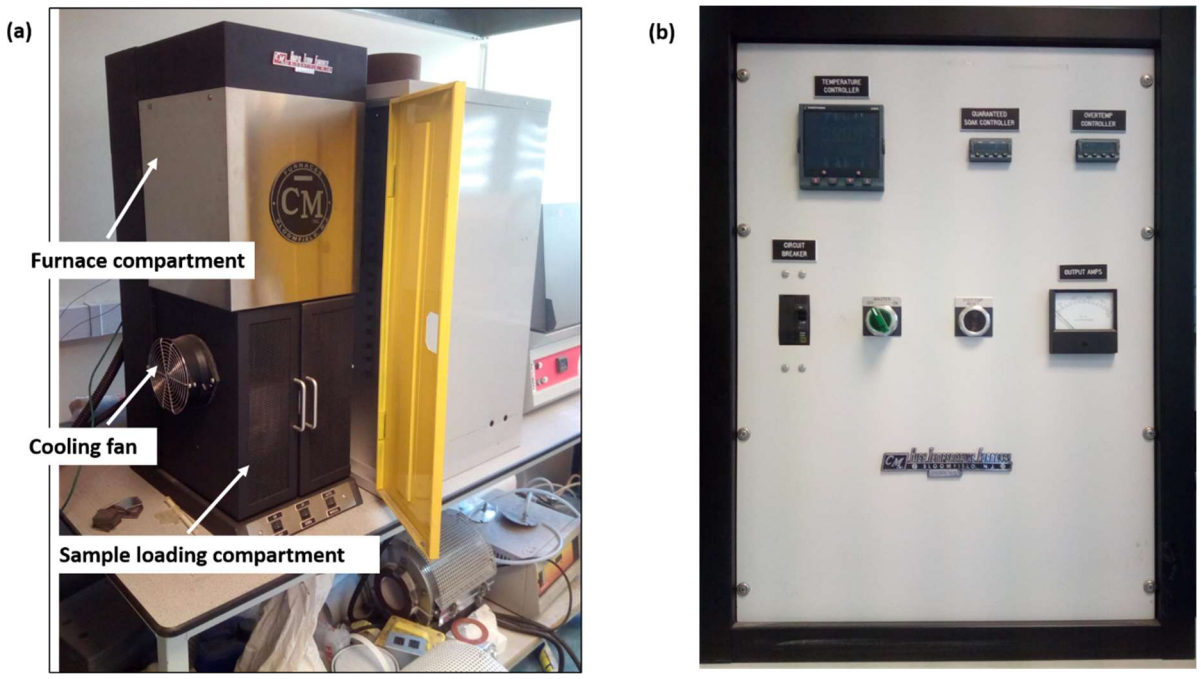

Figure 3-10: Thermal cycling rig (a) the furnace (b) the control panel

3.6 Mechanical Characterization

3.6.1 Microhardness and indentation fracture toughness measurement

The microhardness and indentation fracture toughness of the coatings were measured using a Vickers microhardness tester (Buehler, USA). Each measurement was done on a polished cross–section of the respective coating sample. The microhardness was measured in three rows—five on each—at a load of 10 gf. The locations of the micro indentation points were chosen for the individual coatings to ensure the indents were well situated inside the coating as well as to have the indents separated from one another by at least 40 µm on the horizontal and 20 µm on the vertical. The average microhardness of each row was presented with the associated standard error in mean. The microhardness and indentation fracture toughness of the as–sprayed and the heat–treated coatings were measured at a load of 10 gf and 100 gf respectively. Ten microhardness indentations were performed at the center on the polished cross–

section of the coating. The indentation fracture toughness was estimated from five indents with horizontal and vertical extended radial cracks. The horizontal radial cracks and the vertical radial cracks run parallel and perpendicular to the coating's surface respectively. The fracture toughness calculation was completed based on Equation (3.18) developed by Evans and Charles [188]:

$$K_{IC} = 0.16(c/a)^{-1.5} H a^{0.5}; \frac{c}{a} \geq 2.5$$ ---------- Equation 3.25

Where K_{IC} is the mode–I fracture toughness in MPa.m$^{0.5}$, c and a are the crack length and indentation radius respectively (see Figure 3–10) while H is hardness in GPa. The average microhardness and the indentation fracture toughness was presented with the associated standard error in mean.

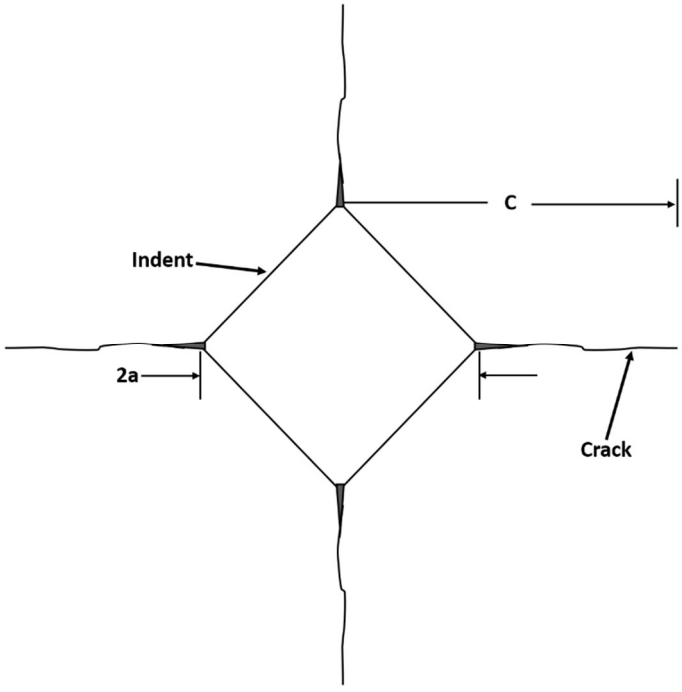

Figure 3-11: Schematic of indent with the indentation cracks, indentation radius and the crack length

3.6.2 Nanohardness and indentation elastic modulus measurement

Nanoindentation was carried out at room temperature on the Platform 3 rig produced by Micro Materials Ltd (Wrexham, UK) using a Berkovich indenter tip. Nanoindentation testing involves a contact measurement of unknown mechanical properties (e.g., elastic modulus and hardness) of a material using an indenter of defined geometry and known properties. The measurement yields reduced elastic modulus as a function of rate of change of applied load (L) to penetration depth (h) while the nanohardness comes from the ratio of the applied load to the projected contact area (A_p). The elastic modulus of the unknown material can then be calculated by Oliver and Pharr method [189] where the reduced elastic modulus, E_r, from the measurement data, the elastic modulus of the indenter material E_i and the coating elastic modulus E_c are related as in Equation (3-26)—v is Poisson ratio while c and i are used to designate coating and indenter, respectively.

$$\frac{1}{E_r} = \frac{1-v_c^2}{E_c} + \frac{1-v_i^2}{E_i} \quad \text{---------- Equation 3.26}$$

$$E_r = \frac{\beta}{2}\sqrt{\frac{\pi}{A_p}}\frac{dL}{dh_p} \quad \text{---------- Equation 3.27}$$

$$A_p = 3\sqrt{3}{h_p}^2 tan^2\theta \quad \text{---------- Equation 3.28}$$

β is the indenter geometry correction factor (1.034 for Berkovich indenter), θ is the indenter face angle (65.3°) and π, a mathematical constant taken as 3.142 [190].

The nanohardness and the reduced elastic modulus of the coatings were obtained from the nanoindentation performed on the polished cross section of the coatings. The loading–dwell–unloading scheme was used maintaining a peak load of 20 mN for 2 s and a rate of 4 mN/s during loading and unloading stages for a total of 30 indentations

per sample in six rows (five in each row) adequately spaced from coating surface and coating–substrate interface. The average nanohardness of each row was presented with the associated standard error in mean. The E_i and v_i are taken as 1140 GPa and 0.07 respectively [191]. The Poisson ratio of bulk Al_2O_3 (0.22) and YSZ (0.31) were used for the coatings in each case [192].

3.6.3 Residual stress measurement

3.6.3.1 X–ray and neutron diffraction residual stress measurement

The X–ray diffraction residual stress surface scan of two coatings (C–Al_2O_3 and YSZ) was conducted on the D8–Discover (Bruker AXS Inc., Madison, WI, USA) with Cu Kα radiation source (1.54 Å) the parameters are as stated in Table 3–5. The defocusing of the diffractometer at tilt angles above zero ($\Psi \neq 0^o$) was minimized with the usage of high diffraction angle planar reflections (hkl) [21]. The scanned data was then analysed using Stress 2.0 software (PANalytical, Almelo, The Netherlands). The average XRD residual stress of the two coatings was calculated based on the differential technique that eliminates the need for a reference strain/stress free sample. A linear relationship is evoked between the surface stress in any direction and the measured interplanar lattice spacing according to Equation (3-29)—the $\sin^2\Psi$ technique [99].

$$\sigma_{\phi} = \left(\frac{E}{1+\nu}\right)\frac{1}{d_{(\phi\psi)0}}\left(\frac{\Delta d_{\phi\psi}}{\Delta sin^2\psi}\right) \text{ ---------- Equation 3.29}$$

Where $d_{(\Phi\psi)0}$ and $(\Delta d_{\Phi\psi}/\Delta \sin^2\psi)$ are the intercept and slope of a plot of $d_{\Phi\Psi}$ against $\sin^2\Psi$ and υ has the usual meaning. E has been used as macroscopic elastic modulus obtained from nanoindentation measurements. The value of E used thus represents

an average value over all possible directions in the crystal lattice; this may vary significantly from the diffraction elastic constant due to anisotropy [193].

Table 3-5: XRD residual stress scan parameters

Parameters	Coatings	
	Al_2O_3	YSZ
2θ, °	139–152	111–120.6
Step size, °	0.1	0.1
Dwell time, sec./step	8	8
orientation angle, φ°	0, 90	0, 90
Tilt angle, ψ°	0–60	0–60
PDF card	γ–Al_2O_3, 00–10–0425	Tetragonal, 01–070–4429
Peak	145.3°	116.2°

Neutron diffraction through thickness residual strain measurements were completed on the two coatings at the Rutherford Appleton Laboratory (RAL) using the time–of–flight (TOF) neutron strain scanner (ENGIN–X) at the ISIS facility. The details of the neutron diffractometer is published elsewhere [194, 195].

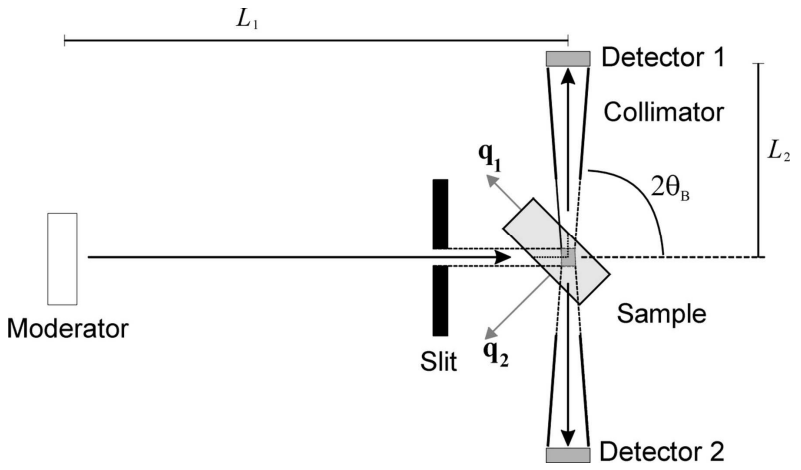

Figure 3-12: Schematic diagram of a time–of–flight (TOF) neutron diffractometer showing the orientation of sample relative to the incident neutron beam passing through a slit and the diffracted beam detectors 1 and 2. The volume of the sample explored by the instrument corresponds to the intersection of the incident and the diffracted beams, as defined by the slits and the collimators [195].

The basic concept underlining the neutron diffraction residual strain experiment involves a pulsed beam of neutrons with a wide energy range incident upon a sample positioned at an angle θ_B to the incident beam; a small fraction of the beam gets scattered into a detector at an angle $2\theta_B$. Figure 3–12 shows the schematic representation of the basic concept. The signal collected on detector–1 (Bank 1) corresponds to those in the longitudinal direction as for the impulse exchange vector marked q_1 in Figure 3–12; this along the length of the sample while the signals collected on detector–2 (Bank 2) corresponds to those in the transverse direction as for the impulse exchange vector marked q_2. The wavelength of the diffracted neutron collected by the detectors is defined from its time–of–flight (TOF) t, as in Equation 3-30, assuming an elastic collision between the incident neutrons and the samples.

$$\lambda = \frac{h}{m(L_1+L_2)}t, \text{ ---------- Equation 3.30}$$

In Equation 3.30, h, is the Planck's constant, m is the mass of the neutron particle, L_1 and L_2 represents the primary and the secondary flight paths respectively. The primary flight path is the distance travel by the incident neutron from the source to the sample while the secondary path is the distance travel by the diffracted neutron from the diffraction point to the detector. The wavelength, λ, obtained from Equation 3.30 is related to the interplanar spacing, d_{hkl}, the Bragg's angle and the specific peak position, t_{hkl}, in the TOF spectrum as in equation 3.31, such that:

$$d_{hkl} = \frac{h}{2\,sin\,\theta_B m(L_1+L_2)}t_{hkl} \text{ ---------- Equation 3.31}$$

The peak positions can be precisely determined by applying the method of least–squares refinement to the TOF spectrum; a typical sensitivity of the estimation of the peak position is approximately 50 με (1 με = 10^{-6}) defined by $\delta\varepsilon = \Delta t_{hkl}/t_{hkl} = \Delta d_{hkl} = d_{hkl}$.

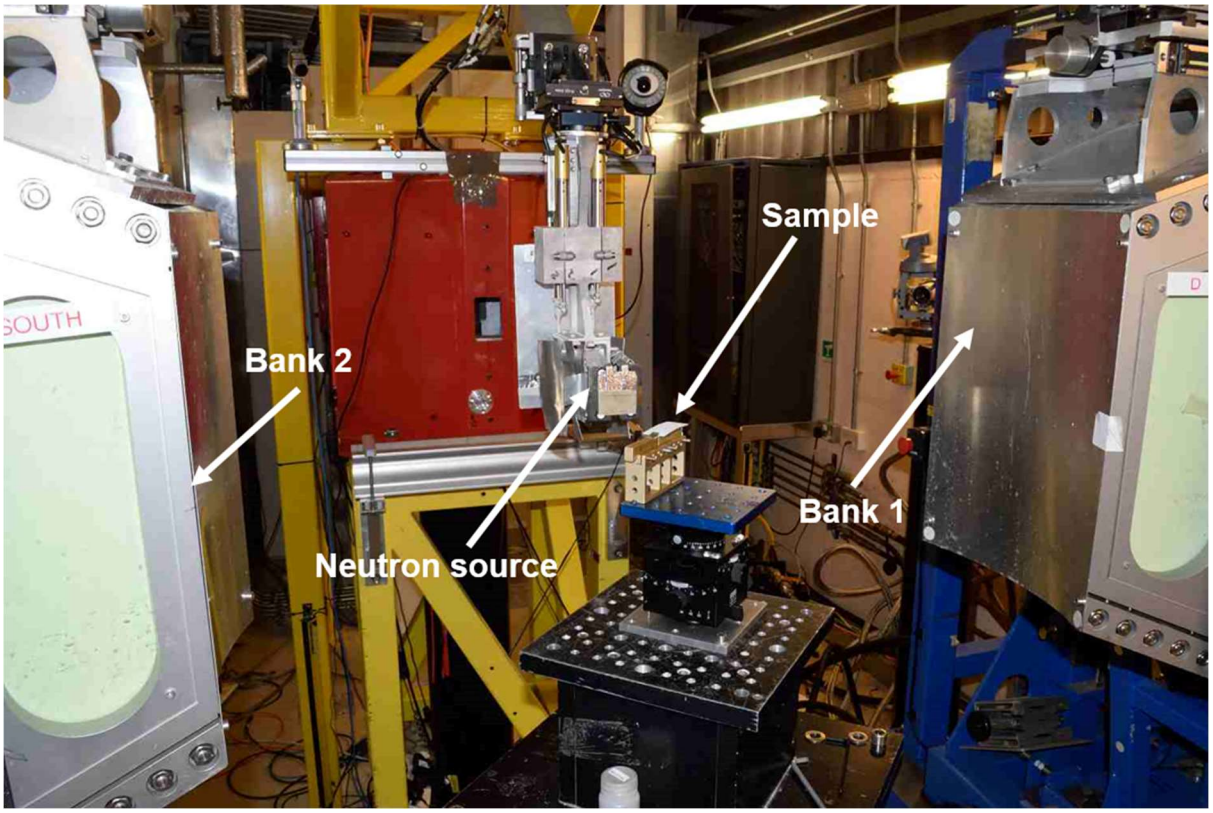

Figure 3-13: Neutron diffraction strain measurement setup on ENGIN–X

The samples for the neutron diffraction experiment comprise as–received AISI 304 stainless steel used as the reference for the substrate, a AISI 304 stainless steel substrate coated with Al_2O_3 and another AISI 304 stainless steel substrate coated with YSZ as well as pulverized coatings of Al_2O_3 and YSZ used as the reference sample for the coatings. The pulverized coating was obtained by repeated mechanical bending of the coated substrates. The set–up of the experiment is as shown in Figure 3–13; at each time during the experiments, samples were oriented at 45° to the neutron source. The sample orientation to the neutron source allows the detectors shown as Bank 1 and Bank 2 collect signals along the length of the sample (longitudinal direction) and the width of the sample (transverse direction) respectively. The incident neutron beam/gauge volume was partially submerged and traversed vertically through the coating thickness and near the coating substrate interface—this ensures high spatial

resolution [196]. The interval between scanned points in the coatings were maintained at 50 μm for the C–Al_2O_3 and 40 μm for the YSZ coating. The substrate was scanned using a fully submerged gauge volume at intervals of 50 μm for depth profiling of strain in the substrate material. The gauge volume used was 4 mm x 4mm x 200 μm with double slits positioned along the neutron incident path. The slit–to–sample separation was ~ 135 mm for the Al_2O_3 coating and ~ 155 mm for the YSZ coating. The respective pulverized coating samples were scanned as a reference for the coating layer in the coating–substrate composite while the as–received AISI 304 stainless steel was scanned as the reference for the substrate layer.

The residual strain in the coatings and the substrates were estimated using the single peak fitting analysis approach [197] using the neutron data analysis software, Open GENIE V2.3, provided by the CCLRC Rutherford Appleton laboratory (Didcot, England). The shift in the individual peaks of the coatings and the substrate were related to the interplanar lattice spacing of the reference samples as in Equation (3-32) to calculate the strain. Details of the peak fitting procedure used to extract the interplanar lattice spacing needed for the calculation of the strain is provided in Appendix A.

$$\varepsilon_{c/s} = \frac{d_{c/s} - d_0}{d_0}$$ ---------- Equation 3.32

In Equation (3-32), ε is the strain, d is lattice spacing, c and s signify coating and substrate while d_0 is the lattice spacing from the reference samples.

The elastic stress was then calculated from Equation (3-33)—it relates the stress to the strain, the elastic modulus and the poison's ratio.

$$\sigma_n = \frac{E}{1+\nu}\left[\varepsilon_n + \frac{\nu}{1-2\nu}\left(\varepsilon_i + \varepsilon_j + \varepsilon_k\right)\right]$$ ---------- Equation 3.33

Here, i, j and k specify measurement directions x, y and z respectively— E, υ, ε and σ have their usual meanings. Plane stress condition is imposed for the calculations because the samples studied fits a flat plate model—the thickness of the samples is small compared to the longitudinal and transverse dimensions. The flat plate model requires the samples were not loaded in the direction perpendicular to the plane of the plate [198]. The flat plate assumption also fits at the interface since the overall coating thickness is 200 μm for the Al_2O_3 coating and 120 μm for the YSZ coating and there is no transversal load applied to the face of the coatings. The weighted average of each of the stresses in the longitudinal and transverse directions were in turn calculated.

3.6.3.2 Incremental hole–drilling residual stress measurement

Through thickness residual stress profile of the two coatings (C–Al_2O_3 and YSZ) was calculated from relaxed strain measured by incremental hole–drilling completed with the Stresscraft Ltd (Loughborough, UK) hole–driller using a diamond impregnated inverted cone cutter (see set–up is shown in Figure 3–14). The data collected from the hole drilling measurement was analysed based on the UK National Physical Laboratory (NPL) Measurement Good Practice Guide 53 [100]. The analysis was completed with the Stresscraft RS INT software (v5.1.3) based on the integral method described by Schajer [199].

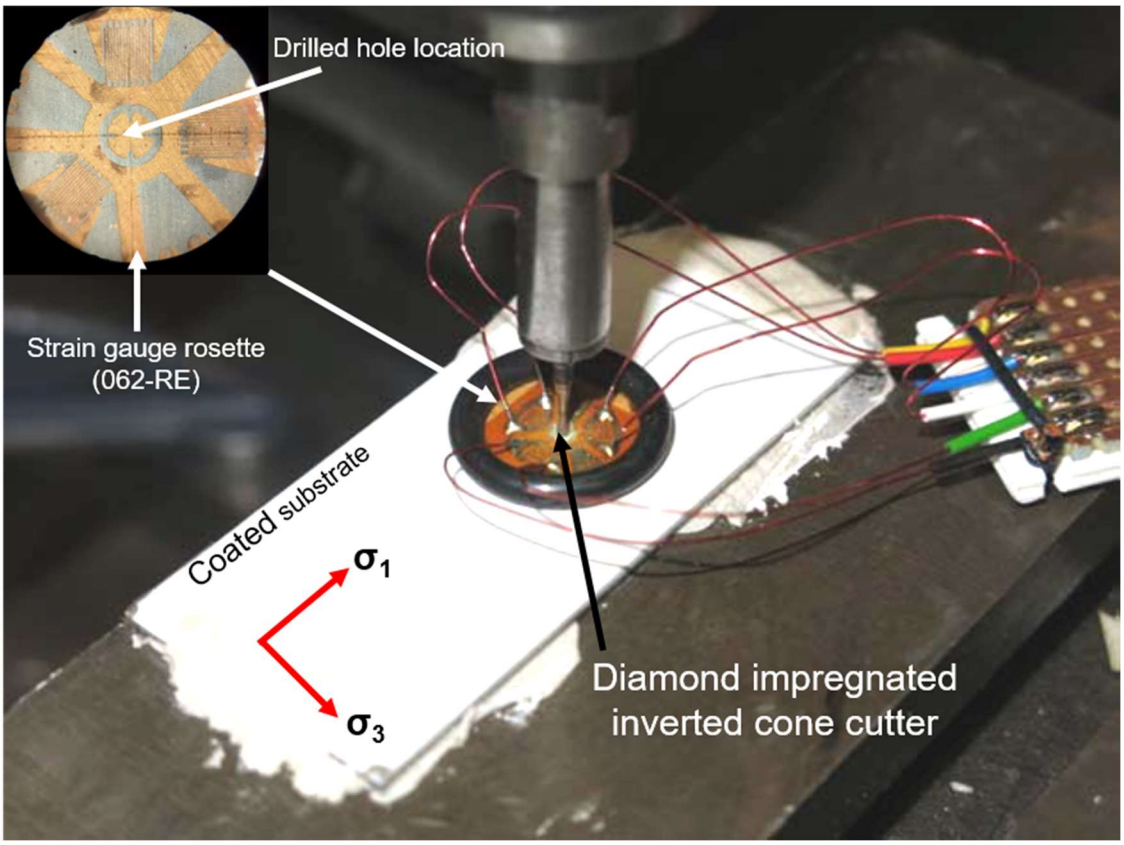

Figure 3-14: Incremental hole–drilling residual stress measurement setup

The integral method is the most reliable analytical procedure for the analysis of relaxed strain data obtained from incremental drilled hole—it uses finite element based calibration procedure [199]. The Integral Method utilizes the contributions of the corresponding stresses (σ(H)) at all depths of the drilled hole to the total measured strain relaxations, such that the relaxed strain as a function of depth, $\varepsilon_r(h)$, is as given in Equation (3.34).

$$\varepsilon_r(h) = \frac{(1+\nu)}{E}\int_0^h \hat{A}(H,h)\,\sigma(H)dH \quad 0 \le H \le h$$ ---------- Equation 3.34

Â(H, h) represents strain relaxation per unit depth caused by a unit stress at a depth H from the surface when the hole is at depth h. v and E are the Poisson ratio and the elastic modulus of the material specimen, respectively. H is the dimensionless depth from the specimen surface while h is the dimensionless hole depth; each one obtained

by dividing the depth from the specimen surface (in mm) and the hole depth (in mm) by the mean radius (r_m, in mm) of the strain gauge rosette, respectively. Practically, $\epsilon_r(h)$ is determined only for at *n* discrete points within the specimen, corresponding to *n number of* hole depths at successive increments, such that h_i, = 1, 2, 3, *n* is known. To that extent, an approximate solution of Equation (3.35) can be achieved using its discrete form as:

$$\sum_{k=1}^{k=i} \bar{a}_{ik}\, \sigma_k = \frac{E}{1+\nu} \varepsilon_i \; 1 \leq k \leq i \leq n$$ ---------- Equation 3.35

where ε_i is the measured strain relaxation after the ith hole depth increment, σ_k is the equivalent uniform stress within the jth hole depth increment, $\bar{a}_{ik}$ is the strain relaxation due to a unit stress within increment j of a hole i increments deep and n is the total number of hole depth increments. Â(H, h) is related to $\bar{a}_{ik}$ as in Equation (3.36)—its solution is obtained through finite element analysis.

$$\bar{a}_{ik} = \int_{H_{k-1}}^{H_k} \hat{A}(H, h_i) dH$$ ---------- Equation 3.36

The hole–drilling was completed using the orbital milling method to forestall damage around the drilled hole yet the microstructure of a thin layer around the hole could change. Also, ceramic coatings are susceptible to micro cracks—this influence residual stress measurement by the hole–drilling method [200]. The relaxed strain was measured by an EA–06–062RE target three–gauge rosette (Vishay Precision Group, Malvern, Pennsylvania, United States) with a mean radius (r_m) of 2.57 mm. The gauges are radially oriented to be 45º to one another [100] to ease the mathematical representation of the relationship between the calibration constants, the relaxed strains and the required stresses [199]. The two perpendicular gauges were oriented to allow one record the longitudinal strain (ϵ_1) and the other record the transverse strain

(ϵ_3). Each gauge recorded relaxed strain data at each depth of a 1 mm diameter hole drilled to 16 incremental depths: of four 32 μm, four 64 μm and eight 128 μm to reach a final hole depth of 1408 μm. This agrees to the recommendation of the hole depth being equal to the diameter of the hole to reduce the accompanying structural damage the hole-drilling technique causes [100].

The through thickness residual stresses were evaluated based on the elastic modulus obtained from the nanoindentation tests. The evaluation yielded longitudinal, transverse and shear stresses converted to the maximum and minimum principal stresses using Equations (3.37) and (3.38) respectively.

$$\sigma_{max} = \frac{\sigma_x+\sigma_y}{2} + \left[\left(\frac{\sigma_x-\sigma_y}{2}\right)^2 + \tau_{xy}^2\right]^{1/2} \quad \text{---------- Equation 3.37}$$

$$\sigma_{min} = \frac{\sigma_x+\sigma_y}{2} - \left[\left(\frac{\sigma_x-\sigma_y}{2}\right)^2 + \tau_{xy}^2\right]^{1/2} \quad \text{---------- Equation 3.38}$$

Where σ and τ represents the normal and shear stress; x and y indicate the longitudinal and the transverse directions, respectively. The average of each of the stresses in the longitudinal and transverse directions were also calculated. All tensile stresses were recorded as positive and the compressive stresses with a negative sign.

3.7 Wear test

The as–sprayed and the heat-treated G–Al_2O_3 coatings polished to 1 μm finish were tested for dry sliding wear at room temperature (~ 25 °C, humidity ~ 60 %) using a conventional ball–on–flat apparatus set up for reciprocating configuration (See Figure 3–15). α–Al_2O_3 balls (Ø 9.5 mm) were used as counterbodies. The setup was balanced in equilibrium by adjusting the distance (z) between the empty weight hanger (M_h) and the balance weight (W_b) before adding the test weight (L) of 650 g on the weight

hanger—this is the minimum weight that ensures the setup remains in equilibrium with the counter body position adjusted between the weight hanger and the pivot as shown in the free body diagram in Figure 3–16. The attained equilibrium position corresponds to a normal contact load (P) of 16.8 N on the test sample. The revolution counter was set to attain 60 rev/min and a sliding speed of 20 mm/s; the total sliding distance was 36 m with a track length of 10 mm for each test. The testing was performed twice on each coating to show repeatability.

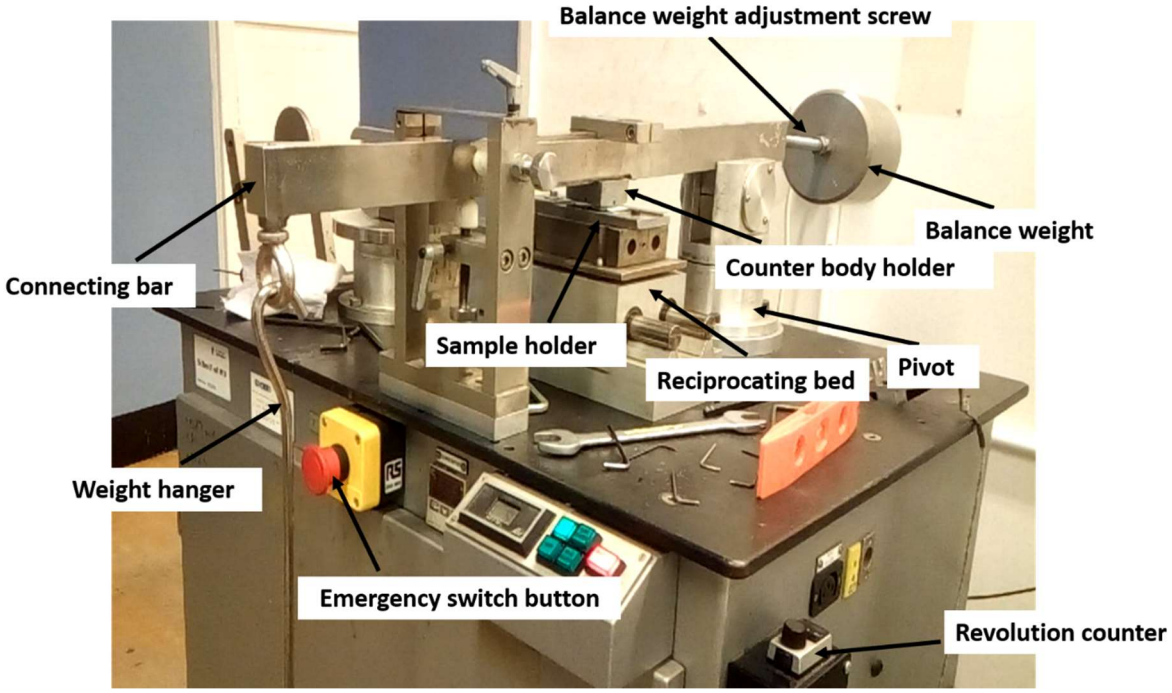

Figure 3-15: Wear test rig

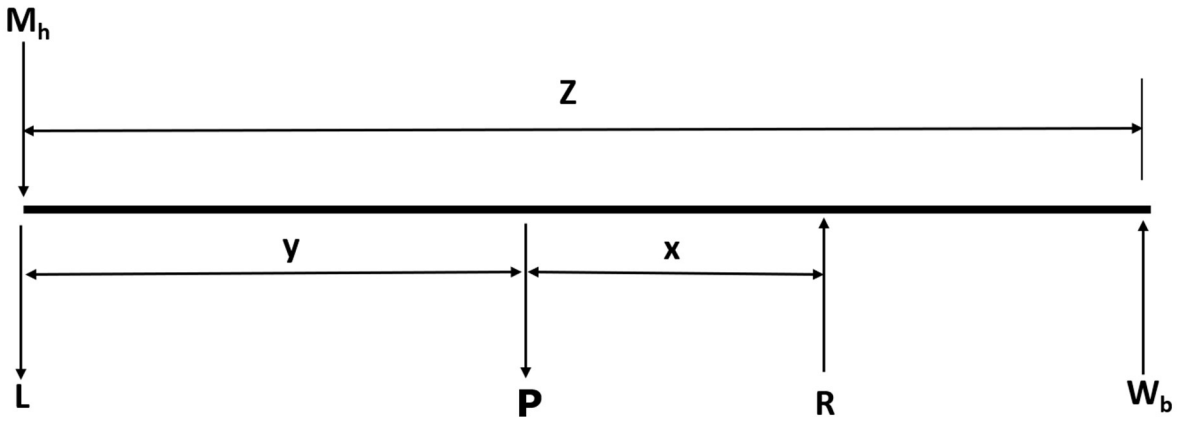

Figure 3-16: Free body diagram of wear test set–up

The depth of the wear track was measured with an Alicona Infinite Focus Advanced 3D System (Raaba/Graz, Austria) to give specific wear rate (SWR). The measurement was based on focus variation microscopy (FVM) in which the topography of a surface is constructed from the collections reflected light coming off the sample surface. A stack of 2D images of the surface is obtained through vertical (z) scans the surface of a sample. The surface of a sample is detected for each pixel by finding the corresponding *z*–location with the highest sharpness. The sharpness of each image pixel is calculated by the system in–built algorithm. The measurement is repeated for each lateral position of interest to obtain the depth profile of a surface [201, 202]. Five cross–sectional profiles were taken at different locations along the wear track length to obtain the effective area of material loss, which were then multiplied by the track length to calculate volumetric material loss. The specific wear rate was thus the ratio of the volumetric material loss to the product of total sliding distance and normal contact load. The wear of the α–Al_2O_3 ball was estimated on the assumption that the flattened wear scar, covering the contact points on its face, depicts a spherical crest see the schematic in Figure 3–17. The volumetric material loss of the counter body was thus estimated from Equations (3-39) and (3-40) described by Tippaban in [203]—

d is the depth of the scar, a is the radius of the scar, r is the radius of the ball while V is the volumetric material loss. Coating wear track morphology was examined using scanning electron microscopy and the scar on the α–Al_2O_3 counter body was examined with an optical microscope (Nikon Eclipse LV100ND–Tokyo, Japan).

$$V = \pi {d_s}^2 \left(r_b - \frac{d_s}{3}\right)$$ ---------- Equation 3.39

$$d_s = r_b - \sqrt{({r_b}^2 - {a_s}^2)}$$ ---------- Equation 3.40

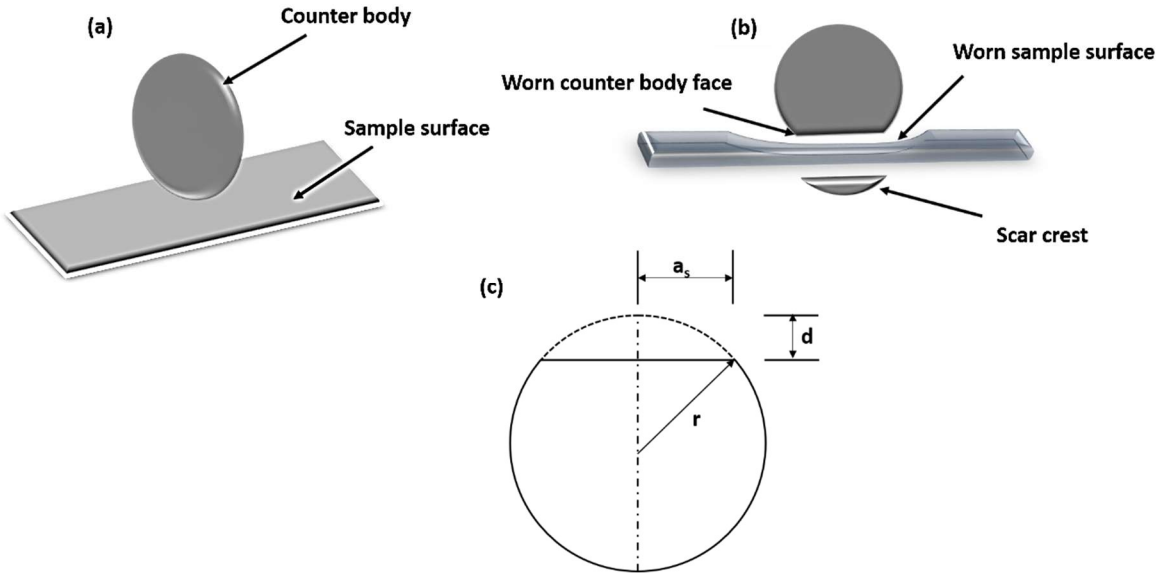

Figure 3-17: Schematic of the sample and the counter body (a) initial set up (b) ball on flat with wear on both the ball and the sample (c) representation of the ball wear showing depth of the scar, d_s, radius of the ball, r_b, and the radius of the scar, a.

3.8 Summary

The experimental techniques described in this chapter were applied in the study of thermally sprayed ceramic coatings deposited using three materials namely: Al_2O_3, YSZ and YAG. The techniques used include X–ray diffraction, neutron diffraction, electron microscopy (SEM and TEM), optical microscopy, image–analysis,

incremental hole–drilling, nano and micro indentation, thermal cycling, thermal conductivity, differential thermogravimetry (DTG), Fourier transform infra–red (FTIR), and diagnostics features analysis. The results of the conducted experiments are presented in the proceeding chapters to provide understanding of the microstructure, the phase compositions, the wear performance and the thermo–mechanical features of the coatings. The understanding provided would guide to the justification of the set objectives of this thesis.

Microstructure and wear resistant Al_2O_3 coating

4.0 Introduction

This chapter presents the results of microstructural study and the wear performance of Al_2O_3 coatings, in the as–sprayed and the heat–treated form. Previous studies on thermally sprayed Al_2O_3 coatings have typically deposited γ–Al_2O_3 coatings from thermodynamically stable α–Al_2O_3 powder [85, 204-206]. Manufacturing thermodynamically stable α–Al_2O_3 feedstock powder is achieved through the Bayer's process. Bayer's process is the commercial route to produce gibbsite [$Al(OH)_3$] from bauxite—a mixture of gibbsite and impurities of iron oxides and silicates. The calcination of gibbsite—the last stage of the Bayer's process yields the desired α–Al_2O_3 at temperatures above 1000 °C. However, many of the transitional Al2O3 phases can be produced at lower temperatures [75, 77]. Producing α–Al_2O_3 powder from Al2O3 salts is energy intensive and ultimately a wasteful process when thermal spraying of the α–Al_2O_3 powder results in the formation of γ–Al_2O_3. An alternative and more sustainable approach is to use a metastable Al_2O_3 feedstock which is easier to obtain and can transform to γ–Al_2O_3 during thermal spraying. Despite the low cost and availability, there has been little attention given to metastable Al2O3 powder as feedstock for thermal spraying. The Al_2O_3 coating used for the work presented in this chapter was deposited by SHVOF thermal spraying of suspension containing metastable Al_2O_3 described as G–Al_2O_3 in Section 3.3. The microstructural evolution of the coatings due to deposition and heat treatment was studied using XRD and electron microscopy (SEM and TEM). Microhardness and indentation fracture toughness of the coatings were also measured to investigate the correlation between the microstructure and the wear performance of the coatings.

4.1 As–received Al_2O_3 suspension: Particle size distribution (PSD) and phase analysis

The SE electron image of the Al_2O_3 powder particles dried from the G–Al_2O_3 suspension is shown in Figure 4–1. The Al_2O_3 particles present as agglomerates; the individual particles in the agglomerates are of irregular morphology. Qualitative inspection of the particle size suggests each particle is less than 200 nm. The particle size from the SEM image agrees with the particle size distribution (PSD) of the suspension shown in Figure 4–2. The PSD is mono–modal based on the distribution shown with a median size (D_{50}) of ~ 137 nm. The other two descriptive sizes for the particles are the D_{10} and the D_{90}, which for the G–Al_2O_3 particles are ~ 83 nm and ~ 225 nm respectively. The ratio of the descriptive sizes is used to calculate the sharpness index of the particles—a measure of the gravitational classification of the particles to suggest the possibility of flocculation or sedimentation in a liquid medium. The ratio of D_{10}/D_{50} is used to define the fine fraction and D_{50}/D_{90} for the coarse fraction [207]. The sharpness index obtained for both the fine and coarse fraction is ~ 0.6 for the particles in the suspension; thus, the suspension has equal proportions of fine and coarse aggregates.

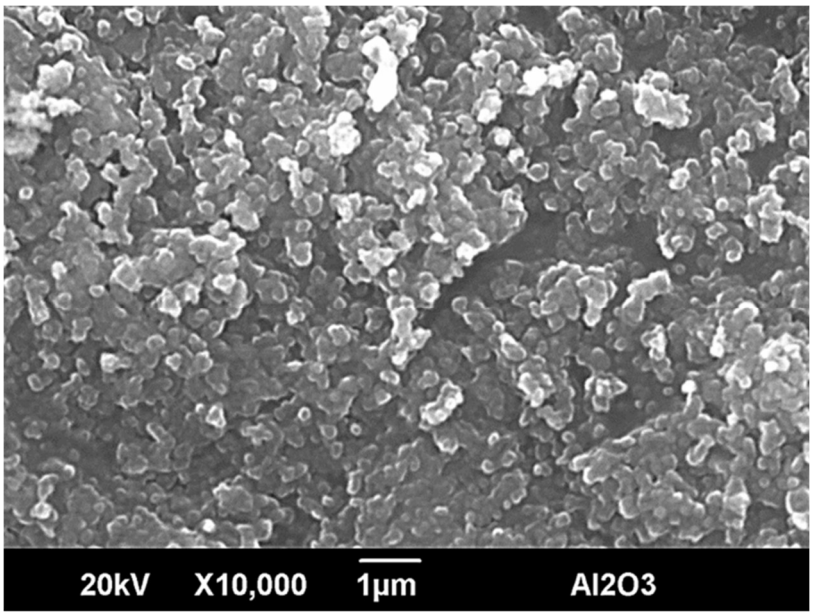

Figure 4-1: Secondary electron (SE) scanning electron micrograph showing nanometric Al_2O_3 powder remaining after drying of suspension.

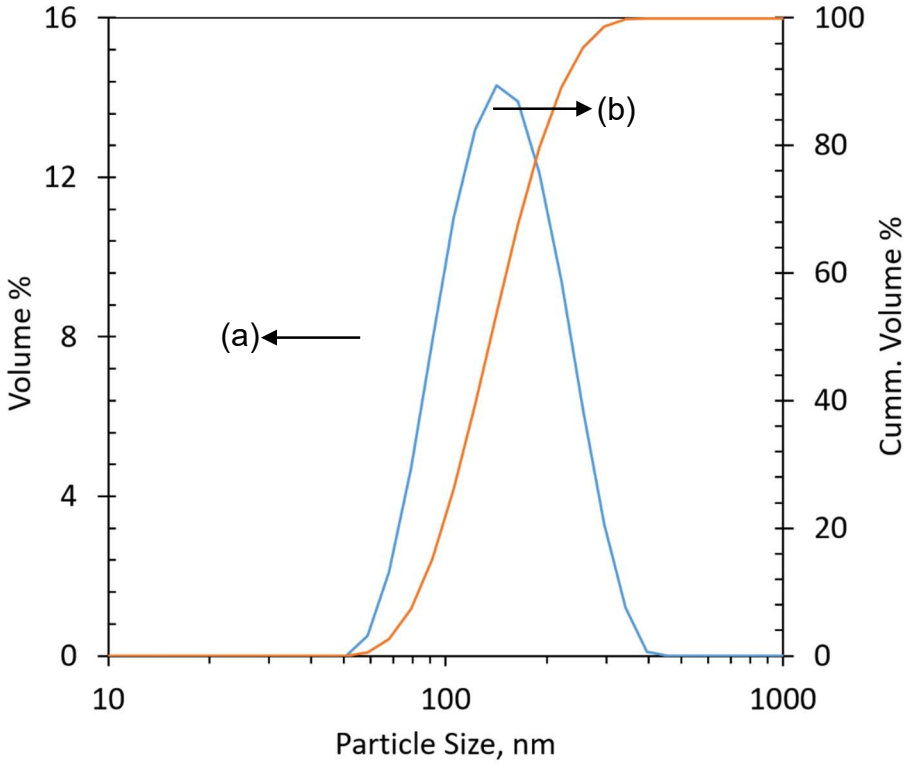

Figure 4-2: Particle size distribution profile of Al_2O_3 particles in the as–received suspension— the curve marked 'a' is the volume % of the particle distribution, the one marked 'b' is the cumulative volume % of the particle distribution

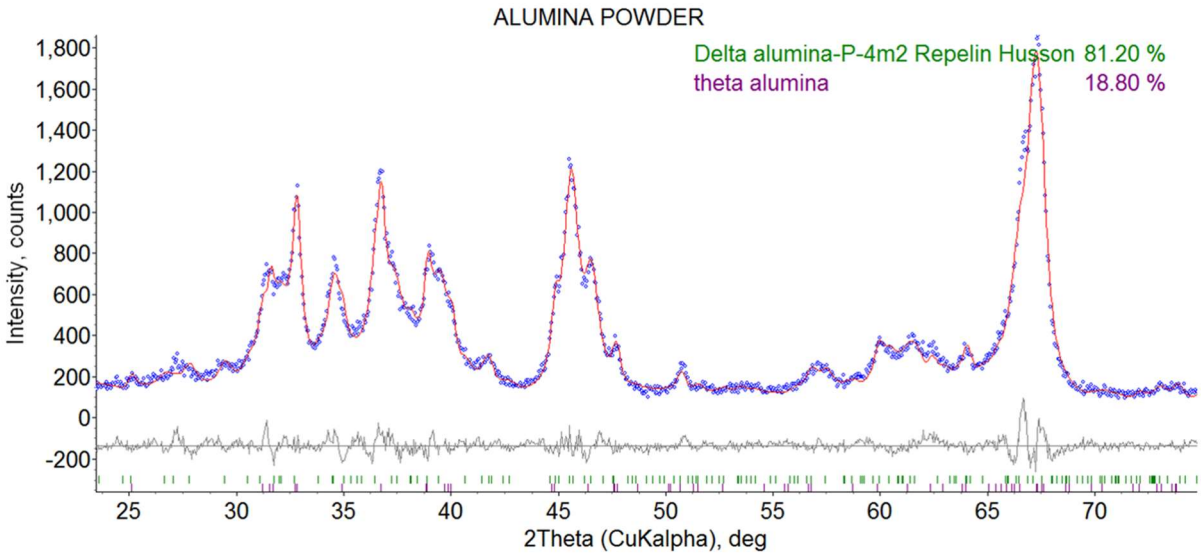

Figure 4-3: XRD profiles of G-Al_2O_3 powder obtained from the as–received Al_2O_3 suspension showing phase composition—Rietveld analysis was done by Dr Zdenek Pala

The XRD profile of the powder dried out of the as–received Al_2O_3 suspension is presented in Figure 4–3. The analysis shows the powder has two metastable phases: delta Al_2O_3 and theta Al_2O_3 [76]. The delta Al_2O_3 with a tetragonal crystal structure makes ~ 81.2 % of the powder while theta Al_2O_3 with the monoclinic crystal structure makes the balance. The peaks as shown in the figure overlap and are broad. The broad peak is characteristic of reduced crystallite size, stacking fault and twinning.

4.2 Splat formation and the diagnostic features of in–flight particles

Splats generated during thermal spray process comes in varying morphology and sizes. The size of the splats can be connected to the size of the individual particles [208] and/or of the agglomerates [9] in the feedstock used during the deposition process. The geometrical morphology of splats could be linked to the initial surface temperature of the substrate [209, 210] and the inclination of the substrate to the vertical axis [211]. The ideal splat morphology is circular with little or no splashing/fragmentation that could have caused the formation of fringes. A circular

splat is obtained when a molten material impacts a substrate maintained at 0° to the vertical axis and/or the substrate is preheated to a temperature above 100 °C before deposition. The substrate preheating would reduce the thermal gradient between the splat and the substrate. An increased thermal gradient means increased heat transfer rate at the interfacial boundary between the splat and the substrate; this will cause rapid solidification at the interface. While the splat contact layer with the substrate solidifies, its top layer remains in the liquid phase; it continues to flow to form other than the circular shape. Under this condition, the splats would lose its circularity; it forms fringes. Besides this interfacial based mechanism, protrusion on the substrate surface either due to grit blasting or presence of already laid splats [210] can also cause splashing.

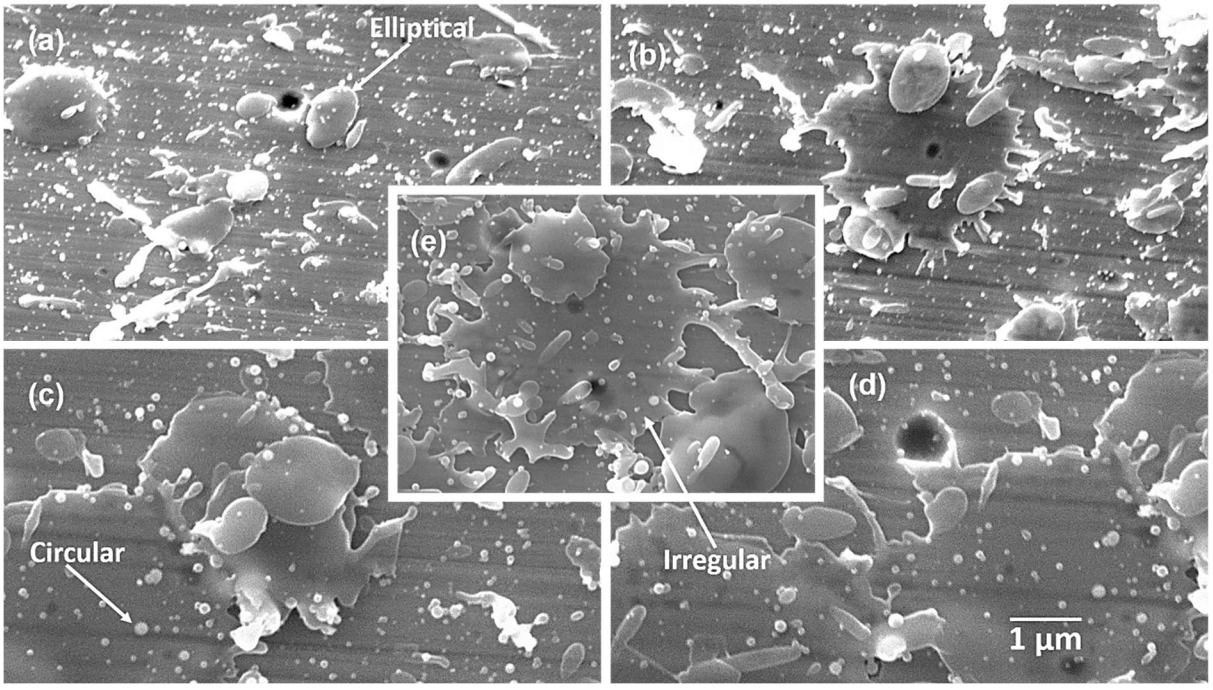

Figure 4-4: SE images showing oval, elliptical and irregular shapes of G–Al_2O_3 splats collected on polished AISI 304 substrate—the individual plate shows the diversity of the splats collected from the fast single swipe of the spray gun.

Al_2O_3 splats collected onto AISI 304 substrate polished to 1 µm are shown in Figure 4–4. The SEM micrograph of the splats suggests three main morphologies dominates the geometry of the splats collected. The geometry of the individual splat types has been described with two parameters—the aspect ratio and the top surface area. The aspect ratio describes the ratio of a major to a minor diameter; it is unity for a circular geometry [211]. The top surface area depicts the size of each splat; the splats with the smallest surface area also have aspect ratio of about unity. The other categories of splats identified have surface area of up to 70 μm^2—See Figure 4–5. A visual inspection of the remaining two categories of splats in addition to aspect ratio suggest some of the splats are elliptical, while the biggest ones have irregular edges characteristic of a splashed liquid.

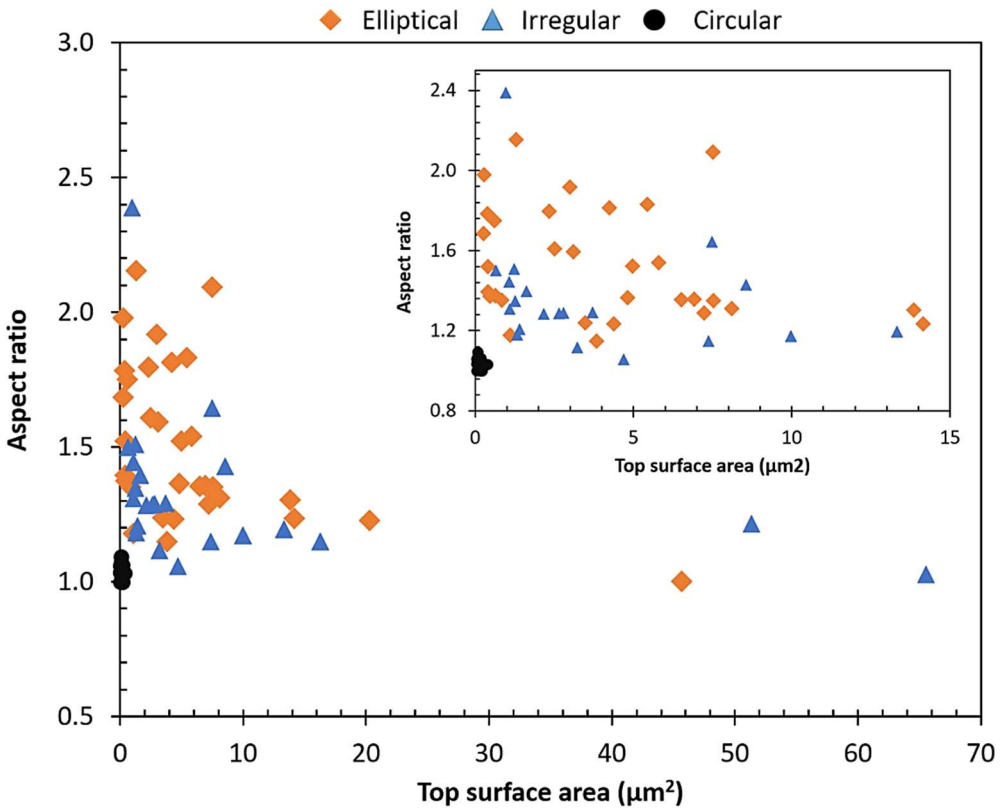

Figure 4-5: Morphological description of G–Al_2O_3 splats—aspect ratio plotted against top surface area

The qualitative features of the splats suggest they are produced from molten particles; this is supported by the diagnostic characteristics of the in–flight Al_2O_3 particles recorded from the Accuraspray—twenty-eight values were analysed for each data set (see Appendix B). The average temperature and velocity of the particles were recorded as 2045 ± 5°C and 1002 ± 20 m/s respectively. The error range for the recorded temperature and velocity due to the uncertainties of the coating deposition process are ±61°C and ±30 m/s respectively. The uncertainties could result from variation in the flame power due to possible varying flow rate of the hydrogen fuel and oxygen. The suspension flow rate could also fluctuate momentarily. It is also impossible to ascertain the inflight particle size after the hydrodynamic break up on injecting the suspension into the combustion chamber. The temperature of the in–flight particles confirm the particles were molten given that the melting point of Al_2O_3 is ~ 2000 °C. The molten Al_2O_3 impinging the substrate at an average velocity of 1002 m/s could not have remained rounded on impact—this is true especially for the large splats which have impacted the substrate directly. The splat morphology thus described here will be shown later to influence the coating build up.

4.3 Microstructural characterization of the coatings

4.3.1 Surface morphology and cross–sectional features of the as–sprayed coating

The top surface and the cross–sectional image of the G–Al_2O_3 coating are presented in this subsection to describe the basic features of the coating in its as–sprayed form. The top surface image of the coating shown in Figure 4–6(a) is presented in low magnification to provide a representative view of the surface morphology of the coating. The coating in its as–sprayed form covers the top face of the substrate; it comprises of splats of varying sizes and morphology. The splats were overlaid

haphazardly; the random splat arrangements engender the formation of inter–splat gaps identified as voids. Despite the presence of the inter–splat voids overall the coating shows no visible cracks.

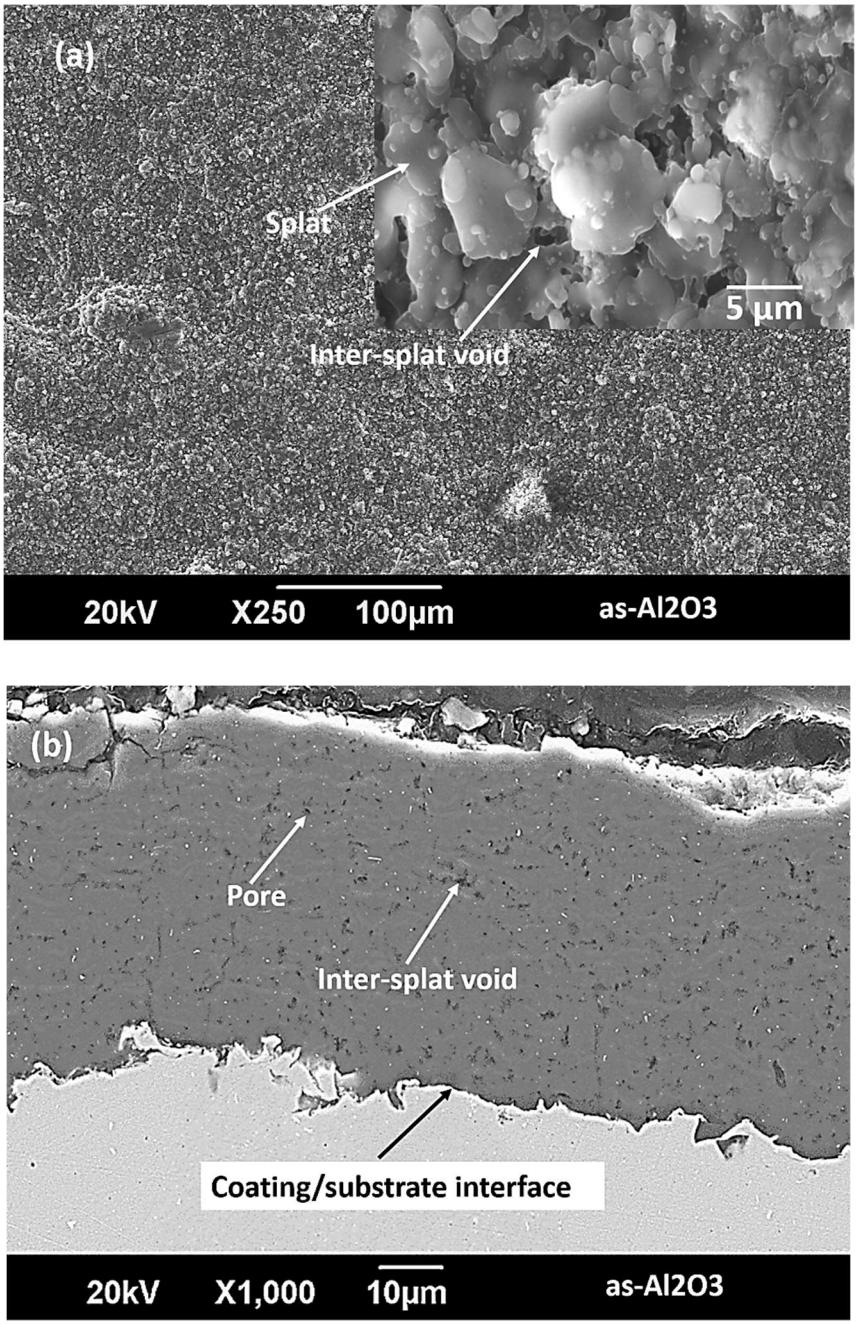

Figure 4-6: Scanning electron micrographs of the as–sprayed G–Al_2O_3 coating showing (a) low magnification SE micrograph of the surface morphology with no visible cracks (b) back scattered electron (BSE) micrograph of the cross–section with good coating–substrate bonding

A BSE cross–sectional image of the as–sprayed G–Al_2O_3 coating shown in Figure 4–6(b) shows the coating thickness, visible defects, and the coating/substrate interface. The coating shows good bonding to the substrate giving the absence of cracks or delamination at the coating–substrate interface. The implication of the random overlay arrangement of the splats also shows as pores and voids as the visible defects on the coating cross–section. The thickness of the coating measured with image analysis procedure is ~ 40 ± 2 μm corresponding to ~ 5 ± 0.3 μm per spray pass.

4.3.2 Amorphous/crystalline phases in the as–sprayed G–Al_2O_3 coating from TEM–SAD

A lamella lift–out was obtained from the as–sprayed G–Al_2O_3 by FIB milling; the sequential order of the lift–out procedure is depicted by Figure 4–7. The FIB milled trench in the coating is shown in Figure 4–7 (a); the milled section was cut open, showing as a cantilever in Figure 4–7 (b) ready to be transferred on to a probe. The milled section on the probe as shown in Figure 4–7 (c) was then thinned to electron transparency as in Figure 4–7 (d). The dimension of the lift–out comes to ~ 5 μm x 3 μm and a thickness of ~ 100 nm.

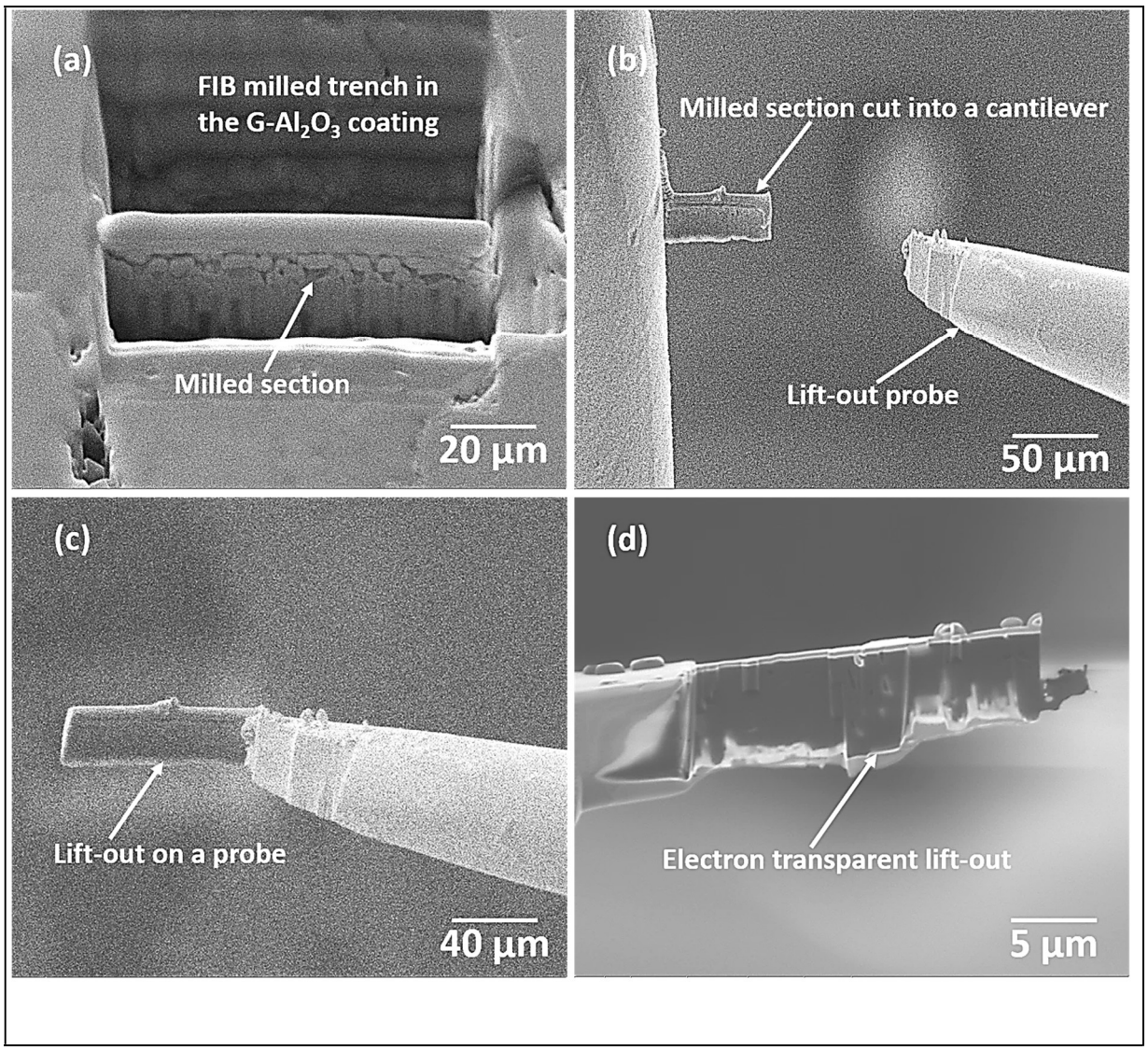

Figure 4-7: FIB milling procedure showing (a) milled trench and the milled section (b) the milled section ready to be transferred to the lift–out probe (c) the lift–out on the probe (d) the electron transparent lift–out—this was obtained with the help of Dr Christopher Permenter

A bright field TEM image was obtained from the lift–out, as shown in Figure 4–8 (a), for selected area electron diffraction pattern (SAED). The bright field image shows two plain sections without overlaid dark patches (marked A) and another with dark patches (marked B). Selected area electron diffraction (SAED) pattern was obtained from each of the regions to identify the phase structure in the representative area from which the lift–out was milled. The SAED patterns from the regions marked “A” and “B” in Figure

4–8 (a) are shown in Figure 4–10 (b) and (c). The SAED pattern in Figure 4–8 (b) shows diffused hallo rings. This indicates the region marked “A” composed of amorphous phase. The region marked “B” shows diffraction contrast to indicate the presence of a crystalline phase. The distinct crystalline phase in the region was identified from the diffraction pattern shown in Figure 4–8 (c) as the FCC γ–Al_2O_3 with the following hkl parameters:(111), $(3\bar{1}1)$ and $(2\bar{2}0)$.

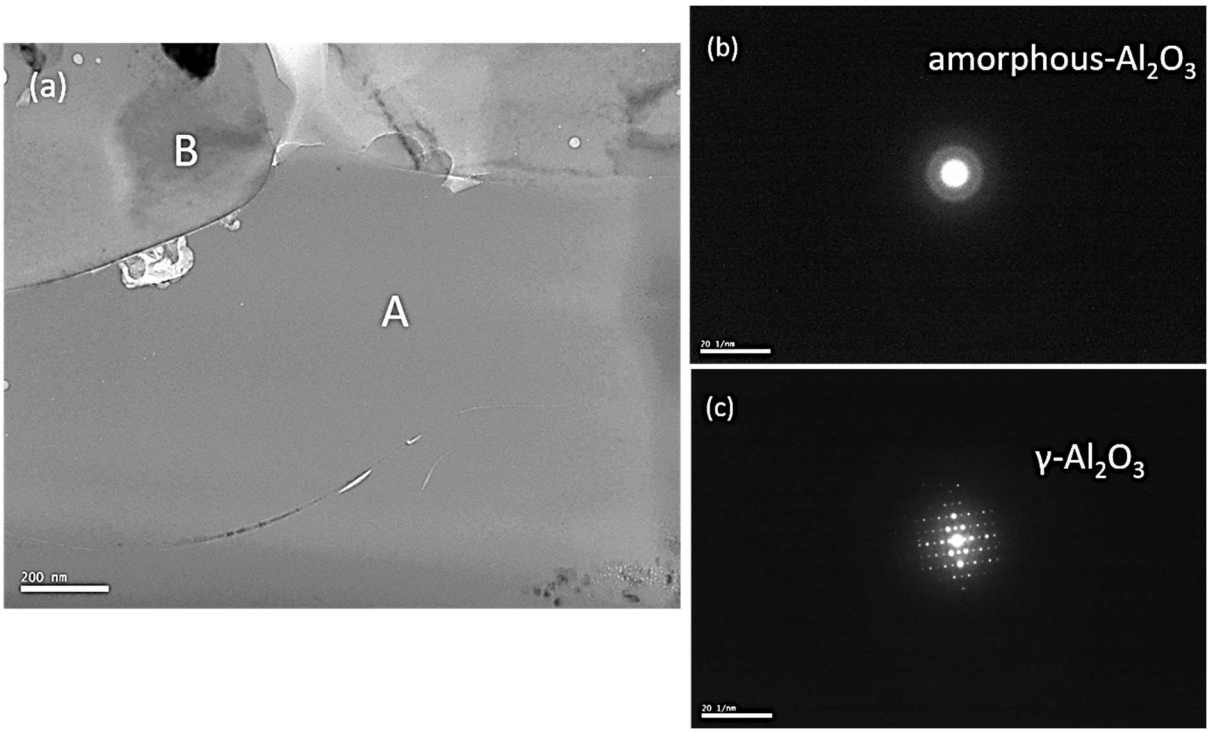

Figure 4-8: (a) Top surface bright field TEM image of the FIB lift–out from the Al_2O_3 coating; (b) SAD pattern corresponding to the region marked "A" in (a); (c) SAD pattern corresponding to the region marked "B" in (a)—this was obtained with the help of Dr Nigel Neate

4.3.3 Phases in the as–sprayed and heat–treated coatings

Combined results of the Rietveld refinement analysis of the XRD data of the as–sprayed and the heat–treated G–Al_2O_3 coatings (HT–600–6h[3], HT–750–6h[4] and HT–750–48h[5]) are shown in Figure 4–9. The as–sprayed coating and the HT–600–6h coating has amorphous and crystalline phases; the amorphous contents show as a broad hump at the 32° and the 62° 2θ positions. The degree of crystallinity of the as–sprayed coating was ~ 20 %; the 20 % crystalline phase predominantly comprises of cubic γ–Al_2O_3. The presence of the cubic γ–Al_2O_3 in the as–sprayed coating reinforces the results of the SAED presented in subsection 4.3.2 above. The ht–600–6h coating though retains the observed amorphosity in the as–sprayed coating, it shows additional crystalline Al_2O_3 phase to the cubic γ–Al_2O_3 detected in the as–sprayed coating; it shows trace amount of corundum (α–Al_2O_3).

[3] 600 °C, 6 h
[4] 750 °C, 6h
[5] 750 °C, 48h

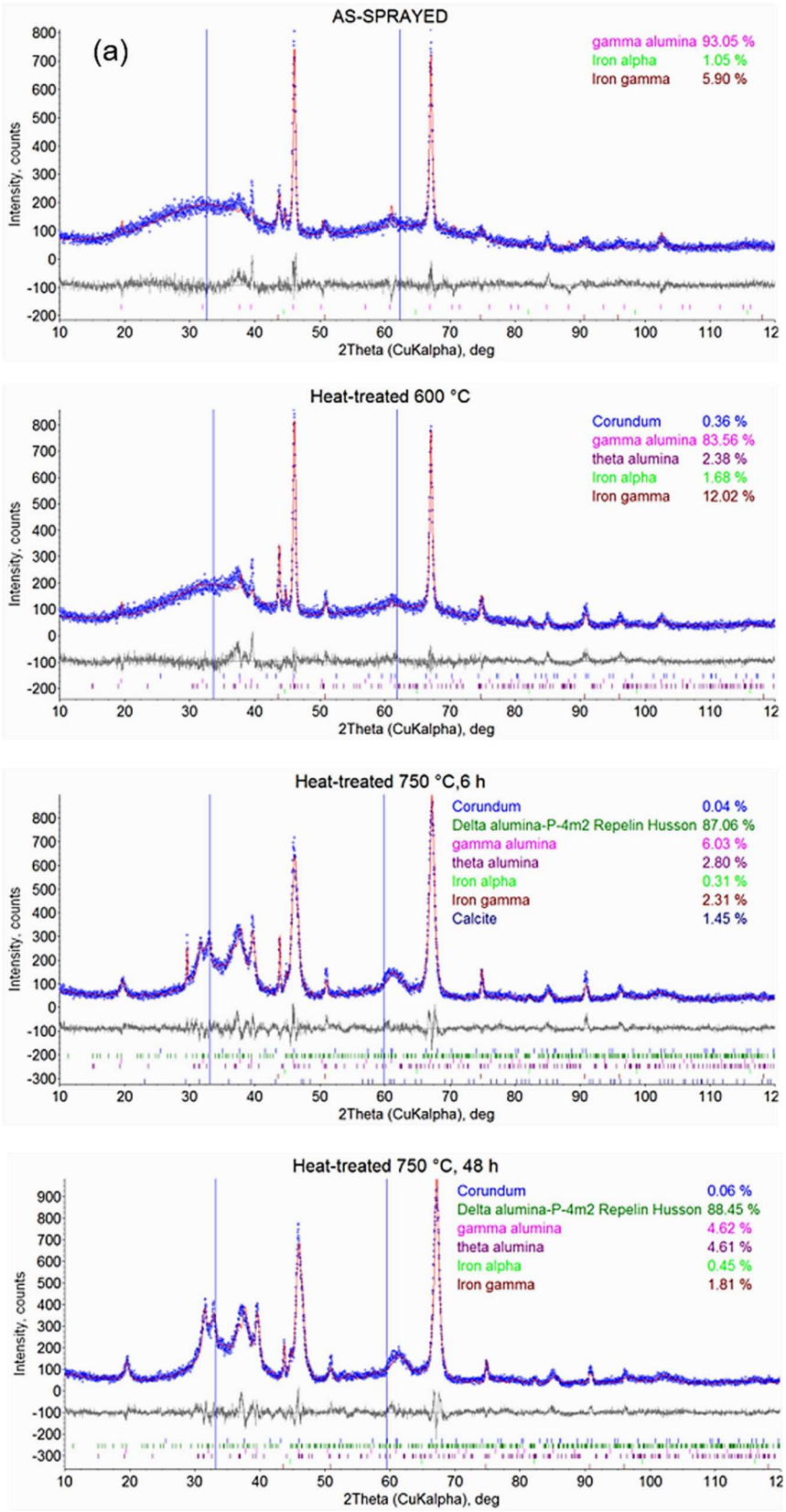

Figure 4-9: XRD scan profile of as–sprayed and heat-treated G–Al_2O_3 coatings—Rietveld analysis was done by Dr Zdenek Pala

Table 4-1: Phase quantification and crystallites size in the Al_2O_3 samples

S/N	Coatings	γ–Al_2O_3		δ–Al_2O_3		θ–Al_2O_3	α–Al_2O_3
		Crystallite size (nm)	(%)	Crystallite size (nm)	(%)	(%)	(%)
	as–sprayed	31.8	93.05	–	–	–	–
2	HT–600–6h	33.5	83.56	–	–	–	0.36
3	HT–750–6h	17.5	6.03	10.9	87.06	2.80	0.04
4	HT–750–48h	17.7	4.62	11.1	88.45	4.61	0.06

The remaining two coatings heat–treated at 750 °C (HT–750–6h and the HT–750–48h) show new Al_2O_3 phases that were not seen in neither the as–sprayed coating nor the HT–600–6h coating. The presence of more crystalline phases was in addition to reduced amorphosity and γ–Al_2O_3 contents; this can be seen in the Rietveld refinement profile of the coatings. The γ–Al_2O_3 and amorphous phases in the as–sprayed coating has mostly transformed to tetragonal δ–Al_2O_3 with trace amounts of monoclinic θ–Al_2O_3 in both the HT–750–6h and the HT–750–48h coatings. Other than the phase transformation engendered by the heat–treatment, each of the coating also show varying crystallite sizes. Table 4–1 shows the summary of the Al_2O_3 phase quantifications and the crystallite size in the four coating samples. The crystallographic features of the as–sprayed coating have not changed much after the heat treatment at 600 °C, only ~ 9% loss in γ–Al_2O_3 phase and an approximate crystallite size range (< 2 nm). The 150 °C increase to the heat treatment temperature

creates significant change in the crystallographic features; over 80% of the γ–Al_2O_3 phase got transformed to two metastable phases and trace amount of corundum. The transformation was accompanied by 50–60% reduction in the crystallite size of either of γ–Al_2O_3 and δ–Al_2O_3. The obvious effect of the crystallite size reduction shows as broad peaks in the Rietveld refinement profiles of both the ht–750–6h and the ht–750–48h coatings. Reflections of α and γ–iron detected in the patterns are from the substrates; this is due to the surface cracks that accompanied the post spray heat treatment. The calcite in the pattern is a sample mounting artefact; it could be avoided by using little amount of calcite that can be hidden away under the sample during the X-ray scan.

4.4 Post spray heat–treatment: porosity, microhardness, and the indentation fracture toughness of the G–Al_2O_3 coatings

The porosity and micro–mechanical properties of G–Al_2O_3 coatings heat–treated at two different temperatures (600 °C and 750 °C) and for two different durations (6h and 48h) are compared to those of the as–sprayed G–Al_2O_3 coating in this sub–section. The change in the microstructure of the coatings after the post spray heat–treatment is presented with magnified BSE micrographs of the cross–sectional images shown in Figure 4–10. The pores in the four coatings shown in the figure are the darker features in contrast to the identified splats; the pores are unevenly scattered across the cross–section of the coatings. The size and morphology of the pores varies in each of the coatings. The summary of the change in the microhardness and the porosity of the heat–treated coatings as they compare to those of the as–sprayed coating is presented in Table 4–2. The porosity analysis was based on the volumetric ratio of pores to solids (splats) in the coatings.

Table 4-2: Porosity and microhardness of as–sprayed and heat–treated G–Al_2O_3

S/N	Coatings	Porosity (%)	Microhardness (GPa)
1.	as–sprayed	7.3 ± 0.4	9 ± 1
2	ht–600–6h	5.4 ± 0.4	12 ± 2
3	ht–750–6h	6.4 ± 0.5	14 ± 3
4	ht–750–48h	5.7 ± 0.5	16 ± 3

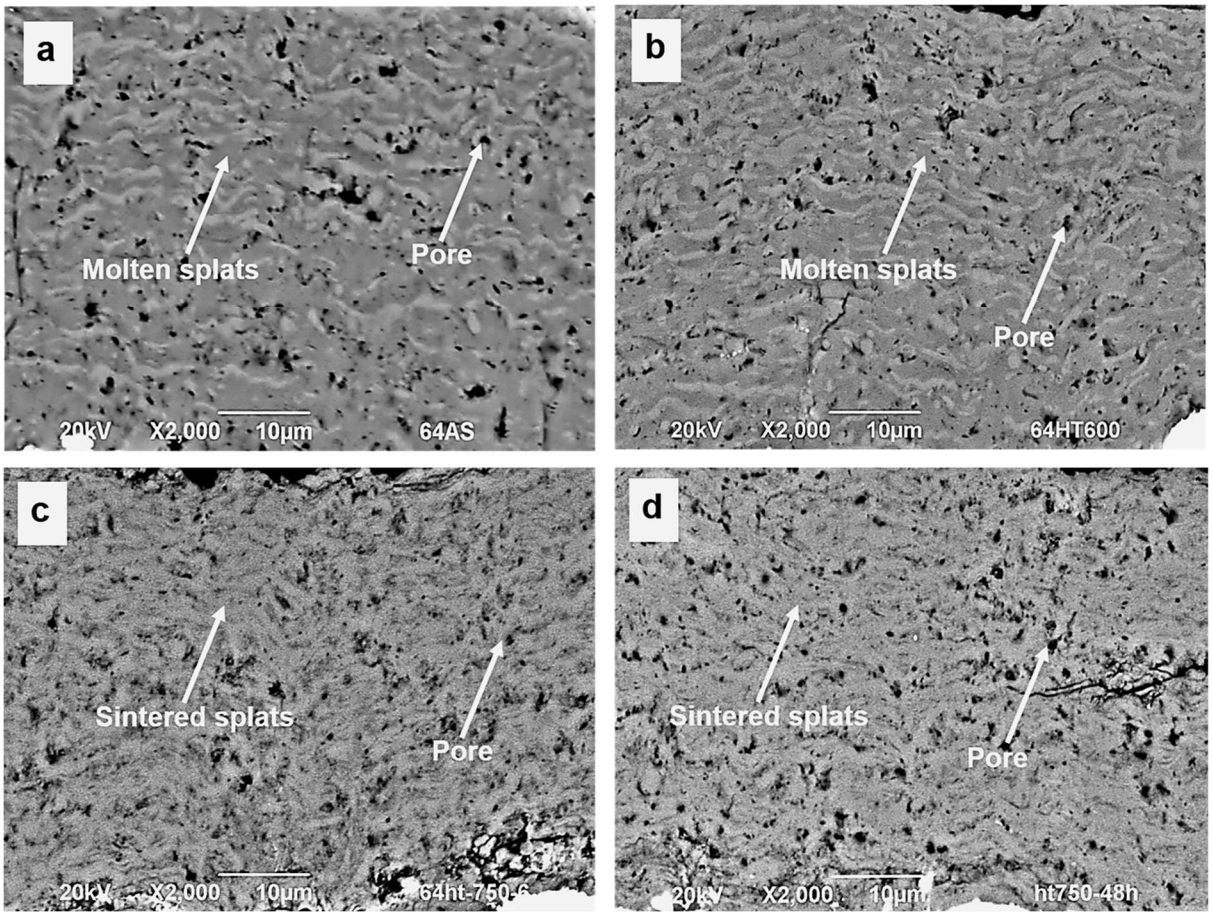

Figure 4-10:BSE micrographs of the cross–section of G–Al_2O_3 coatings showing molten splats and pores in (a) as–sprayed coating (b) heat treated coating at 600 °C for 6 h—ht–600–6h.

(c) and (d) show coatings heat treated at 750 °C for 6 h and 48 h—ht–750–6h and ht–750–48h respectively with sintered splats and pores

The observed changes in the microhardness scales with the change in the microstructure of the coatings as depicted by the change in the porosity. A typical indent obtained by Vickers microhardness testing on the cross section of the coatings is shown in Figure 4-11. The as–sprayed coating had a mean microhardness of 9 ± 1 GPa, which falls in the reported range of 6–9 GPa for SHVOF thermally sprayed Al_2O_3 coatings [212]. The microhardness of the ht–600–6h coating was 12 ± 2 GPa, which is an improvement of 30 % over the as–sprayed coating. A further increase was seen for the ht–750–6h and the ht–750–48h coatings with microhardness values of 14 ± 3 GPa and 16 ± 3 GPa respectively.

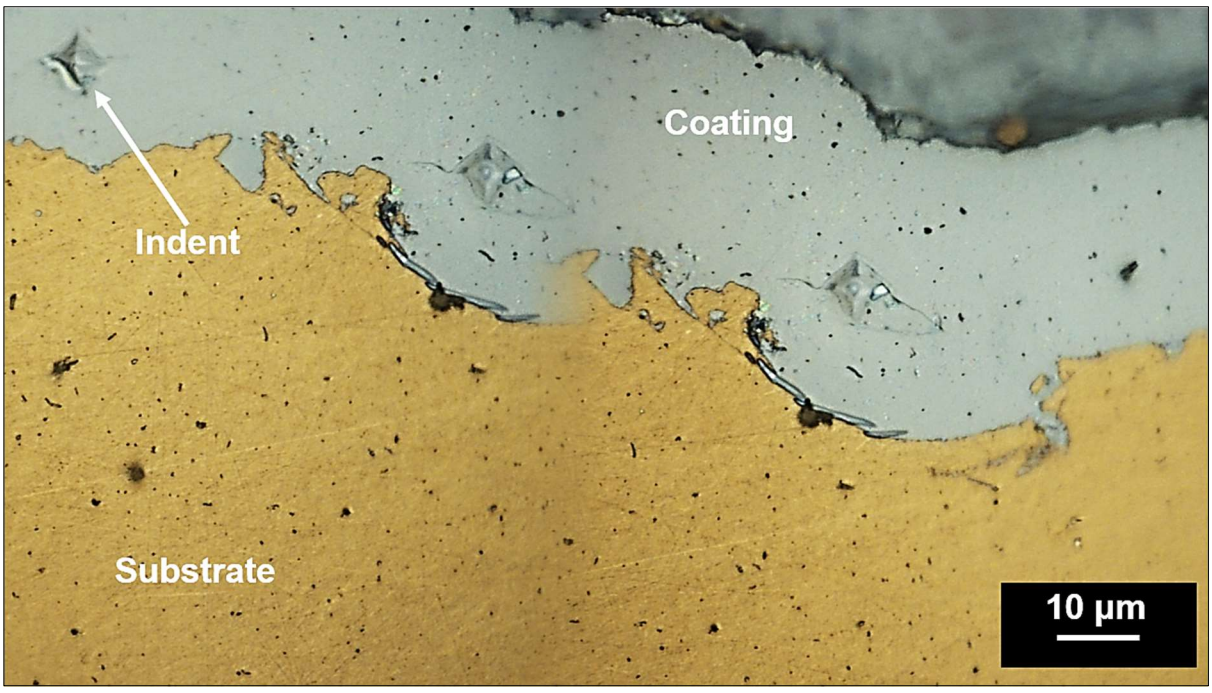

Figure 4-11: Optical image of the cross section of G-Al_2O_3 coating showing Vickers micro indents

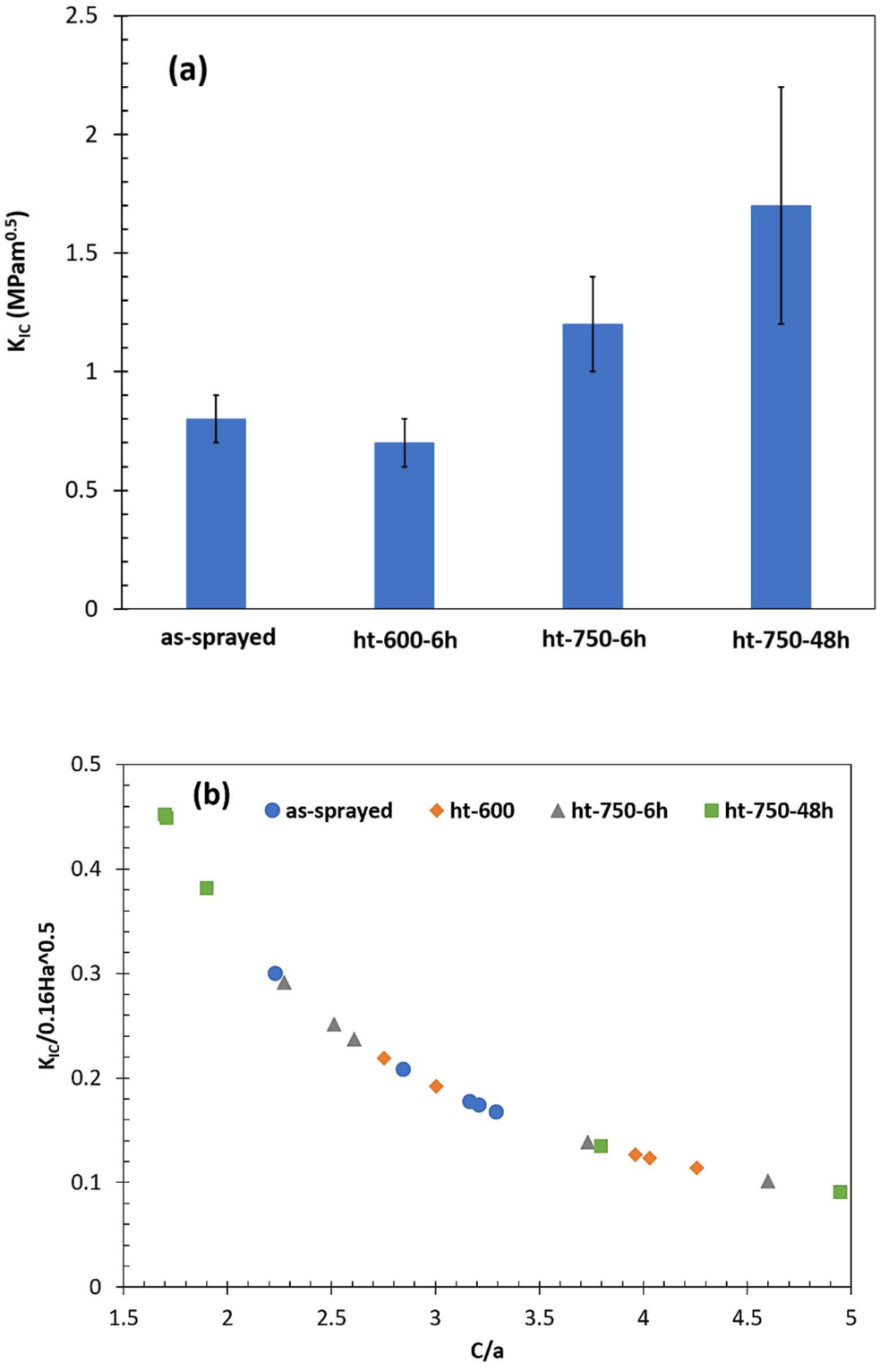

Figure 4-12: (a) Fracture toughness of as–sprayed and heat treated Al_2O_3 coatings at various time and temperature (b) Crack extension plot for the measured fracture toughness of as–sprayed and heat treated Al_2O_3 coatings—see Table 19 in Appendix E for the 95 % confidence level of the mean of the data set.

The fracture toughness (K_{IC}) of the as–sprayed and heat–treated coatings is shown in Figure 4–12 (a). The as–sprayed and ht–600–6h coating have the lowest K_{IC} with values of ~ 0.8 ± 0.1 $MPam^{0.5}$ and 0.7 ± 0.1 respectively while the ht–750–6h and ht–750–48h coatings have values of ~ 1.2 ± 0.2 $MPam^{0.5}$ and 1.7 ± 0.5 $MPam^{0.5}$ respectively. The normalised crack extension plot in Figure 4–12 (b) shows c/a values which indicate the compliance of the obtained values calculated with the Evans and Charles model [188]. It shows the tendency of c/a to increase as $K_{IC}/0.16Ha^{0.5}$ decreases. The corresponding c/a value to an estimated K_{IC} should be ≥ 2.5 to fit the model. The compliance of the values obtained for the ht–750–48h coating are reduced if its c/a range is considered.

4.5 Wear performance of the Al_2O_3 coatings

The wear performance of the individual Al_2O_3 coatings, the as-sprayed and the heat-treated, was tested in a dry sliding mode of like–on–like using α–Al_2O_3 ball as the counter body on flat samples. The specific wear rates of the coatings and the counter bodies were obtained based on the descriptions provided in Section 3.7. The sliding wear test results showed good repeatability, considering the data in SWR–1 (test 1) and SWR–2 (test 2). The four coatings exhibit specific wear rates below 10^{-6} mm^3 $(Nm)^{-1}$ as shown in Figure 4–13—)—further statistical analysis of the data is presented in Appendix E. The as–sprayed and the ht–600–6h coating showed a similar order of specific wear rate after a sliding distance of 36 m. This performance is about one order of magnitude lower than what was measured in the ht–750–6h coating that was only tested for a sliding distance of ~ 4 m. The ht–750–6h and the ht–750–48h coatings differ by up to one order of magnitude, although the latter only lasted for a sliding distance of ~ 1 m after which it showed severe wear behaviour. The counter

body only experienced measurable wear against the as–sprayed and the ht–600–6h coatings. The specific wear rates on the α–Al_2O_3 balls was a little more than one order of magnitude higher than the specific wear rates seen on the coatings—Figure 4-14. The counter–body on the HT–750–6h and the HT–750–48h coatings did not show any measurable wear.

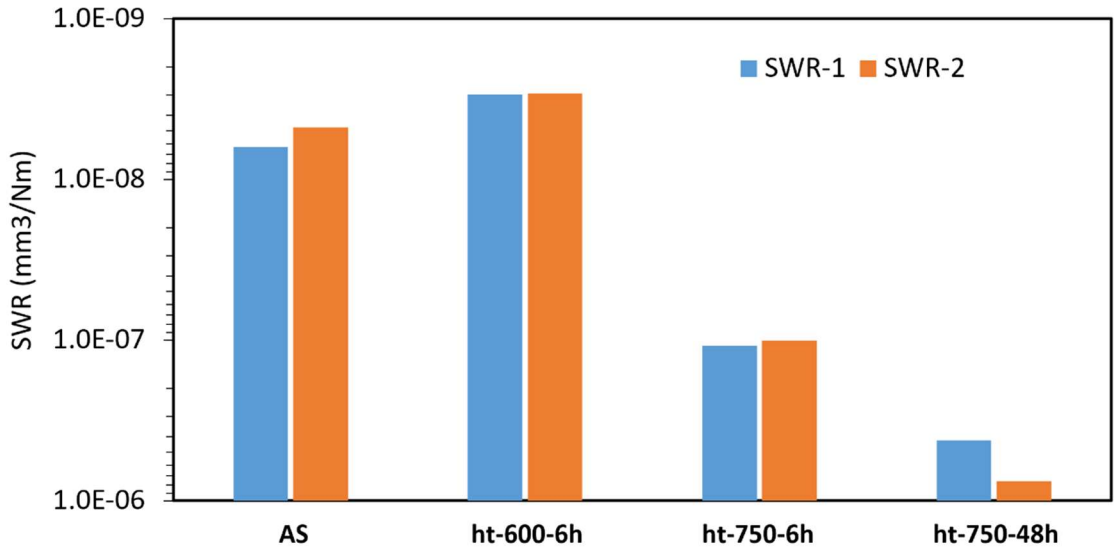

Figure 4-13: Specific wear rate in unlubricated sliding wear tests of as–sprayed and heat treated Al_2O_3 coatings tested against α–Al_2O_3 ball (9.5 mm diameter, 16.8 N normal load)—see Table 20 in Appendix E for the 95 % confidence level of the mean of the data set.

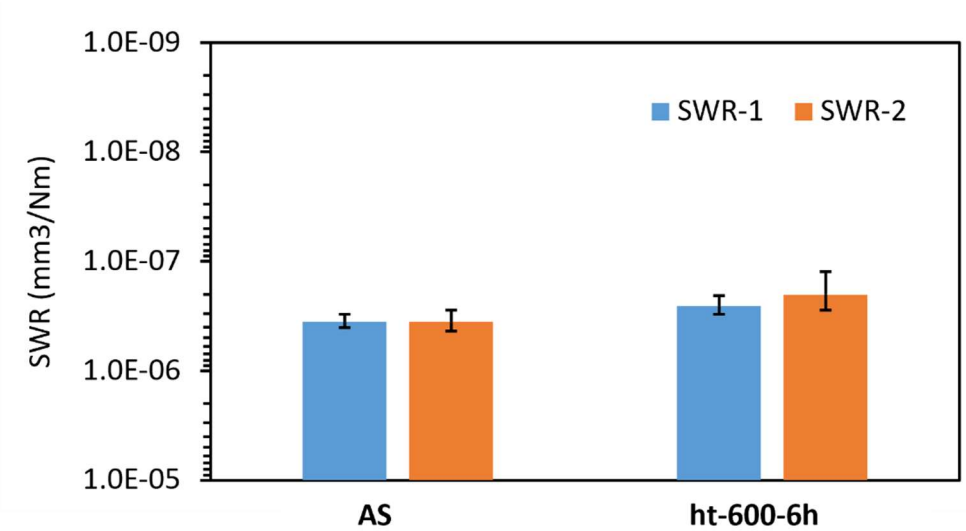

Figure 4-14: Specific wear rate of counter body α–Al_2O_3 balls for as–sprayed and coating heat treated at 600 °C for 6h (HT–600–6h)—no measurable wear for the HT–750–6h and the HT–750–48h coatings, so not presented here.

4.5.1 Top surface micrographs of wear samples

The SE top surface micrographs of the wear tracks on the four coatings were obtained to provide insight into the possible wear mechanism exhibited by the respective coatings. The images of the worn contact areas of the counter bodies were obtained by optical microscopy. In either of the cases of the coatings and the counter bodies, the samples of the as-sprayed coating are compared to the heat-treated samples. Figure 4–15 shows the combined SE micrographs of the tested four coatings. The as–sprayed and the HT–600–6h coatings appear to have experienced less material loss; the image of the wear for the two coatings only show fine–grooved tracks marked by the arrows. The ht–600–6h coating showed additional features of tribofilm features as in Figure 4–15(b); this feature is similar to a type II tribofilm described by Yang et al. [213]. The type II tribofilm would consist of fine grains of similar size as may be compared to the ones identified on the wear track of the ht–600–6h coating. In contrast, the wear tracks of the ht–750–6h and the ht–750–48h coatings presented in Figure 4–15 (c) and (d) respectively are covered by wear debris. The debris are piled delaminated materials of the coatings which has been crunched in between the reciprocating contact between the coating top surface and the counter body. The wear regime of the four coatings is distinct; the as-sprayed coating and the ht–-600–6h show mild wear as against the severe wear of the ht–750–6h and the ht–750–48h coatings. This will be further checked by examining the images of the counter bodies worn against each of the coatings as shown in Figure 4–16.

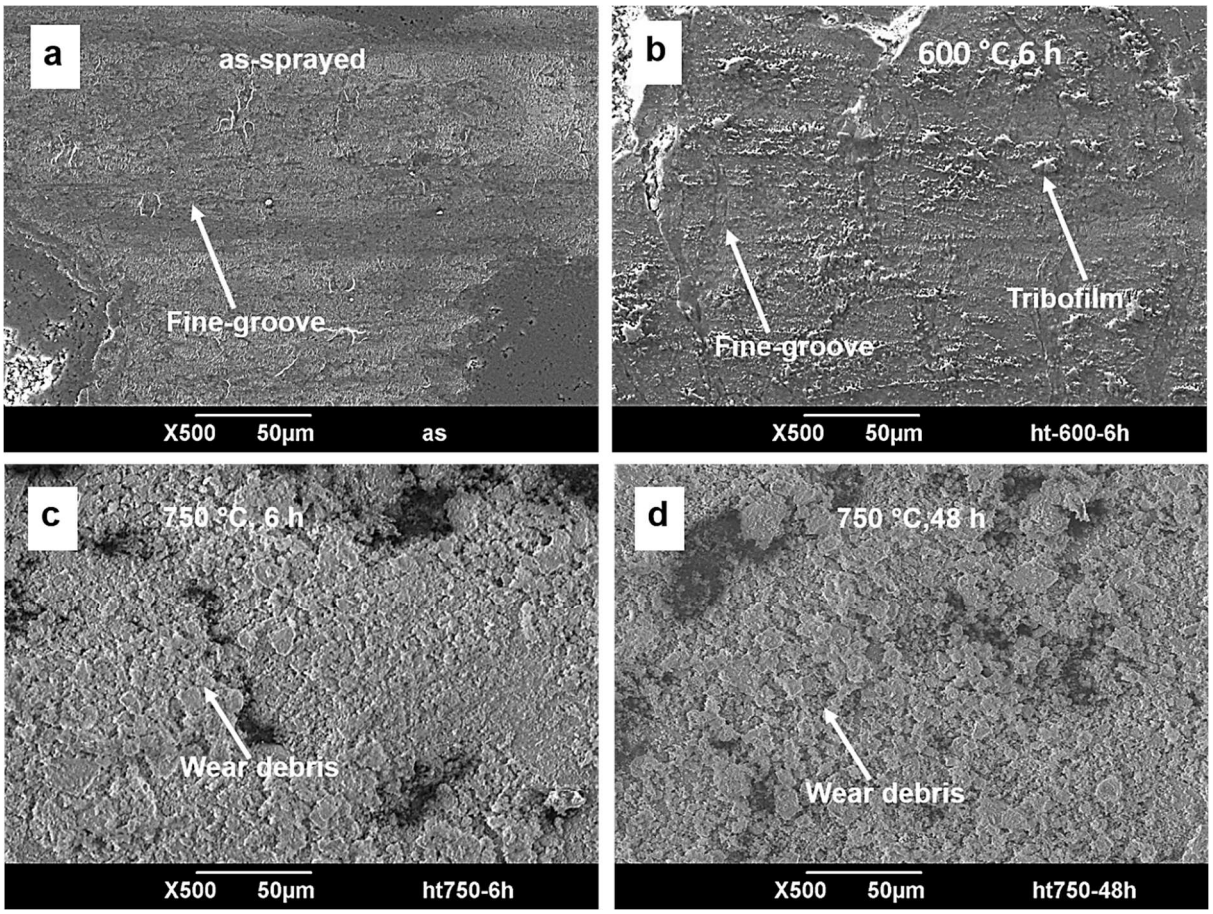

Figure 4-15: SE micrographs of the wear track of the sliding wear tests of (a) the as–sprayed coating (b) the HT–600–6h coating—test was for a sliding distance of 36 m; arrows show incipient plastic shearing and tribofilm. (c) the HT–750–6h coating, test was for a sliding distance of ~ 4 m and (d) the HT–750–48h test was for a sliding distance of only ~ 1, arrows show wear debris.

A further understanding of the wear mechanism is supported through the examination of the counter bodies worn against each of the four coatings. Mild wear will leave or no track on the counter body while a severe wear would show material transfer to the counter body or scar showing material loss to the tested sample [214]. The optical image of the individual counter bodies worn against the as-sprayed coating and the ht–600–6h coating show wear scars; no proof material transfer is evident as shown in

Figure 4–16 (a) and (b) respectively. This suggests mild material loss in the test samples and on the counter body. Differently, the counter bodies worn against the ht–750–6h and the ht–750–48h coatings have no presence of scar instead, the contact area on the balls show materials transferred onto it from the test samples as in Figure 4–16 (c) and (d). This supports the proofs of severe wear regime seen on the SE micrographs of the test samples.

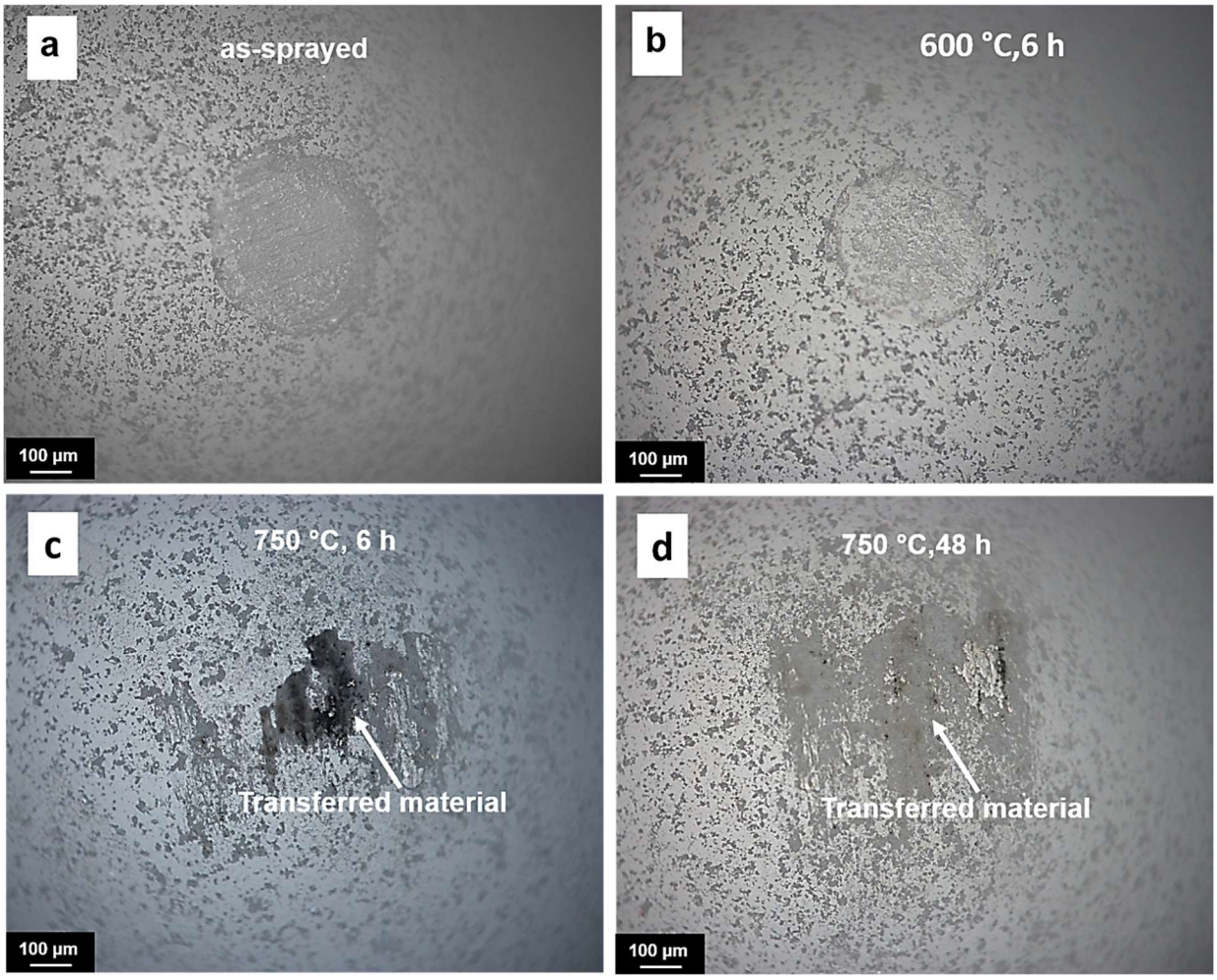

Figure 4-16: Optical images of α–Al_2O_3 ball counter bodies used in sliding wear tests of the (a) as–sprayed coating (b) HT–600–6h coating (c) HT–750–6h coating (d) HT–750–48h—the arrows show material transferred from the worn coatings.

4.6 Discussion

The discussion section is separated into two parts—the first part explains the coating microstructure and phase evolution while the second part explains the wear performance of the coatings.

4.6.1 Microstructure and evolution of phases

Whether or not a thermal spray coating is deposited as a dense or porous coating is connected to the morphology of the individual splats that forms the microstructure of the coating. Disk-like splats or splats with aspect ratio of ~ 1.0 would yield coatings of dense microstructure with improved adhesion strength [215]. The morphology of the splats which forms the microstructure of a thermal spray coating depends on the spread and solidification of the splats. The spread and solidification of the individual splat is preconditioned on the temperature and velocity of the particle/agglomerate from which it will be formed—this is in addition to the deposition surface condition of temperature and/or roughness [209, 211]. Increased deposition surface temperature creates disc-like splats, increased splat cooling rate and high substrate/coating bonding or inter-splat bonding. While most of the published work on Al_2O_3 splat studies have been based on APS process; the coatings presented in this thesis were produced using a modified HVOF gun which produces coatings at hypersonic speed [205].

The homogenous microstructure of the as–sprayed Al_2O_3 coating presented here was built from splats of varying sizes and morphologies which formed from molten agglomerates of particles of different sizes. The deposition process precludes pre-heating of the substrates, a condition that should promote the formation of disk-like splats in the formation of the coating microstructure. This must be the reason why most

of the splats collected in the buildup of the as-sprayed coating where either elliptical or of irregular morphology. Despite the dominance of the non-disk-like splats in the coating build up, its porosity still fits the 5–7 % range reported of typical Al_2O_3 coatings developed from nano and micro sized feedstock [9]. This porosity level of the as-sprayed coating though less than the 8–10 % range for conventional APS Al_2O_3 coating, it exceeds that of the conventional HVOF by only 2 % [73]. The origin of the discrepancy in the porosity level of the as-sprayed coating must be due to the many irregular splats in the makeup pf the coating.

Post spray heat treatment of the coating caused the porosity of the coatings to drop by ~2% across the four samples. This must be due to the sintering observed in the heat-treated samples. Sintering is known to produce a bridging effect in addition to coalescence between adjacent splats that can initiate localized crack resistance [216]. The localized crack resistance phenomenon could be the reason for the increased fracture toughness observed for the heat–treated Al_2O_3 coatings. However, the fracture toughness results are inconclusive and will require further investigation. Where the post spray heat treatment caused the formation of refined crystallite size in addition to reduced porosity, it can contribute to improved microhardness of the heat-treated coatings. The increased microhardness due to refined crystallite size can be explained by the Hall–Petch effect, which describes how the microhardness of non–work hardened bulk material can increase with a reduction in grain size [217, 218]. The microhardness values of the coatings were nonetheless below those reported by Murray et al. [85] for Al_2O_3 coatings sprayed with the same UTP TopGun. However, in that case a α–Al_2O_3 feedstock was used and so a direct comparison cannot be made.

Coating microstructures built from rapidly quenched molten agglomerates of Al_2O_3 particles typically consist of amorphous and/or cubic γ–Al_2O_3 [21, 62, 85, 88, 214]. This is because γ–Al_2O_3 is the most energetically favourable crystalline phase during solidification of Al_2O_3 melt [89]. γ–Al_2O_3 is energetically favourable as the formation of Al_2O_3 phases is governed by the Ostwald rule of successive formation [74, 219], which states that the least stable reaction product precipitates first [220]. γ–Al_2O_3 precipitates before other phases of Al_2O_3 from the melt as the least stable phase of Al_2O_3 based on the Ostwald rule. Its formation from the melt is a positive entropy change reaction [221] and it is the closest phase to the highly disordered molten Al_2O_3. Amorphous Al_2O_3 can also be formed during solidification of Al_2O_3 melt instead of the γ–Al_2O_3 when long range order is lost [222].

The favourable formation of γ–Al_2O_3 can be understood by considering the coordination of the Al_2O_3 phases. Rhombohedral α–Al_2O_3 has only octahedral coordination whereas cubic γ–Al_2O_3 has both octahedral and tetrahedral coordination [223]. This has been attributed to its higher entropy state compared to the α–Al_2O_3 phase [221]. The phase formation in Al_2O_3 can be further understood by considering both the thermodynamics of the formation and the mechanism of the formation [224]. At temperature just above the melting point, ions have lower coordination number and for Al_2O_3 melt, the prevalence of oxygen with four times the coordination number of aluminium is most likely [225]. However, alpha Al_2O_3 requires two–third of its octahedral sites to be filled by Al^{3+} [223] but this often is not the case because of the rapid quenching in thermal spray. As such, the structures with tetrahedral coordination form more readily than structures with only octahedral coordination. This explains the

amorphous hump and γ–Al_2O_3 [21, 42, 57] observed in the X–ray diffraction pattern of the as–sprayed coatings.

Further effect of post spray heat treatment of the as–sprayed coatings was phase transformation [226]. Phase transformation from γ–Al_2O_3 to δ–Al_2O_3 was observed for the coatings after the heat treatment. δ–Al_2O_3 is a superstructure of γ–Al_2O_3 with tripled c–axis due to ordering of cationic vacancies on the octahedral site as governed by a screw tetrad parallel to the c–direction [227]. The observed phase transformation (γ–Al_2O_3 to δ–Al_2O_3) can be attributed to stacking of the cubic crystals that resulted into the tetragonal structure as shown in Figure 4–17.

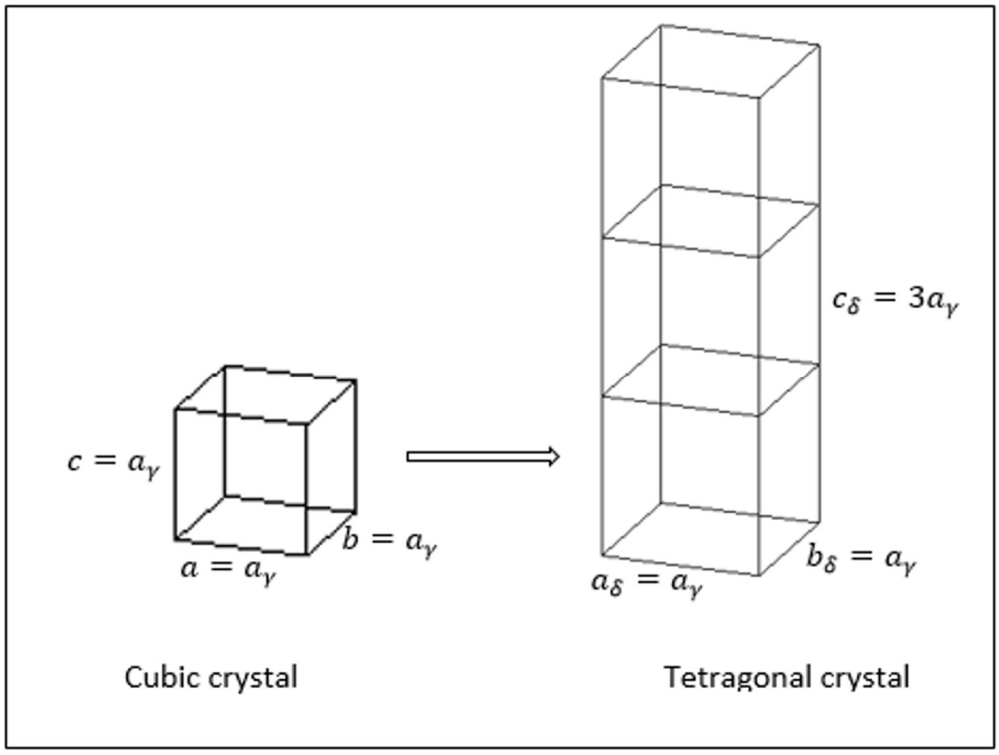

Figure 4-17: a schematic diagram of transformation between cubic and tetragonal crystal lattices

The x–ray diffraction pattern of the heat–treated coatings showed peak broadening (see subsection 4.6.2). Peak broadening in x–ray diffraction is a measure of crystal imperfections and it can occur due to one or all of the following: dislocation density, stacking faults, twinning, micro–stress, grain boundaries, and chemical heterogeneities and reduced crystallite size [228, 229]. Due to the post–spray heat treatment of the coatings, the broadened peaks can be reliably attributed to crystallite size reduction, though there is a possible contribution from stacking faults, due to the process of piling of the cubic crystals of the γ–Al_2O_3 to form the tetragonal crystals of the δ–Al_2O_3 (see Figure 4–17). The transformations described so far are consistent with reported phase transitions in bulk Al_2O_3 [76] and post–spray heat treated Al_2O_3 coatings [21].

Sintering has been mentioned as one the accompanying effects of post spray heat treatment. The mechanisms promoting sintering during heat treatment include, but are not limited to, lattice diffusion via interstitials and lattice diffusion via vacancies. In this work, the latter is most applicable as the observed phase transformation appeared to be through vacancy ordering. δ–Al_2O_3, as a superstructure of γ–Al_2O_3, was formed from the ordering of the vacant octahedral sites on the γ–Al_2O_3 cubic crystal through stacking [227]. The grain growth stage of the sintering process could have facilitated the fusion of adjacent cubic crystals of γ–Al_2O_3 that then grew in size to attain the tetragonal crystal structure of the δ–Al_2O_3 [230]. As the grain growth then progresses, the interfacial energy balance is broken to allow pore elimination and coalescence [231]. Twinning may have resulted from this process which then contributed to the observed peak broadening.

4.6.2 Tribology and wear behaviour

The wear of ceramic materials like other materials is either in the mild or severe wear regime. Polycrystalline Al_2O_3 subjected to dry sliding wear under ambient conditions at low normal loads between 10 and 20 N implemented at low speeds of 10–20 mm/s shows mild wear. The mild wear regime in ceramics presents with low wear rate, smooth surface and wear mechanisms dominated by plastic flow and tribochemical reactions. In contrast, severe wear shows high wear rate, rougher wear track and wear mechanism dominated by brittle fracture. The mild wear regime can be sustained even at higher speeds if the load is kept the same; an increase in the applied normal load at the same sliding speed will cause a change from mild to severe wear [82]. The wear test conditions implemented on the four wear Al_2O_3 samples suggests the coatings wear response should be within the mild wear regime. Two of the coatings, the as–sprayed and the ht–600–6h coatings, show specific wear rate in the mild wear regime—the recorded specific wear rate from the dry sliding wear tests was of the order of ~ 10^{-8} $mm^3(Nm)^{-1}$ for each of the two coatings. Both coatings show adhesive wear that involves loss of material from the softer of the two contacting bodies; the proof of this lies in the creation of scar on the counter bodies worn against each of the coatings which in turn showed fine–grooved tracks. The grooves must have formed from the materials loss from the counter body which get welded onto the coating surfaces and the continuous movement between the surfaces caused ‘ploughing’ into the attached materials to create the grooves. The additional mild wear proof on the wear track of the ht–600–6h coating was the presence of tribofilm.

Notable wear mechanism for ceramics is brittle fracture; the fracture occurs when the applied mechanical stress exceeds the fracture strength at the asperity contacts to cause localized fracture and grain pull out, the grain boundary energy release rate, and the residual stress at the point of contact. There was no obvious case of grain pull–out artefact on the wear track of the as-sprayed coating and the ht–600–6h coating giving that the sample surface was polished down to 1 μm surface finish before the wear test; it may also be that the contact stresses were below the fracture strength at the grain boundaries to initiate cracking and pull out. The presented analysis suggested the as-sprayed coating and the ht–600–6h coating share similar wear mechanism as supported by the size of the scar left on the counter–body by both coatings, similar microstructures, microhardness, and indentation fracture toughness.

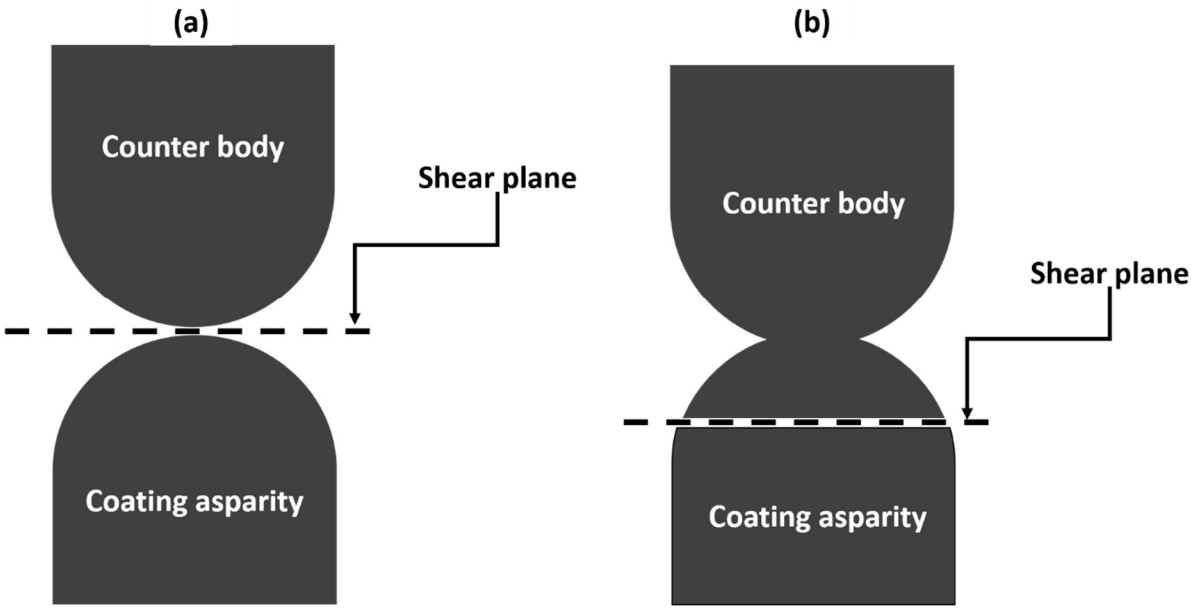

Figure 4-18: Schematic for adhesive wear mechanism—(a) before shear (b) after shear

On a different note, despite the higher microhardness and indentation fracture toughness of the coatings heat treated at 750 °C (see sub-section 4.4), the integrity of the coatings appears to have been compromised. The surface of the coatings developed surface fragmentation; the fragmentation was the response of the coatings to the thermal stress induced in the coating/substrate combination giving that the coefficient of thermal expansion of the substrate about twice that of the coatings' material. The specific wear rate range and the micrographs of the two coatings provides proofs of severe wear. Severe wear is facilitated by intergranular cracking [232] and in the case of the coatings at hand, there is additional defect of surface fragmentation due to the post spray heat treatment and as a result the coating suffered severe wear. A possible progression of the severe wear recorded in the ht–750–6h and the ht–750–48h coatings involves rapid stages of wear governed by three different mechanisms of adhesion, abrasive wear and delamination [83]. The adhesive wear mechanism of the first stage was due to a stronger interfacial strength at the contact point between the counter body the coating surface than the cohesive strength binding the grains of the coatings—see the schematic in Figure 4–18. In this case the shear plane moves downwards into the weaker material to cause part of it to be transferred onto the other body, was the case for each of the ht–750–6h and the ht–750–48h coatings. The wear debris trapped in between the sliding bodies thereby cause a 3–body abrasive wear resulting in further material removal [233]. This explains the poor wear performance observed in the ht–750–6h and the ht–750–48h coatings—interestingly, it suggests the possibility of an optimum heat treatment temperature of 600 °C in Al_2O_3 on stainless steel applications.

4.7 Summary

A delta–theta Al_2O_3 suspension was deposited onto an AISI 304 stainless–steel substrate using SHVOF thermal spraying. The as–sprayed and post–sprayed heat–treated coatings were studied for microstructure and phase evolution using SEM, TEM and XRD. The wear performance of the coatings was also investigated, and the following conclusions can be drawn:

- The microstructure of the as–sprayed coating from a delta–theta Al_2O_3 suspension is consistent showing fully molten splats with the characteristics of amorphous and γ–Al_2O_3.
- A γ–Al_2O_3 (cubic) phase in the coating partially transformed to become δ–Al_2O_3 (tetragonal) at a heat treatment temperature of 750 °C. The transformation likely occurred through vacancy ordering and crystallite size refinement. This resulted in peak broadening within the XRD profiles of the heat–treated coatings.
- The microhardness and the fracture toughness of the as–sprayed coating and the coating heat treated at 600 °C were similar. The microhardness and the fracture toughness of the coatings heat treated at 750 °C increased by an approximate factor of two. This was attributed to grain refinement, pore consolidation and phase transformation from amorphous and cubic γ–Al_2O_3 to tetragonal delta Al_2O_3.
- The wear rate of the as–sprayed coating was 5.53 x 10^{-9} mm^3 $(Nm)^{-1}$ and 2.94 x 10^{-9} $mm^3(Nm)^{-1}$ for the coating heat treated at 600 °C, which seems to be an optimum heat treatment temperature for Al_2O_3 on stainless–steel substrates. In both cases, the integrity of the coating was retained as no surface defects

developed due to heat treatment. This enabled the wear of the coating to not progress beyond the mild regime. The coatings heat treated at 750 °C for both 6 h and 48 h both failed abruptly by severe wear due to pre–cracked surfaces.

Residual stress and microstructure of suspension thermal sprayed ceramic coatings: Al_2O_3 and YSZ

5.0 Introduction

This chapter presents the results of residual stresses measured with hole–drilling technique and non–destructive techniques (NDT): X–ray and time–of–flight (TOF) neutron diffraction. Two SHVOF thermal sprayed ceramics coatings, Al_2O_3 and YSZ, are presented. Despite Al_2O_3 and YSZ being widely used and studied engineering ceramics, limited work has been reported on the through–thickness residual stress behaviour of SHVOF thermal sprayed Al_2O_3 and none on YSZ coatings. A detailed understanding of residual stress of these coatings will provide further insight into the performance evaluation of the coatings vis–à–vis the role of residual stress. The microstructure of the coatings was studied in detail in SEM and XRD to rationalize the residual stress behaviour in terms of microstructure. The work presented in this chapter was done to provide a means by which thermally sprayed coatings on large aerospace industry parts can be investigated for residual stress. That was why the established industry-based hole drilling technique was investigated alongside the neutron-based NDT that can be used to study large parts without comprising structural integrity of the parts. The intended measurements involves penetration capabilities of the techniques; hole drilling technique is not limited by depth of penetration; X-ray technique penetration depth is less than 10 μm while neutron can penetrate thick metals but will be absorbed by water and concrete (see Figure 5-1). The Al_2O_3 coating used for this residual stress study was the Al_2O_3 coating deposited from the CR1 Al_2O_3 grade described as C–Al_2O_3 in Section 3.3; it will be called “Al_2O_3 coating” in this chapter. Similarly, the YSZ coating used for this residual stress study was the YSZ

coating deposited at 110 kW described as T1–YSZ in Section 3.3; it is here–in after referred to as “YSZ coating”.

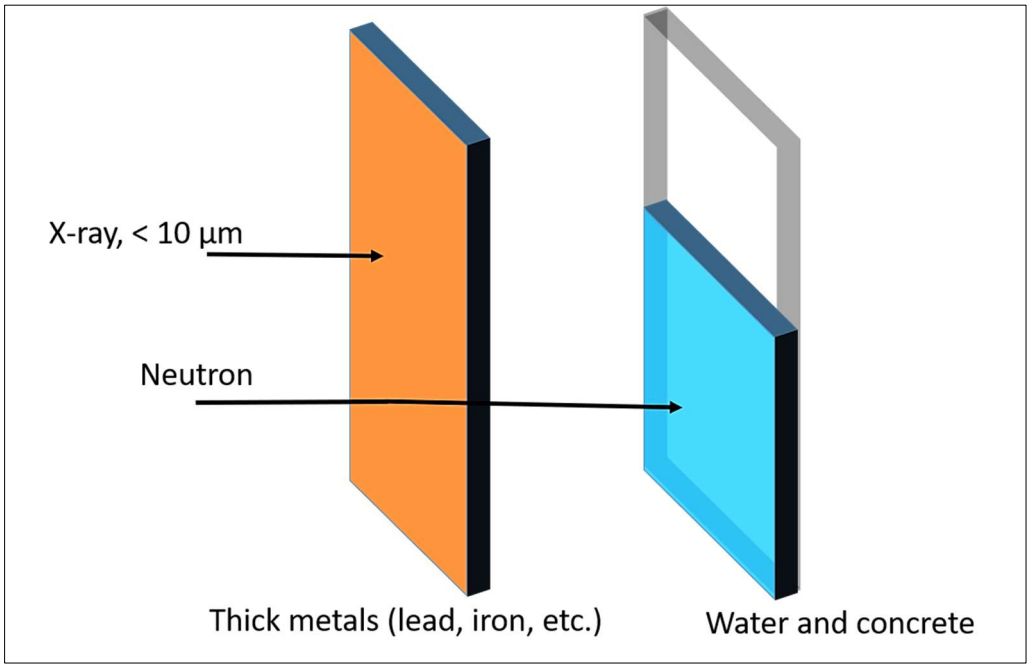

Figure 5-1: Schematic penetration depth for X-ray and neutron radiations

5.1 Microstructure: feedstock and coatings

5.1.1 Al_2O_3 powder and as–sprayed coating

Figure 5–1 presents the scanning electron micrographs of the as–received Al_2O_3 feedstock and the as–sprayed Al_2O_3 coating. The Al_2O_3 feedstock shown in Figure 5–2 (a) presents particles of angular morphology with a size range of ~ 100–200 nm. The image of the particles as seen in Figure 5–2(a) shows that the particles in the suspension were smaller than the mean size (D_{50}) of 1 µm provided by the supplier. The mean size of the particles provided by the supplier represents the size for agglomerates of the particles. The BSE cross sectional view of the as–sprayed Al_2O_3 coating presented in Figure 5–2 (b) shows the coating thickness is ~ 200 ± 2 µm with horizontal cracks and voids at the inter–spray layers. The coating–substrate interface

shows good bonding without any defect or delamination. The surface roughness of the substrate, from the grit blasting offers interlocking sites for the impinging splats. The porosity of the Al_2O_3 coating obtained from its cross–sectional views by image analysis technique was 5.6 ± 1.0 %.

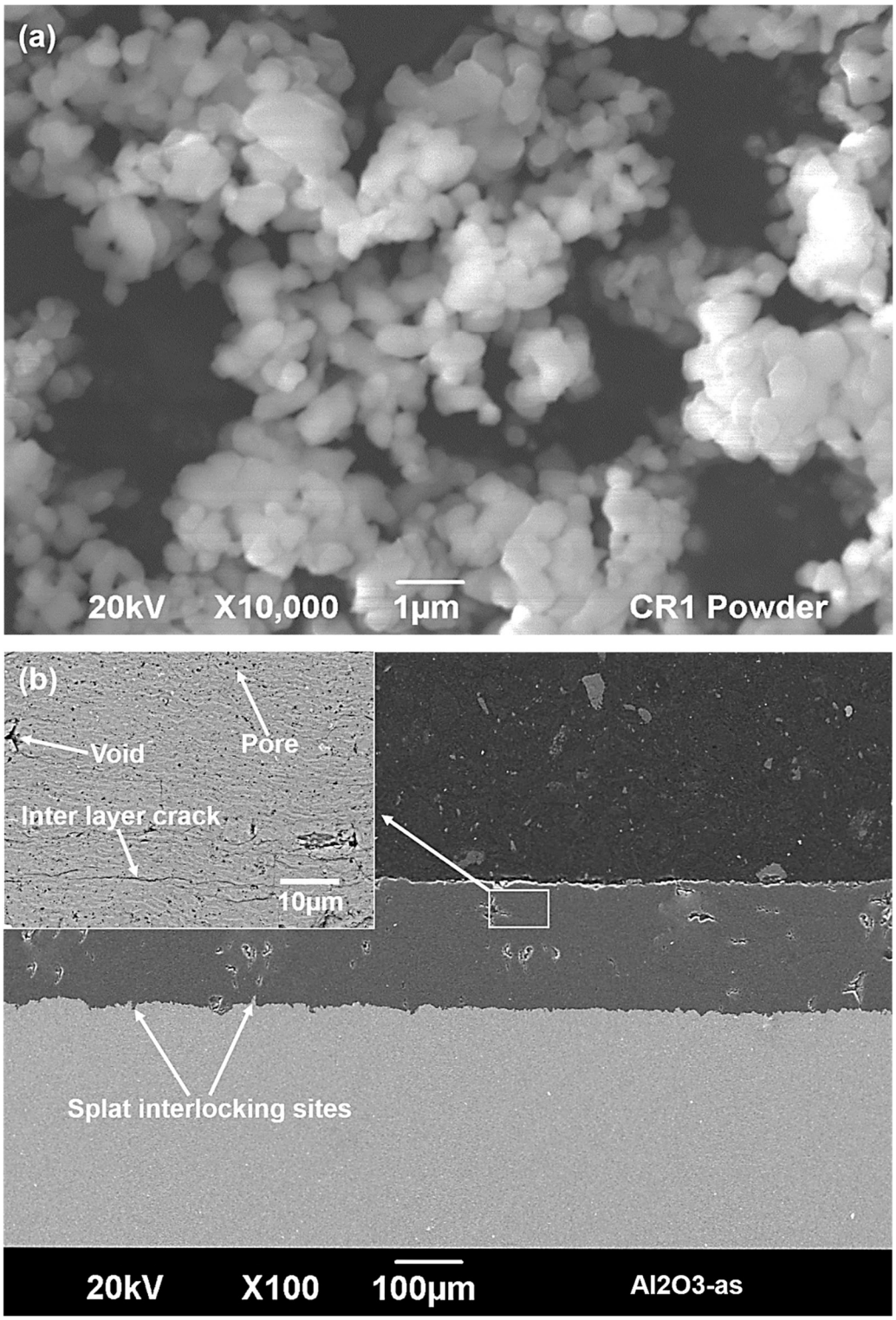

Figure 5-2: Al_2O_3 (a) Secondary electron high magnification SEM micrograph of the as–received powder D_{50} = 1 μm (b) Back scattered electron low magnification SEM micrograph of the as–sprayed coating with inset showing pores, voids and inter layer crack

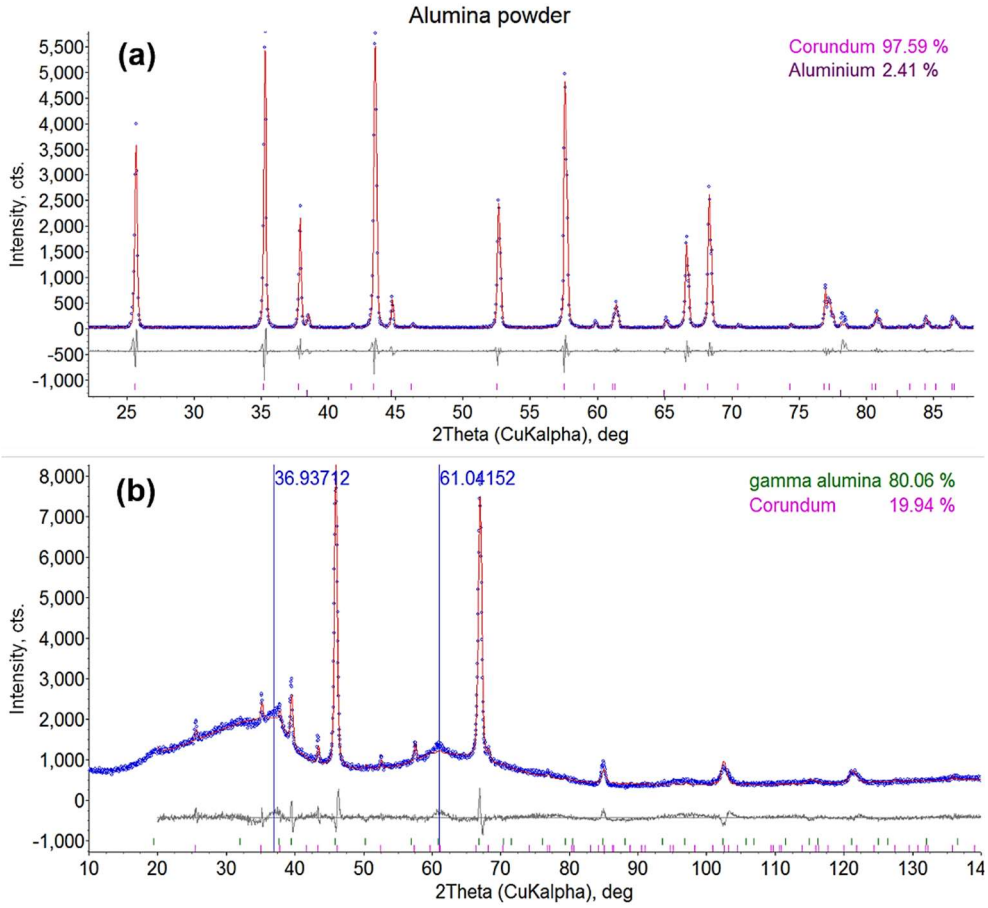

Figure 5-3: (a) Rietveld refinement of the as–received powder showing whole α–Al_2O_3 (b) Rietveld refinement of the as–sprayed coating showing gamma–Al_2O_3 and corundum quantification—Ritveld analysis was done by Dr Mingwen Bai

The phase analysis and the phase quantifications of the powder and the coating are shown in Figure 5–3. The Rietveld refinement analysis of the raw data of the XRD scan of the CR1 Al_2O_3 powder is shown in Figure 5–3 (a). The analysis confirms the as–received CR1 Al_2O_3 powder is entirely corundum (α-Al_2O_3)—it has no metastable Al_2O_3 phase. The phase quantification of the powder shows small amount of aluminium; the aluminium signal could not have been a contamination in the powder itself, given the nature of the Bayer's process through which Al_2O_3 is obtained. The aluminium signal came from the sample holder during the XRD scan experiment. The corundum crystallites in the analysed powder are coarse with calculated size being

141± 4 nm. The large crystallite size is consistent with the absence of broad peaks in the XRD profile of the powder. The phase analysis of the as–sprayed Al_2O_3 coating shown in Figure 5–3 (b) presents two amorphous humps at the ~ 40º and 60º 2θ positions and two crystalline phases of gamma–Al_2O_3 and corundum. The crystalline contents of the coating has ~ 19.94 % corundum with the balance being gamma–Al_2O_3 which has a crystallite size of 48 ± 2 nm.

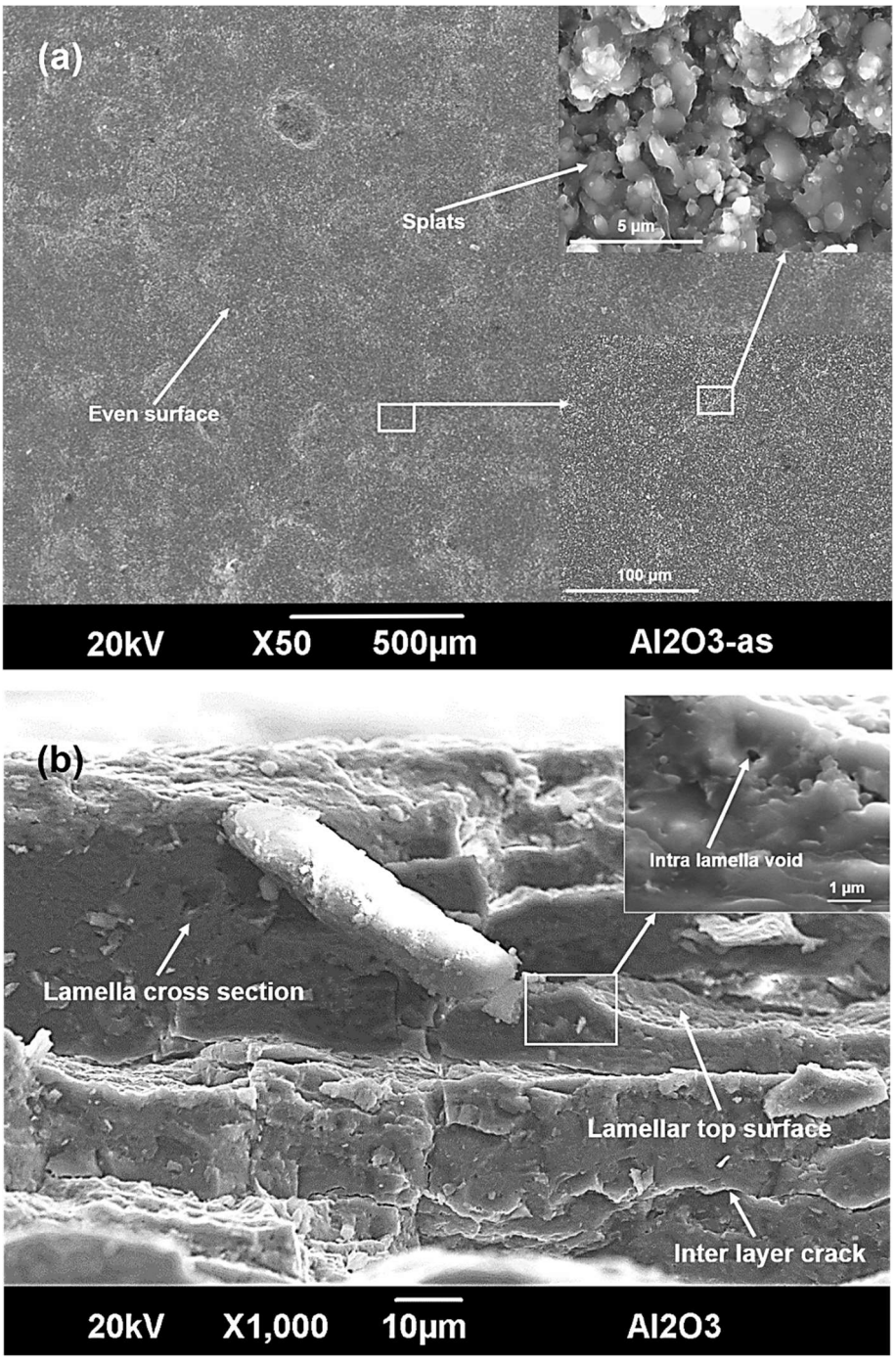

Figure 5-4: (a) Surface morphology showing as–sprayed Al_2O_3 coating with even surface covered by splats of varying sizes and geometry (b) Fractograph showing lamella cross section, lamella top surface, intra lamella void and inter layer crack in the as–sprayed Al_2O_3 coating

The surface morphology and the fractured surface of the Al_2O_3 coating present different architecture as shown in Figure 5–4 (a) and (b). The surface of the coating shown in Figure 5–4 (a) is flat, covered by splats of varying geometry and size. Individual splat here is larger than the size of the individual particle in the feedstock; the splats are made up of one or more particle agglomerates. The fractured surface of the coating shown in Figure 5–4 (b) revealed different features of the coating lamellae. The morphologies of the lamellae are different than what has been described of SHVOF thermal sprayed Al_2O_3 coatings—the lamellae are larger and thicker [90].

5.1.2 YSZ powder and as–sprayed coating

The SE micrograph of the powder dried out of the as–received YSZ suspension feedstock is shown in Figure 5–5 (a). The powder comprises discrete particles of angular morphology; the image of the particles shows no evidence of agglomeration. The size of the individual particles revealed in the image supports the 0.6 μm D_{50} mean size provided by the supplier of the YSZ suspension. The BSE cross–sectional view of the as–sprayed YSZ coating presented in Figure 5–5 (b) shows the coating thickness is ~ 120 ± 1 μm. The vertical cracks captured on the magnified section of the image has a measured length of 56 ± 4 μm. The coating– substrate interface shows good bonding; qualitative visual inspection of the image does not reveal any defect at the interface between the coating and the substrate. There are however visible dark features along the interface; these are substrate preparation artefacts. The porosity of the YSZ coating obtained from its cross–sectional views analysed using image processing technique gives 14.5 ± 1.0 %.

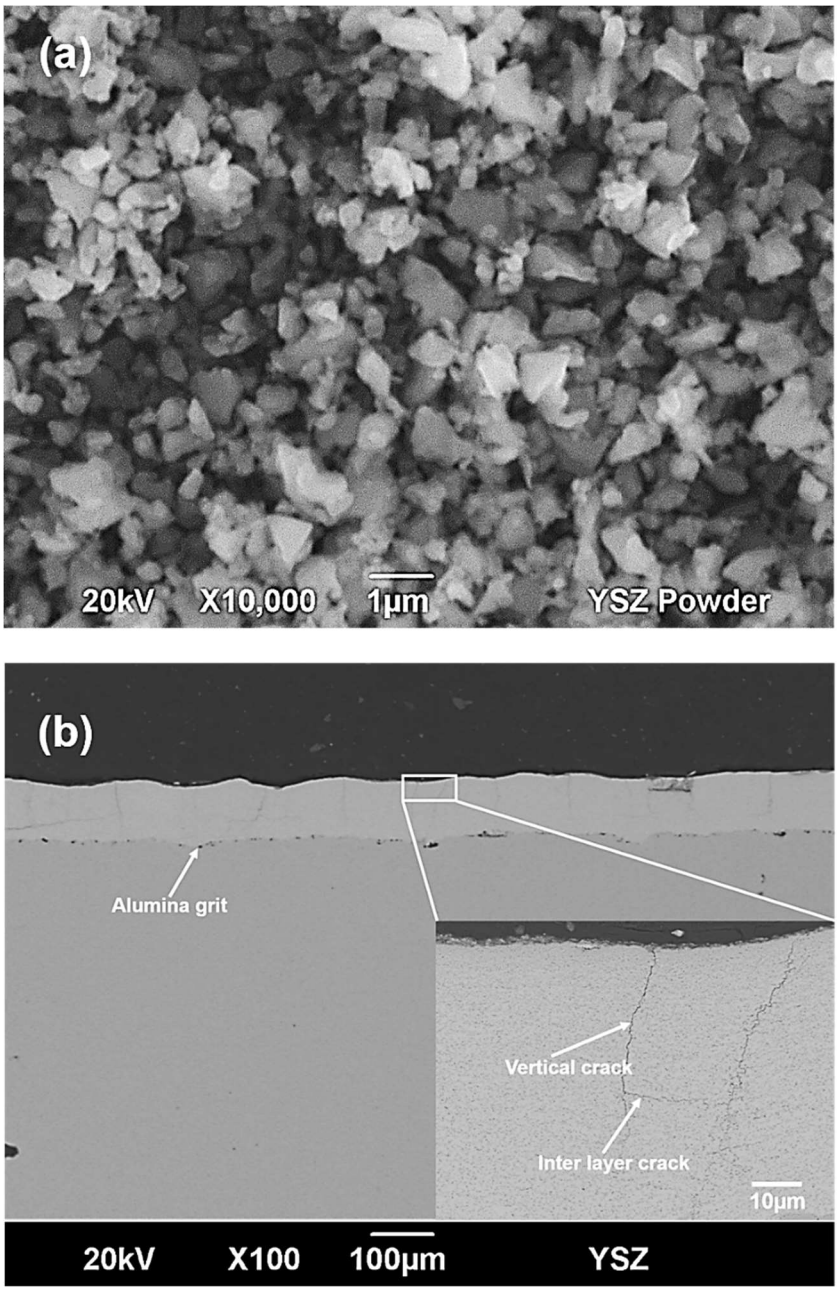

Figure 5-5: YSZ (a) Secondary electron high magnification SEM micrograph of the as–received powder D_{50} = 1 µm (b) Back scattered electron low magnification SEM micrograph of the as–sprayed coating showing vertical cracks

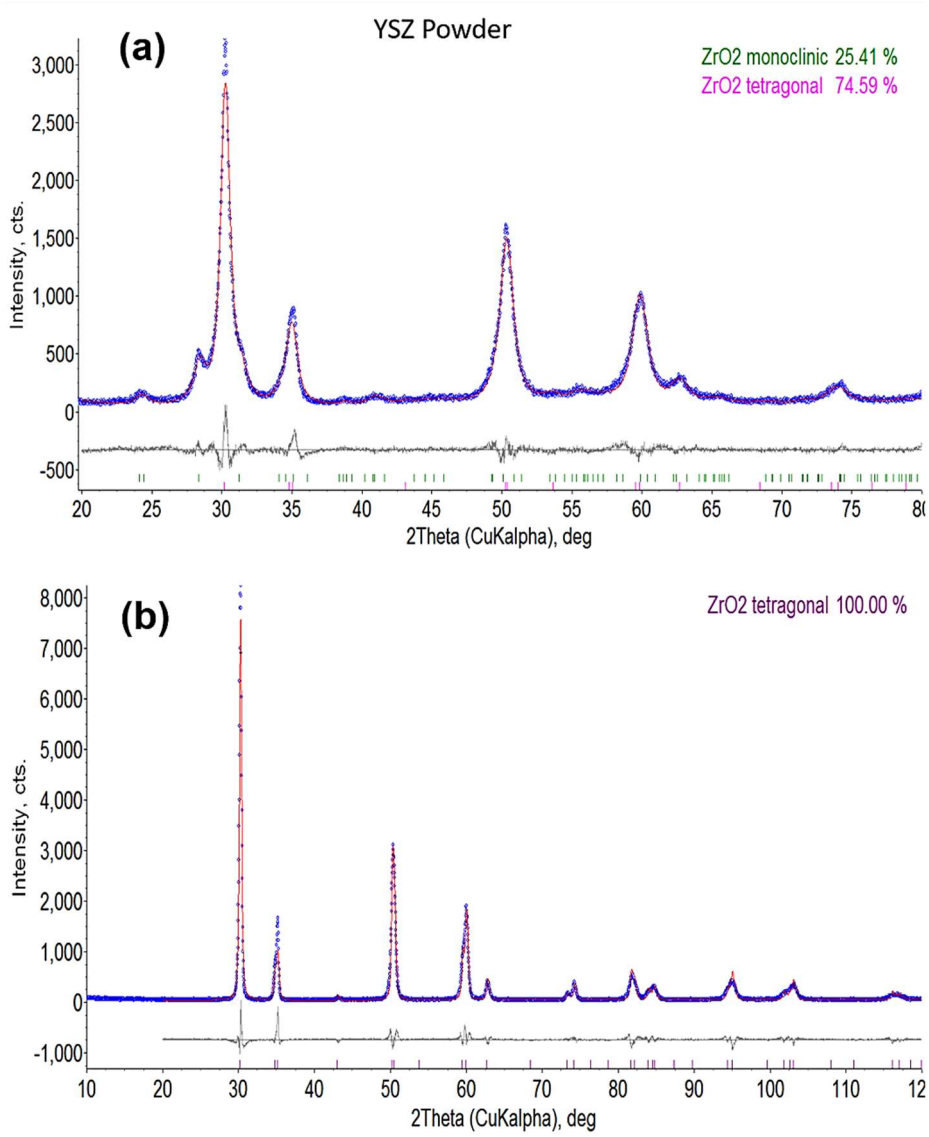

Figure 5-6: (a) Rietveld refinement of as–received powder showing monoclinic and tetragonal quantification (b) Rietveld refinement of as–sprayed coating showing full tetragonal transformation—Rietveld analysis was done by Dr Mingwen Bai

Figure 5–6 (a) shows the phase analysis of the powder dried out from the as–received suspension. The powder contains two phases of ZrO_2—the metastable tetragonal (~75 %) and the balance is monoclinic phase. The crystallite size of the individual phases in the powder are different; the tetragonal phase has a crystallite size of 14 ± 0.3 nm while the monoclinic phase has 28 ± 5 nm. The crystallite sizes of each of the phases are small which may be a reason for the observed broad peaks in the analysed

profile amongst other reasons for which broad peaks could occur in an XRD profile. The Rietveld refinement analysis of the as–sprayed YSZ coating gave a good fit. The dual phase feedstock has converted to a single–phase coating without any detectable amorphous content. The entire profile shows distinct peaks of tetragonal ZrO_2 (Figure 5–6 (b)). However, the tetragonal crystallites have become coarse; the sizes as determined from the Rietveld refinement analysis came to 71±1 nm. The increased crystallite size matches the reduction in peak broadening observed in the profile of the coating as analysed.

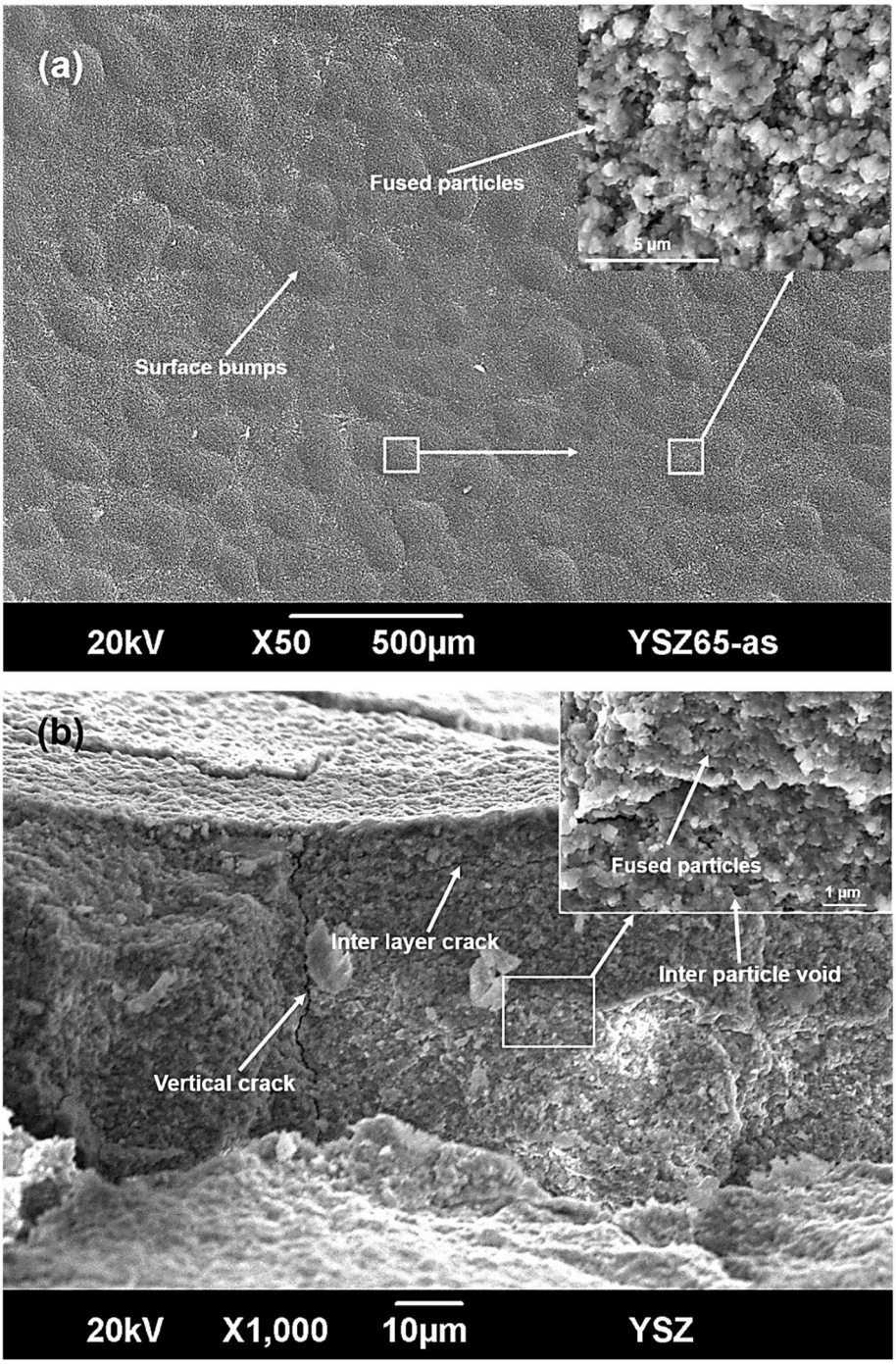

Figure 5-7: (a) Surface morphology showing as–sprayed YSZ coating with uneven distribution of bumps built of fused particles. (b) Fractograph showing fused particles, vertical crack and inter layer crack in the as–sprayed YSZ coating

The surface of the YSZ coating has bumps and these are unevenly distributed as shown in Figure 5–7 (a)—each one describes a planner view of “ant heap”. A magnified view reveals each bump as a lump of fused particles due to sintering. The

size of the individual particle in a lump is less than 1 μm. Individual particle in the lump has modified geometry from the angular shape presented in the as–received feedstock suggesting some degree of particle melting. The fusion of the particles produced lumps of varying geometry and sizes. The fractured surface of the YSZ coating shown in Figure 5–7 (b) shows the internal features of the coating. The coating build–up has fused particles rather than forming well molten splats. The size of the individual particle in the fused lump is less than 1 μm which agrees to the size ranges observed in the as–received feedstock. The morphology of the individual particle in the fused lump also shows reduced angularity when compared to those of the feedstock. The fusion of the particles was not however uniform; the lumps have voids.

5.2 Microhardness and nanoindentation

The micro and nanoindentation response of the coatings are presented together here to show the variation of the microhardness of the coatings across its thickness on the on the one hand and the nanohardness/elastic modulus on the other. The results will show that the microhardness and the nanoindentation values were obtained at varying depths within the coating—this is due to the peculiarity of the individual measurement procedure and features. A nano–indent will fit into the thickness of a lamellar as against a micro–indent that will overlap two or more lamellae. So, the locations of the micro indentation points were chosen to ensure the indents were well situated inside the coating. That was such that the top row precludes any edge effect close to the coating top surface and the bottom row near the coating–substrate interface, respectively.

5.2.1 As–sprayed Al_2O_3 coating

Figures 5–8 shows the results of the nanoindentation on the cross section of the as–sprayed Al_2O_3 coating. Figure 5–8 (a) gives the nanohardness of the Al_2O_3 coating. The nanohardness results on each row shows consistent nanohardness except for the third row at a depth of 90 μm from the coating top surface—this row has the lowest nanohardness of 9 ± 1 GPa. The reduced nanohardness at this depth shows there was increase in the projected area relative to the constant applied load. The elastic modulus of the Al_2O_3 coating is shown in Figure 5–8 (b). The values plotted in the Figure were obtained from Equation (3-26). The lowest stiffness of the coating shows at the depth of 90 μm; the average value at this depth is 171 ± 15 GPa. Again, the reduced stiffness at the 90 μm depth shows that the reduced modulus from which the elastic modulus was calculated was low. The decrease in the reduced modulus resulted from the increased projected area of the indentation point and the reduced rate of change of applied load to the penetration depth. Despite the reduction in the elastic modulus calculated at this depth, the average elastic modulus from the thirty indentations—200 ± 7 GPa—agrees with the reports of other researchers [21]. The microhardness of the as–sprayed Al_2O_3 coating measured on three rows is presented in Figure 5–9. Each of the bars in the Figure represents average of five indentations in a row with the associated standard error in mean. The lowest microhardness of the coating (7.4 ± 0.3 GPa) is measured at the depth of 15 μm from its top surface. This value is within the error range of the effective microhardness of the Al_2O_3 coating obtained as 8 ± 0.3 GPa.

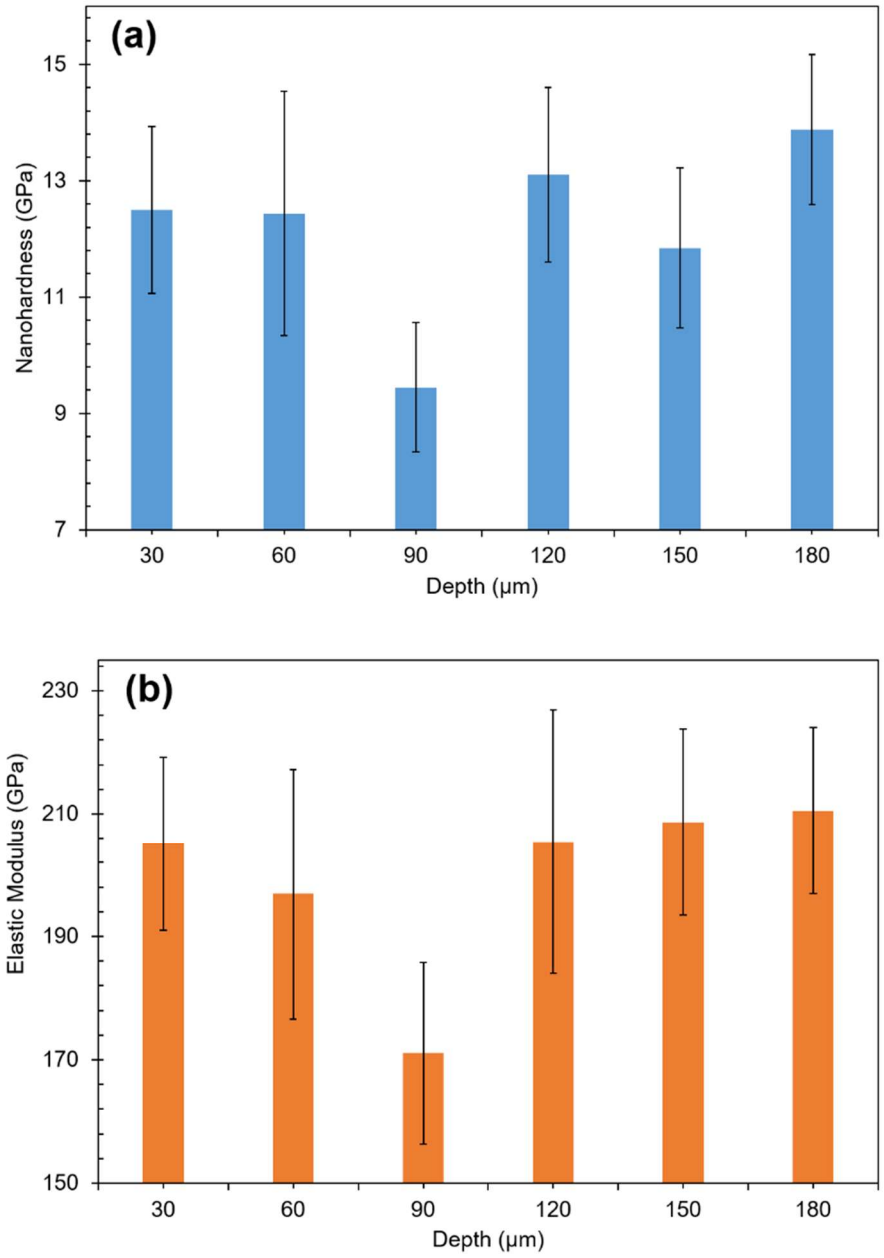

Figure 5-8: Depth profile of the (a) Nanohardness of the as–sprayed Al_2O_3 coating (b) Elastic modulus of the as–sprayed Al_2O_3 coating—see Table 21 in Appendix E for the 95 % confidence level of the mean of the data set.

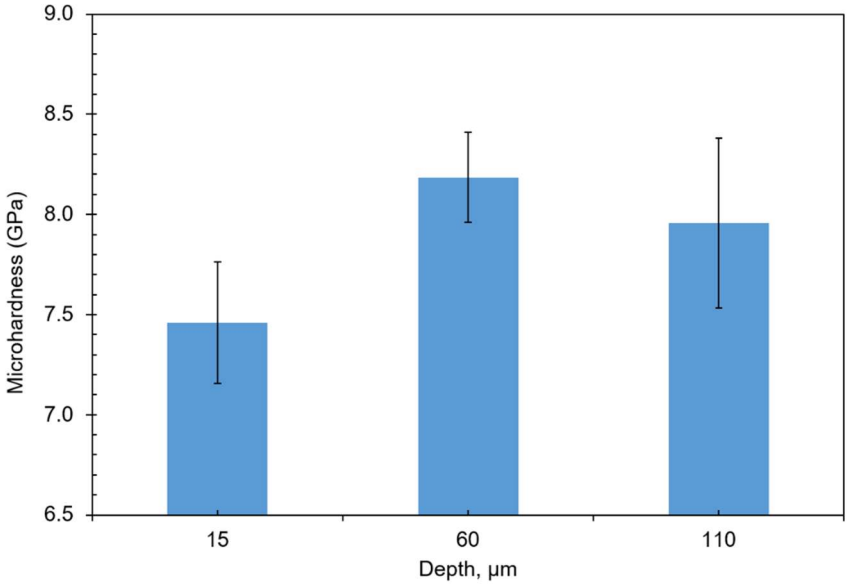

Figure 5-9: Depth profile of the Microhardness of the as–sprayed Al_2O_3 coating—see Table 22 in Appendix E for the 95 % confidence level of the mean of the data set.

5.2.2 As–sprayed YSZ coating

The results of the nanoindentation performed on the cross section of the as–sprayed YSZ coating is presented in Figure 5–10. The average nanohardness of the YSZ coating is 11 ± 0.5 GPa; the variation of the nanohardness at different depths within the coating is shown in Figure 5–10 (a) with the associated standard error in mean. The measurement at the 60 µm depth from the top surface shows a standard error in mean of 2 GPa. However, the average nanohardness at this depth is equal to that at the 90 µm; both have the same average value of 10 GPa. This is the lowest nanohardness within the coating layer which shows there was increase in the projected area relative to the constant applied load. The average elastic modulus from the thirty indentations is 183 ± 7 GPa—this value agrees with the report of Rauch et al. [204]. The elastic modulus of the YSZ coating varied with increasing depth from the coating top surface as shown in Figure 5–10 (b). The values plotted in the Figure are obtained from Equation (3-26). The lowest stiffness of the coating was measured at

the depth of 60 μm from the top surface; the average value at this depth is 168 ± 24 GPa. The microhardness of the as–sprayed YSZ coating measured on three rows is presented in Figure 5–11. The microhardness of the coating measured at the depth of 40 μm from its top surface gave showed a standard error in mean of 0.4 GPa—the average microhardness at this depth ~ 8 GPa. This microhardness value is with the error range of the average microhardness of the YSZ coating (~ 8 ± 0.3 GPa) as obtained from fifteen micro indents.

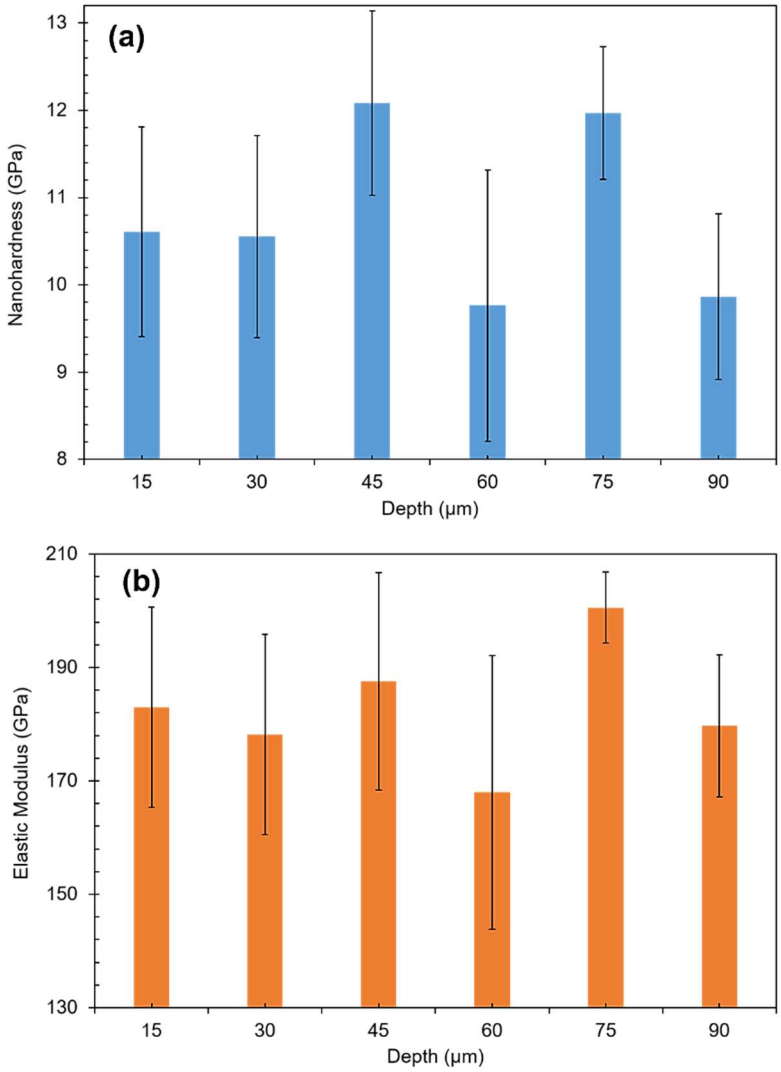

Figure 5-10: Depth profile of the (a) Nanohardness of the as–sprayed YSZ coating (b) Elastic modulus of the as–sprayed YSZ coating—see Table 23 in Appendix E for the 95 % confidence level of the mean of the data set.

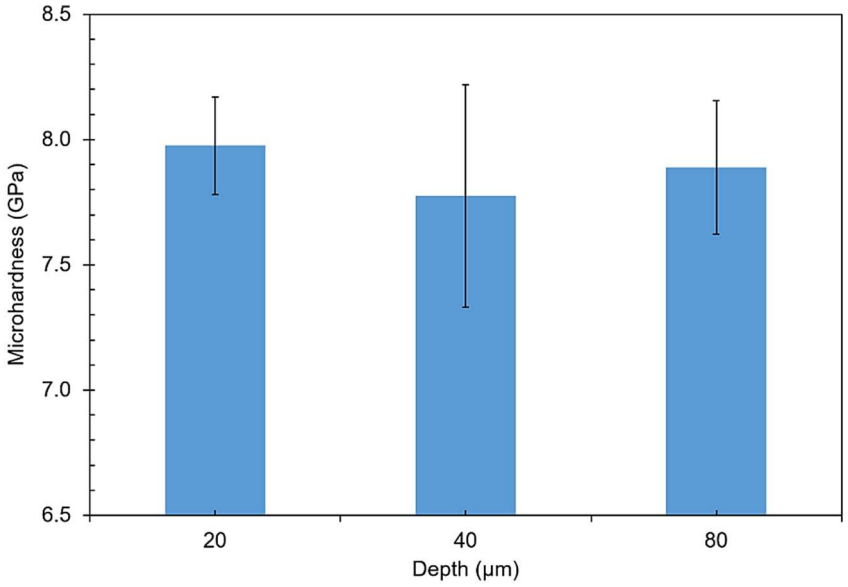

Figure 5-11: Depth profile of the Microhardness of the as–sprayed YSZ coating—see Table 24 in Appendix E for the 95 % confidence level of the mean of the data set.

5.3 Diffraction residual stress

5.3.1 Neutron diffraction residual stress in the Al_2O_3 coating

The stresses are presented as longitudinal stress along the length of the samples and transverse stress along the width of the sample; they are taken as equivalent principal stresses in the coatings by imposing plane stress condition while assuming negligible shear stress contributions. The peaks used for the through thickness residual strain analysis of the Al_2O_3 coating as stated in sub–section 3.6.3.1 is shown in Figure 5–12. The Al_2O_3 coating again shows the presence of gamma–Al_2O_3 (Figure 5–12) in congruence with the XRD pattern of the coating and the specific peaks used in the residual strain calculation are identified as γ(440) and the γ(400) while the remaining peaks are from the substrate. These peaks have been reported by Ahmed et al. [96] where the residual strain of APS and HVOF deposited Al_2O_3 coatings were investigated.

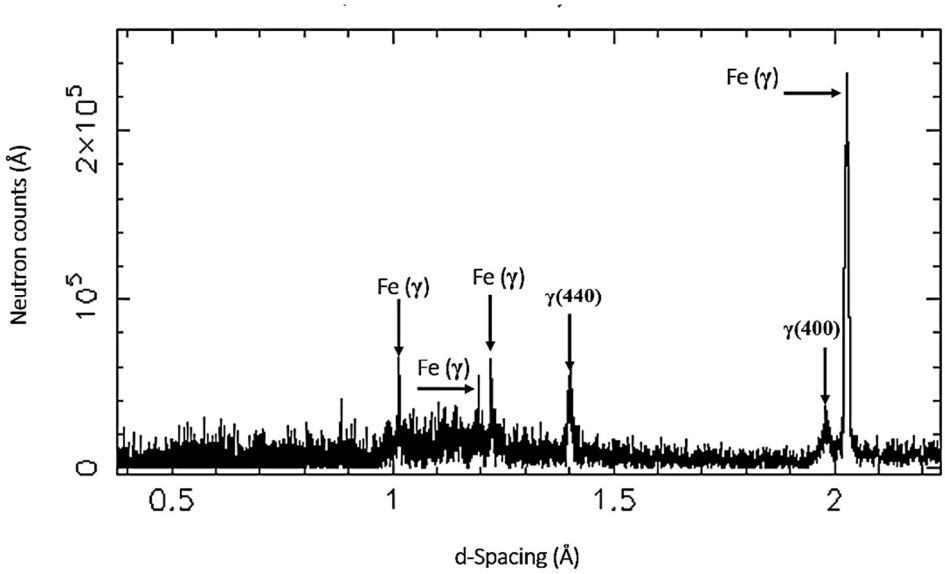

Figure 5-12: Neutron diffraction pattern showing the gamma–Al_2O_3 peaks of the as–sprayed Al_2O_3 coating and the Fe(γ) peaks from the substrate.

The precise positions of the Al_2O_3 peaks shown Figure 5–12 was obtained by single peak fit procedure using a range of t_{hkl} on the time–of–flight (TOF) (see Appendix A). For each of the through–depth position scanned in the Al_2O_3 coating, d_{hkl} for the γ(440) and the γ(400) peaks were obtained from Bank 1 and Bank 2 detectors alike. Longitudinal strains were calculated from the data obtained from Bank 1 while the transverse strains were calculated from the data obtained from Bank 2. For each scanned through–depth position in the coating, longitudinal strain and transverse strain were calculated based on the d_{hkl} obtained for each of γ(440) and the γ(400) peak; the average of the two strains were then calculated for every position through the depth of the coating. For the peaks associated with the substrate shown as Fe(γ), the d_{hkl} was obtained by full TOF spectrum analysis to capture every peak that has minimal overlap with an adjoining peak; this was done with data from both the Bank 1 and the Bank 2 detectors to obtain the longitudinal strains and the transverse strains respectively for every position through the depth of the substrate.

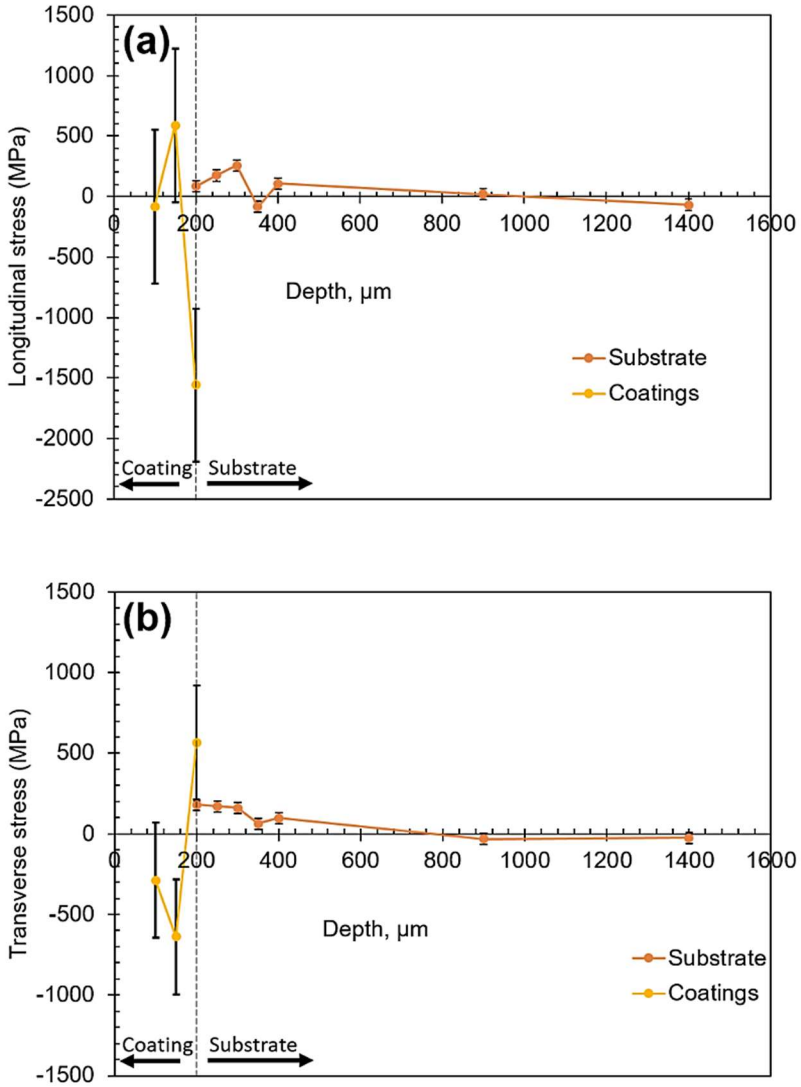

Figure 5-13: Neutron diffraction through depth residual stress profile the as–sprayed Al_2O_3 coating (a) longitudinal stress (b) transverse stress

The stresses calculated using Equation 3-32 for each of the scanned positions through the depth of the coating–substrate composite was based on the strain analysis presented above. The plot of the calculated stresses against increasing depths from the coating top surface is shown in Figure 5–13—the longitudinal stress profile is presented in Figure 5–13 (a) while the transverse stress profile is shown Figure 5–13 (b). The stress profiles show the Al_2O_3 coating to be in compression at the 100 µm depth in both the longitudinal and the transverse directions. The stress states at the

150 μm depth were in alternate directions with the longitudinal stress in tension while the transverse stress remains compressive. The stress profile in the substrate for both the longitudinal and the transverse direction agrees. In each case, the substrate tends to be stress free as depth increases away from the interface—at a depth of 1.4 mm the stress comes to – 68 MPa (longitudinal) and –24 MPa (transverse).

5.3.2 Neutron diffraction residual stress in the YSZ coating

The peaks used for the through thickness residual strain analysis of the YSZ coating as stated in Sub–section 3.6.3.1 is shown in Figure 5–14. The tetragonal phase shows as the only phase in the pattern of the YSZ coating; the remaining peaks are from the substrate. The strong Fe (α) peaks shown in the pattern could have been from the incident neutron beam scanning the coating and substrate simultaneously despite the cadmium slit inserted along the incident path to minimize divergence and ensure a concise gauge volume [195].

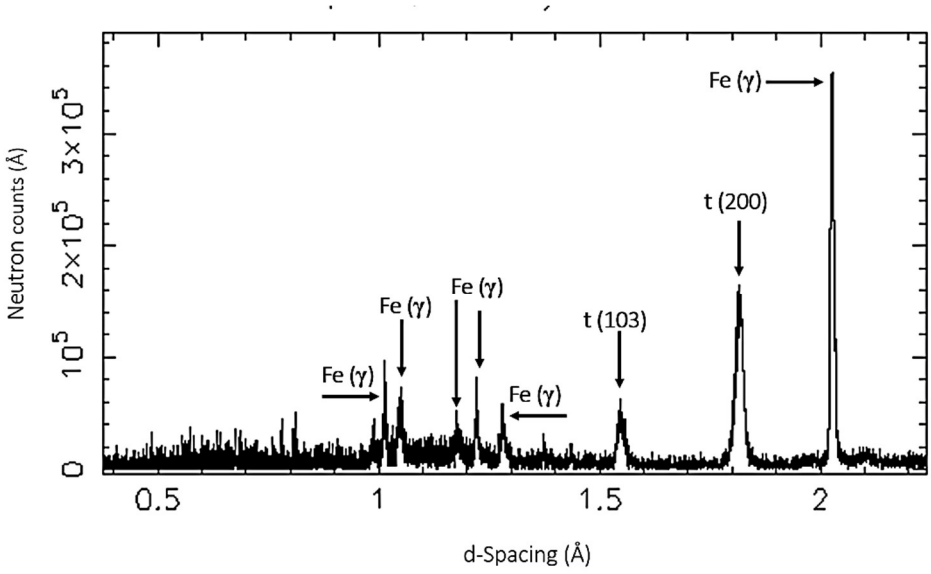

Figure 5-14: Neutron diffraction pattern showing the tetragonal peaks of the as–sprayed YSZ coating and the Fe(γ) peaks from the substrate

Like the analysis of the strain in the Al_2O_3 coating, the precise positions of the YSZ peaks shown Figure 5–14 were obtained by single peak fit procedure using a range of t_{hkl} on the time–of–flight (TOF) (see Appendix A). The peaks selected for the calculations of the strain were those with minimal overlap with the crest of adjoining peaks. Each of the peaks selected for the strain calculation at the scanned positions within the coating and the substrate were such as detected in both the reference sample and the main samples. The (t–200) peak reflection at the 1.8 Å was detected in the reference YSZ sample but undetected in the scanned data for the YSZ coating layer in the YSZ coating–substrate composite sample. As such, this peak was not used in the calculation of the strain associated with the YSZ samples. Longitudinal strains were calculated from the data obtained from the Bank 1 detector while the transverse strains were calculated from the data obtained from Bank 2 detector.

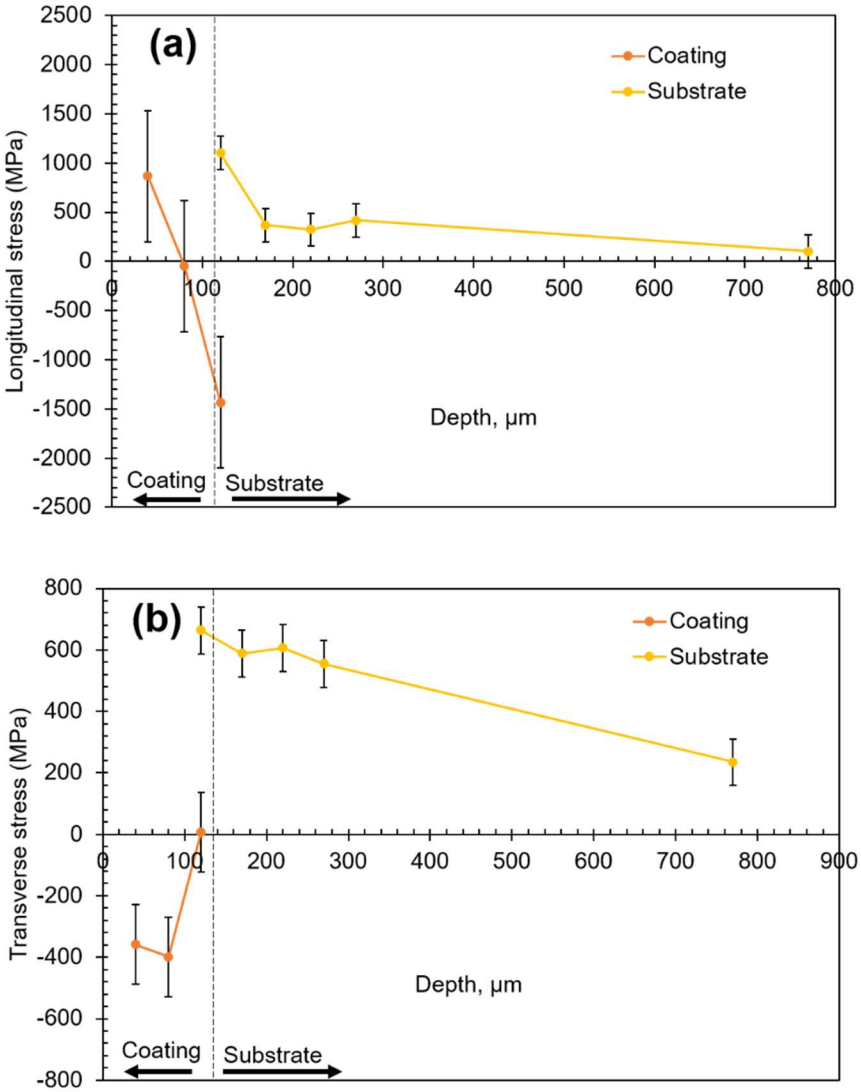

Figure 5-15: Neutron diffraction through depth residual stress profile the as–sprayed YSZ coating (a) longitudinal stress (b) transverse stress

The plot of the calculated stresses against depths for the scanned positions in the YSZ coating and the adjoining substrate is shown in Figure 5–15. The stresses were calculated using Equation 3-33 based on the strain analysis presented earlier. The longitudinal stress profile is shown in Figure 5–15 (a); the coating has tensile longitudinal stress near its surface (40 μm depth) before changing to compression –48 MPa at the 80 μm depth. Figure 5–15 (b) shows the transverse stress profile with the first two points in compression with the same order of magnitude (–358 MPa at 40

μm and –398 MPa at the 80 μm depth). The substrate was tensile in both the longitudinal and the transverse directions; however, the stress reduces towards the center of the substrate.

5.3.3 X–ray diffraction residual stress in the Al_2O_3 and the YSZ coatings

The residual stress of the as–sprayed coatings was measured through the XRD scan of a high diffraction angle planar reflection, at eight different tilt angles (ψ). The stresses were calculated based on Equation 3-29 described in subsection 3.6.3.1; the equation linked the interplanar spacing ($d_{\Phi\psi}$), the tilt angle and the diffraction elastic constant of a material. The diffraction elastic constant has been replaced with the elastic modulus obtained from the nanoindentation measurements. Tensile stresses were obtained from increasing interplanar spacing ($d_{\Phi\psi}$) as the tilt angle increases as against compressive stresses obtained from decreasing $d_{\Phi\psi}$ as the tilt angle increases.

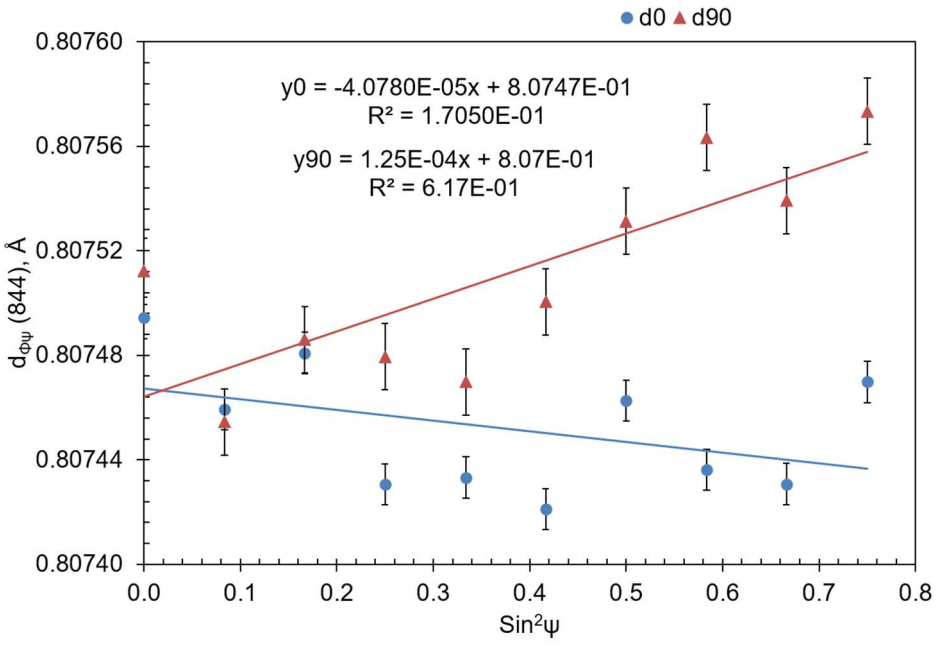

Figure 5-16: XRD d–spacing against $sin^2\psi$ Plot for the near surface residual stress in the as–sprayed Al_2O_3 coating

The residual stress of the as–sprayed Al_2O_3 coating was measured through the XRD scan of the (844) gamma–Al_2O_3 peak, a high diffraction angle planar reflection, at eight different tilt angles (ψ). Figure 5–16 shows the plot of $d_{\Phi\psi}$ against $\sin^2\psi$ for the Al_2O_3 coatings. The results show the near surface of the Al_2O_3 coating is in a compressive stress state with a magnitude of –8.3 ± 0.2 MPa (σ_{0°) in the longitudinal direction giving that the interplanar spacing decreased as the tilt angles increased. The stress in the transverse direction was tensile with a magnitude of 25.3 ± 0.8 MPa (σ_{90°) given that the interplanar spacing was increasing with increasing tilt angle.

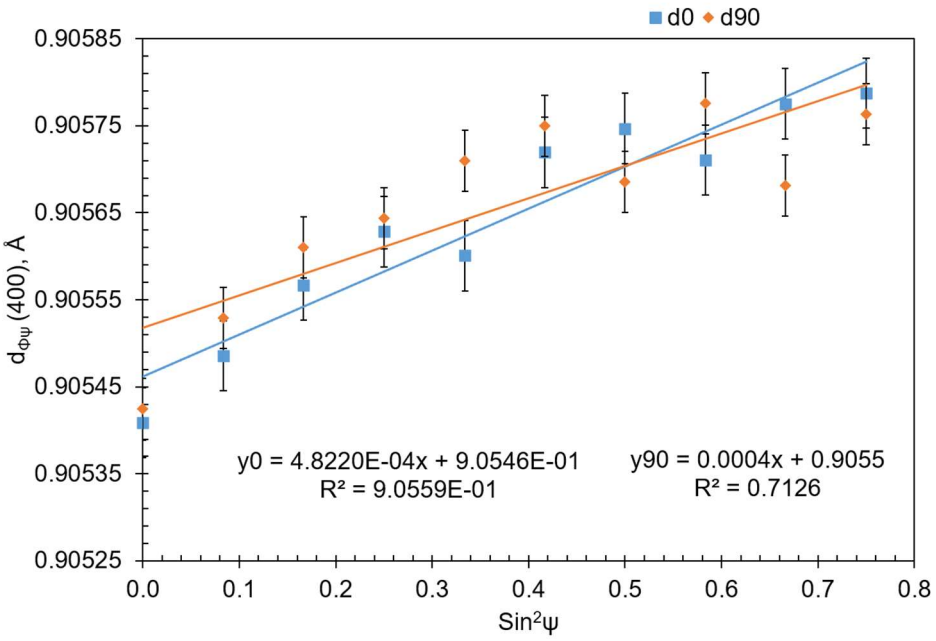

Figure 5-17: XRD d–spacing against $\sin^2\psi$ Plot for the near surface residual stress in the as–sprayed YSZ coating

Similarly, the residual stress of the as–sprayed YSZ coating was measured through the XRD scan of the (400) tetragonal peak, a high diffraction angle planar reflection, at eight different tilt angles (ψ). The $d_{\Phi\psi}$ obtained in the measurements was plotted against $\sin^2\psi$ for the YSZ coatings as shown in Figure 5–17. Positive slope linear graph was obtained in both the longitudinal and the transverse directions; this indicates

tensile residual stress state in the two directions. The magnitude of the stresses in the longitudinal and the transverse direction were 74.3 MPa ($\sigma_{0°}$) and 57.3 MPa ($\sigma_{90°}$) respectively.

5.4 Incremental hole–drilling residual stress

The residual stress from the hole–drilling measurement is presented in this section. The directional stress (longitudinal or transverse) and the calculated principal stresses for the individual coatings are presented separately. Directional stress on a body act through an axis perpendicular to the plane through a point in the body; this directional stress is thus called normal stress. Its counterpart, the shear stress acts parallel to the plane through the point of action of the normal stress. The normal stress reaches a maximum or a minimum value when the plane through its point of action is rotated by an angle θ such that the shear stress goes to zero. The plane in its new orientation is called the principal plane while the stress acting through an axis perpendicular to the principal plane is termed the principal stress. There are two principal stresses under a plane stress condition: the maximum principal stress and the minimum principal stress. The algebraically larger of the two principal stresses is the maximum while the smaller of the two is taken as the minimum principal stress [198] . The maximum and the minimum principal stresses presented for each of the coatings were calculated based on Equations (3.37) and (3.38) presented in sub–section 3.6.3.2.

5.4.1 Residual stress profile in the Al_2O_3 coatings

The residual stress profile of the Al_2O_3 sample from the hole–drilling is shown in Figure 5–18. Figure 5–18 (a) shows the longitudinal and transverse stresses were compressive near the coating surface. The stresses changed to tensile with

increasing depth; the longitudinal stress reached 12 MPa and 219 MPa while the transverse stress reached 81 MPa and 321 MPa at the 112 µm and 160 µm depths respectively. The stresses in the substrate changed from tensile to compressive as depth increased. At the depth of 224 µm, the longitudinal stress was 60 MPa; it reached –113 MPa at the 1.02 mm depth. Similarly, the transverse stress was 139 MPa at the depth of 224 µm and has reached –138 MPa at the 1.02 mm depth.

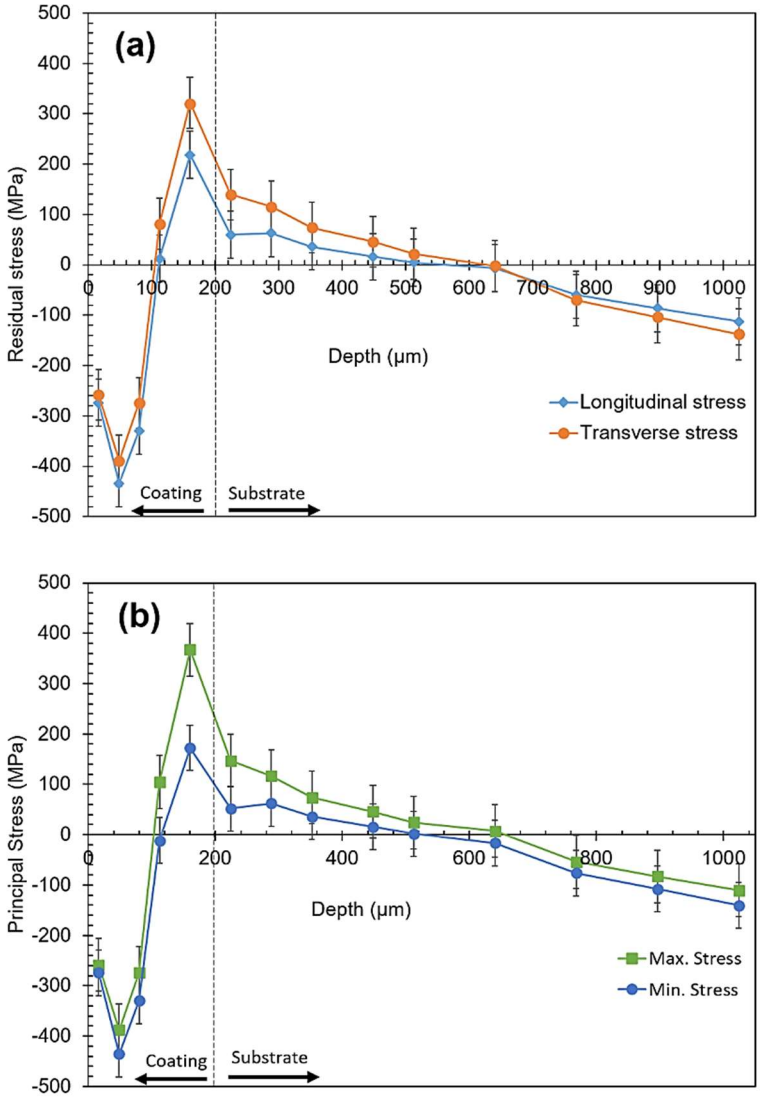

Figure 5-18: Incremental hole–drilling (a) longitudinal and transverse residual stresses in the as–sprayed Al_2O_3 coating (b) principal residual stresses in the as–sprayed Al_2O_3 coating

The principal stresses for the Al_2O_3 sample obtained from Equations (3.30) and (3.31) shows the same trend as the longitudinal and the transverse stresses (Figure 5–18 (b)). The principal stresses in the coating at the 112 μm and 160 μm depths provides useful information comparable to the information obtained from the neutron data at depths 100 μm and 150 μm. The maximum and minimum stresses at the 112 μm depth are 105 MPa and –11 MPa respectively. At the 160 μm depth, the maximum and minimum stresses are both tensile with the values of 367 MPa and 172 MPa respectively. The maximum and minimum stresses at the midpoint of the substrate (1.02 mm) seem equal to the longitudinal and the transverse stress indicating the shear stress contribution at this depth is negligible.

5.4.2 Residual stress profile in the YSZ coatings

The residual stress profile of the YSZ sample from the hole–drilling is shown in Figure 5–19. The longitudinal and transverse stresses shown in Figure 5–19 (a) show the same trend. The YSZ coating has near surface (16 μm depth) compressive transverse and longitudinal stresses before the nature of the stresses start to change in both directions. The longitudinal stresses rise from 17 MPa at the 48 μm depth up to 389 MPa at the 112 μm depth while the transverse stress transit from –20 MPa at the 48 μm depth to 312 MPa at the 112 μm depth. Stress in the substrate, however, eases out as the depth increased—the longitudinal stress dropped to 13 MPa while the transverse stress reached – 29 MPa at the 1.02 mm depth.

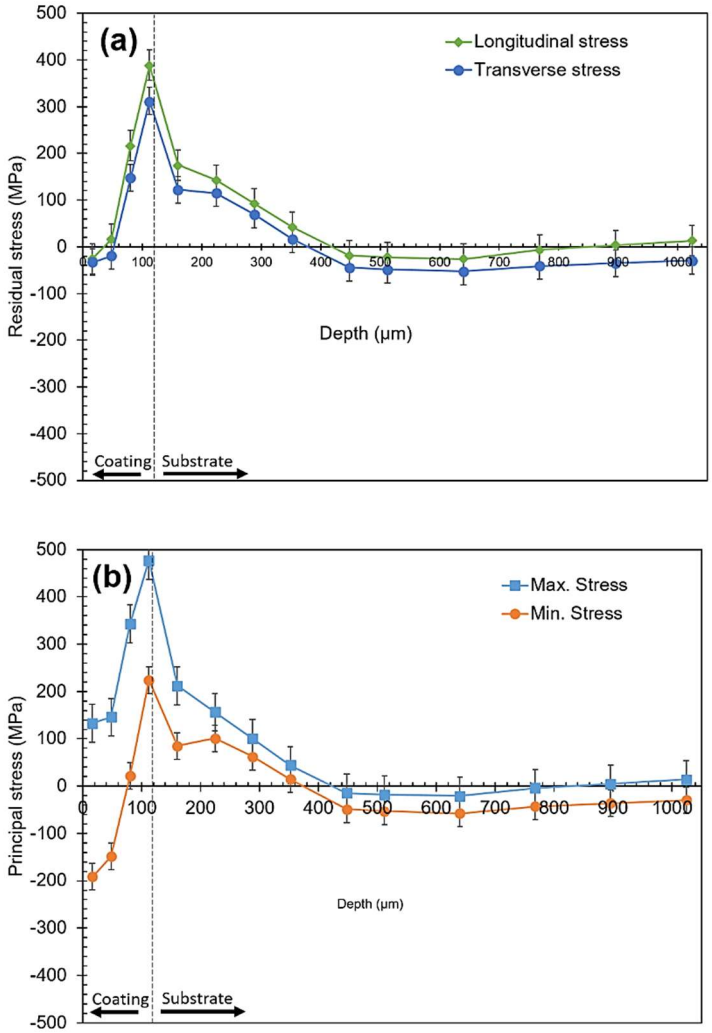

Figure 5-19: Incremental hole–drilling (a) longitudinal and transverse residual stresses in the as–sprayed YSZ coating (b) principal residual stresses in the as–sprayed YSZ coating

The principal stresses in the YSZ sample (Figure 5–19 (b)) shows a different trend to the directional stresses—this must have resulted from the increased shear stress recorded for the YSZ coating. The initial points of the minimum principal stress were compressive –192 MPa at the 16 μm depth and –148 MPa at the 48 μm depth; it became tensile 21 MPa at 80 μm depth and 224 MPa at the 112 μm depth. The stress value at the 80 μm depth represents the coating stress state half–way its depth from the top while the stress value at the 112 μm depth gives the coating stress state near the coating–substrate interface. The maximum principal stress was entirely tensile; it

has a stress state of 133 MPa at the 16 μm depth near the coating surface, 343 MPa at the 80 μm depth and 477 MPa at the 112 μm depth near the coating–substrate interface. The maximum and minimum stresses at the midpoint of the substrate (1.02 mm) are 14 MPa and –30 MPa—this has not changed significantly from the longitudinal stress 13 MPa and the transverse stress –29 MPa. This suggests the shear stress contribution at this depth is negligible. However, in all the cases presented in the coating, where the stresses maintained the same trends as in the directional stresses; the magnitudes were mostly different. This indicates significant shear stress contribution—a marked difference between the YSZ sample and the Al_2O_3 sample with negligible shear stress contribution

5.5 Discussion

5.5.1 Microstructure and coating formation

The microstructure of the two coatings reflects the different thermal properties of the feedstock from which they were sprayed. The processing parameters caused the Al_2O_3 particles to melt producing coatings with lamellae unlike the softened and sintered YSZ particles that produced coatings with fused particles. The thermal properties of the two materials, their enthalpy of fusion, could also be significant to the microstructure obtained in the two coatings [35]. The enthalpy of fusion represents the thermal energy needed to liquefy a solid mass—its magnitude depends on the mass of the substance. The instantaneous thermal energy of the flame varies from the combustion chamber downstream up to the substrate given the temperature gradient established for SHVOF thermal spray process [234]. The hypersonic speed of the combusted gases carrying the particles and the short spray distance (85 mm) suggest the particles have short in–flight time. This further suggests the mass/size of the

particles plays significant role in the resulting microstructure of a coating. It is expected that small size particles would attain sufficient heating because they will have low enthalpy of fusion in kJ. If the particles/agglomerate in the sprayed suspensions are considered spherical, the mass of an agglomerate/particle can be estimated by relating the volume of the spherical agglomerate to the material density of either of Al_2O_3 and YSZ. So, in this case, an Al_2O_3 agglomerate with a mean diameter of D_{50} = 1 μm is five order of magnitude smaller in mass than a discrete YSZ particle, even though the mean diameter of the YSZ discrete particles is D_{50} = 0.6 μm. This is so because the mass density of zirconia is ~ 6 times the mass density of water (1000 kg/m^3) compared to the mass density of Al_2O_3 which is ~ 4 times the mass density of water. If the mass argument is considered, the Al_2O_3 particles would have lower enthalpy of fusion and should melt. The Al_2O_3 particles melt to produce dense individual lamellae even though the in–flight time of a particle during SHVOF spray is in μs. This is supported by the absence of intra–lamella cracking as shown through the fractograph of the coating. However, the YSZ particles should also melt giving the magnitude of the mass of the particles in addition to the enthalpy of fusion of YSZ (700–820 kJ/kg) being lower than the enthalpy of fusion of Al_2O_3 (620–1360 kJ/kg). The observed microstructure of the YSZ coating showed the YSZ particles did not melt; they reached the substrate as fused solids. This may be due to the low thermal conductivity of the YSZ material (1.7–2.7 W/m.K); YSZ conducts about ten times less thermal energy per each degree temperature gradient when compared to Al_2O_3 with a thermal conductivity range of 12–38 W/m.K. It therefore seems the resident time of the YSZ particles in the combustion chamber, where it should acquire the largest instantaneous thermal energy is inadequate. It may be necessary to further study the deposition of the YSZ particles using different combustion chamber lengths longer

than the 22 mm type used in the deposition of the current YSZ coating. This might help to address the question of whether the deposition parameters used for the current YSZ coating is sufficient to guarantee the melting of the YSZ particles.

The suspension medium besides processing parameters and material properties determines the physical interaction between the flame and the particles (and molten droplets) in a SHVOF thermal spray process. Aqueous carrier cools the flame as it consumes the thermal energy of the flame due to its high specific enthalpy of vaporization (2.26 MJ/kg) while organic solvents (like ethanol) enhances the energy of the flame with its heat of combustion [57]. Where the evaporation of water or the burning of the ethanol occurs in the combustion chamber, it creates higher chamber pressure that increases combustion gas velocity—this often translates to high particle velocity that yields dense coatings [235, 236]. The velocity could reach between 2000–2500 m/s [236] in the case of aqueous base suspension injected into the combustion chamber whereas the velocity reaches 1000–1500 m/s when the suspension is ethanol based [237]. The spray condition used for the Al_2O_3 coating has been shown by Chadha et al. [236] to match the case of the aqueous base suspension. In spite of the cooling of the combusted gas by the aqueous carrier of the Al_2O_3 particles, most of the particles melt to form droplets due to the size of the individual particles in the agglomerates [9] and the flame temperature being higher than 2100 °C [236]. The droplets were propelled by the high velocity combustion gas onto the substrates to form well adhered splats that built into densely packed individual lamellae shown on the fractograph of the Al_2O_3 coating. The thickness of the lamellae varies up to 10 µm—the lamellae size range shows these are created from molten agglomerates of the Al_2O_3 particles. The large size of the lamellae is possibly due to coalescence of

droplets. The top surface of the lamella appears smooth while the cross section of the lamellae shows non–uniform fine intra–lamella voids. The origin of the defects shown through the coating fractograph and its cross–section can be linked to the buildup of the lamellae. The initial droplets adhere to the substrate due to the improved surface roughness of the substrate achieved from the grit blasting process. It is possible that the surface roughness between successive lamellae layers failed to provide similar interlocking sites as on the grit blasted substrate; this creates weak bonding between the lamellae which resulted in interlayer cracks observed in the coating. The dense microstructure of the YSZ coating suggest the fused particles that make up the coating were also carried by high velocity combustion gas—the evaporation of the feedstock carrier must have occurred in the flame. The vertical crack and the interlayer crack in the YSZ coating could have resulted from adjoining inter–particle voids.

The fluid dynamic properties of the suspension medium and its surrounding combustion gas also affect the coating formation from an atomization point of view [235]. These dynamic properties are combined in dimensionless numbers—Weber number (*We*) and the Reynolds number (*Re*). Essentially, *Re* number is the ratio of the fluid inertia (ρ*u*d) to viscosity (μ)—ρ is the fluid density, u is the relative velocity of particles to the surrounding fluid and d is the particle diameter. *We* number on the other hand gives the ratio of the fluid inertia to the surface tension (σ) which describes the resistance of suspension drops to increased surface area accompanying atomization process [238]. Primary atomization occurs near the injector exit, and the secondary atomization (aerodynamic breakup) occurs downstream into the combustion chamber or the expansion barrel—in the case of axial injection [235]. The

suspension injection process can be classified as a dense spray process—it has large number of droplets accompanied by disintegration and droplets interactions [239].

Secondary atomization is the rate controlling process in dense spray because the primary breakup is unstable [240]. *We* number is mostly considered for the secondary atomization study; its increase changes the breakup regime in succession from bag to catastrophic break up [50]. More so, it can be inferred from the work of Dai and Faeth [240] that the *Re* number in the combustion chamber of SHVOF thermal spray gun offers a flow regime where the drag properties of the suspension droplets is unaffected by the viscosity of the combustion gas. The size of the lamellae in the fractograph and the size of the splats from the surface morphology images of the Al_2O_3 coating suggests they were formed from bigger suspension droplets obtainable at the bag breakup level of the secondary atomization—this suggests the *We* number of the suspension droplets are in the range of 12–50 [50]. On the other hand, the YSZ coating being built from sintered particles—each one identifiable—could have formed from suspension droplets produced at the shear breakup level of the secondary atomization. At this stage, the *We* number ranges between 100 and 350—its major features include continuous shearing and entraining that produces fine droplets. The fine droplets were too small to be carried on at the center of the gas so the particles they released did not get sufficient heating to melt—they got softened. The soften particles collide and fuse together in flight or as they impact the substrate to produce the sintered particles in the YSZ coating as shown by its surface morphology and the fractograph.

5.5.2 Phase evolution in the coatings

The impact of the thermal treatment on both Al_2O_3 and YSZ particles caused different type of structural response. Most of the Al_2O_3 particles melted to form amorphous Al_2O_3 and γ–Al_2O_3 although some α–Al_2O_3 were detected in the as–sprayed coating as shown by the XRD results—these are from the unmolten feedstock. The retention of the α–Al_2O_3 could have been due to entrapment during molten droplet formation inflight or the α–Al_2O_3 particles arrived at the substrate surface and get buried in the large lamellae that forms the coating. The particles were, however, undetected in the fractograph due to their nanometric sizes. In another vein, peak broadening in x–ray diffraction profile reflects crystal imperfections; it occurs due to any or combination of reduced crystallite size, increased dislocation density, stacking faults, twinning, micro stress, grain boundaries, and chemical heterogeneities [229]. The crystallite size of the Al_2O_3 powder which is corundum presents as coarse crystallites (141 ± 4 nm). However, after deposition the crystalline contents of the coating that has transformed to gamma–Al_2O_3 presents refined crystallite size of 48 ± 2 nm; this seems to cause peak broadening on the high 2θ angle peaks between 100 and 130°.The mechanism of the phase formation in SHVOF thermal sprayed Al_2O_3 has been presented in Subsection 4.8.1 of this thesis. The broad peaks in the YSZ XRD profile on the other hand could appear due to one or combination of reduced crystallite size, stacking faults and dislocation density. Bailey and Rotherham [241] reported both the monoclinic and the tetragonal phases contains dislocation defects in addition to the stacking faults found in the (010) plane of the monoclinic phase. This appears to explain the origin of the broad peaks seen in the powder which contains two zirconia phases—monoclinic and tetragonal—with the crystallite sizes of each one being 28 ±

5 nm and 14 ± 0.3 nm respectively. The YSZ particles in the coating were sintered and predominantly unmolten after deposition yet the monoclinic phase in the feedstock transformed completely to produce all tetragonal phase in the as–sprayed coating. It is unlikely that the particles melted and recrystallized for the realization of the monoclinic to tetragonal transformation [242]. Monoclinic is the last phase in the transformation of ZrO_2 when it is cooled from melting point to room temperature. The monoclinic to tetragonal phase transition is a reversed transformation that occurs when the cooled monoclinic phase is heated above 1000 °C [243]. The mechanism of the monoclinic to tetragonal transformation observed in the YSZ coating is unclear and may require further work. Nonetheless, the transformation in YSZ is athermal—it occurs over a range of temperature rather than at a specific temperature [244]. Increase in temperature causes structural imbalance in the monoclinic lattice and gradual cooling interrupted with short dwelling time prevents proper reordering to monoclinic. Even so suspension droplets experience temperature gradient from the combustion chamber, downstream up to the substrate [234], the abrupt quenching at the substrate surface does not guarantee a full lattice reordering required for the disarranged monoclinic structure—hence the formation of the tetragonal phase.

The observed phase transformation in the YSZ coating has further effect on the lattice structure of the material. Tetragonal–monoclinic transformation causes ~7 % volumetric expansion in the lattice structure with an accompanying transformation shear of 0.18 and intergranular cracks—the intergranular crack is not found in the reverse transformation [241]. However, in the present coating a reverse transformation has been observed—monoclinic to tetragonal, which suggests a corresponding ~7 % volumetric contraction in the lattice structure. Bailey and Rotherham [241] described

monoclinic–tetragonal transformation in thin–film samples as martensitic shear transformation. The transformation is rapid which precludes coexistence of the monoclinic and the tetragonal phases in addition to distinct crystal orientations and morphological changes on the grains.

5.5.3 Indentation properties of the coatings

The observed microstructure of the two coatings also impacts on their measured properties. The nanohardness measured in the Al_2O_3 coating represents the hardness of individual lamella—the indents were small enough to fit within a lamella. The nanohardness has higher value compared to the microhardness which is lower by ~ 5 GPa; this can be attributed to the high density of each lamella as seen on the fractograph. The micro indents cover multiple lamellae and inter–lamellae defects (voids, micro cracks)—the defects reduce the measured microhardness [19, 66]. More so, the presence of defects like micro cracks (vertical and horizontal) and interparticle voids will interfere with the measured microhardness of the coating—the large micro indents will encompass defects and sintered particles. In addition, particle size refinement can increase the hardness of a non–work hardened material by grain boundary strengthening due to Hall–Petch effect [218]. Sintered materials also become hardened through the reduction of defects [13]—this might account for the high nanohardness of the YSZ coating

Typically, coating is built–up from lamellae while the lamellae consist of overlaid splats formed from droplets [18]. Dense lamellae are formed from splats with high intersplat contact area [66]. Turunen et al. [66] has demonstrated that the indentation modulus of thermally sprayed coatings correlates with its density. The average indentation modulus of the two coatings reflects the nature of their building blocks—lamellae in

the case of the Al_2O_3 coating and sintered particles in the YSZ coating. The Al_2O_3 coating has a high indentation modulus of 200 ± 7 GPa indicative of its dense building block—the lamellae while the YSZ coating has 183 ± 7 GPa due to the inter particle porosity that dominates its entire microstructure.

5.5.4 Residual stress distribution

The residual stresses from three measurement techniques have been presented to provide complimentary insight into the residual stress behaviour of coatings with different microstructural make–up. Albeit the results of the individual techniques may not be compared directly, the sources of the disparity can be due to underlying assumptions of each technique, the material properties of each coating and the microstructure of the individual coating. Diffraction techniques have the unique capability to measure residual stress due to crystalline phase transformation when compared to the hole–drilling technique. The magnitudes and/or the nature of the residual stress obtained from diffraction–based analysis depends the crystallographic planes considered in the strain analysis [95]. In the diffraction technique strain analysis only considered the dominant crystalline phase in the coating to calculate strain in the coating—it precludes contribution from the amorphous phase and crystalline phases that may be present in trace amount. This can be improved upon to ensure that we are able to estimate the contribution of all planes in phase(s) contained in a coating even though there has not been any diffraction technique to estimate the contribution of the amorphous phase in a coating. X–ray diffraction can provide an approximate surface stress needed to understand the immediate response of the coating to its functional environment, while the neutron diffraction technique can only provide stress information at further depths below the coating surface. Single peak fitting approach

was implemented in both the X–ray diffraction strain analysis and the neutron diffraction strain analysis presented in this thesis. The results of the residual stress obtained from diffraction analysis can be deemed complementary.

Incremental hole–drilling technique on the other hand estimated relaxed strain through the entire coating—amorphous and crystalline. The hole–drilling technique provides the combined contribution of all the constituents of a coating irrespective of its microstructural make up [200]. The hole–drilling technique provides stress information at further depths below a coating surface through its thickness; it assumes homogeneity of the sample for each point of measurement. However, thermal spray coatings are often built from lamellae and could have property variations across its thickness as it has been shown for the two coatings studied in this case.

Table 5-1: Results of the X–ray residual stress compared to the weighted average of the hole–drilling and the neutron diffraction residual stress

Samples		X–ray		Neutron diffraction		Hole–drilling	
		σ_{0° (MPa)	σ_{90° (MPa)	σ_1 (MPa)	σ_3 (MPa)	σ_1 (MPa)	σ_3 (MPa)
Al_2O_3	Coating	– 8.3	25.3	– 351	– 120	– 162	– 104
	Substrate	na	na	70	88	– 10	9
YSZ	Coating	74.3	57.3	– 205	– 250	149	102
	Substrate	na	na	462	529	40	7

The differences in the calculated stresses of the individual coatings can be narrowed down through a closer inspection by estimating the average of each of the stress obtained from both the hole–drilling and the neutron diffraction. Bolelli et al. [21] has used this approach to present stresses measured by X–ray diffraction and the hole–drilling technique. Table 5–1 shows the X–ray diffraction stresses and the average of the stresses measured from neutron diffraction and hole–drilling. The overall stresses presented in Table 5–1 have contributions from the four types of stresses identified in thermal spray coatings. These stresses are attributed to two sources: the coating deposition process and the property mismatch between the coating and the substrate. The deposition process is the source of the quenching (tensile), the peening (compressive), and the phase transformation stress (tensile/compressive) while the thermal stresses (tensile/compressive) results from the coefficient of thermal expansion (CTE) mismatch between the coating and the substrate. The nature of the stresses found in a coating, whether compressive or tensile, would suggest if any of the sources and/or types of the stresses can be considered dominant [245].

5.5.4.1 Residual stress response of the Al_2O_3 coating

The peening stress contribution to the overall stress in the Al_2O_3 coating is significant given the continuous impact of overlaid splats at hypersonic speeds which leaves the overall coating in compression. The collision of splats in this case can be considered inelastic where most of the kinetic energy of the arriving splats is transferred to the underlying splats—both the top and bottom splats spread out stuck together in a composite pile compressed. This is further justified by the average stresses from the three techniques (as in Table 5–1) being mostly compressive characteristic of peening effect. There could also be some compressive stress contribution from the phase

transformation stress based on the microstructure of the coating described in sub–section 3.1 above. Considering the coating as a composite mix of amorphous Al_2O_3 matrix reinforced with crystalline Al_2O_3 (gamma and alpha), the amorphous Al_2O_3 in the coating will compress the sparsely distributed crystalline phases which makes ~ 20 % of the entire mix. This is so in that amorphized material exerts compressive stresses on its surrounding due to its increased disorderliness and volumetric expansion [246].

The neutron diffraction strain analysis for the Al_2O_3 coating gives more detailed analysis based on two planes, (440) and (400), while the X–ray diffraction analysis gave the strain analysis based on the (844) plane. The residual stress calculated based on the strain analysis of planes (440) and (400) are compressive in the two directions; there is difference in the nature of the residual stress based on the (844) plane in the σ_{0° (longitudinal) and σ_{90° (transverse) directions (see Table 5–1). The absolute difference in the magnitude of the residual stress between the transverse and the longitudinal directions of the (844) plane is 33 MPa. It is not entirely clear why the difference exists, but it could be down to the crystallographic orientation of this specific plane in the two directions. It is worth mentioning that the residual stress variation identified in the (844) plane is unrelated to the shape or the dimensions of the sample. As evidenced from Figure 5–18, the differences between residual stress in the longitudinal and transverse directions—measured through the hole drilling technique—are well within the error range of the measurements. This concludes that similar stress profile exists in both the longitudinal and the transverse directions of the Al_2O_3 coating; however, the directional tensile stress shown in the X–ray result might be manifestation of the thermal and quenching stresses in the coating.

The quenching stress (tensile) contribution to the residual stress in the Al_2O_3 coating can be deemed reduced giving the poor inter lamellae bonding identified through the fracture surface, micro cracks between adjacent lamellae and inter layer passes—interlayer defects help in stress redistribution. More so, because the Al_2O_3 coating is built from large overlaid lamellae (> 10 μm, see Figure 5–4(b)) with good intra–lamellae bonding; each lamella then acts as distinct entities such that when the whole lamellae experience cooling and shrinkage, the tensile stress generated is released through the inter–lamellae micro cracks. This phenomenon has been reported for Al_2O_3 coating with similar large lamellae make up [21].

Table 5-2: Material properties

Property	Materials		
	Al_2O_3	YSZ	AISI 304
Elastic modulus–E (GPa)	200 ± 7	183 ± 7	190 – 203 [247]
Poisson's ratio	0.21 – 0.33 [248]	0.22 – 0.32 [249]	0.26 – 0.27 [247]
Coefficient of thermal expansion–α (/K)	4.5 – 10.9 [248]	2.3 – 12.2 [249]	16 – 18 [247]
Thickness–t (μm)	200 ± 2	120 ± 1	2000

In addition, the contribution of the thermal stress resulting from the cooling of the combine coating–substrate composites can be deemed to be tensile [93]. This can be demonstrated given that the average of the substrate–coating CTE ratio was ~ 2.2 based on Equation 5-1 [95] and the material properties shown in Table 5–2.

$$\sigma_c = \frac{1}{t_c}\left(\frac{\Delta T*(\alpha_s - \alpha_c)}{\frac{1-\upsilon_s}{t_s*E_s} + \frac{1-\upsilon_c}{t_c*E_c}}\right)$$ ---------- Equation 5.1

Where σ, t, α, ν, ΔT and E are the thermal stress (MPa), sample thickness (μm), CTE (/K), Poisson's ratio, change in temperature (K) and the elastic modulus (GPa) respectively—the subscript s means substrate while c means coating. While the presence of the thermal stress and the quenching stress can be established , their respective contributions to the residual stress in the Al_2O_3 coating are reduced considering that the overall stress remains compressive. This suggests that of the two sources of stresses in thermal spray coatings, the deposition process is dominant for the Al_2O_3 coating. Similarly, of the four types of stress identified in the Al_2O_3 coating, the peening stress can be considered the dominant through the depths of the coating given that the deposition process was HVOF based.

5.5.4.2 Residual stress response of the YSZ coating

The overall stress state of the YSZ coating presented in Table 5–1 shows mix modes in the nature of the stresses; where the nature agrees, the magnitude varies. It has been mentioned that the stresses obtained by diffraction techniques are dependent on the crystallographic planes considered. Recall that the YSZ coating has just the tetragonal phase after deposition; so, the planes considered for the stress/strain analysis are from the tetragonal phase. The neutron diffraction technique showed that the stress contribution based on the (103) plane is compressive as against the tensile contribution from the (400) plane based on the X–ray diffraction technique. These results can be taken as the phase transformation stress contribution to the stress state of the coating. It has been mentioned earlier that the phase transformation stress could be either tensile or compressive; the results presented here showed that what

determines whether it will be tensile or compressive can be down to the crystallographic orientation of the planes considered. Differently, the hole drilling technique provided the overall contribution of the constituents of the coating irrespective of the microstructural difference. This combines stress state showed as tensile.

The sources for the mixed mode residual stresses manifested in the diffraction techniques and the hole–drilling technique can be theorised. The microstructure of the coating revealed by the fractured surface could be represented by a pile of depressed spheres with increased contact angle relative to the substrate. This configuration will suggest an enhanced contribution from the quenching stress. However, the quenching stress so generated at near the coating top surface is reduced as it could have been released by the presence of interlayer and vertical cracks through the sintered particles. There is another source of the continued tensile stress shown by the hole–drilling measurement—the thermal stress contribution. The tensile thermal stress contribution can be justified based on Equation 5-1 using the properties in Table 5–2. The substrate–coating CTE ratio can be shown to be ~ 2.3; this shows significant mismatch between the CTE of the coating and the attached substrate.

On the other hand, there is compressive stresses observed below the coating surface as shown by the neutron diffraction measurement which gives the stress state of the coating from 40 μm down through the coating thickness. This is stress state is due to the peening stress engendered by the hypersonic speed of the HVOF thermal spray process. Continuous impact of the unmolten YSZ particles delivered at hypersonic speed generated the compressive peening stress shown by the neutron diffraction measurements. The coatings response to this mixed mode compressive and tensile

stress appears to be the vertical crack identified on both the cross section and the fractograph of the coating. In all, for the YSZ coating there is mutual contribution from the two sources of the stresses: the deposition process and the substrate–coating CTE mismatch; neither of them appears to be dominant. This conclusion also holds for the four types of stress: the peening stress, the thermal stress, the quenching stress, and the phase transformation stress—none of the four is dominant.

5.6 Summary

Residual stress of SHVOF thermal sprayed Al_2O_3 and YSZ coatings were investigated using a combination of the time–of–flight (TOF) neutron diffraction, X–ray diffraction and the incremental hole–drilling techniques. It has been demonstrated that SHVOF thermal spray is able to deposit coatings of up to ~ 200 μm with suitable integrity. The microstructure of both coatings shows distinct building elements—lamellae in the case of Al_2O_3 and fused particles in the case of YSZ. It was shown that the microstructure of coatings has considerable impact on the residual stress behaviour of thermal spray coatings. However, coating deposition by SHVOF does not alter the internal microstructure of the underlying substrate. Regarding the techniques used for the residual stress measurement, the following conclusions can be drawn:

The X–ray diffraction technique provided the surface stress needed to understand the immediate response of the coating to its functional environment. This is so in that its method of data collection by scanning the sample surface with reduced signal penetration compared to neutron diffraction and hole–drilling techniques.

Through thickness residual stress in the Al_2O_3 coating has been compressive from the neutron diffraction measurements and the hole–drilling techniques.

Through thickness residual stress in the YSZ coating has been compressive from the neutron diffraction measurements and tensile from the hole–drilling measurement.

The shear stress contribution to the hole–drilling residual stress varies in the two coatings; it was negligible in the Al_2O_3 coating but significant in the YSZ coating.

The results of the individual residual stress techniques presented in this chapter do not agree when compared to one another; it can be rationalized the three techniques offered complimentary understanding of the residual stress behaviour of the coatings. The disparities between the diffraction-based techniques results and those of the hole-drilling technique could be resolved if the diffraction-based technique would account for the amorphous contents of the coatings. This will be an object of further research.

Thermal barrier coating ceramic topcoats from YAG and YSZ

6.0 Introduction

The microstructure and residual stress behaviour of coatings processed from suspension feedstock had been presented through the previous two result chapters—Chapter Four and Chapter Five. This chapter presents the results of three more coatings produced from suspension and solution precursor thermal spray; they have been studied as thermal barrier coating. The integrity of the thermal barrier coating relies on the effectiveness of its ceramic uppermost layer which provides shield to the underlying bond coat and the superalloy—the ceramic layer is otherwise called topcoat. Three topcoats were sprayed from different feedstock as presented in Sub-Section 3.3: two were produced from yttrium aluminium garnet (YAG) while the remaining one was produced from yttria stabilized zirconia (8 wt. % YSZ). One of the two YAG topcoats was produced from solution precursor while the other was produced from a YAG suspension. The solution precursor was a stoichiometry solution of aluminium trioxonitrate V nonahydrate and yttrium trioxonitrate V hexahydrate represented as $Al(NO_3)_3.9H_2O$ and $Y(NO_3)_3.6H_2O$, respectively. The YAG topcoat sample from the solution precursor is referred to as the SP–YAG while the one from suspension is taken as S–YAG. Two YSZ samples presented in this thesis, the first one (T1–YSZ) presented in Chapter 5 was deposited with a flame power of 110 kW while the one presented in this chapter was deposited with a flame power of 99 kW here after referred to as the T2–YSZ.

The results on the YAG topcoats presented in this chapter constitute the first on the study of YAG processed by HVOF spray technique. The processing-microstructure-properties relationships were studied through a range of characterization techniques and thermal cycling. The mechanism of formation of YAG from the solution precursor was also studied with the combination of TGA/DSC and XRD; the formation mechanism of both the YAG suspension and the YSZ suspension are trade information since they were both sourced from commercial suppliers (see Table 3–1). The thermal conductivity of the topcoats was also investigated from 25 °C–1000 °C using the samples with the topcoats on a AISI 304 stainless steel. The topcoats on Ni–alloy which had bond coat deposited on it was used for the thermal cycling tests meant to show the lifespan of the topcoats under thermal fatigue loading. The microstructure of the topcoats was studied with SEM, XRD and EDS before and after thermal cycling to understand the microstructural variation in the coatings from the as-sprayed state to the thermal cycled state.

6.1 Synthesis of YAG from solution precursors

The combined plot of the thermogravimetric (TG) and the differential scanning calorimetry (DSC) plots of the solution precursor described in subsection 3.2.2 are shown in a combined plot Figure 6-1(a). The figure shows the combined weight loss of ~ 56 % due to evaporation of absorbed water, molecular water, and decomposition of the nitrate [250]. The weight loss occurred during the heating process from the temperature of 50 °C to end at ~650 °C; the weight loss stopped at the point on the TG curve where it plateaued. The DSC curve shows four successive endothermic peaks between 100 °C and 500 °C with an exothermic peak at ~940 °C—this puts the total reaction enthalpy at about +915.89 J/g. Three temperature stages were identified

from the DSC plot: the initial, intermediate, and the final; the marked temperature regimes were used to understand the reaction path towards the formation of the YAG sample. The temperature at the end of the initial endothermic reaction stages was 450 °C; it was 750 °C for the intermediate stage while the final stage was marked at 900 °C.

The reaction of the solution precursor through the three temperature stages mentioned earlier is termed calcination—a thermal decomposition reaction that involved evolution of gases. FTIR was used to investigate the progress of the reaction of the solution precursor. The FTIR spectra (1800–500 cm^{-1}) of the solution precursor and the samples calcined at the three temperatures identified from the DSC plot are shown in Figure 6–1(b). The spectrum for the solution precursor shows a band at 1640 cm^{-1} associated to the bending mode[6] of water and two vibration bands centered at ~1600 cm^{-1} and ~1200 cm^{-1} associated with the stretching vibration mode of the nitrate group [250, 251]. Other nitrate vibration bands appear at ~1025 cm^{-1}, ~800 cm^{-1} and between 780–660 cm^{-1}. The nitrate vibration bands weaken as temperature increased; at 750 °C and 900 °C the triplet bands appear between 800 cm^{-1} and 600 cm^{-1} and at ~567 cm^{-1}. The triplet band shows the Al-O metal-oxygen vibration stretching at 788 cm^{-1} and 688 cm^{-1} while the Y-O vibration appears at the 722 cm^{-1}. The unilateral band at the 567 cm^{-1} represents another Y-O [250, 251].

[6] Bending mode means a molecular vibration in which bond angles are expanded and compressed

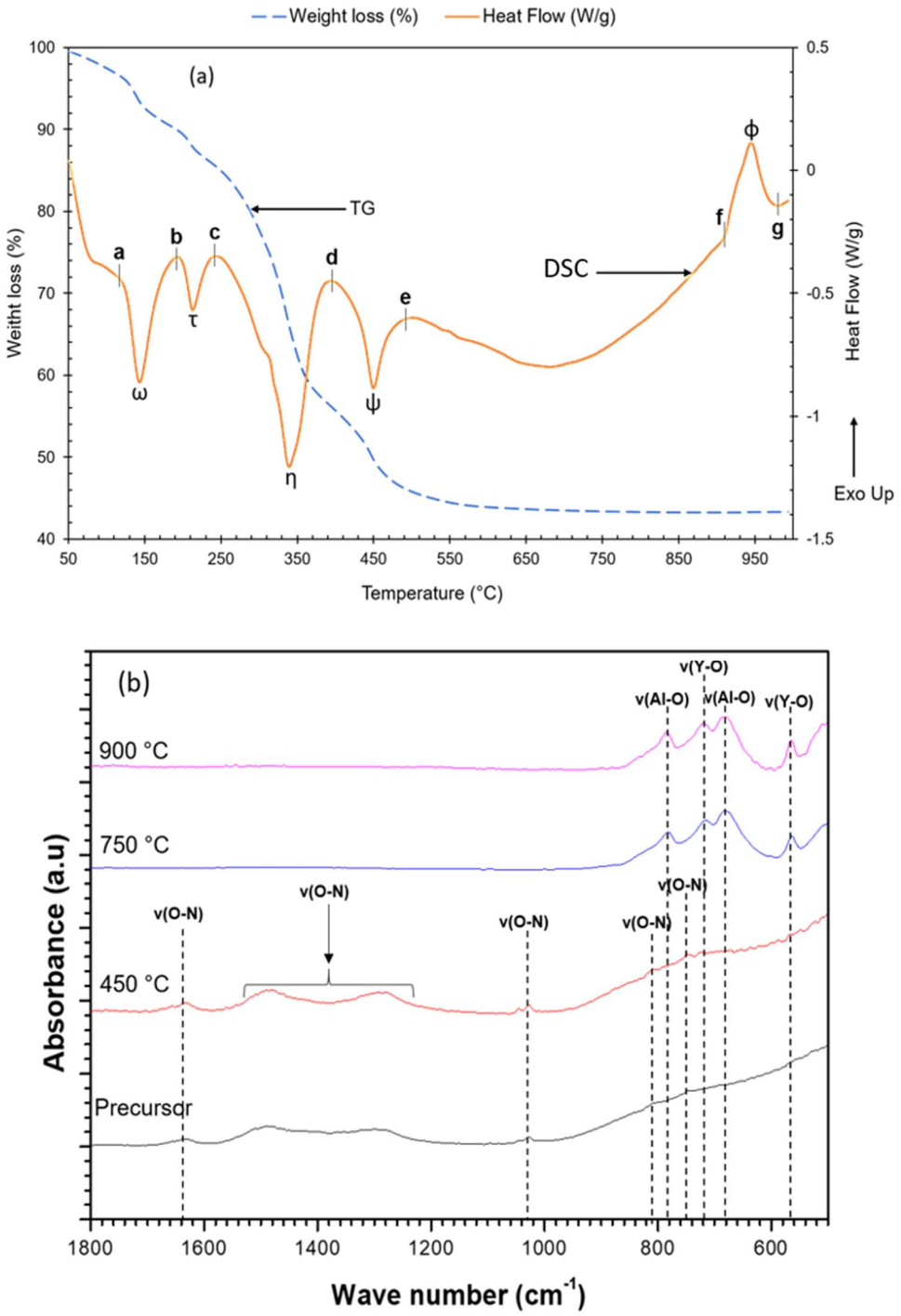

Figure 6-1: (a) Combined plot of the thermogravimetric (TG) and the differential scanning calorimetry (DSC) of the solution precursor showing percent water loss (56.19 %) from the sample, the endothermic peaks labelled as: ω, τ, η, and ψ in the temperature ranges marked (a–b, b–c, c–d, d–e) and the exothermic peak Φ in the temperature range f–g respectively. (b) FTIR spectra of the solution precursor and the sols calcined at different temperatures (450 °C, 750 °C and 900 °C)

Figure 6–2(a) and (b) show the XRD diffractograms of the calcined samples which decomposed on heating from room temperature to temperatures above 900 °C. The first stage of the calcination marked by the temperature of 450 °C constituted material loss stage during which water and evolution of gases occurred. During this stage no crystallization had occurred. The following stage at the temperature of 750 °C showed crystalline YAG phase is beginning to form with the emergence of the most prominent peak of the YAG phase—the peak (420) at the 2theta 33° position. However, the domination of amorphous phase in the first two stages of the calcination manifested as two broad humps stretching between 20°–40° 2θ for the first stage and 40°–70° 2θ for the intermediate stage. The calcination done at 900 °C, the final stage yielded crystalline samples identified as cubic YAG—the Rietveld refinement analysis of the XRD scan profile provides the crystallite size of the YAG to be 28±0.3 nm. The lack of crystallinity in the first and intermediate stages of the YAG formation made it unnecessary to analyze the XRD scan profiles of the two stages by Rietveld refinement.

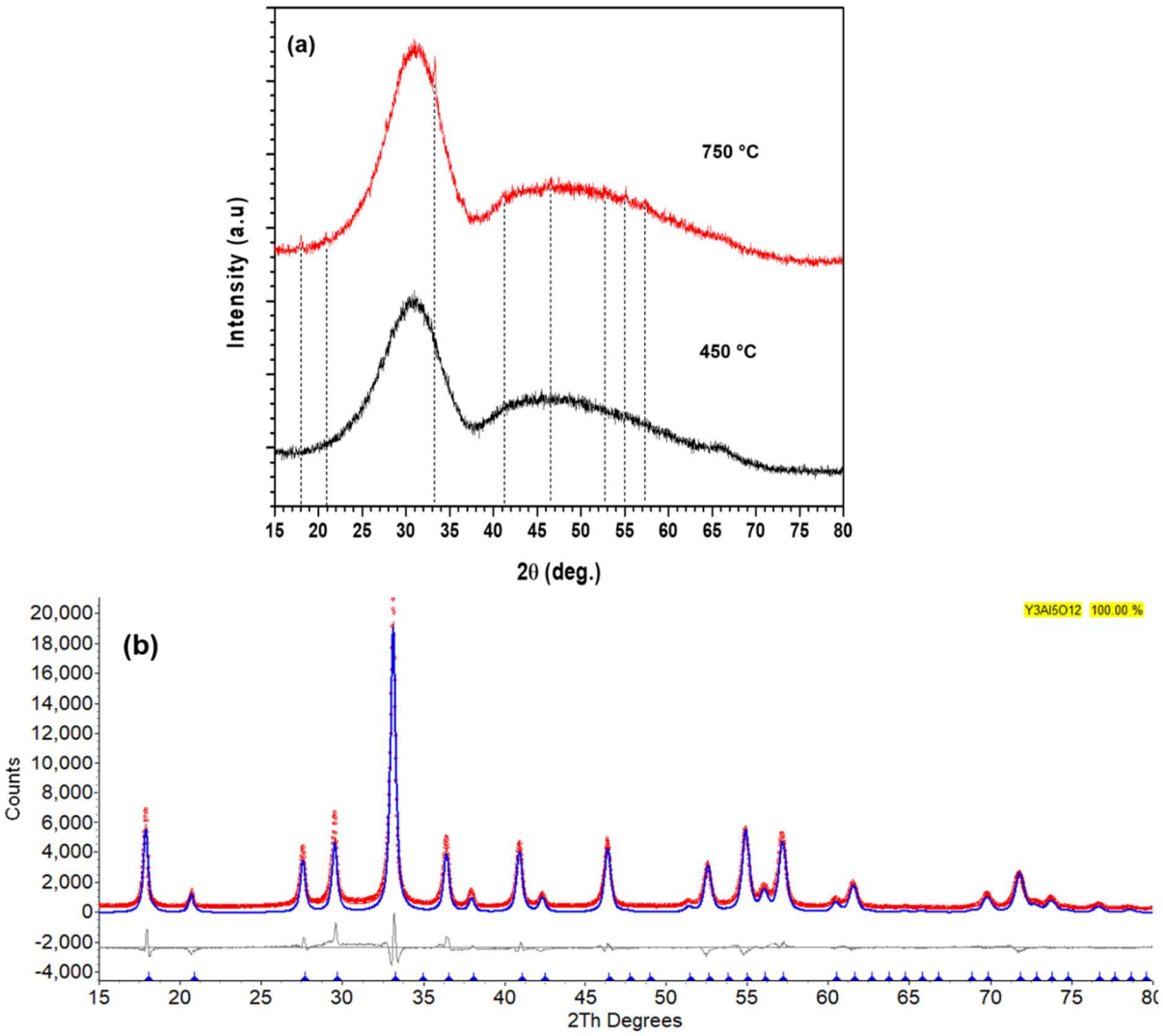

Figure 6-2: (a) XRD scan profile of precursor calcined at 450 °C and 750 °C—mostly amorphous (b) Rietveld refinement of the XRD scan profile of the precursor calcined at 900 °C showing crystalline phase composition—a pure YAG phase.

6.2 Microstructure and phase composition: feedstock and as-sprayed coatings

6.2.1 YAG powder from the as-received suspension

A typical SEM micrograph and particle size distribution curve for the YAG particles in the as-received YAG suspension are shown in Figure 6–3. The particles appear as agglomerates (Figure 6–3(a)), with the size of the constitutive particle in an agglomerate being ~100 nm, as shown in the inset. The particle size distribution in the as-received suspension is shown in Figure 6–3(b) depicting D_{10}, D_{50} and D_{90} to be 1.37 μm, 5.08 μm and 11.36 μm respectively. The D_{10} size meant 90 % of the particles in the suspension were larger than 1.37 μm; D50 meant half of the particles in the suspension have a size of 5.08 μm while the D90 size suggested that 10 % of the particles in the suspension were larger than 11.36 μm This particle size distributions confirm the YAG particles in the suspension were agglomerates.

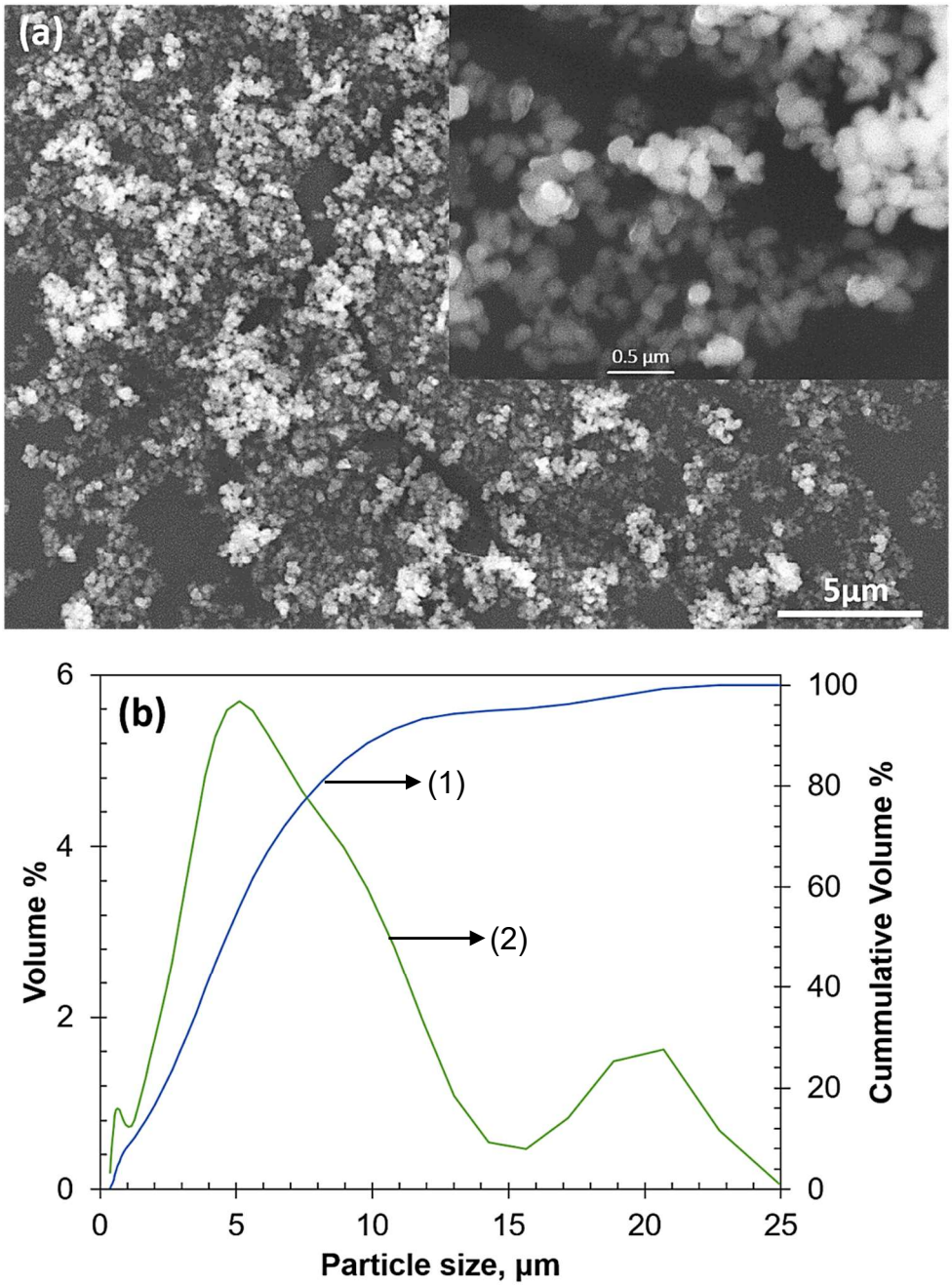

Figure 6-3: (a) SE SEM micrograph showing agglomerates of YAG particles dried out from the as-received suspension—the inset presents the higher magnification micrograph of the powder particles showing details of the particles in size and morphology (b) Particle size distribution of YAG particles in the as-received suspenion—the curve marked '1' is the cumulative volume % of the particle distribution, the one marked '2' is the volume % of the particle distribution

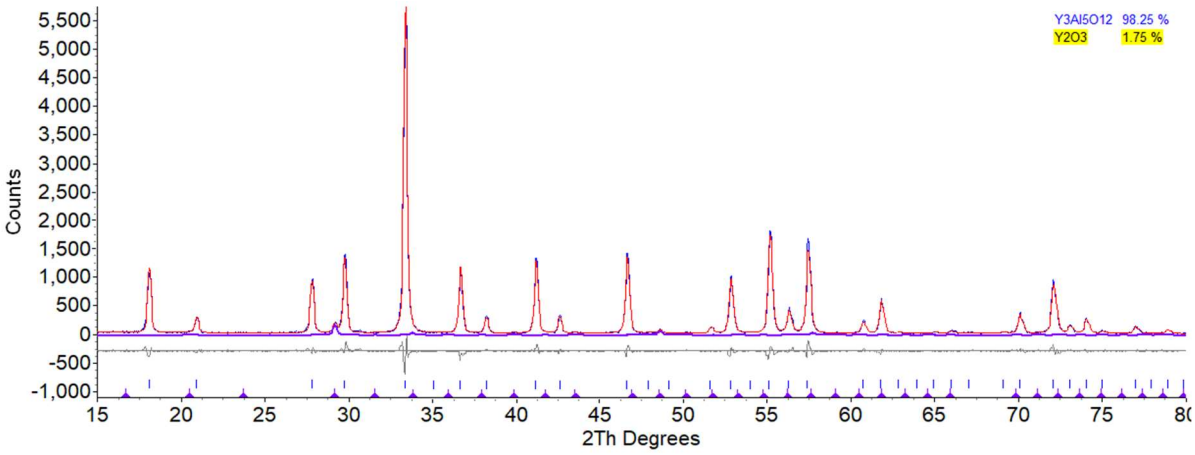

Figure 6-4: Rietveld refinement of the XRD scan profile of the box furnace dried powder from the as-received YAG suspension showing crystalline phase composition of YAG and Y_2O_3— Rietveld Analysis was done by Dr Zdenek Pala

The Rietveld refinement analysis of the powder from the as-received YAG suspension shows the presence of two crystalline phase compositions. The powder particles consist of ~98 % cubic YAG; the powder contains some Y_2O_3 impurities which makes the balance, as shown in the Figure 6–4. The crystallite size of the cubic YAG phase as analysed gives 92±5 nm.

6.2.2 Single splat study and the particle diagnostic features: S–YAG, SP–YAG and YSZ

The building blocks of thermal spray coatings are mostly splats; however, the results of the T1–YSZ coating presented in this thesis (see sub-section 5.1.2) shows a coating can as well be made of sintered particles. The SP-YAG and the S-YAG coatings consist of splats and lamellae as against the sintered particles in the YSZ coating. The SP-YAG splats collected onto a polished substrate from the single pass of the fast-traversed gun moving vertically across the length of the substrate are shown in Figure 6–5; the splats formed from molten particles into irregular morphology and varying sizes. The dominant morphology of the splats is the irregular ones; a few more of the

splats takes the elliptical and circular shape on visual inspection. In terms of the sizes, the irregular splats are bigger and well spread out to cover the surface of the substrate. The pile of the splats built dense lamellae with submicron and micron size intra-lamellar voids as in the fractograph shown in Figure 6–6.

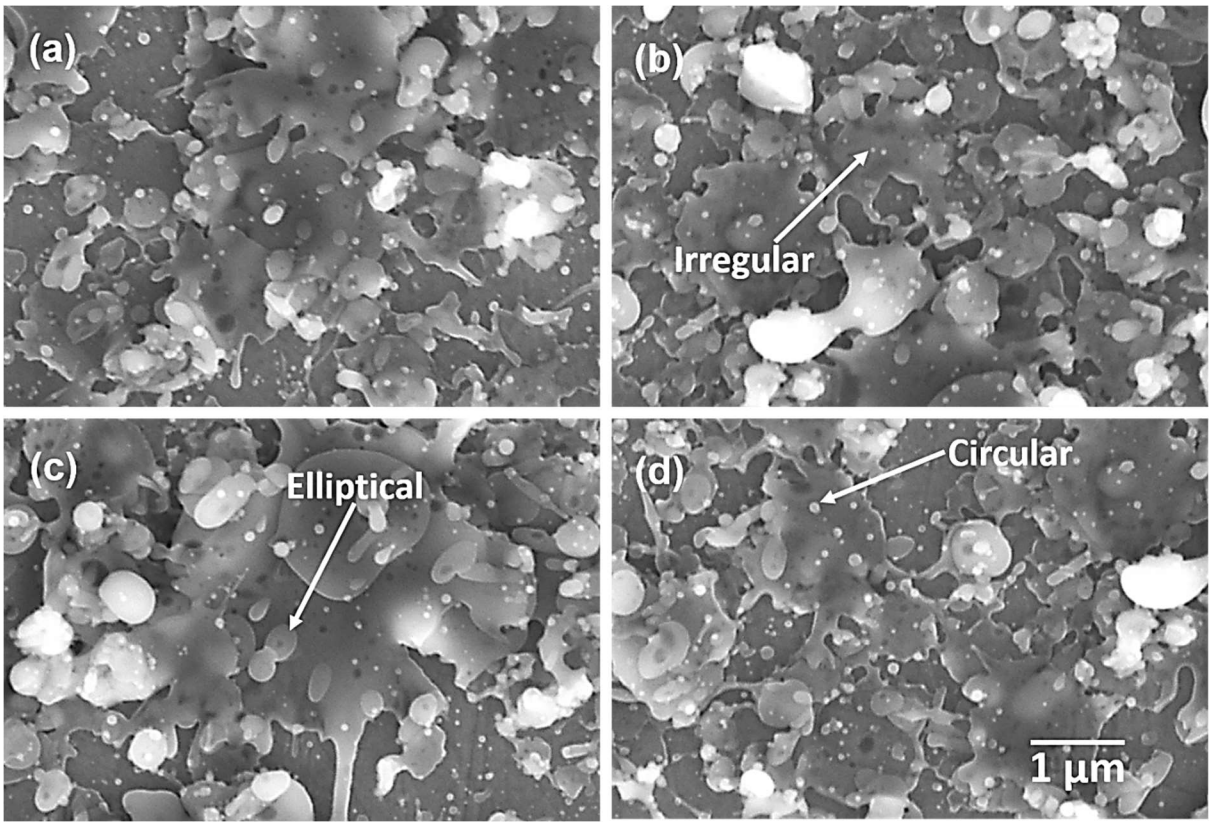

Figure 6-5: SE scanning electron micrograph of molten SP–YAG topcoat splats collected on polished AISI 304 stainless steel showing the splat morphology and spread after impact—the individual plate shows the diversity of the splats collected from the fast single swipe of the spray gun.

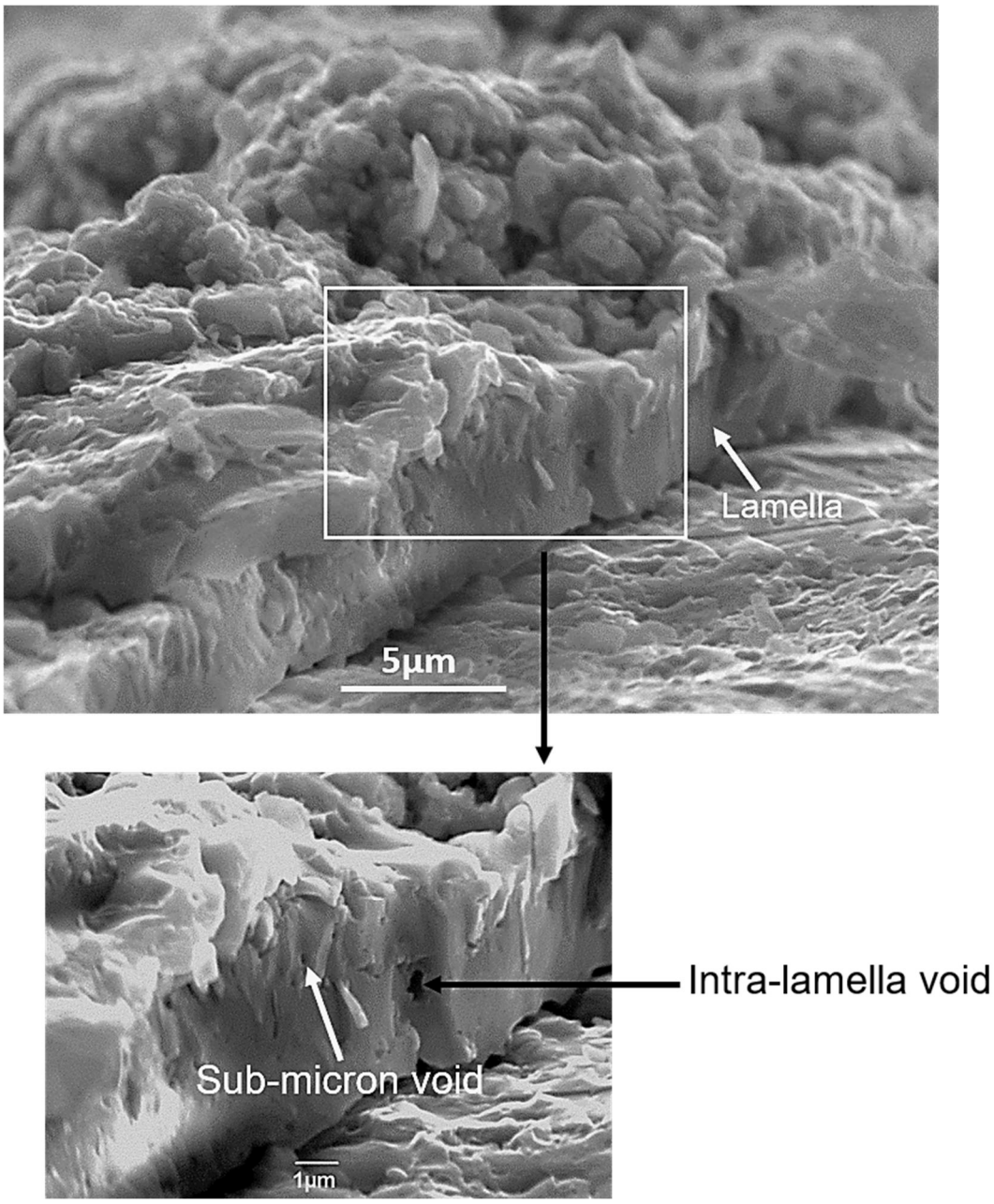

Figure 6-6: SE scanning electron fractograph of the SP–YAG topcoat showing lamella cross-section and intra-lamella void

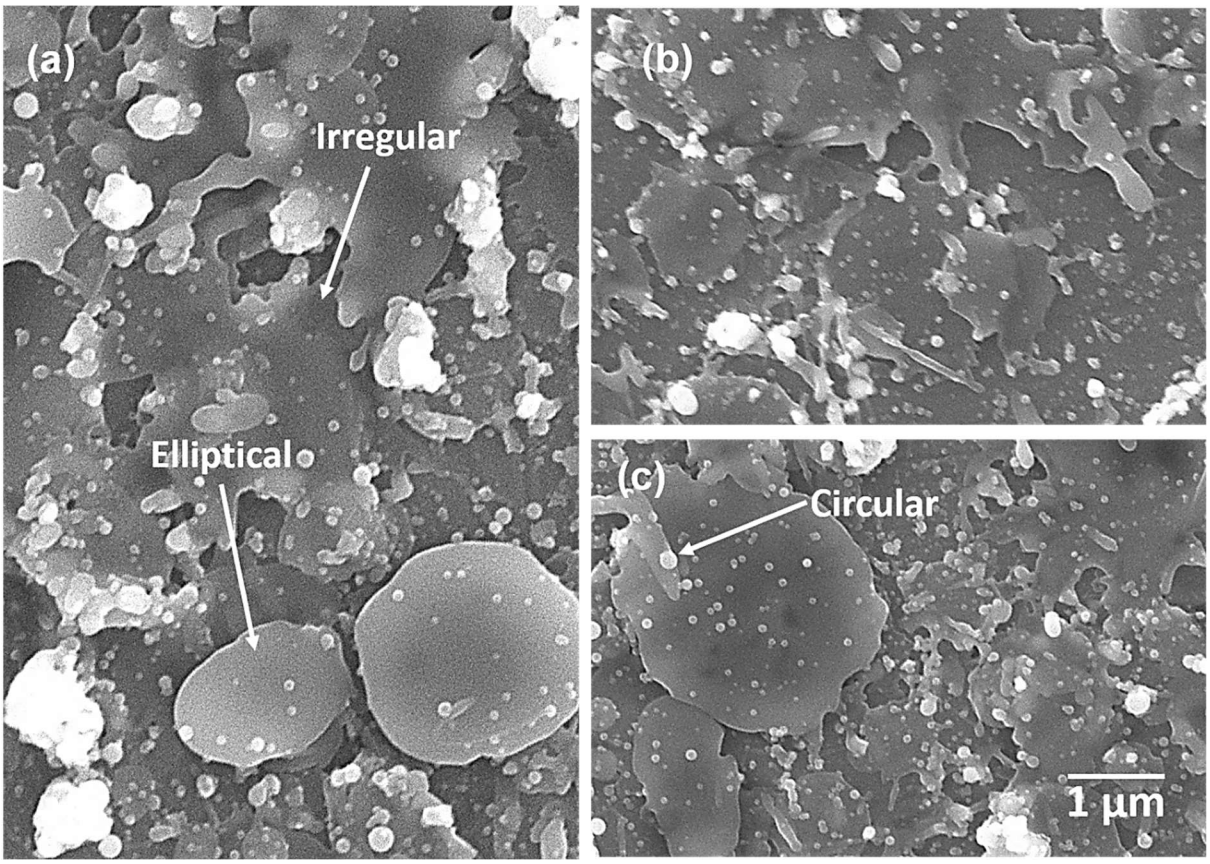

Figure 6-7: SE scanning electron micrograph of molten S–YAG topcoat splats collected on polished AISI 304 stainless steel showing the splat morphology and spread after impact—the individual plate shows the diversity of the splats collected from the fast single swipe of the spray gun.

Similarly, the S-YAG splats collected from the single pass of the gun are shown in Figure 6–7; molten particles impact the substrate to form splats of varying sizes and morphology. Three morphologies are identifiable by visual inspection from the scanning electron micrograph as shown: circular, elliptical, and the irregular. The circular splats make the most of the splats in number; the circular splats are mostly on the top face of the irregular splats. Most of the irregular splats laid in direct contact with the substrates with splashed edges which compliments the spread on the surface. Few of the splats takes the elliptical morphology with reduced spread compared to the irregular splats. As in the SP–YAG, the splats over laid on top of one another to build

dense lamellae with micron size intra-lamellar voids as shown on the fractograph presented in Figure 6–8. The lamella size of the S-YAG is ~ 25 µm as against ~ 5 µm in the SP-YAG.

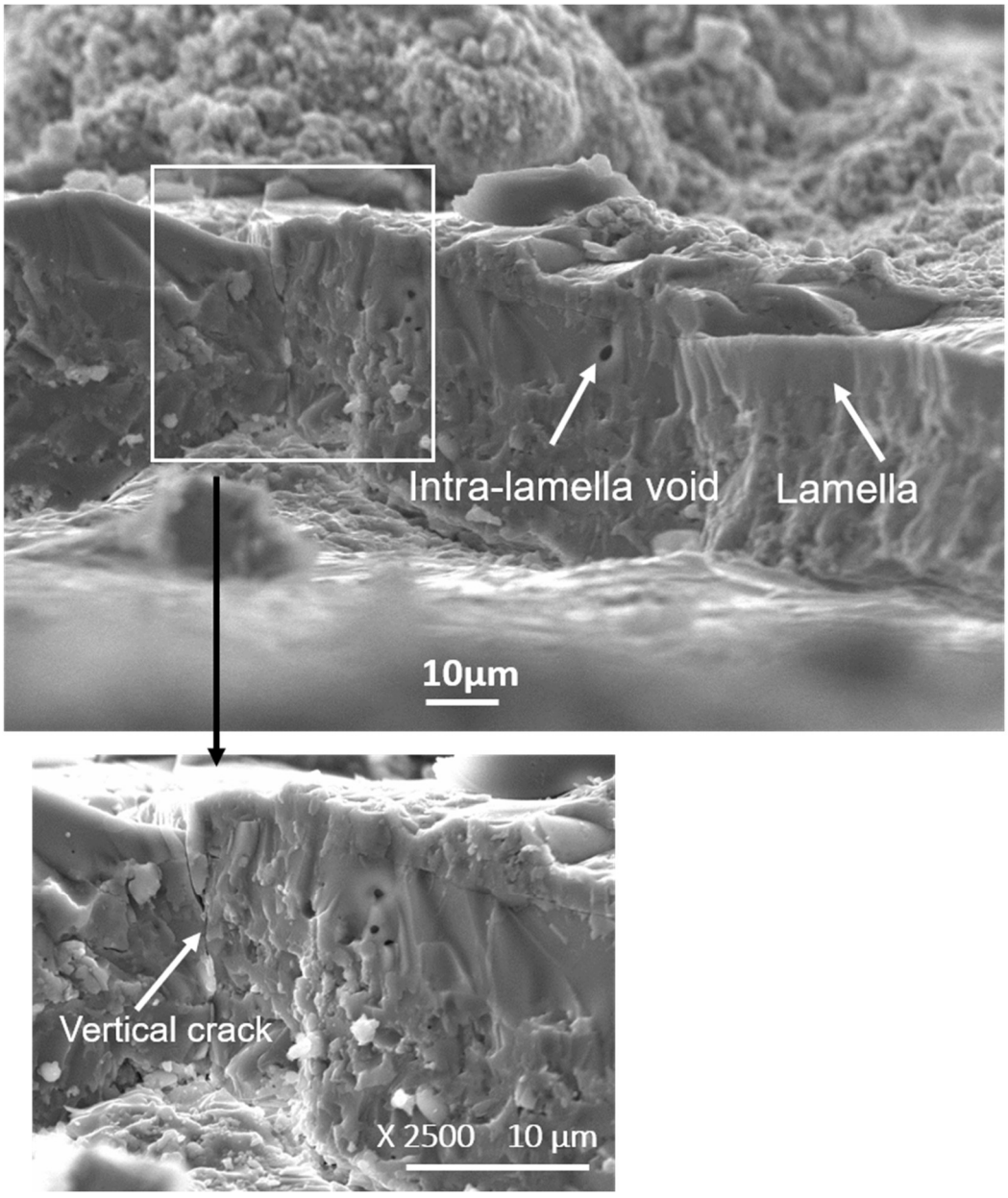

Figure 6-8: SE scanning electron fractograph of the S–YAG topcoat showing lamella cross-section and intra-lamella void

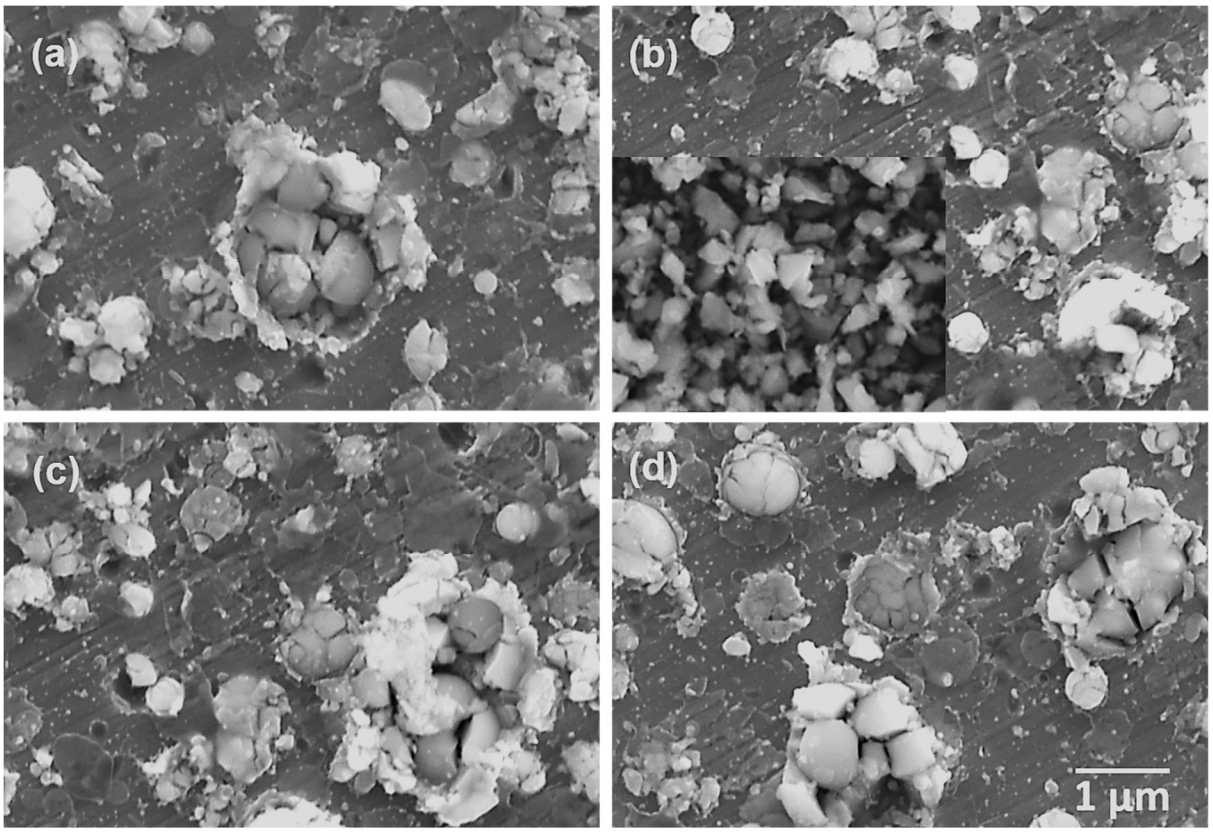

Figure 6-9: SE scanning electron micrograph of partly molten YSZ particles collected on polished AISI 304 stainless steel showing the particle morphology and sizes—the individual plate shows the diversity of the particles collected from the fast single swipe of the spray gun while the inset in (b) shows the as-received YSZ powder particles.

The clusters of YSZ particles collected onto polished AISI 304 stainless plate are shown in Figure 6–9. The morphology of the individual particles in the collected clusters is angular; it does not deviate from the morphology of the particles identified in the as received suspension of the YSZ shown in the inset of Figure 6–9 (b). The size of each cluster ranges from 0.5–2.5 µm; the individual particle in the big clusters matches the D_{50} of 0.6 µm PSD described in subsection 3.1 (Table 3–1). Each of the clusters also show fringes which appear as a thin molten layer that has burst due to the impact force upon landing on the substrate. The spread of the fringes is reduced; the extent of the spread around each cluster appears to be relative to the size of the clusters. The pile of the particle clusters makes the coating microstructure as shown

in the fractograph of the YSZ topcoat shown in Figure 6–10. This fractograph matches with the fractograph of the T1-YSZ presented in sub-section 5.1.2.

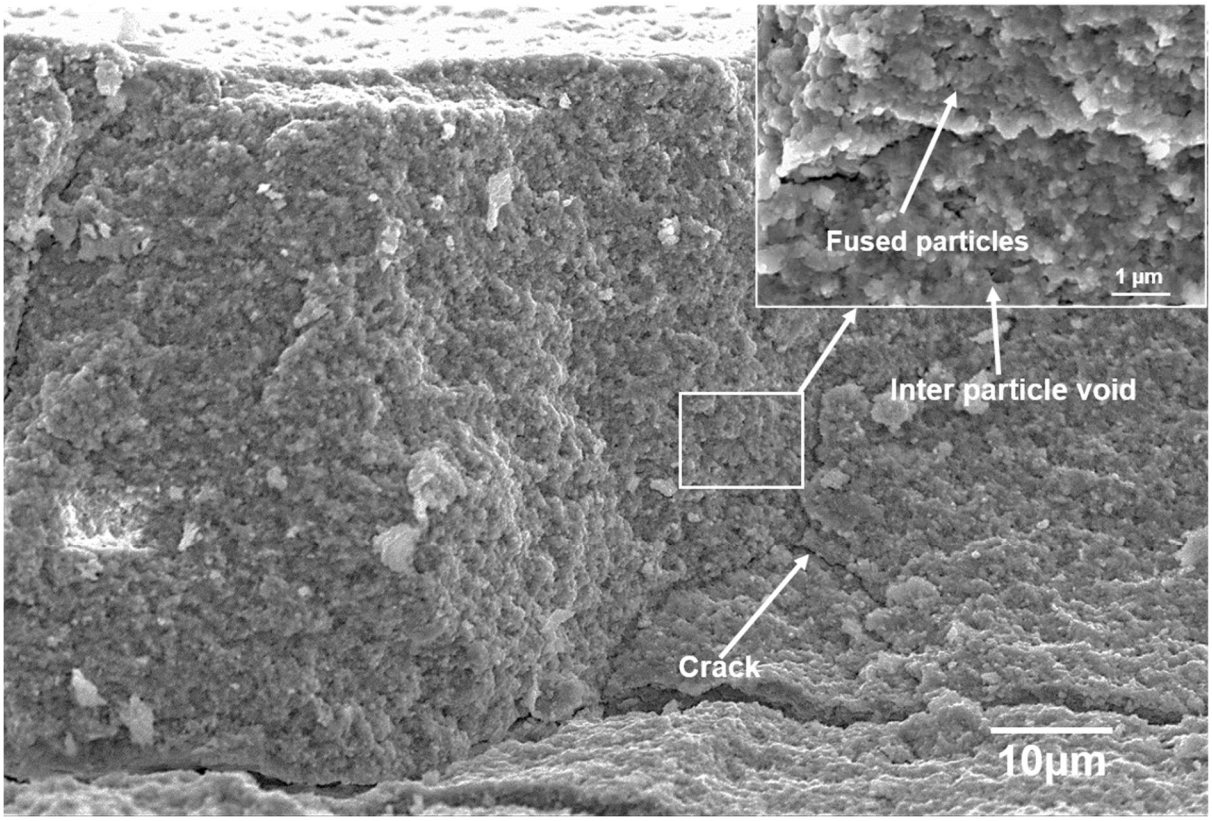

Figure 6-10: Fractograph showing fused particles, inter layer crack in the as–sprayed YSZ topcoat

6.2.2.1 In-flight particle diagnostics

The diagnostic features, temperature, and velocity, of the particles impacting the substrate to form the splats or as partly molten particles were measured at the same spray distance used in the deposition process for the respective coatings. The measurements were completed without the substrates to ensure free flow of the particles. The data as collected for the individual materials, SP–YAG, S–YAG and T1-YSZ are presented in Appendix B. The velocity and temperature values recorded represent the average for the particles in a control volume defined as 3.2 mm x 10 mm x 25 mm. Multiple measurements (~60) were taken at a reaction time of 5s. Each

temperature and velocity measurement taken will have an associated measurement error ±3 % to account for the uncertainties in the coating deposition process. The particle temperature and the associated velocity for each of the topcoats are shown in Table 6-1; the associated errors are due to the accuracy of the instrument, as presented in sub-section 3.3.1. The uncertainties associated with the temperature values are ± 48 °C and ± 64 °C while for the velocity values, the uncertainties come to ± 25 m/s and ± 28 m/s for the SP–YAG and the S–YAG respectively. The temperature and the velocity of the YSZ particles were measured to be 2683 ± 80 °C and 1156 ± 35 m/s respectively. The upper limit of the temperature puts the particles temperature above the ~2700 °C melting point for YSZ while the lower limit suggests the particles could not have melt at temperature difference of ~100 °C to the melting point. In addition, the in-flight velocity of the particles suggests the resident time of the particles inflight precludes the possibility of melting. This further supports why the YSZ coating presents as a pile sintered particles.

Table 6-1: In-flight particle diagnostics

S/N	Topcoats	Temperature, °C	Velocity, m/s
1.	SP–YAG	1612 ± 48	843 ± 25
2.	S–YAG	2132 ± 64	933 ± 28
3.	YSZ	2683 ± 80	1156 ± 35

6.2.3 SP–YAG and S–YAG topcoats

This section presents the top surface morphologies of the two YAG coatings as shown in Figure 6–11. The common feature of the two coatings consists of randomly distributed bumps throughout the spread of their surfaces; the planner view of the bumps shows like the top of a cauliflower. The bumps on the SP–YAG coating (Figure 6–11(a)) appear smaller compared to those on the S–YAG coating (Figure 6–11(b)). The magnified view of the bumps on each of the two coatings are shown as insets; each one presents clusters of particles. Each of the clusters on the SP–YAG surface could be piles of formed particles from the solution precursor or resolidified or unmolten YAG particles in the case of the S–YAG.

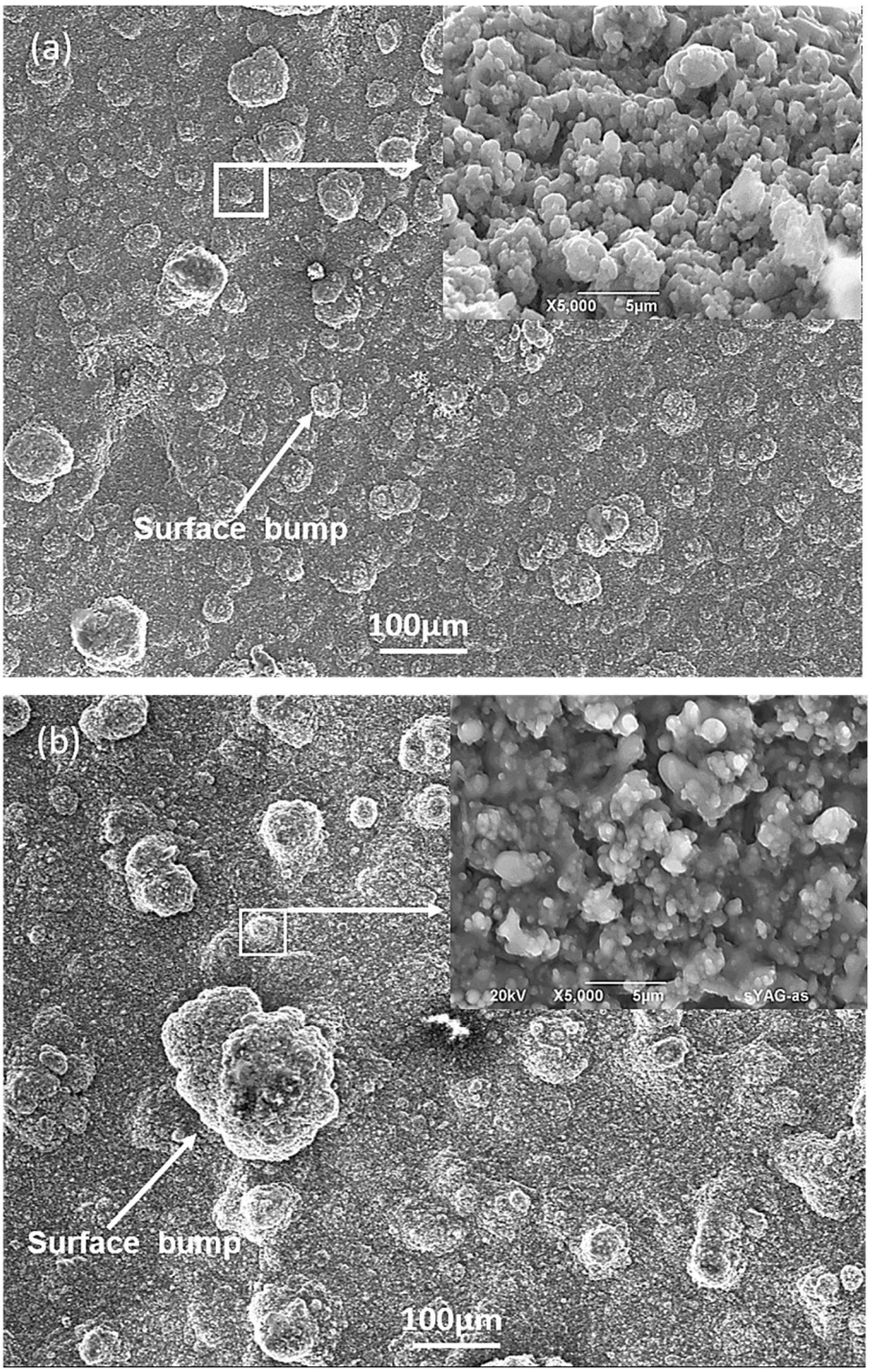

Figure 6-11: (a) SE scanning electron micrograph showing surface morphology of SP-YAG topcoat with randomly distributed bumps (b) SE scanning electron micrograph showing surface morphology of S-YAG topcoat with randomly distributed bumps.

The BSE micrographs of the cross section of the two coatings are shown in Figure 6–12. The micrograph of the SP-YAG coating in Figure 6–12(a) shows the three layers of the TBC system: the SP-YAG topcoat, the MCrAlY bond coat and the Ni-super alloy substrate. The SP-YAG topcoat has a thickness of 33 ± 1 μm; the higher magnified image in Figure 6–12(b) shows randomly distributed pores, inter splat boundaries and it shows no crack nor delamination at the interface with the bond coat. Figure 6–13 shows the micrograph of the as-sprayed S-YAG topcoat on the MCrAlY bond coat laid on the Ni-superalloy substrate. The topcoat microstructural features present inter-splat boundaries, pores, vertical and horizontal micro cracks. The S-YAG topcoat has a thickness of 139 ± 4 μm, showing good interface adhesion with the bond coat with no observable crack nor delamination.

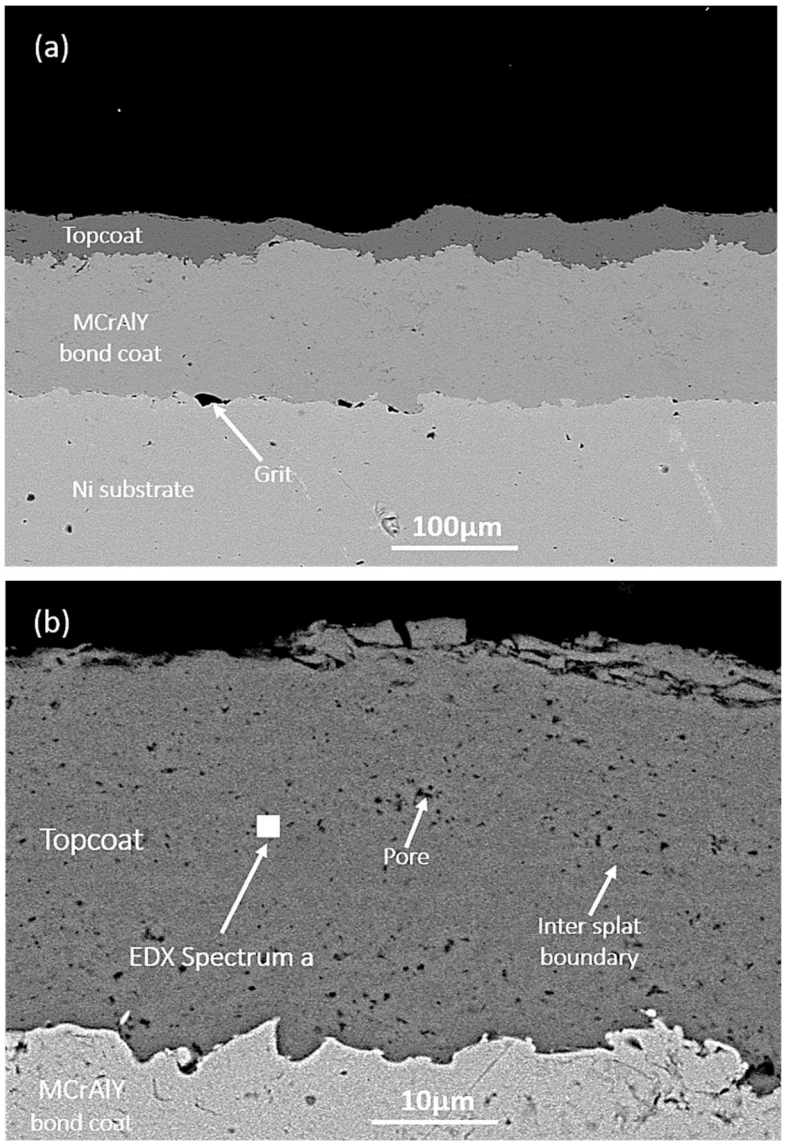

Figure 6-12: (a) Back scattered electron (BSE) scanning electron micrograph showing the cross section of as-sprayed SP-YAG topcoat on bond coated nickel (Ni) substrate with a white square dot designating the EDX spectrum collection spot a (see Table 6-2) (b) higher magnification of the SP-YAG topcoat showing pores, inter splat boundary and the interface with the MCrAlY bond coat.

Table 6-2: EDX analysis of the atomic % of Al, O, and Y in the as-sprayed SP-YAG and S-YAG topcoats; the EDX collection areas are marked in Figure 6–12 and 6–13

Elements	Topcoat samples	
	SP-YAG (spectrum a)	S-YAG (spectrum b)
O	60.2	61.3
Al	23.4	22.7
Y	16.4	16.0
	100.0	100.0

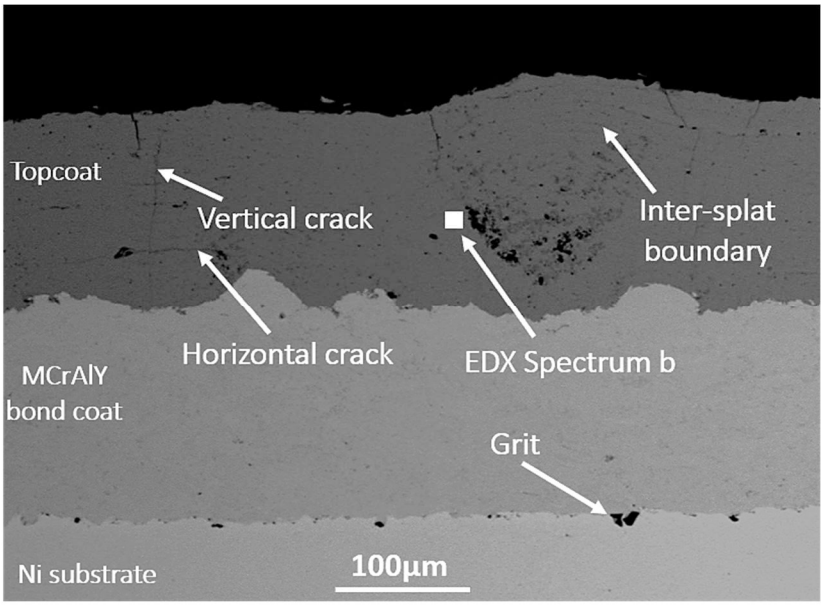

Figure 6-13: Back scattered electron (BSE) scanning electron micrograph showing the cross section of as-sprayed S-YAG topcoat on bond coated nickel (Ni) substrate with a white square dot designating the EDX spectrum collection spot b, pores, vertical and horizontal cracks, inter splat boundary and the interface of the S-YAG topcoat with the MCrAlY bond coat.

A check on whether the YAG produced from the solution precursor matches the YAG sprayed from the commercially sourced YAG suspension was done through elemental composition analysis. The two coatings were analysed to compare the three major elements in the yttrium-aluminium system (Al, Y, and O) based on its structural formula— $Y_xAl_qAl_mO_n$. The elemental composition analysis of the SP-YAG (Figure 6–11(b)) and S-YAG (Figure 6–12) topcoats show the two coatings consist of the same elements and in the same proportion by atomic wight percent as presented in Table 6–2. The carbon signal from the carbon coating of the samples was excluded from the analysis.

6.2.4 YSZ topcoat

The as-sprayed YSZ topcoat presented here is the T1-YSZ named in sub-section 3.3. ; a visual inspection of the top surface of the YSZ topcoat shown in Figure 6–14(a) reveals the distribution of bumps throughout the entire surface of the coating. The bumps in this case were more regular and less pronounced compared to those identified on the two YAG coatings. The magnified view of the bumps shown as inset provides that the bumps consist of fused particles; this is consistent with what has already been shown in sub-section 6.2.2 that the building block for the YSZ coating consist of partially molten particles. The surface morphology as shown for the YSZ topcoat matches the T1-YSZ coating presented in Chapter 5; the feedstock used for the deposition was the same, but the difference was the spray parameters implemented. The variation of spray parameter was part of an experiment to ascertain the optimized deposition parameters for YSZ suspension sprayed with HVOF spray technique.

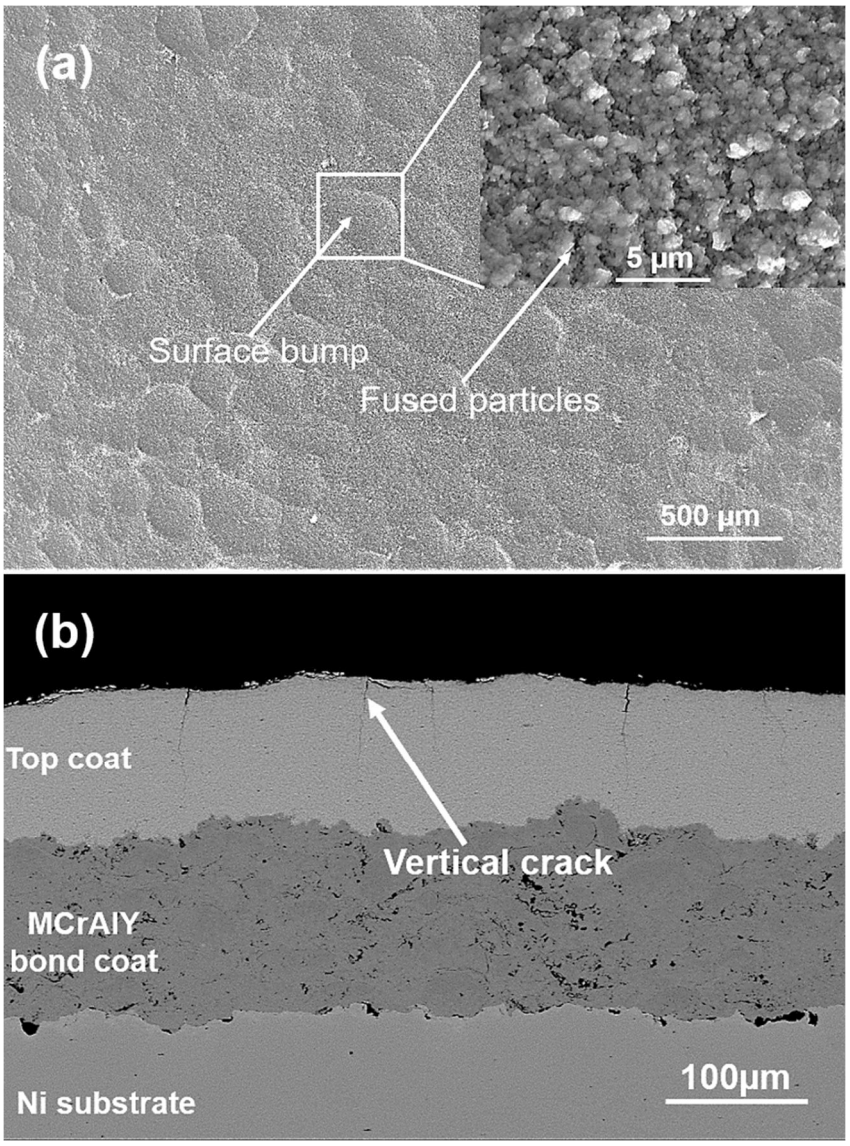

Figure 6-14: SE micrograph of the top surface morphology of the YSZ topcoat showing surface bumps and fused particles (b) BSE micrograph of the cross-section of the YSZ topcoat on bond coated nickel (Ni) substrate showing vertical cracks

The micrograph showing the cross section of a coating provides information about the coating thickness in addition to observable defects. The YSZ topcoat shown in figure 6–14 has no interlayer defect at the boundary with the underlying bond coat. The obvious defect as shown on the cross section is the vertical crack which extends from the top of the coating to a depth of ~30 µm. The thickness of the topcoat is measured to be 107 ± 5 µm.

6.2.5 Phase composition in the topcoats due to deposition process

Phase transformation is a usual phenomenon identified with materials processed with thermal spray techniques. The transformation could be from crystalline to amorphous where melting of the feedstock occurs; it may as well be from one crystalline phase to another where the material involved exhibit polymorphism. The materials presented here, YAG and YSZ, both have more than one polymorph. Rietveld refinement analysis of the XRD scan of the coatings SP-YAG, S-YAG and YSZ was performed to identify and quantify the phase compositions of the respective coatings because of the deposition process. The analysis on the XRD scan of the SP-YAG and the S-YAG coating top surface was done to tell if in addition to YAG there are more contributors from the Al-Y-O family, $AlYO_3$ (YAP) and $Y_4Al_4O_9$ (YAM), in the as-sprayed topcoats. It is also possible to have one or both of Al_2O_3 (aluminium oxide) and Y_2O_3 (yttrium oxide) in a case of inhomogeneous decomposition of the solution precursor [116]. The results of the analysis are shown in Figure 6–15(a) and (b)). The SP-YAG coating has ~10 wt. % crystallinity; the remaining amorphous contents makes the balance, which forms the bulk of the coating. This the reason for the two amorphous humps in the XRD scan profile (Figure 6–15(a)) with the peaks at ~32.0° and ~47.5° 2θ, respectively. The S-YAG coating (Figure 6-15(b)) on the other hand has ~12 % crystallinity; its amorphous humps have peaks at ~31.5° and ~48.9° 2θ, respectively. The crystalline contents of the SP-YAG coating present ~23% less YAG ($Y_3Al_5O_{12}$) compared to the S–YAG and ~17% more of hexagonal YAP ($AlYO_3$) than was quantified in the S–YAG. The crystallite sizes in the two YAG coatings also vary; the SP-YAG has crystallite size of 72±8 nm compared to 53±5 nm in the S-YAG. The crystallite size of the S-YAG has reduced after the deposition process; this is in

comparison to the 92±5 nm crystallite size of the as-received YAG particles which is very close to the 100 nm estimate for the individual particles in the agglomerates identified in the SEM micrograph of the particles.

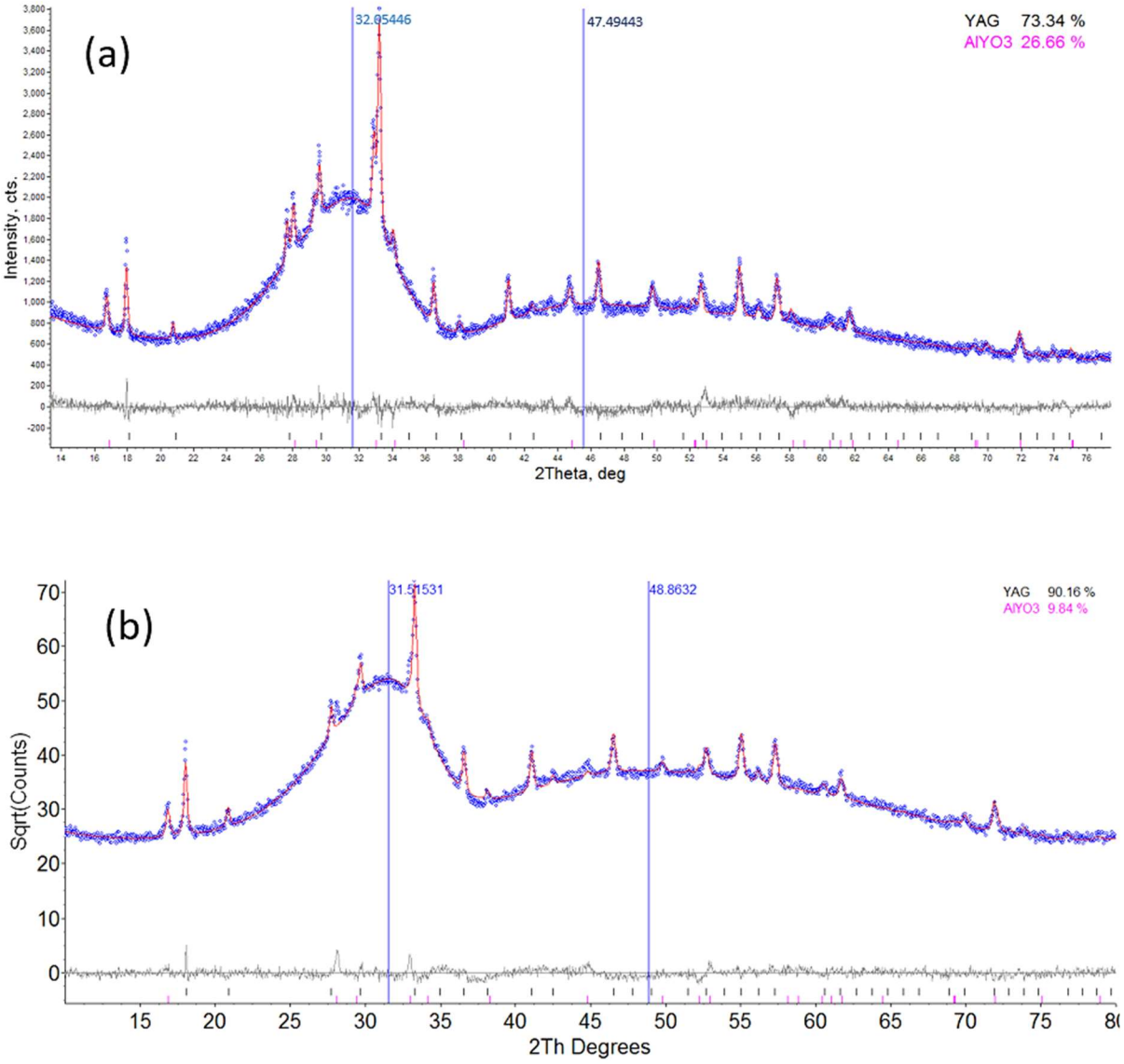

Figure 6-15: Rietveld refinement profile of the XRD scan of the as-sprayed (a) SP-YAG topcoat (b) S-YAG topcoat deposited onto MCrAlY bond coat; each showing amorphous humps and two crystalline phase compositions with varying proportions—Rietveld analysis was done by Dr Zdenek Pala.

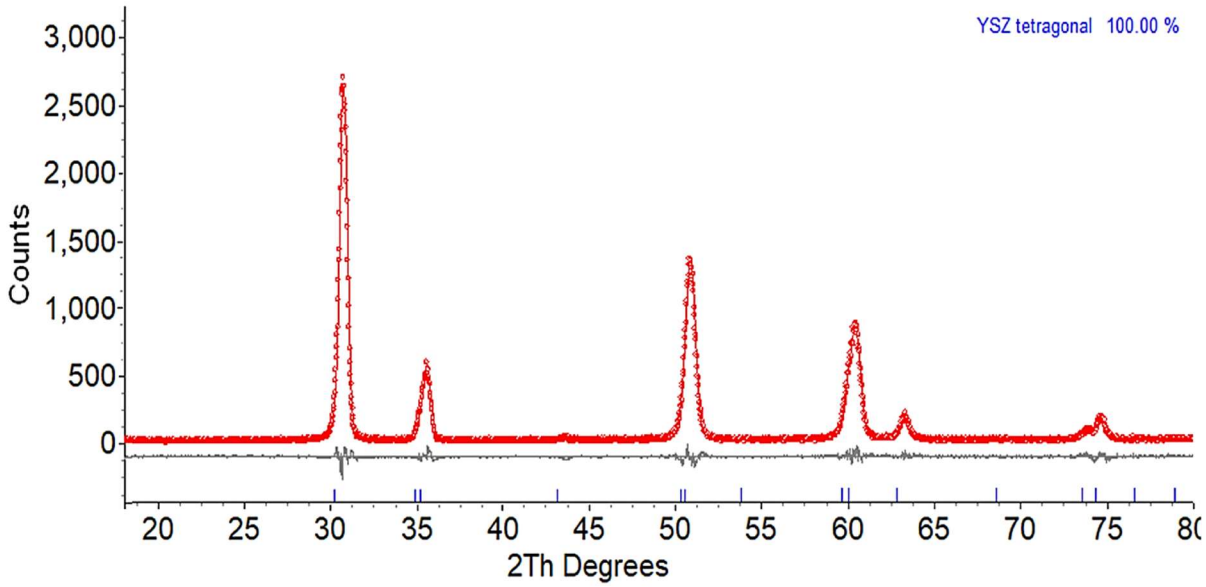

Figure 6-16: Rietveld refinement profile of the XRD scan of the as-sprayed YSZ topcoat showing total tetragonal phase transformation—Rietveld analysis was done by Dr Mingwen Bai.

The phase composition of the YSZ topcoat (se Figure 6-16) consists of a single phase despite the dual phase contained in the starting feedstock—monoclinic 25 % and tetragonal ~75 %. The only phase in the YSZ topcoat in its as-sprayed form is the tetragonal polymorph; the crystallite size calculated for the single phase is 72 ± 2 nm. The crystallite size in this as-sprayed coating is larger than the respective sizes of the monoclinic (28 ± 5 nm) and the tetragonal (14 ± 0.3 nm) phase in the feedstock.

6.3 Thermal conductivity of ceramic topcoats: SP-YAG, S-YAG and T2-YSZ

The thermal conductivities of the respective topcoat ceramics were obtained by double layer approach detailed in subsection 3.5.1; in this case, the double layer consists of the ceramic topcoat on AISI 304 substrate [252]. The thermal conductivity of the topcoat was calculated from the thermal conductivity of the composites using Equation 3.17. The composite conductivity varies with the individual topcoats on the substrate. For the composite of SP-YAG coating on the substrate AISI 304, the thermal

conductivity was ~ 6.7 W/m*K at 25 °C; it rose to ~19.4 W/m*K at 1000 °C. For the AISI 304 coated with S-YAG, the conductivity was ~ 0.6 W/m*K and ~1.7 W/m*K at 25 °C and 1000 °C respectively; it was ~7.6 W/m*K and ~17.5 W/m*K at 25 °C and 1000 °C respectively for the composite of the T2-YSZ on the substrate. The thermal conductivity data of the three topcoats on AISI 304 is presented in detail in Appendix D. The calculated thermal conductivity based on Equation 3.17 for the three topcoats, SP-YAG coating, S-YAG coating and the T2-YSZ coating layers without the substrate contribution are shown in Figure 6–17. The conductivity of each of the three topcoats layer was less than 1.0 W/m*K at 25 °C; at the 1000 °C temperature, only the SP–YAG remained below 1.0 W/m*K. The S-YAG topcoats had its thermal conductivity reached ~1.7 W/m*K at the 1000 °C while the T2-YSZ topcoat layer showed increased thermal conductivity at the 1000 °C temperature reached ~2.0 W/m*K; for each of the S-YAG and the T2-YSZ, the increment was about 300% from 25 °C to 1000 °C.

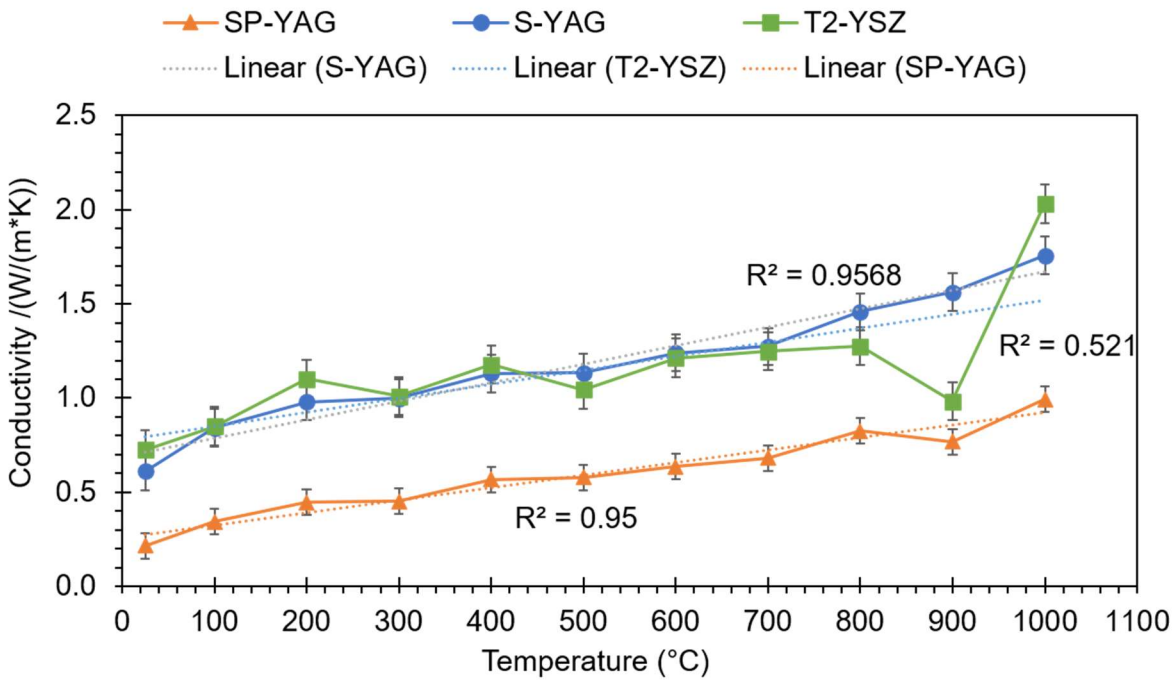

Figure 6-17: Thermal conductivity of the three ceramic topcoats plotted against temperature from 25 °C to 1000 °C—see Table 25 in Appendix E for the 95 % confidence level of the mean of the data sets.

6.4 Microstructure and phase transformation due to thermal cycling

6.4.1 Microstructure of thermal cycled ceramic topcoats

Each of the TBC samples were subjected to hundred 80-minute thermal fatigue cycles for evaluation performance; a cycle consists of a ramp up to 1100 °C and holding at the elevated temperature before it was forced cooled to near room temperature to complete a cycle. The cross section of the thermally cycled SP-YAG and S-YAG are shown in Figure 6–18(a) and (b) respectively. The cross section of the sample with the SP-YAG topcoat in Figure 6–18(a) shows regions of partial and total topcoat spallation, the TGO layer and EDX spectra collection point (see Table 6–2). The EDX spectrum of the partial spallation region marked ‘1’ shows Al, O, and Y as its main compositional elements with traces of Cr (0.3 %) and Ni (0.2 %). The spectrum

designated by 2 shows the elemental distribution in the bond coat layer after the thermal cycling. The magnified view of a partial spallation region is shown as an inset. The inset shows horizontal micro cracks that run between the topcoat and TGO layer (~8 μm in thickness) and from the TGO into the topcoat layer. The inset also shows an internal oxidation site and an additional brighter region above the TGO layer with an EDX spectrum spot marked ‘3’.

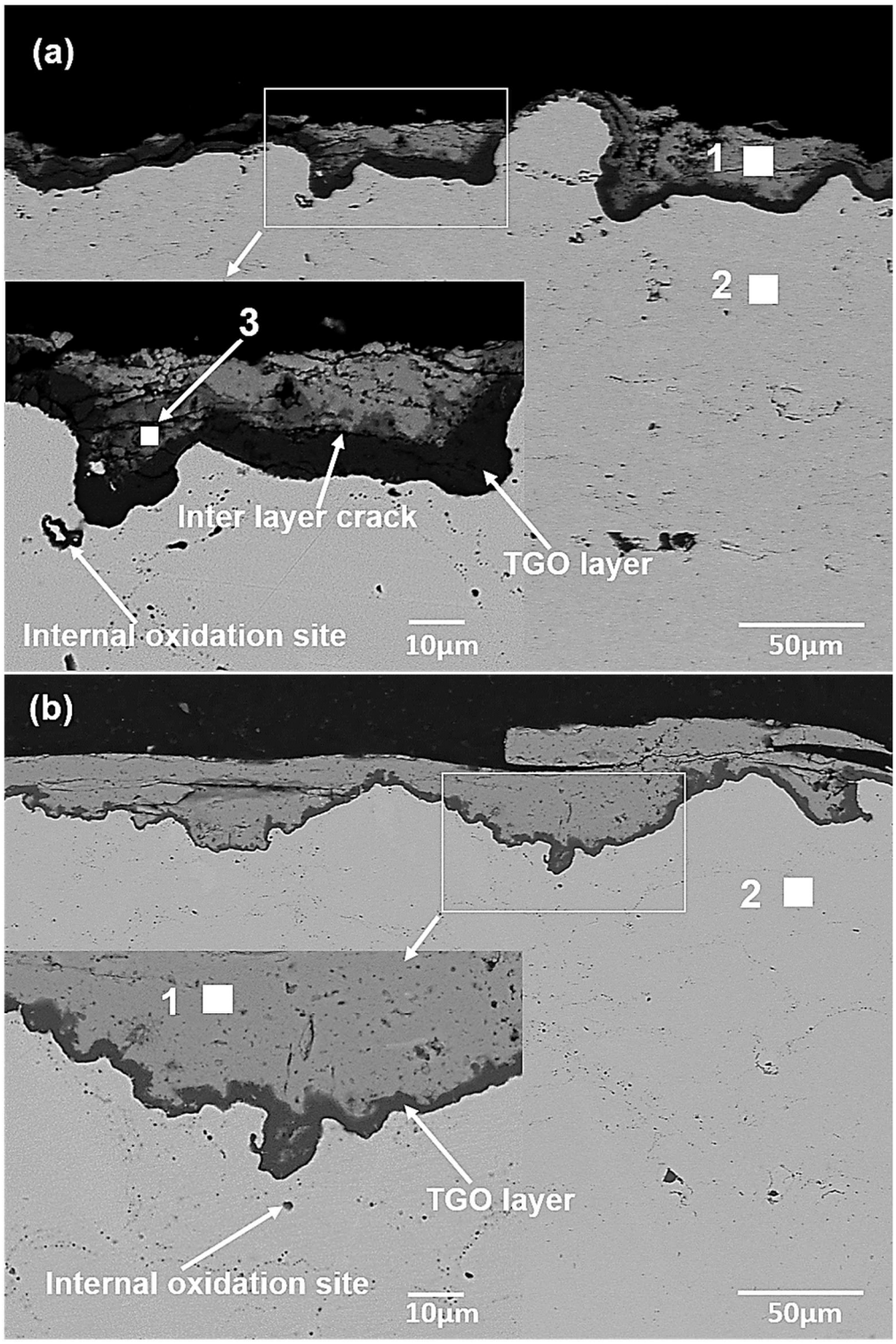

Figure 6-18: BSE scanning electron micrograph showing the cross section of (a) thermally cycled SP–YAG topcoat (b) thermally cycled S–YAG topcoat respectively with the TGO layer and white square dots representing EDX spectrum collection spots (1,2, and 3 see Table 6–3)

Table 6-3: EDX analysis on the cross section of the thermally cycled TBC samples showing atomic % of elemental composition

Elements	SP-YAG spectra			S–YAG spectra		T2–YSZ	
	1	2	3	1	2	2	3
O	66.6	–	69.7	61.5	–	–	58.7
Al	19.5	8.9	19.1	22.7	10.8	8.0	24.8
Y	13.4	–	2.8	15.8	–	–	–
Ti	–	0.9	–	–	0.6	0.6	–
Cr	0.3	22.2	2.0	–	21.7	23.9	3.4
Co	–	29.9	3.8	–	31.0	33.5	7.6
Ni	0.2	37.0	2.5	–	35.9	34.0	5.5
Mo	–	1.1		–	–	–	–
Total	100.0	100.0	100.0	100.0	100.0	100.0	100.0

Figure 6–18(b) shows the cross section of the sample with the S-YAG topcoat. It presents partial topcoat spallation region with intra layer micro cracks running parallel to the top, the TGO layer and EDX spectra collection points (see Table 6–3). The EDX spectrum of the partial spallation region marked ‘1’ shows only Al, O, and Y as its compositional elements. The magnified view of a partial spallation region is shown as an inset; it shows an internal oxidation site, the TGO layer (~3 μm in thickness), and micro pores.

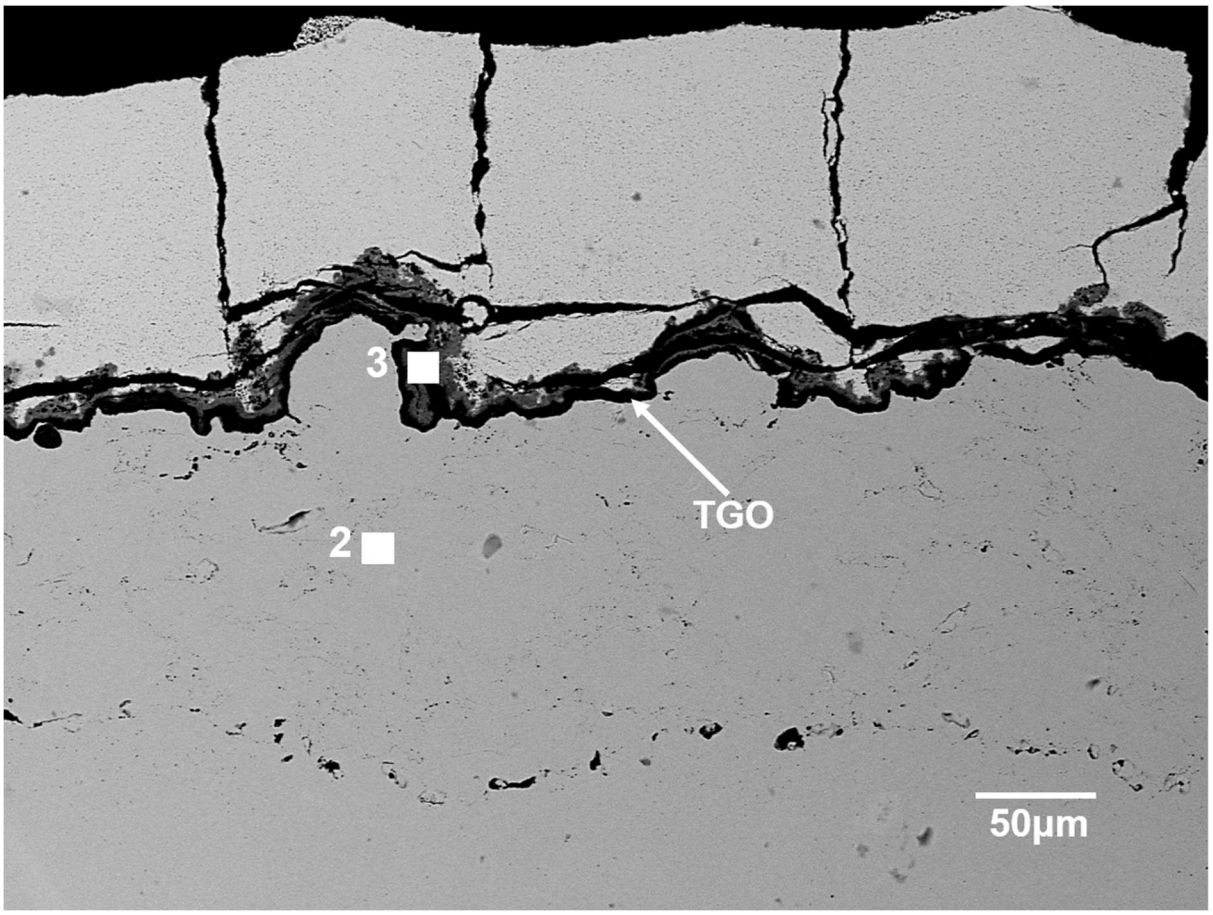

Figure 6-19: BSE scanning electron micrograph showing the cross section of thermally cycled T2-YSZ topcoat with the TGO layer and white square dots representing EDX spectrum collection spots (2 and 3, see Table 6–3).

The response of the T2-YSZ coating to the thermal cycling process was different from those of the two YAG topcoats. The micrograph of the thermal cycled T2-YSZ coating presents different features to the microstructure of the two YAG coatings after thermal cycling. The topcoat remains on the bond coat, as shown in Figure 6–19 although with identified cracks and the growth of the TGO. The delamination of the topcoat from the bond coat initiates from within the mixed oxide layer above the TGO layer. The failure of the topcoat was accompanied by linked vertical and horizontal cracks. The EDX analysis of the brighter layer (spectrum 3, see Table 6–3) above the TGO shows the presence of oxygen in addition to elements from the bond coat; the composition of the

layer fits the description of mixed oxides identifiable in thermally cycled TBCs. The remaining spectrum (marked 2) shows only metals without any contribution from oxygen.

6.4.2 Phase transformation of the coatings due to thermal cycling

Phase transition results from post spray heat treatment of thermal spray coatings; in this case, the amorphous contents of the two YAG topcoats became crystalline while the T2-YSZ topcoat experienced whole or partial transition from tetragonal phase to monoclinic phase at the thermal cycling dwell temperature of 1100 °C. The quantitative analysis of the resulting crystalline phase was obtained with the Rietveld refinement profile of the XRD scan of the thermally cycled topcoats. The analysed XRD profiles for the YAG topcoats are shown in Figure 6–20(a) and (b). The two YAG coatings show amorphous to crystalline transition as the amorphous humps at the 2θ positions of ~32.0° and ~47.5° 2θ in the SP-YAG and at the ~31.5° and ~48.9° 2θ position in the S-YAG got replaced with crystalline peaks; the same phase compositions were identified in the two coatings although to varying percentage quantities. The SP-YAG topcoat shows ~6% more corundum (alpha Al_2O_3) than found in the S–YAG, ~9 % more of spinel and ~1 % more of FCC cobalt. The S-YAG however, contains ~15% more of crystalline YAG than the SP-YAG topcoat.

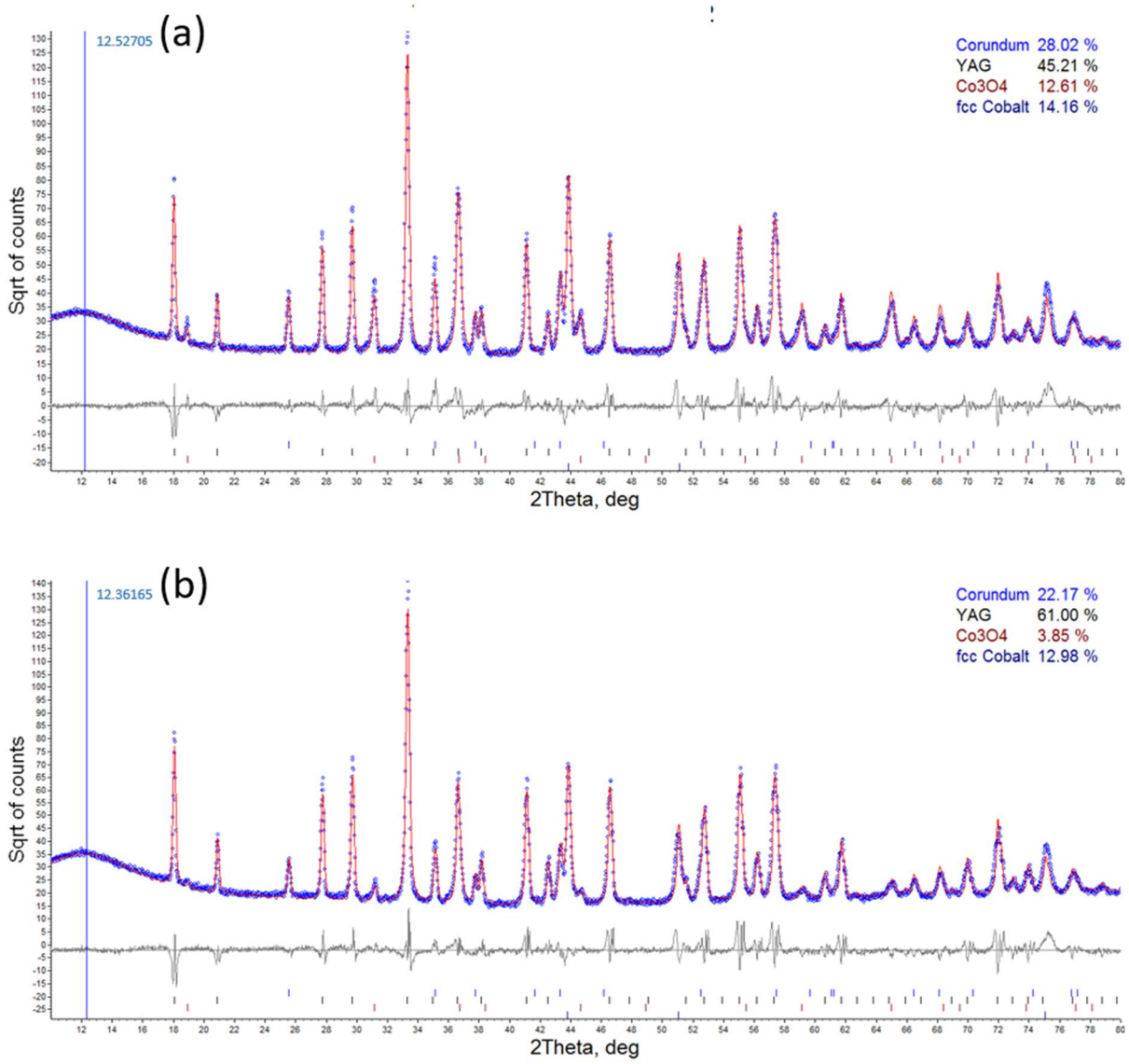

Figure 6-20: Rietveld refinement profile of the XRD scan of the thermally cycled (a) SP-YAG topcoat (b) S-YAG topcoat; each showing four crystalline phase compositions with varying proportions—Rietveld analysis was done by Dr Zdenek Pala.

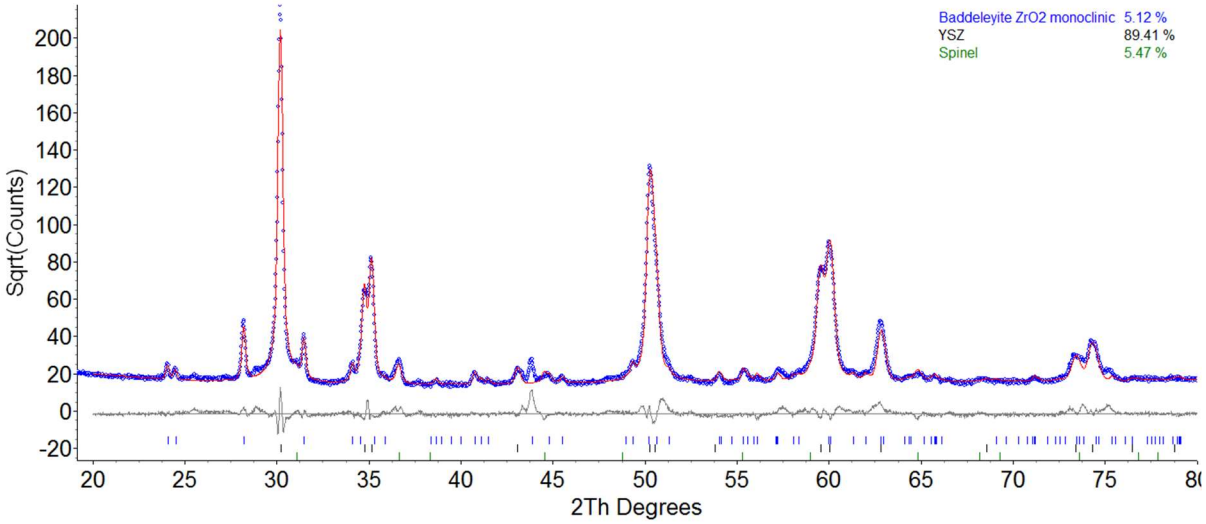

Figure 6-21: Rietveld refinement profile of the XRD scan of the thermally cycled T2-YSZ topcoat showing three crystalline phase compositions with varying proportions—Rietveld analysis was done by Dr Zdenek Pala.

The YSZ topcoat shows two more crystalline phases in addition to the tetragonal phase compared to the as-sprayed form of the coating. The new phases are monoclinic zirconia and a spinel; each of these new phases contribute only ~5% to the phase composition of the thermal cycled topcoat. More of the desirable tetragonal phase is retained although the quantity is ~10% less compared to the quantity of tetragonal phase in the as-sprayed form. The thermal cycled YSZ topcoat shows no presence of corundum, nor the FCC cobalt as found in the two YAG topcoats (SP-YAG and S-YAG); this observation suggests how much protection each of the three topcoats offers to prevent the depletion of the elemental compositions in the underlying bond coat.

6.5 Discussion

6.5.1 Topcoat coating formation

The formation mechanism of the respective topcoats presented in this chapter varies from one another based on the thermal properties of each of the materials and processing conditions. The formation of the YSZ topcoat has been elucidated in chapter 5, sub-section 5.5.1; the formation mechanism for the respective YAG topcoats is presented in this sub-section. The YAG coatings obtained from the solution precursor (SP-YAG) built from molten splats as did the YAG coating obtained from the YAG suspension (S-YAG); however, the splat formation mechanism and the deposition efficiency of the two coatings, set them apart. Similarly, the microstructure of a coating is influenced by its building block which could be one or all of splats, semi-molten particles, resolidified particles and unmolten particles based on the coating formation mechanism [7, 15]. Depending on the spray deposition parameters, the coating microstructure will be dominated by one of the coating microstructural constituents listed earlier. Splats as a coating building block dominate the microstructure of the two YAG coatings given the ratio of amorphous to crystalline contents of the two coatings, ~9:1 in the SP–YAG compared to ~7:1 in the S–YAG.

The SP-YAG formed from the thermal decomposition of nitrates solution precursor; a YAG formation method like the combustion synthesis described by Kakade et al. [253] and Ramanathan et al. [254]. The combustion synthesis of ceramics involves precise mix of precursors (referred to as oxidizers) and fuel to prevent the formation of ceramics contaminated by unburned precursors and unreacted carbonaceous

products [254]. The formation process presented by the SP-YAG, however, differs from the combustion synthesis in that no fuel was mixed with the solution precursor before it was sprayed to form YAG. The thermal decomposition route of the solution precursor is an endothermic reaction process; it presents a different coating formation mechanism from that of a suspension spray process. Low deposition efficiency, however, characterizes coating deposition using solution precursor [145]—the SP-YAG is not an exception, it has < 2 μm/pass as against the ~ 3.5 μm of the S-YAG. The S-YAG microstructure formed from the evaporation of the aqueous medium carrying the particles, melting and re-solidification of the YAG particles carried in the medium. This formation mechanism has been reported for SHVOF thermal sprayed ceramics [13, 144]; molten particles of the YAG material which solidify into splats have been shown in Figure 6–7. The S–YAG has lamellae size of ~25 μm and 7:1 ratio of amorphous to crystalline contents in comparison to ~5 μm lamellae size and 9:1 ratio of amorphous to crystalline contents in SP-YAG.

More so, the variation in the formation mechanism of the SP-YAG and S-YAG drives the measured temperature of their respective in-flight particles. The SP-YAG particle temperature of 1612 ± 48 °C resulted from thermal energy lost due to cooling because of evaporation in addition to the endothermic heat of reaction consumed from the combusted gases. In contrast, the S-YAG particles has retained much of its thermal energy to have a temperature of 2132 ± 64 °C as it was only cooled due to the thermal energy lost from the evaporation of the aqueous medium carrying the particles. More so, the variation in the measured temperatures could have been due to the resident time of the feedstock in the flame—the in-flight particle velocity for the particles of each

the SP-YAG and the S-YAG differ by ~90 m/s although the spray parameter conditions were the same for the deposition of both coatings.

It is, however, not an aberration that the temperature of the SP-YAG particles at the spray distance of 85 mm was less than the melting point of YAG (1970 °C), yet it presents splats often formed from molten particles (see Figure 6–5). The mechanism of coating formation from solution precursor proceeds from evaporation of liquid medium to precipitation, pyrolysis before melting [255]—in this case the molten particles had cooled in-flight prior to the rapid quenching that accompanied the impact on the substrate. The inflight cooling springs from the nature of the deposition process; HVOF flame exhibits temperature gradient downstream away from the combustion chamber [236]. As the molten particle travels through the flame, it experiences continuous heat transfer with the combusted gases and the flame causing it to cool. The evaporation of the liquid carrier in addition to the endothermic nature of the reaction synthesis forces proportionate cooling of combusted gases and the flame downstream at the gun exit up to the substrate onto which the YAG product was deposited. This explains why the temperature of the SP-YAG particles (~1612 °C) measured at spray distance of 85 mm from the gun exit varies significantly from the temperature of 2927 °C of the combustion chamber based on the numerical modelling of the deposition of the SHVOF studied by Chadha et al. [236]. It is thus possible that the temperature profile for the SP-YAG deposition process lies between 2927–1612 °C; this temperature range exceeds the formation temperature range of 800 °C to 1100 °C reported for pure YAG synthesis by thermal decomposition synthesis [253]. Should the temperature range of 2927–1612 °C be confirmed for the SP–YAG coating formation, it suggests the YAG in the SP-YAG formed and melt in-flight to justify the

splat build up associated with the SP-YAG; the evidence of the inflight melting was in the amorphous humps identified in the as-sprayed coatings.

The top surface morphology of the two YAG coatings present with an additional feature than just molten particles; randomly distributed bumps cover the top surface of the respective YAG coatings. The bumps in S-YAG on the coating surface formed due to in-flight re-solidification of molten particles; the re-solidified particles coalesce into aggregates that piled up as surface bumps with a conical base shown on the coating cross section. The molten particles that formed the SP-YAG also exhibit in-flight re-solidification and coalescence to form surface bumps which although look different to those identified in the S-YAG as in Figure 6–11.

6.5.2 Phase formation in the as-sprayed YAG topcoats

The produced SP-YAG deviates from the conventional route widely used in the production of engineering ceramics; stoichiometric precursor solution was injected into a mixture of hot turbulent combusted gases and flame with central static temperature in excess of 2927 °C [236]. The combination of the DSC results, the FTIR and the XRD scan of the calcined samples provide insight on how the phases in the SP-YAG form. The formation process presents two endothermic amorphous stages: the first (150-450 °C) due to water loss and the decomposition of the nitrates accompanied by effervescence of nitrous oxides [253], the second (500-900 °C) due to aluminium ion (Al^{3+}) coordination site rearrangement and yttrium ion (Y^{3+}) substitution [256, 257]. The rearrangement of the Al^{3+} ions and the Y^{3+} ions mark the formation of YAG from the precursor. The precursor calcined at 450 °C represents the end of the stage where the material was entirely amorphous stage giving that the results of the precursor calcined at 750 °C was representative of a stage containing mostly the amorphous

phase; at this stage there was no contribution from the nitrate decomposition process as the FTIR result contains no nitrate ions. The amorphous phase at this stage (750 °C) represents the onset of the YAG phase formation since YAG forms by aluminium ion (Al^{3+}) coordination site rearrangement and yttrium ion (Y^{3+}) substitution. The rate of chemical reactions increases with increased surface area and temperature; therefore, the breakup that accompanies the atomization of the solution precursor when it was injected into the combustion chamber provides a higher surface area while the combustion chamber temperature of 2927 °C provides the high reaction temperature. These two conditions facilitate the rapid evaporation of the liquid medium and the onset of the decomposition reactions of the precursor reactants. This explains why the SP-YAG contains crystalline YAG despite the reduced deposition time while the precursor calcined for 3 hours at 750 °C remains mostly amorphous.

The variation in temperature of deposited splats—the building blocks of coating—also impacts on the degree of crystallinity of the YAG coatings. The two coatings are mostly amorphous, SP-YAG with amorphous contents of ~90% shows 2% less crystallinity compared to the S-YAG with amorphous contents of ~88% however, this disparity is not significant. The crystalline compositions of the two coatings presents no variation; each one shows cubic YAG and hexagonal YAP, though in varying proportions. In a reaction with intermediate products, the least stable reaction product precipitates first based on the Ostwald rule of successive formation [220]. The hexagonal structure of YAP forms first from the amorphous Al_2O_3-Y_2O_3 system. This explains why both the SP-YAG and the S-YAG contain YAP (hexagonal) though in varying quantities as the two coatings quenched from different temperature. The presence of YAG and YAP in coatings sprayed from YAG powder was reported by Weyant and Faber [148]—the

occurrence was attributed to the rapid quenching effect of thermal spray processes. It is, however, unclear what the constituents of the amorphous phases in the two coatings are. On this, even if the FTIR confirms metal-oxygen bond (M-O-M) formation in a material, it does not give conclusive proof of the possible compounds and/or phases in a coating. The FTIR analysis of the sprayed precursor for the SP-YAG confirms the formation of Al-O, and the Y-O vibration bonds. The FTIR analysis does not confirm which of the Al_2O_3-Y_2O_3 formation is present—$AlYO_3$ (YAP), $Y_4Al_4O_9$ (YAM) and $Y_3Al_5O_{12}$ (YAG). YAP, a form of the Al_2O_3-Y_2O_3 system is unstable—unlike YAM and YAG, exists peritectically at 1875 °C and has hexagonal, cubic and orthorhombic crystal structure, in sequential order from the amorphous phase [257].The EDX analysis of the two YAG coatings however shows no significant difference in the atomic % compositions of Al, Y, and O (see Table 6–1) unlike the FTIR.

6.5.3 Phase evolution of the ceramic topcoats after thermal cycling

Phase evolution and failure in TBC systems relate to the operating or the test temperature of the TBC system; in this case 1100 °C in air, as detailed in sub-section 3.5.3. The phase evolution of the three topcoats from the as-sprayed forms to the identified phases in the thermal cycled topcoats varies. At the test temperature of 1100 °C, amorphous to crystalline YAG [148] and hexagonal YAP to YAG [251] transitions were present in the SP-YAG and the S-YAG. The amorphous-crystalline transition in the two YAG topcoats proceeded with volume reduction due to the establishment of structural order. The kinetics of amorphous to crystalline YAG transition shows the transformation gets completed in a temperature range of 900–1100 °C in less than 20 minutes [148]—this suggests the two coatings have

transformed to full YAG in the first cycle of the thermal cycle test. The temperature range precludes the possibility of forming intermediate phases of hexagonal and cubic YAP in succession before the formation of YAG from the thermal decomposition cubic YAP to yield YAG and YAM [257]—see the phase diagram for Al_2O_3–Y_2O_3 system in Appendix C.

This is true for the shown coatings; no YAM phase showed in the coatings after the thermal cycling test. Differently, the missing hexagonal YAP in the two coatings after thermal cycling could have transformed directly to YAG; this has been reported by Ramanujam et al. [251]. The two coatings also show corundum phase after thermal cycling. This shows that the amorphous humps in both the SP-YAG and S-YAG were an amorphous phase with YAG composition with no Al_2O_3; this is because amorphous Al2O3 does not transit directly to corundum for structural and thermodynamic reasons. It will transit through the metastable Al_2O_3 phases to corundum based on Ostwald step rule [13]—see sub-section 4.6.1. The percent composition of corundum in the SP-YAG coatings was 28.02 % while its appearance in the S-YAG was up to 22.17 %. The corundum here is likely to have formed from the oxidation of the aluminium in the underlying bond coat; since YAG does not conduct oxygen unlike YSZ [140]. The percent content of corundum in the two coatings reflects the initial microstructure of the coatings prior to thermal cycling. The SP-YAG has reduced defects that could have created pathway for oxygen to reach the bond coat unlike the S-YAG where its vertical cracks could channel oxygen to the bond coat. The corundum in the two TBCs with YAG topcoats may have formed due to the oxygen reaching the bare surface of the bond coat after the simultaneous partial and complete spallation sites created in the topcoats during the thermal cycling.

For the T2-YSZ topcoat shows ~11% less of its tetragonal phase and some 5% monoclinic phase at the test temperature of 1100 °C with overall duration of the test cycle reaching 133 hours. The test temperature of 1100 °C matches the transition temperature at which zirconia switches between the monoclinic and the tetragonal phase [243]; only 5% monoclinic zirconia forms in the coating after 133 hours. On the kinetics of the phase transition, Mingwen et al. [144] showed that YSZ coating deposited from ethanol-based suspension exhibited phase stability but not beyond 1000 °C for 72 hours. For the coating under consideration, a change in temperature of 100 K for additional 61 hours of thermal treatment meant that YSZ coating deposited from ethanol-based suspension did not engender phase instability. The kinetics of the phase transition therefore seems to favour the retention of the tetragonal phase at 1000 °C but from 1100 °C upwards the monoclinic phase could be formed as in the case presented here and it could be cubic phase as reported for nano sized electrospun 8 wt. % YSZ fiber calcined at 1100 °C [258]. The accompanied phase transformation stress to the tetragonal to monoclinic transition in the topcoat contributed to the partial spallation of the topcoats. The phase transformation stress is one of the of three stresses engendered by the deposition process; the remaining two are the quenching stress and the peening stress.

6.5.4 Failure modes of the ceramic topcoats

The failure of the ceramic topcoats in TBCs is often defined as when the topcoats get separated from the underlying bond coat. The spallation will be a function of one or combination of any of the TGO growth effect, the strain compliance of the topcoat microstructure and phase transformation stress. The two YAG coatings studied in this thesis might have failed due to reduced strain compliance, phase transformation stress

due to amorphous to crystalline transition and internal oxidation. The absence of vertical cracks and the reduced pore distribution in the SP-YAG reduces its strain compliance—a precondition for failure facilitated by microstructural make up of a coating. The SP–YAG also showed interfacial crack between the topcoat layer and the TGO layer; this interfacial crack must have developed with the driving force at the crack tip coming from the TGO growth rate. The failure mode seen in the SP-YAG sample matches the schematic in Figure 6-22(b).

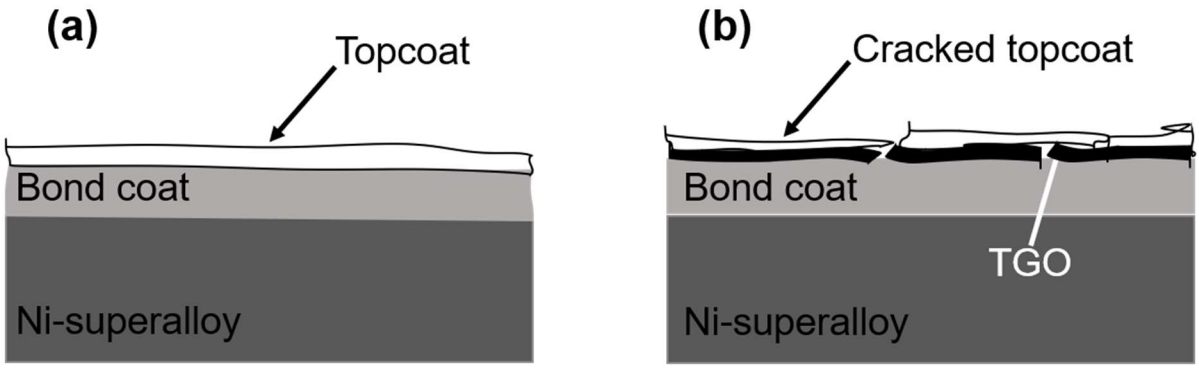

Figure 6-22: Schematic of the failure modes in the SP-YAG topcoat (a) before thermal cycling (b) after thermal cycling

The S-YAG on the other hand has vertical cracks that could have ensured strain tolerance of the coating, but several horizontal micro cracks compromised the relevance of the vertical cracks. The failure of the S–YAG topcoat thus appears to have been from within the topcoat layer; the boundary of the topcoat with the TGO presented no visible micro crack that could have driving interfacial spallation; this failure mode matches the schematic in Figure 6-23(b). The T2–YSZ topcoat on the other hand has strain compliance feature linked to vertical cracks shown on its cross-section. More than 80% of the YSZ topcoat was retained after the thermal cycle as against the less than 10% of the two YAG topcoats. The failure of the YSZ topcoat showed boundary cracks with the TGO in addition to the vertical and the horizontal

cracks within the topcoat itself; this again matches the failure schematic shown in Figure 6-22(a). That the boundary crack between the topcoat and the TGO is less pronounced compared to the horizontal crack within the topcoat suggested the TGO growth rate may be lower compared to the one found in the YAG topcoat TBC samples especially the SP–YAG.

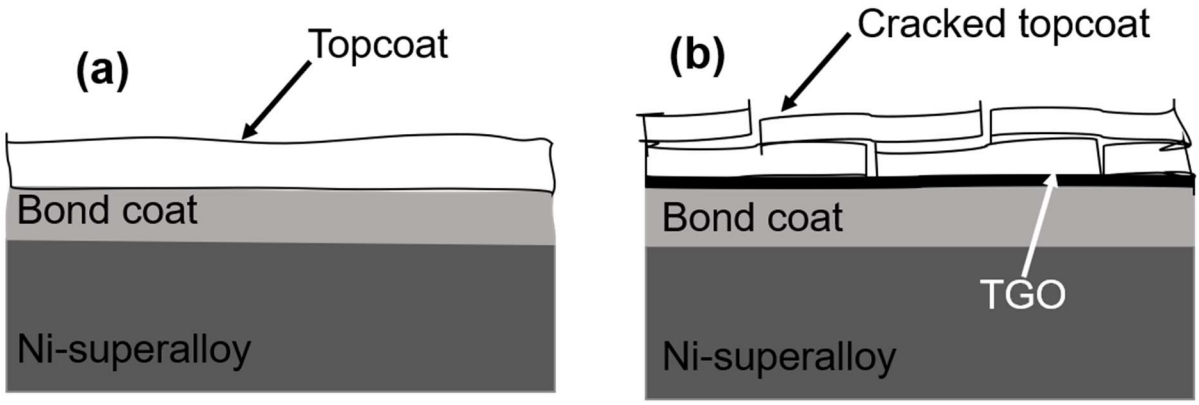

Figure 6-23: Schematic of the failure modes in the S-YAG topcoat (a) before thermal cycling (b) after thermal cycling

The growth rate of the TGO can be linked to the eventual TGO thickness found in each of the TBC samples; the thickness of the TGO will also suggest how aluminium constituent of the bond coat get used [259]. The depletion of the aluminium contents of the bond coat of the TBC samples which initially have ~ 15.6 (atomic %) aluminium shows as ~8 μm TGO layer in the SP-YAG, ~3 μm in the S-YAG and ~5 μm in the T2–YSZ TBC sample following the exposure of the bond coat surface to air after the topcoat failed during thermal cycling. The TGO layer could reach between 1 and 10 μm in a TBC [6] but the ~8 μm TGO layer thickness in the SP-YAG exceeds the critical TGO thickness of ~6 μm suggested by Dong et al. [260]. The critical TGO thickness represents the thickness above which the TBC cyclic life could reduce rapidly. Contrary to this assertion, the failure of the YAG TBC samples studied in this thesis

proceeded from the spallation of the topcoats due their reduced strain tolerance. The spallation then allowed oxygen to reach the bond coat surface through the spallation sites to cause the growth of the TGO.

6.5.5 Thermal conductivity

The controlling features which drive the thermal conductivity mechanism in a ceramic topcoat are intrinsic to the material in question and the microstructural buildup of the coating. The thermal conductivity of YAG decreases with temperature based on either intrinsic phonon scattering which causes thermal conductivity to scale as inverse of temperature [146] or on engineered layered porosity termed inter-pass boundary (IPB) that impedes heat flow by prolonging heat conduction path in which case the porosity layers are positioned perpendicular to the direction of heat flow [145]. In the former case, Padture and Klemens [146] measured the thermal conductivity of dense YAG pellets; a 3.2 W/mK at 1000 °C meant ~ 63 % reduction from 8.7 W/mK at 23 °C. In the latter, the reduction in the thermal conductivity of SPPS YAG with light IPB from 1.68 W/mK at room temperature to 0.95 W/mK at 1300 °C corresponds to ~ 43 % reduction. Differently, amorphous-crystalline transition could lead to increased thermal conductivity in the absence of defects. The formation of defects like grain boundaries, micro cracks, voids and atomic vacancies lowers thermal conductivity; the defects are additional scattering domains which raise the thermal resistance of the material [261].

The three topcoats presented have varying microstructural defect concentrations with the YAG topcoats being predominantly amorphous in the as-sprayed form. The low thermal conductivity of the two YAG coatings showed at 25 °C, ~0.2 W/mK in SP-YAG and ~0.6 W/mK in S-YAG could be due to the large amorphocity in the two coatings: ~90 % in SP-YAG and ~88 % in the S-YAG. The S-YAG possessed more features

that may have contributed to its reduced thermal conductivity; its many distributed micro cracks and voids will serve as extra scattering domains to raise its thermal resistance. The YSZ topcoat on the other hand only has its conductivity linkable to its microstructural build up; the controlling features were just the pores and the cracks which again were the scattering domains. Those were in addition to the intrinsic conductivity of YSZ as a ceramic material with high concentration of zero-dimension defects distributed through its crystal structure. The zero-dimension defects otherwise called the point defect in the YSZ structure exist as oxygen atoms and substitute solute atoms.

The thickness of the topcoat is also significant to the measured thermal conductivity because laser flash technique takes the sample thickness into account as presented in sub-section 3.5.1. A thicker coating would have reduced thermal conductivity because it takes longer time for the temperature rise at the sample rear face to reach one-half of its maximum value. Although both coatings showed increased thermal conductivity at 1000 °C, the increment in the SP-YAG was ~78 % while the increment in the S-YAG was just ~ 19 %. More so, the fact that both coatings showed increased thermal conductivity as temperature increased could be attributed to the amorphous-crystalline transition observed in the two coatings. Despite the thickness of the T2-YSZ topcoat being intermediate between the SP–YAG and the S–YAG, it has ~2.0 W/mK thermal conductivity at 1000°C which is three times its room temperature value. This observation shows that the T2–YSZ must have sintered to have reduced porosity as the temperature rose because the known thermal conductivity for a fully dense YSZ at high temperature reaches 2.3 W/mK at 1000°C for a fully dense YSZ with little or no scattering points than its intrinsic point defects [6].

Furthermore, the thickness of the topcoats relative to the thickness of the substrate will also have effect on the thermal conductivities that is calculated for the topcoats. R. E Taylor [154] reported that in layered thermal conductivity measurement approach, a ratio of 1:40 between the thickness of a topcoat and its underlying substrate could undermine the accuracy of the thermal conductivity of the topcoat significantly. The SP-YAG thickness ratio to the substrate showed 1:55, while the S-YAG thickness to its substrate was 1:8; for the T2-YSZ thickness to its substrate it was 1:19. The ratio for the SP-YAG suggested its thermal conductivity was inundated by the conductivity of the substrate while the duo of the S-YAG and the T2-YSZ on the other hand were less affected. A further check on the validity of the results is to calculate the ratio of the thermal conductivity of the substrate to that of the topcoat. A ratio of the order of 10:1 meant the experiment was acceptable; the larger the ratio the better. The S-YAG and the T2-YSZ both showed reasonable compliance with a ratio in the range 17–25 and 14–21 respectively; the SP-YAG value was in the range 29–70—see Figure 7-1 in Appendix D. The SP-YAG value again appears to be outliers; the source of its errors has been mentioned earlier. However, all the topcoats satisfied the thermal resistance (see Equation 6.1) requirements for a valid measurement as given by the thermal diffusivity equipment manufacturer—NETZSCH Instruments (Selb, Germany). The thermal resistance of every layer in a multilayer sample must be at least 20 % of the total thermal resistance of the multilayer sample—see Figure 7-4 to 7-6 in Appendix D.

$$R_{th} = \frac{t}{\lambda_{th}} = \frac{t_s}{\lambda_s} + \frac{t_c}{\lambda_c}$$ ---------- *Equation 6.1*

R_{th} is the total thermal resistance of the composite (coating and substrate), t is the thickness of a layer while λ_{th} is thermal conductivity of a layer—c and s as subscript denotes coating and substrate.

To summarize on YAG formation, the formation is influenced by both temperature and kinetics; ~ 20 minutes of heat treatment is sufficient to obtain crystalline YAG from amorphous YAG at 900–1000 °C. While thermal spray could produce crystalline YAG at much reduced time, the deposition process must be optimized to control the degree of crystallinity of coatings deposited by HVOF spray. A combination of spray parameter and deposition hardware modification might be the key. Bolelli et al. [21] showed that longer combustion chamber increased feedstock heating time; a modification of the fuel-oxygen mix to achieve lower thermal energy in the combustion chamber with increased length could produce YAG coatings with the right mix of amorphous, crystalline contents and microstructural defects. The coating so engineered is proposed to have a balance of structural integrity and thermal conductivity.

6.6 Summary

This chapter presents the results of the investigations on the SP-HVOF and SHVOF thermal spray of YAG topcoats compared to SHVOF sprayed YSZ. This is the first time YAG coating has been produced from suspension and solution precursor using HVOF spray technique. The as-sprayed and thermally cycled topcoats presents distinct microstructural evolution, which affects the performance of the respective topcoats; the following conclusions were drawn:

- SP-HVOF spray of stoichiometric solution of nitrates of aluminium and yttrium produces YAG coating comparable in phase contents to the YAG coating

deposited from YAG suspension. Even though the SP–YAG coating exhibit reduced deposition efficiency, the challenge has been reported for other solution precursor thermal spray process.

- The as-sprayed SP-YAG and S-YAG has multiple phases of hexagonal YAP, amorphous and cubic YAG in varying proportions, while the T2–YSZ has just the tetragonal zirconia phase.
- The SP-YAG contains micro pores as its main defects, the S-YAG has vertical and horizontal micro cracks, pores and inter splat boundaries while the T2–YSZ only had pores and vertical micro cracks. The two YAG topcoats show less sintering effect unlike the T2–YSZ which was abinitio built from sintered particles.
- The kinetics and thermodynamics of the thermal cycling favoured the transformation of amorphous YAG and hexagonal YAP to cubic YAG; the T2–YSZ also retained most of the starting tetragonal phase after the thermal cycling.
- The failure of the SP-YAG spans from the absence of strain compliance defects as vertical cracks while the S-YAG experienced failure within the topcoat due to the presence of horizontal cracks in its microstructure which compromise its strain tolerance. The T2–YSZ topcoat showed the most strain tolerance compared to the two YAG topcoats; that was due to its microstructural build-up. In addition to those, the three TBC samples experienced change in the chemistry of the underlying bond coat causing partial and total spallation, respectively.

Conclusions and future work

7.0 Conclusions

The aim of the research work presented in this thesis was investigated under specific objectives built around (i) deposition of coatings from ceramic suspensions and solution precursor of inorganic salts using HVOF spray process, (ii) microstructure and mechanism of formation study and (iii) failure modes and performance evaluation. The findings from the investigations were then presented in three result chapters; the summary from the three result chapters is given in this section.

γ–Al_2O_3 coating was successfully deposited from the suspension of delta–theta Al_2O_3 processed with HVOF; the as-sprayed coating showed fully molten splats which predominantly contained amorphous Al_2O_3. Thermal treatment of the as-sprayed coating over different temperature ranges caused the γ–Al_2O_3 to partially transformed to become δ–Al_2O_3 (tetragonal). The observed transformation occurred through vacancy ordering and crystallite size refinement. Besides the phase transformation, the microhardness and the fracture toughness of the heat-treated coatings increased compared to the as–sprayed coating. It was demonstrated that the heat treatment of the coatings was only beneficial to the wear performances of the as-sprayed coating and the coating heat treated at 600 °C; the wear performance of the coating heat treated at 600 °C were two order of magnitude better than the wear rate Al_2O_3 coatings produced from conventional α– Al_2O_3 suspension.

Microstructure and coating formation mechanism was further investigated with Al_2O_3 and YSZ suspension; it was demonstrated that the HVOF spray process is able to produce thick coatings from suspension feedstock. Particularly, the process was able to deposit Al_2O_3 coating of up to ~200 µm with suitable integrity. It was also shown

that the building blocks of coatings could be either splat/lamellae based if the starting material gets molten or sintered particles where the starting materials only get thermally softened. So, depending on the microstructural build-up of coatings, the residual stress behaviour of the coatings can be impacted.

The residual stress of the Al_2O_3 and YSZ coatings was investigated using a combination of the time–of–flight (TOF) neutron diffraction, X–ray diffraction and the incremental hole–drilling techniques; the three techniques offered complimentary understanding of the residual stress behaviour of the coatings. The X–ray diffraction technique provided the surface stress needed to understand the immediate response of the coating to its functional environment. This is so in that X–ray diffraction technique collects data from the top surface of samples with reduced signal penetration compared to neutron diffraction and hole–drilling techniques. This further provides possible application for the X–ray diffraction technique to measure the stress state of the top surface of coatings meant for contact-based applications. This will provide pathway to understating the potential in-service failure modes of the coating.

This thesis also showed that the through thickness residual stress in the studied coatings can be different in magnitude and nature away from the top surface towards the interface between the coating and the substrate. The lamellae based Al_2O_3 coating, has been found to be mostly compressive through its thickness as against the YSZ coating with sintered particles which showed both tensile and compressive stress. Its compressive stress is the stress transformation stress obtained from the neutron diffraction measurements.

This thesis also showed successful deposition of YAG coating (SP–YAG) topcoat using solution precursor made from inorganic nitrate salts; it was found that YAG

formed through combined endothermic and exothermic stages through the reaction stages at 900 °C. The SP–YAG was studied alongside another YAG coating (S–YAG) deposited from suspension which were then compared to SHVOF sprayed YSZ topcoat (T2–YSZ). This is the first time YAG coating has been produced from suspension and solution precursor using HVOF spray technique. The as-sprayed and thermally cycled topcoats presents distinct microstructural evolution, which affects the performance of the respective topcoats. Specifically, the as-sprayed SP-YAG and S-YAG has hexagonal YAP, amorphous and cubic YAG in varying proportions, while the T2–YSZ had just the tetragonal zirconia phase. The kinetics and thermodynamics of the thermal cycling favoured the transformation of amorphous YAG and hexagonal YAP to cubic YAG; the T2–YSZ lost only 11% of the starting tetragonal phase after the thermal cycling.

The SP-YAG contains micro pores as its main defects, the S-YAG has vertical and horizontal micro cracks, pores and inter splat boundaries while the T2–YSZ only had pores and vertical micro cracks. The thickness of the topcoats influenced the thermal conductivities of the respective samples; it was shown that a ratio of 1:55 between the SP-YAG topcoat and the substrate led to a disproportionate thermal conductivity result. The thermal conductivity of the topcoats increased after the thermal cycling; for the two YAG topcoats, it did not exceed 1.1 W/m.K but the thermal conductivity of T2–YSZ increased up to ~2.0 W/m.K due to increased sintering effects as the T2-YSZ topcoat was initially built from sintered particles.

The thermal cycling evaluation on the topcoats showed that the presence of pores alone was insufficient to guarantee strain tolerance in a topcoat. Coatings with vertical cracks without adjoining horizontal micro cracks performed better than a coating with

only pores or that shows vertical and horizontal micro cracks. That was why the T2–YSZ topcoat showed the most strain tolerance compared to the two YAG topcoats. In addition to those, the three TBC samples experienced change in the chemistry of the underlying bond coat at the spallation sites on each of the topcoats.

7.1 Future work

The current work as presented in this thesis was focused on producing ceramic coatings and the performance of the produced coatings was evaluated for wear and thermal barrier applications. The microstructure of the as-sprayed coatings had high amorphous contents (80–90%) with the exception of the two YSZ coatings. It is now required to optimize the deposition process to ensure the higher crystallinity for the as-sprayed coatings of Al_2O_3 and YAG deposited using the HVOF spray technique modified for the processing of suspension and the solution precursor. A more crystalline Al_2O_3 coating will find further applications for high temperature wear such that the coatings will not fail due to the stress transformation stress of amorphous to crystalline transition.

The YSZ coating showed that coatings can be deposited without melting the particles; this observation can be taken forward to optimize the spray parameters that deposits Al_2O_3 coating and YAG coating from suspension with reduced melting or sintered particles. The delta-theta Al_2O_3 suspension can be used in this case to provide further insight into the wear performance of a coating containing metastable Al_2O_3 phases other than the usual gamma phase in as-sprayed Al_2O_3 coatings. Similar method can be developed to deposit crystalline YAG coatings built from sintered particles; this can eliminate the amorphous phase and the horizontal micro cracks in a bid to improve the thermal cycling life of the YAG coating.

Coatings from solution precursor can be further pursued for YAG and YSZ. For the solution precursor based YAG, this thesis showed that the YAG formation temperature (900 °C) is much less than the inflight temperature of the YAG particles (~1623 °C). So, a new deposition parameter can be implemented such as ensures the formation of YAG from the solution precursor but prevents the melting of the formed YAG particles. Not melting the formed particles will reduce the chance of forming amorphous YAG. Besides, the challenge of the reduced deposition efficiency in the YAG coating obtained from the solution precursor can be further looked into using higher concentration of the solution. The concentration can be increased with increasing the mass of salts dissolved per volume of the solvent; this will increase the number reacting ions to form the desired YAG.

On the solution precursor YSZ, this will be aimed at producing nano fibre of 3 wt.% YSZ using combination electrospinning technique and calcination. The 3 wt.% YSZ has been reported to have improved fracture toughness [258]; it will be fascinating to study the properties of the elctrospun nano fibre YSZ for structural applications. The nanofibers can be used to create fibre reinforced composite topcoats. The composite can be developed with 8 wt.% YSZ matrix deposited from suspension; it can also be used to reinforce YAG matrix deposited from suspension YAG or from solution precursor. The composite will enhance the structural integrity of the composite topcoat for improved thermal cycling life; the mechanism for the enhanced structural integrity will be expected to be by crack bridging.

The results from the residual stress work presented in this chapter provides that the X–ray diffraction technique can be used to ascertain the stress state of the top surface of a coating sample meant for contact applications such as wear. The through

thickness residual stress study will be useful in the further study of the ceramic topcoats presented in this thesis; this is to provide insight into the stress conditions of the entire topcoat layer. This will inform the decision on the possible failure modes of the topcoat hinged on the coating microstructure.

Appendix A

Procedure to obtain the interplanar spacing required to calculate the residual strain used in the calculation of the residual stress presented in Chapter 5.

1. Focus the data to be analysed using the command—w=xfocus(run number, bank number) then hit the enter key e.g., w=xfocus(274305, 1)
2. Run the 'analyze_scan' command to obtain the range of time of flight (TOF) within which the required peaks fall.

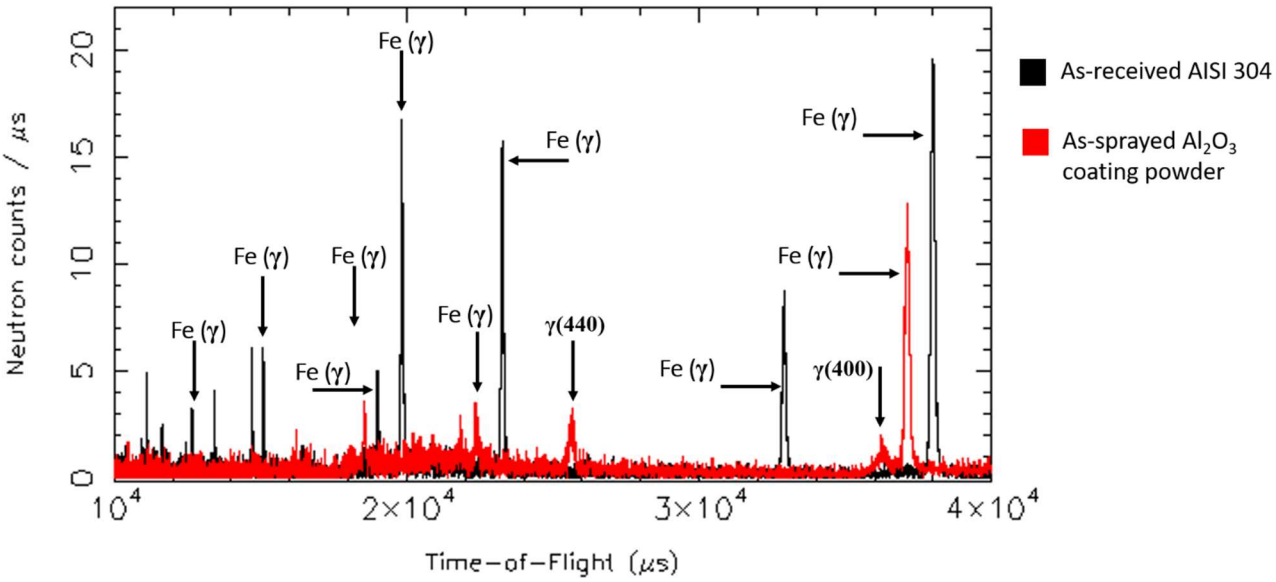

Figure 7-1: Analysed peaks of the SS304 and the alumina coating

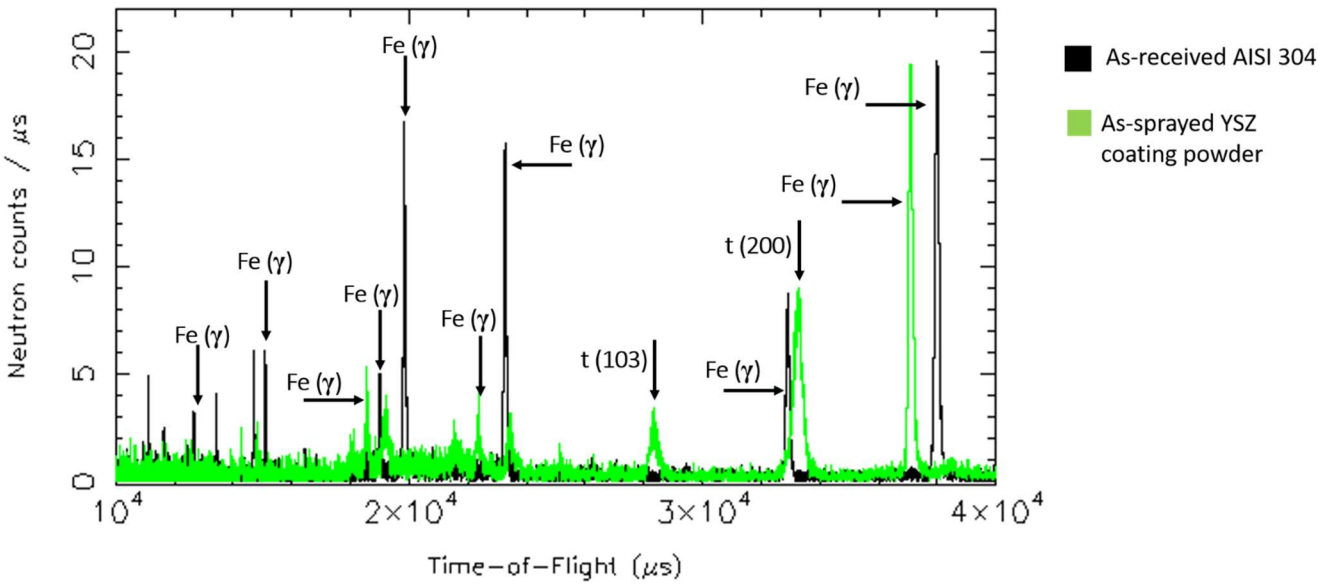

Figure 7-2: Analysed peaks of the SS304 and the YSZ coating

3. Implement the 'analyze' command to obtain the interplanar spacing for the specific peak to be used for the strain analysis. The interplanar spacing is displayed as the lattice parameters for a cubic structure as in the current case.

```
###### Calculating PHASE=1 -- BANK=1 ########
STOP EXPEDT terminated successfully statement executed
        1 file(s) copied.
scale factor=
0.000035104992559
####################################################
####################################################
 The current sample is Iron
 The min TOF to be used in the analysis is 20000.0
 The max TOF to be used in the analysis is 40000.0
 There are 3 reflections within this range
 The lowest hkl reflection in this range is (1,1,1)  at  38170.0
 The highest hkl reflection in this range is (2,2,0)  at  23370.0
 The highest intensity peak (assuming random texture) is (1,1,1)  at  38170.0
####################################################
Pawley fitting, free gamma, and peak 1 as seed
Reading focussed datafile: C:\Engin-X\focus\ENGINX274167_1.his
####################################################
Lattice parameter a=3.590688+/-0.00016
Lattice parameter b=3.590688+/-0.00016
Lattice parameter c=3.590688+/-0.00016
####################################################
```

Appendix B

Table 7-1: Diagnostic features of ceramic coatings

	GTV Al_2O_3		SP-YAG		S-YAG		T2-YSZ	
	Temp (°C)	V (m/s)	Temp (°C)	V(m/s)	Temp (°C)	V (m/s)	Temp (°C)	V (m/s)
1.	2029.23	1005.48	1604.31	800.63	2186.40	985.00	2692.67	1222.54
2.	2038.05	1044.82	1682.88	859.95	2205.98	978.46	2676.56	1149.86
3.	2049.02	1076.86	1709.09	879.83	2203.68	968.21	2680.55	1144.34
4.	2062.59	1098.83	1690.89	852.16	2198.50	957.09	2682.41	1146.16
5.	2071.92	1113.42	1678.98	848.75	2191.01	941.51	2684.03	1147.44
6.	2082.62	1121.53	1661.98	852.93	2190.79	938.60	2684.18	1151.39
7.	2083.21	1126.08	1656.22	867.63	2185.33	948.71	2685.28	1156.90
8.	2090.18	1126.87	1650.18	881.05	2183.76	944.11	2685.30	1154.18
9.	2089.45	1124.00	1624.17	880.53	2175.90	954.84	2681.42	1157.25
10.	2075.56	1117.36	1600.94	856.42	2155.68	947.19	2681.25	1156.29
11.	2072.36	1107.19	1581.52	814.45	2150.83	934.88	2679.79	1155.74
12.	2067.06	1096.91	1558.49	801.21	2154.12	928.48	2680.17	1154.79
13.	2051.15	1080.56	1549.11	799.53	2120.93	914.37	2680.84	1150.16
14.	2038.43	1043.19	1555.39	786.74	2116.10	909.51	2682.51	1150.26
15.	2038.42	1009.28	1570.62	819.42	2086.56	899.68	2686.40	1151.87
16.	2033.67	973.25	1591.81	850.33	2081.31	900.32	2688.42	1151.91
17.	2033.45	933.53	1619.29	845.13	2073.12	897.51	2686.32	1150.82
18.	2040.24	940.63	1625.82	868.79	2087.42	898.87	2687.11	1155.80
19.	2035.48	943.13	1625.51	875.55	2087.11	898.63	2682.93	1158.95
20.	2028.83	949.05	1622.94	873.60	2087.54	901.41	2680.65	1157.60
21.	2011.46	955.35	1625.07	852.07	2092.34	903.16	2682.05	1160.37
22.	2012.46	934.01	1622.60	845.44	2089.39	898.44	2683.57	1156.19
23.	2015.19	887.97	1614.75	834.74	2064.60	896.35	2685.89	1157.91
24.	2018.39	850.21	1584.68	825.56	2065.27	896.62	2685.98	1155.04
25.	2021.22	812.58	1580.03	819.18	2071.29	918.06	2686.74	1154.16
26.	2024.85	808.62	1556.81	842.89	2098.35	962.02	2683.78	1155.18
27.	2036.96	856.48	1551.24	848.31	2132.59	995.45	2681.60	1155.17
28.	2018.44	919.37	1556.78	836.02	2163.75	1031.21	2683.97	1149.68
Average	2045.35	1002.02	1612.58	843.53	2132.13	933.88	2683.66	1156.00

Appendix C

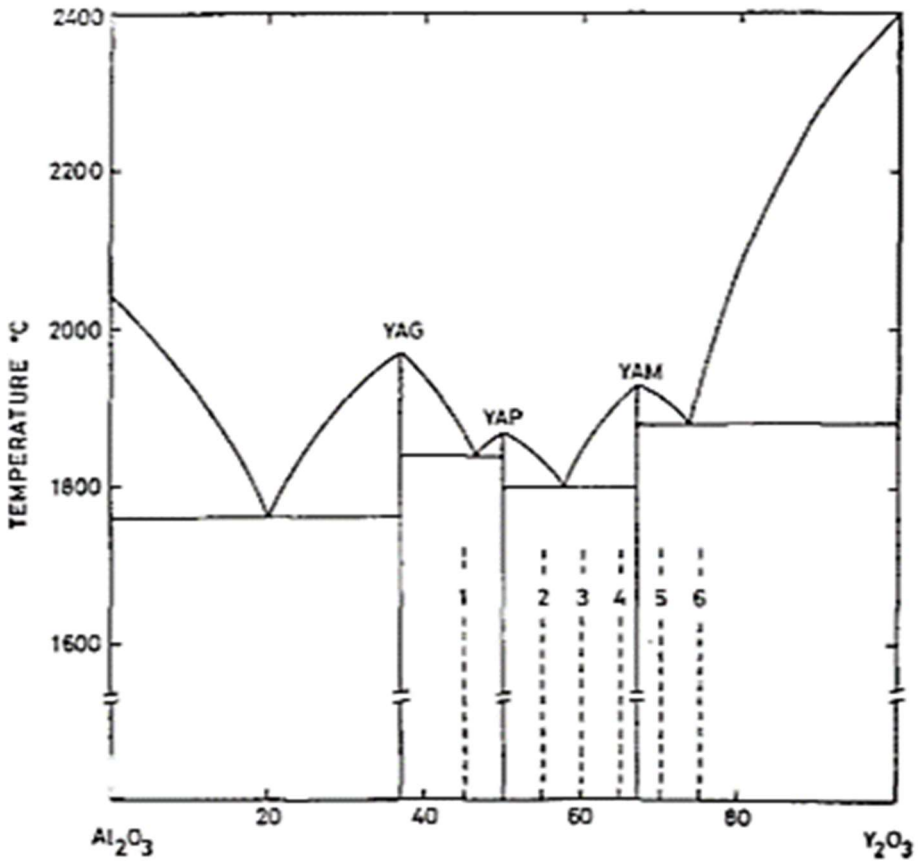

Figure 7-3: Schematic phase diagram for the Y_2O_3:Al_2O_3 system showing the three reported compounds, YAG, YAP and YAM together with the compositions whose structure were studied and summarized in Table 7-3 [147].

Table 7-2: Phases detected by X-ray diffraction in melts of various compositions in the pseudo-binary Y_20_3 :Al_2O_3 system at room temperature, both in the as-crushed and heat-treated states, and at elevated temperature. The phases YAG, YAP and YAM are abbreviated to G, P and M respectively and the phases present are given in order of predominance [147].

Composition Y_2O_3:Al_2O_3		Phases at room temperature			Phases up to T°C
		As-crushed	Post anneal	Anneal conditions	
YAG	37.5:62.5	G	G	2h, 1600 °C	G 1500
1	45:55	G + P	G + X + P (4 lines)	2h, 1600 °C	G + P 1380
YAP	50:50	P	G + X +P	2h, 1600 °C	P + G + (X) 1500
2	55:45	P + M	P + M + G (3 lines)	2h, 1600 °C	P + M 1460
3	60:40	M + P	M + P + G (1 line)	2h, 1600 °C	M + P 1500
4	65:35	M + P	M + P + G (1 line)	2h, 1600 °C	M + P + G 1510
YAM	66.7:33.3	M	M + G + X (1 line)	2h, 1600 °C	M + G 1500
5	70:30	M + Y_2O_3	M	19h, 1500 °C	M + Y_2O_3 1425
6	75:25	M + Y_2O_3	M + Y_2O_3	19h, 1500 °C	M + Y_2O_3 1525

Appendix D

Table 7-3: Combined thermal conductivity of the topcoats on AISI 304

Temperature (°C)	AISI 304 W/m*K	SP-YAG+AISI304 W/m*K	S-YAG+AISI304 W/m*K	T2-YSZ+AISI304 W/m*K
25	15.036	6.747	4.271	7.572
100	15.925	8.810	5.465	8.439
200	17.224	10.322	6.223	9.946
300	18.467	10.784	6.441	9.908
400	19.911	12.378	7.178	11.093
500	21.152	12.937	7.335	10.774
600	23.330	14.251	8.042	12.207
700	24.853	15.215	8.352	12.774
800	25.768	16.741	9.268	13.145
900	28.181	17.233	9.998	11.823
1000	29.244	19.396	10.952	17.513

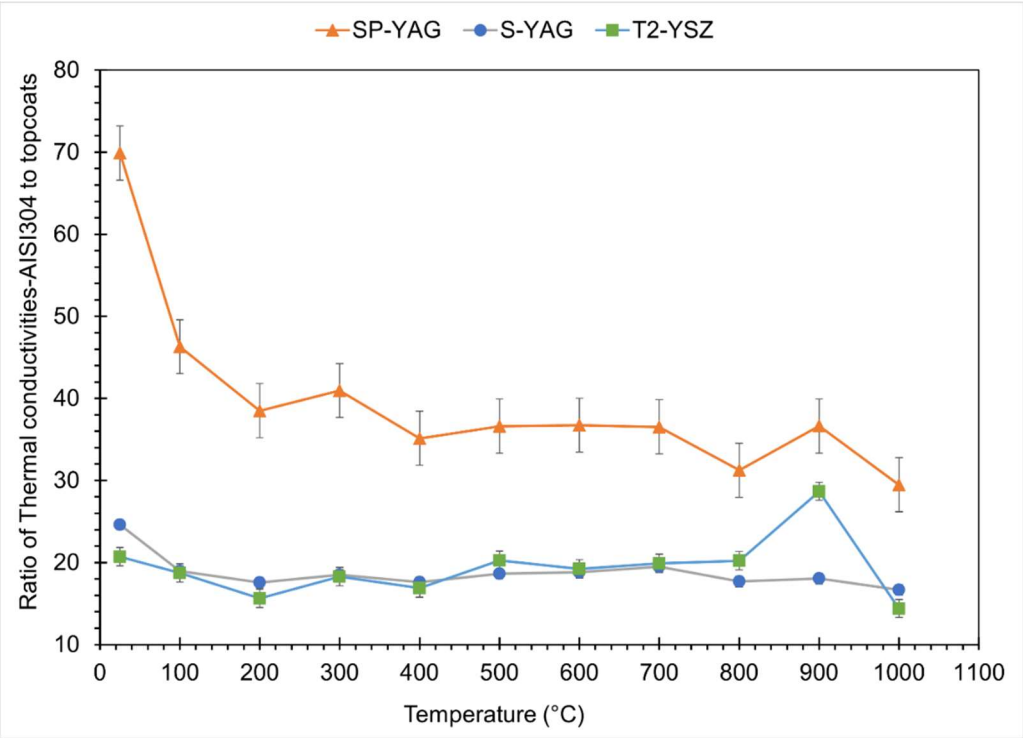

Figure 7-4: Plot of the ratio of the thermal conductivities of the individual topcoats to the thermal conductivity of the AISI304 substrate against temperature

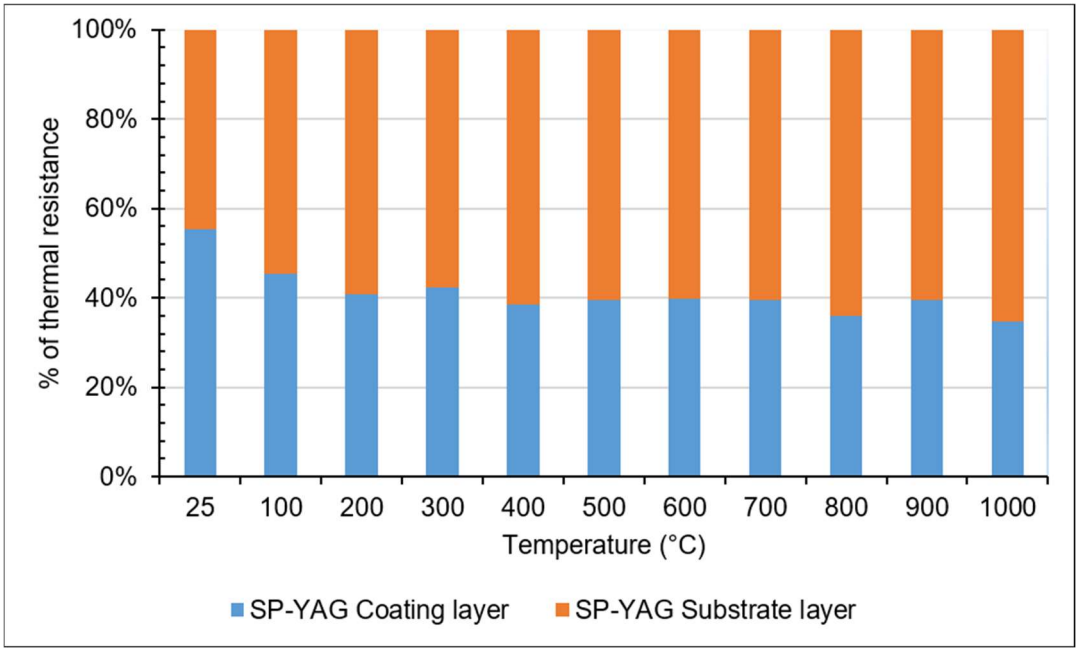

Figure 7-5: Plot of the % contribution of each layer to the total thermal resistance in the composite of substrate and SP-YAG topcoat

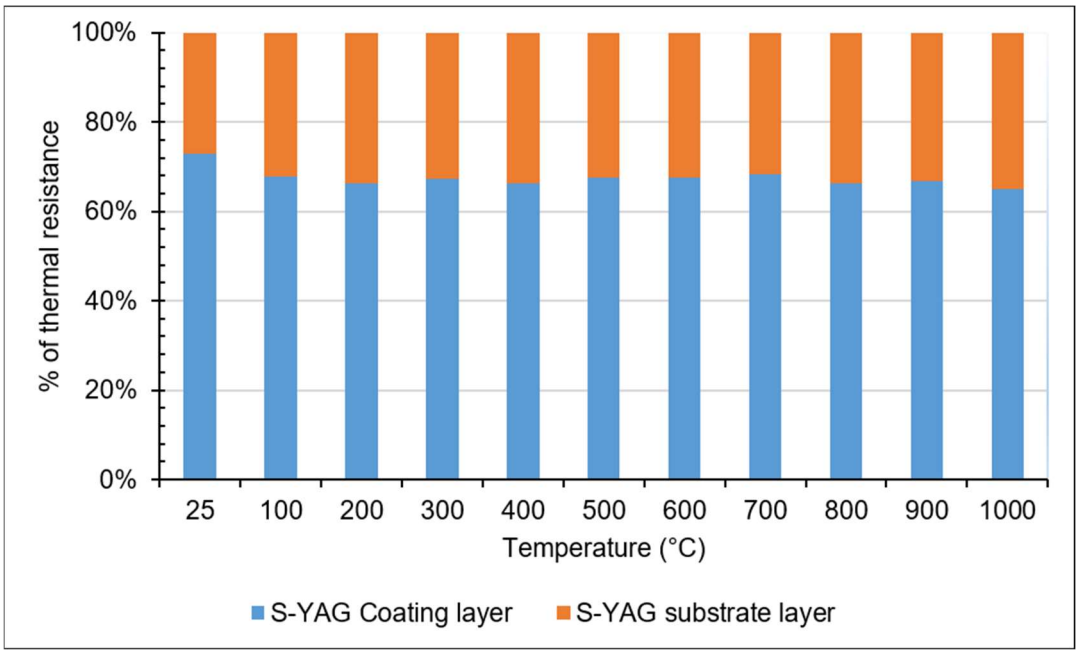

Figure 7-6: Plot of the % contribution of each layer to the total thermal resistance in the composite of substrate and S-YAG topcoat

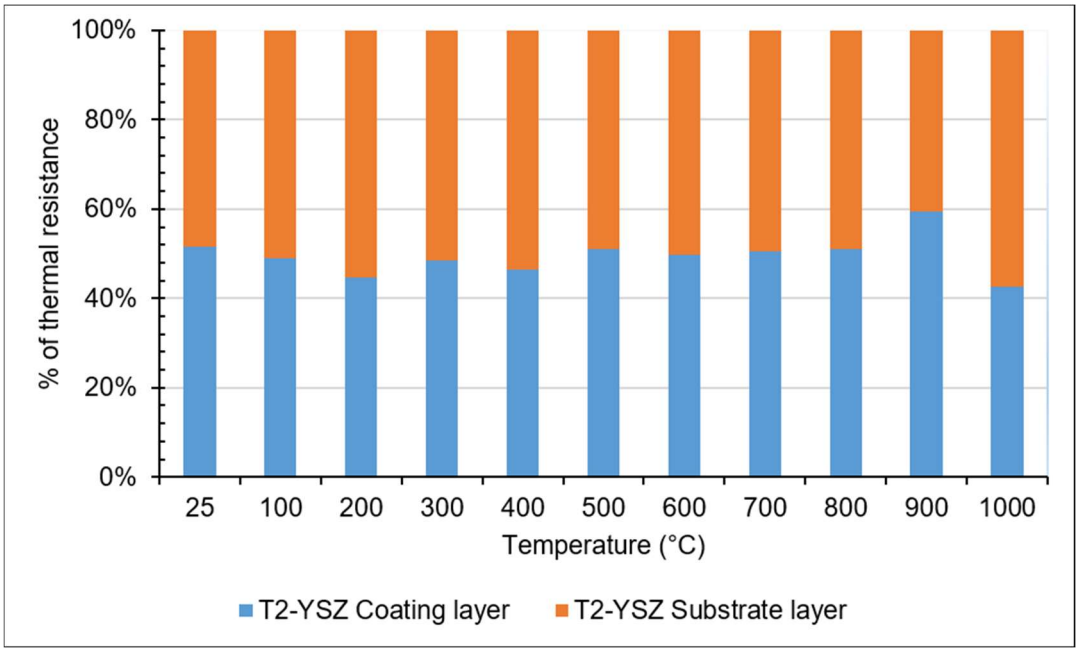

Figure 7-7: Plot of the % contribution of each layer to the total thermal resistance in the composite of substrate and T2-YSZ topcoat

Appendix E

Table 7-4: 95 % Confidence level for mean of the data shown in Figure 4-12

Samples	K_{IC} ($MPam^{0.5}$)
as-sprayed	0.32
ht-600-6h	0.50
ht-750-6h	0.51
ht-750-48	1.75

Table 7-5: 95 % Confidence level for mean of the data shown in Figure 4-13

Samples	SWR-1 (mm^3/Nm)	SWR-2 (mm^3/Nm)
as-sprayed	4.4478E-09	4.4337E-09
ht-600-6h	1.1614E-09	1.2215E-09
ht-750-6h	9.3927E-08	4.6895E-08
ht-750-48	5.2054E-07	3.3562E-07

Table 7-6: 95 % Confidence level for mean of the data shown in Figure 5-8

Depth	Nanohardness (GPa)	Elastic modulus (GPa)
30	5.74	57.34
60	8.55	83.36
90	4.55	60.26
120	5.87	80.80
150	5.64	59.25
180	4.58	53.65

Table 7-7: 95 % Confidence level for mean of the data shown in Figure 5-9

Depth	Microhardness (GPa)
15	0.84
60	0.62
110	1.17

Table 7-8: 95 % Confidence level for mean of the data shown in Figure 5-10

Depth	Nanohardness (GPa)	Elastic modulus (GPa)
15	4.83	67.55
30	3.35	61.20
45	2.99	63.72
60	0.81	10.29
75	2.35	20.10
90	3.11	42.11

Table 7-9: 95 % Confidence level for mean of the data shown in Figure 5-11

Depth	Nanohardness (GPa)
20	0.54
40	1.24
80	0.74

Table 7-10: 95 % Confidence level for mean of the data shown in Figure 6-17

Samples	Conductivity (W/m*K)
SP-YAG	0.15
S-YAG	0.22
T2-YSZ	0.23

References

1. Rajendran, R., *Gas turbine coatings – An overview.* Engineering Failure Analysis, 2012. **26**: p. 355-369.

2. DeMasi-Marcin, J.T. and D.K. Gupta, *Protective coatings in the gas turbine engine.* Surface and Coatings Technology, 1994. **68-69**: p. 1-9.

3. Davis, J.R., ed. *Handbook of Thermal Spray Technology*. 2004, ASM International: USA. 332.

4. Toma, F.L., et al., *Microstructures and Functional Properties of Suspension-Sprayed Al2O3 and TiO2 Coatings: An Overview.* Journal of Thermal Spray Technology, 2010. **19**(1-2): p. 262-274.

5. Marr, M., et al., *Electrochemical performance of solid oxide fuel cells having electrolytes made by suspension and solution precursor plasma spraying.* Journal of Power Sources, 2014. **245**: p. 398-405.

6. Padture, N.P., M. Gell, and E.H. Jordan, *Materials science - Thermal barrier coatings for gas-turbine engine applications.* Science, 2002. **296**(5566): p. 280-284.

7. Pawlowski, L., *The Science and Engineering of Thermal Spray Coatings*. 2nd ed. 2008, West Sussex, England: John Wiley & Sons Ltd. 597.

8. Bolelli, G., et al., *Microstructural and tribological comparison of HVOF-sprayed and post-treated M-Mo-Cr-Si (M = Co, Ni) alloy coatings.* Wear, 2007. **263**: p. 1397-1416.

9. Bolelli, G., et al., *Effect of the suspension composition on the microstructural properties of high velocity suspension flame sprayed (HVSFS) Al2O3 coatings.* Surface and Coatings Technology, 2010. **204**(8): p. 1163-1179.

10. Gell, M., *Application opportunities for nanostructured materials and coatings.* Materials Science and Engineering a-Structural Materials Properties Microstructure and Processing, 1995. **204**(1-2): p. 246-251.

11. Gell, M., et al., *Development and implementation of plasma sprayed nanostructured ceramic coatings.* Surface & Coatings Technology, 2001. **146**: p. 48-54.

12. Fan, W., et al., *Microstructural design and properties of supersonic suspension plasma sprayed thermal barrier coatings.* Journal of Alloys and Compounds, 2017. **699**: p. 763-774.

13. Owoseni, T.A., et al., *Suspension high velocity oxy-fuel (SHVOF) spray of delta-theta alumina suspension: Phase transformation and tribology.* Surface and Coatings Technology, 2019. **371**: p. 97-106.

14. !!! INVALID CITATION !!! [12-14].

15. Tejero-Martin, D., et al., *Splat formation and microstructure of solution precursor thermal sprayed Nb-doped titanium oxide coatings.* Ceramics International, 2019.

16. Dutta Majumdar, J. and I. Manna, *21 - Laser surface engineering of titanium and its alloys for improved wear, corrosion and high-temperature oxidation resistance*, in *Laser Surface Engineering*, J. Lawrence and D.G. Waugh, Editors. 2015, Woodhead Publishing. p. 483-521.

17. Dearnley, P.A., *Introduction to Surface Engineering*. 2017, New York, USA: Cambridge University Press.

18. Espallargas, N., *1 - Introduction to thermal spray coatings*, in *Future Development of Thermal Spray Coatings*. 2015, Woodhead Publishing. p. 1-13.

19. Ang, A.S.M. and C.C. Berndt, *A review of testing methods for thermal spray coatings.* International Materials Reviews, 2014. **59**(4): p. 179-223.

20. Turunen, E., et al., *Parameter optimization of HVOF sprayed nanostructured alumina and alumina–nickel composite coatings.* Surface and Coatings Technology, 2006. **200**(16-17): p. 4987-4994.

21. Bolelli, G., et al., *Properties of Al2O3 coatings by High Velocity Suspension Flame Spraying (HVSFS): Effects of injection systems and torch design.* Surface and Coatings Technology, 2015. **270**: p. 175-189.

22. Faisal, N.H., et al., *An improved Vickers indentation fracture toughness model to assess the quality of thermally sprayed coatings.* Engineering Fracture Mechanics, 2014. **128**: p. 189-204.

23. Żórawski, W., et al., *Microstructure and tribological properties of nanostructured and conventional plasma sprayed alumina–titania coatings.* Surface and Coatings Technology, 2015. **268**: p. 190-197.

24. Guilemany, J.M., et al., *Study of the properties of WC-Co nanostructured coatings sprayed by high-velocity oxyfuel.* Journal of Thermal Spray Technology, 2005. **14**(3): p. 405-413.

25. Carlton, C.E. and P.J. Ferreira, *What is behind the inverse Hall-Petch effect in nanocrystalline materials?* Acta Materialia, 2007. **55**(11): p. 3749-3756.

26. Gan, J.A. and C.C. Berndt, *Nanocomposite coatings: thermal spray processing, microstructure and performance.* International Materials Reviews, 2014. **60**(4): p. 195-244.

27. Sampath, S. and R. McCune, *Thermal-Spray Processing of Materials.* MRS Bulletin, 2011. **25**(07): p. 12-13.

28. Herman, H., S. Sampath, and R. McCune, *Thermal Spray: Current Status and Future Trends.* MRS Bulletin, 2000. **25**(7): p. 17-25.

29. Fauchais, P. and M. Vardelle, *Sensors in Spray Processes.* Journal of Thermal Spray Technology, 2010. **19**(4): p. 668-694.

30. Toma, F.-L., et al., *Demands, Potentials, and Economic Aspects of Thermal Spraying with Suspensions: A Critical Review.* Journal of Thermal Spray Technology, 2015. **24**(7): p. 1143-1152.

31. Khosravifard, A., et al., *Tribochemical behavior of alumina coatings deposited by high-velocity oxy fuel spraying.* Ceramics International, 2015. **41**(4): p. 5713-5720.

32. Fauchais, P., *2 - Current status and future directions of thermal spray coatings and techniques A2 - Espallargas, Nuria*, in *Future Development of Thermal Spray Coatings*. 2015, Woodhead Publishing. p. 17-49.

33. Fauchais, P., et al., *Key Challenges and Opportunities in Suspension and Solution Plasma Spraying.* Plasma Chemistry and Plasma Processing, 2014. **35**(3): p. 511-525.

34. Pawłowski, L., *5 - Application of solution precursor spray techniques to obtain ceramic films and coatings A2 - Espallargas, Nuria*, in *Future Development of Thermal Spray Coatings*. 2015, Woodhead Publishing. p. 123-141.

35. Sivakumar, G., R.O. Dusane, and S.V. Joshi, *A novel approach to process phase pure alpha-Al2O3 coatings by solution precursor plasma spraying.* Journal of the European Ceramic Society, 2013. **33**(13-14): p. 2823-2829.

36. Govindarajan, S., R.O. Dusane, and S.V. Joshi, *In situ Particle Generation and Splat Formation During Solution Precursor Plasma Spraying of Yttria-Stabilized Zirconia Coatings.* Journal of the American Ceramic Society, 2011. **94**(12): p. 4191-4199.

37. Ozturk, A. and B.M. Cetegen, *Experiments on ceramic formation from liquid precursor spray axially injected into an oxy-acetylene flame.* Acta Materialia, 2005. **53**(19): p. 5203-5211.

38. Saremi, M. and Z. Valefi, *The effects of spray parameters on the microstructure and thermal stability of thermal barrier coatings formed by solution precursor flame spray (spfs).* Surface & Coatings Technology, 2013. **220**: p. 44-51.

39. Carpio, P., et al., *Effect of particle size distribution of suspension feedstock on the microstructure and mechanical properties of suspension plasma spraying YSZ coatings.* Surface and Coatings Technology, 2015. **268**: p. 293-297.

40. Santacruz, I., K. Anapoorani, and J. Binner, *Preparation of high solids content nanozirconia suspensions.* Journal of the American Ceramic Society, 2008. **91**(2): p. 398-405.

41. Santacruz, I., et al., *Wet forming of concentrated nano-BaTiO3 suspensions.* Journal of the European Ceramic Society, 2009. **29**(5): p. 881-886.

42. Pawlowski, L., *Suspension and solution thermal spray coatings.* Surface & Coatings Technology, 2009. **203**(19): p. 2807-2829.

43. Bolelli, G., et al., *Comparison between Suspension Plasma Sprayed and High Velocity Suspension Flame Sprayed bioactive coatings.* Surface and Coatings Technology, 2015. **280**: p. 232-249.

44. Rampon, R., et al., *Influence of suspension characteristics on coatings microstructure obtained by suspension plasma spraying.* Surface and Coatings Technology, 2008. **202**(18): p. 4337-4342.

45. Singh, B.P., et al., *Stability of dispersions of colloidal alumina particles in aqueous suspensions.* Journal of Colloid and Interface Science, 2005. **291**(1): p. 181-186.

46. Johnson, L.D.a.D., *Surface Tension of Charge-Stabilized Colloidal Suspensions at the Water-Air Interface*. 2003. 5.

47. Tingaud, O., et al., *Suspension Plasma-Sprayed Alumina Coating Structures: Operating Parameters Versus Coating Architecture.* Journal of Thermal Spray Technology, 2008. **17**(5-6): p. 662-670.

48. Furbank, R.J. and J.F. Morris, *Pendant drop thread dynamics of particle-laden liquids.* International Journal of Multiphase Flow, 2007. **33**(4): p. 448-468.

49. Kim, H.J., et al., *The electrical insulation behavior and sealing effects of plasma-sprayed alumina-titania coatings.* Surface & Coatings Technology, 2001. **140**(3): p. 293-301.

50. Lee, C.S. and R.D. Reitz, *Effect of liquid properties on the breakup mechanism of high-speed liquid drops.* Atomization and Sprays, 2001. **11**(1): p. 1-19.

51. Ashgriz, N., *Handbook of Atomization and Sprays: Theory and Applications*. 2011. 1-935.

52. Bemporad, E., et al., *Structural characterisation of High Velocity Suspension Flame Sprayed (HVSFS) TiO2 coatings.* Surface & Coatings Technology, 2010. **204**(23): p. 3902-3910.

53. Singh, B.P., et al., *Electrokinetic and adsorption studies of alumina suspensions using Darvan C as dispersant.* Journal of Colloid and Interface Science, 2005. **289**(2): p. 592-596.

54. Singh, B.P., et al., *Characterization of concentrated colloidal ceramics suspension: A new approach.* Journal of Colloid and Interface Science, 2006. **300**(1): p. 163-168.

55. Bhattacharjee, S., B.P. Singh, and L. Besra, *Effect of Additives on Electrokinetic Properties of Colloidal Alumina Suspension.* Journal of Colloid and Interface Science, 2002. **254**(1): p. 95-100.

56. Moreno, R. and E. Bannier, *3 - Feedstock suspensions and solutions A2 - Espallargas, Nuria*, in *Future Development of Thermal Spray Coatings*. 2015, Woodhead Publishing. p. 51-80.

57. Killinger, A., *4 - Status and future trends in suspension spray techniques A2 - Espallargas, Nuria*, in *Future Development of Thermal Spray Coatings*. 2015, Woodhead Publishing. p. 81-122.

58. Yin, Z.J., et al., *Particle in-flight behavior and its influence on the microstructure and mechanical properties of plasma-sprayed Al2O3 coatings.* Journal of the European Ceramic Society, 2008. **28**(6): p. 1143-1148.

59. Deshpande, S., et al., *Application of image analysis for characterization of porosity in thermal spray coatings and correlation with small angle neutron scattering.* Surface and Coatings Technology, 2004. **187**(1): p. 6-16.

60. Du, H., J.H. Shin, and S.W. Lee, *Study on porosity of plasma-sprayed coatings by digital image analysis method.* Journal of Thermal Spray Technology, 2005. **14**(4): p. 453-461.

61. Herman, H., *Plasma-Sprayed Coatings.* Scientific American, 1988. **259**(3): p. 112-117.

62. Di Girolamo, G., et al., *Microstructure and mechanical properties of plasma sprayed alumina-based coatings.* Ceramics International, 2014. **40**(8, Part B): p. 12861-12867.

63. Kulkarni, A., et al., *Studies of the microstructure and properties of dense ceramic coatings produced by high-velocity oxygen-fuel combustion spraying.* Materials Science and Engineering: A, 2004. **369**(1-2): p. 124-137.

64. Wang, Z., et al., *Effects of pores and interfaces on effective properties of plasma sprayed zirconia coatings.* Acta Materialia, 2003. **51**(18): p. 5319-5334.

65. Kulkarni, A., et al., *Processing effects on porosity-property correlations in plasma sprayed yttria-stabilized zirconia coatings.* Materials Science and Engineering a-Structural Materials Properties Microstructure and Processing, 2003. **359**(1-2): p. 100-111.

66. Turunen, E., et al., *On the role of particle state and deposition procedure on mechanical, tribological and dielectric response of high velocity oxy-fuel sprayed alumina coatings.* Materials Science and Engineering: A, 2006. **415**(1-2): p. 1-11.

67. Saravanan, P., et al., *Influence of spraying variables on structure and properties of plasma sprayed alumina coatings.* British Ceramic Transactions, 2000. **99**(6): p. 241-247.

68. Kulkarni, A., et al., *Comprehensive microstructural characterization and predictive property modeling of plasma-sprayed zirconia coatings.* Acta Materialia, 2003. **51**(9): p. 2457-2475.

69. Fauchais, P., *Suspension and solution plasma or HVOF spraying.* Journal of Thermal Spray Technology, 2008. **17**(1): p. 1-3.

70. Yang, Y., et al., *Influence of composite powders' microstructure on the microstructure and properties of Al2O3–TiO2 coatings fabricated by plasma spraying.* Materials & Design (1980-2015), 2015. **65**: p. 814-822.

71. Pakseresht, A.H., et al., *Evaluation of hot corrosion behavior of plasma sprayed thermal barrier coatings with graded intermediate layer and double ceramic top layer.* Surface and Coatings Technology, 2016. **288**: p. 36-45.

72. Muller, P., A. Killinger, and R. Gadow, *Comparison Between High-Velocity Suspension Flame Spraying and Suspension Plasma Spraying of Alumina.* Journal of Thermal Spray Technology, 2012. **21**(6): p. 1120-1127.

73. Bolelli, G., et al., *Comparison between plasma- and HVOF-sprayed ceramic coatings. Part I: microstructure and mechanical properties.* International Journal of Surface Science and Engineering, 2007. **1**(1): p. 38-61.

74. Damani, R.J. and P. Makroczy, *Heat treatment induced phase and microstructural development in bulk plasma sprayed alumina.* Journal of the European Ceramic Society, 2000. **20**(7): p. 867-888.

75. Levin, I. and D. Brandon, *Metastable alumina polymorphs: Crystal structures and transition sequences.* Journal of the American Ceramic Society, 1998. **81**(8): p. 1995-2012.

76. Busca, G., *The surface of transitional aluminas: A critical review.* Catalysis Today, 2014. **226**: p. 2-13.

77. Levin, I., et al., *Cubic to monoclinic phase transformations in alumina.* Acta Materialia, 1997. **45**(9): p. 3659-3669.

78. Levin, I. and D. Brandon, *Metastable Alumina Polymorphs: Crystal Structures and Transition Sequences.* Journal of the American Ceramic Society, 2005. **81**(8): p. 1995-2012.

79. Uma Devi, M., *On the nature of phases in Al2O3 and Al2O3–SiC thermal spray coatings.* Ceramics International, 2004. **30**(4): p. 545-553.

80. Uma Devi, M., *New phase formation in Al2O3-based thermal spray coatings.* Ceramics International, 2004. **30**(4): p. 555-565.

81. Er-Juan, Y., et al., *Effect of intersplat interface bonding on the microstructure of plasma-sprayed Al 2 O 3 coating.* IOP Conference Series: Materials Science and Engineering, 2014. **61**(1): p. 012022.

82. Shipway, I.H.a.P., *Tribology*. 2nd ed. 2017: Butterworth-Heinemann. 386.

83. Singh, V.P., A. Sil, and R. Jayaganthan, *A study on sliding and erosive wear behaviour of atmospheric plasma sprayed conventional and nanostructured alumina coatings.* Materials & Design, 2011. **32**(2): p. 584-591.

84. Bolelli, G., et al., *Wear behaviour of high velocity suspension flame sprayed (HVSFS) Al2O3 coatings produced using micron- and nano-sized powder suspensions.* Surface and Coatings Technology, 2010. **204**(16-17): p. 2657-2668.

85. Murray, J.W., et al., *Suspension High Velocity Oxy-Fuel (SHVOF)-Sprayed Alumina Coatings: Microstructure, Nanoindentation and Wear.* Journal of Thermal Spray Technology, 2016. **25**(8): p. 1700-1710.

86. Singha Roy, R., et al., *Sliding wear behavior of submicron-grained alumina in biological environment.* Journal of biomedical materials research. Part A, 2007. **83**(2): p. 257-62.

87. Bolelli, G., et al., *Microstructural and Tribological Investigation of High-Velocity Suspension Flame Sprayed (HVSFS) Al2O3 Coatings.* Journal of Thermal Spray Technology, 2009. **18**(1): p. 35-49.

88. Murray, J.W., et al., *Alumina-graphene nanocomposite coatings fabricated by suspension high velocity oxy-fuel thermal spraying for ultra-low-wear.* Journal of the European Ceramic Society, 2018. **38**(4): p. 1819-1828.

89. Mcpherson, R., *On the Formation of Thermally Sprayed Alumina Coatings.* Journal of Materials Science, 1980. **15**(12): p. 3141-3149.

90. Bolelli, G., et al., *Microstructural and Tribological Investigation of High-Velocity Suspension Flame Sprayed (HVSFS) Al2O3 Coatings.* Journal of Thermal Spray Technology, 2008. **18**(1): p. 35.

91. Withers, P.J. and H.K.D.H. Bhadeshia, *Residual stress. Part 1 – Measurement techniques.* Materials Science and Technology, 2013. **17**(4): p. 355-365.

92. Fauchais, P., et al., *Knowledge Concerning Splat Formation: An Invited Review.* Journal of Thermal Spray Technology, 2004. **13**(3): p. 337-360.

93. Kuroda, S. and T.W. Clyne, *The Quenching Stress in Thermally Sprayed Coatings.* Thin Solid Films, 1991. **200**(1): p. 49-66.

94. Arif, A.F.M., K.S. Al-Athel, and J. Mostaghimi, *Residual Stresses in Thermal Spray Coating*, in *Comprehensive Materials Finishing*, M.S.J. Hashmi, Editor. 2017, Elsevier Inc. p. 56-70.

95. Faisal, N.H., et al., *Neutron Diffraction Residual Strain Measurements of Molybdenum Carbide-Based Solid Oxide Fuel Cell Anode Layers with Metal Oxides on Hastelloy X.* Experimental Mechanics, 2017.

96. Ahmed, R., et al., *Residual Strain and Fracture Response of Al2O3 Coatings Deposited via APS and HVOF Techniques.* Journal of Thermal Spray Technology, 2012. **21**(1): p. 23-40.

97. Bolelli, G., et al., *Residual stresses in HVOF-sprayed ceramic coatings.* Surface & Coatings Technology, 2008. **202**(19): p. 4810-4819.

98. Matejícek, J., S. Sampath, and J. Dubsky, *X-ray residual stress measurement in metallic and ceramic plasma sprayed coatings.* Journal of Thermal Spray Technology, 1998. **7**(4): p. 489-496.

99. M.E. Fitzpatrick, A.T.F., P. Holdway, F.A. Kandil, Shackleton, L. Suominen, *Determination of Residual Stresses by X-ray Diffraction-Issue 2*, in *Measurement Good Practice Guide*. 2005, National Physical Laboratory: Middlesex, United Kingdom.

100. Grant, P.V., Lord, J D, Whitehead, P S*, *The measurement of residual stresses by the incremental hole drilling technique*, in *Measurement Good Practice Guide*. 2006, National Physical Laboratory.

101. Matejicek, J. and S. Sampath, *In situ measurement of residual stresses and elastic moduli in thermal sprayed coatings - Part 1: apparatus and analysis.* Acta Materialia, 2003. **51**(3): p. 863-872.

102. Zhu, J., et al., *Residual stress in thermal spray coatings measured by curvature based on 3D digital image correlation technique.* Surface and Coatings Technology, 2011. **206**(6): p. 1396-1402.

103. Wenzelburger, M., D. Lopez, and R. Gadow, *Methods and application of residual stress analysis on thermally sprayed coatings and layer composites.* Surface & Coatings Technology, 2006. **201**(5): p. 1995-2001.

104. Bobzin, K., et al., *Comparison of Residual Stress Measurements Conducted by X-ray Stress Analysis and Incremental Hole Drilling Method.* Journal of Thermal Spray Technology, 2020.

105. Hu, Y.Y. and W.M. Huang, *Thermal Stress Analysis and Characterization of Thermomechanical Properties of Thin Films on an Elastic Substrate*, in *Handbook of Manufacturing Engineering and Technology*, A. Nee, Editor. 2013, Springer London: London. p. 1-71.

106. Orteu, J.-J., *3-D computer vision in experimental mechanics.* Optics and Lasers in Engineering, 2009. **47**(3-4, SI): p. p.282-291.

107. Macwan, A., et al., *Residual stresses in suspension plasma sprayed electrolytes in metal-supported solid oxide fuel cell half cells.* Journal of Power Sources, 2013. **221**: p. 397-405.

108. Zou, Z., et al., *A comparative study on the performance of suspension plasma sprayed thermal barrier coatings with different bond coat systems.* Surface and Coatings Technology, 2015. **275**: p. 276-282.

109. Bakan, E. and R. Vaßen, *Ceramic Top Coats of Plasma-Sprayed Thermal Barrier Coatings: Materials, Processes, and Properties.* Journal of Thermal Spray Technology, 2017. **26**(6): p. 992-1010.

110. Clarke, D.R., M. Oechsner, and N.P. Padture, *Thermal-barrier coatings for more efficient gas-turbine engines.* MRS Bulletin, 2012. **37**(10): p. 891-898.

111. Saeidi, S., K.T. Voisey, and D.G. McCartney, *Mechanical Properties and Microstructure of VPS and HVOF CoNiCrAlY Coatings.* Journal of Thermal Spray Technology, 2011. **20**(6): p. 1231-1243.

112. Wu, R.T., X. Wang, and A. Atkinson, *On the interfacial degradation mechanisms of thermal barrier coating systems: Effects of bond coat composition.* Acta Materialia, 2010. **58**(17): p. 5578-5585.

113. Zhao, X., et al., *Evolution of interfacial toughness of a thermal barrier system with a Pt-diffused gamma/gamma ' bond coat.* Acta Materialia, 2011. **59**(16): p. 6401-6411.

114. Allen, A.J., et al., *Microstructural characterization studies to relate the properties of thermal-spray coatings to feedstock and spray conditions.* Surface & Coatings Technology, 2001. **146**: p. 544-552.

115. Vassen, R., A. Stuke, and D. Stover, *Recent Developments in the Field of Thermal Barrier Coatings.* Journal of Thermal Spray Technology, 2009. **18**(2): p. 181-186.

116. Gell, M., et al., *Higher Temperature Thermal Barrier Coatings with the Combined Use of Yttrium Aluminum Garnet and the Solution Precursor Plasma Spray Process.* Journal of Thermal Spray Technology, 2018. **27**(4): p. 543-555.

117. Sobhanverdi, R. and A. Akbari, *Porosity and microstructural features of plasma sprayed Yttria stabilized Zirconia thermal barrier coatings.* Ceramics International, 2015. **41**(10): p. 14517-14528.

118. Guo, H.B., R. Vassen, and D. Stover, *Atmospheric plasma sprayed thick thermal barrier coatings with high segmentation crack density.* Surface & Coatings Technology, 2004. **186**(3): p. 353-363.

119. Sampath, S., et al., *Processing science of advanced thermal-barrier systems.* MRS Bulletin, 2012. **37**(10): p. 903-910.

120. Schulz, U., J. Miinzer, and U. Kaclen, *Influence of Deposition Conditions on Density and Microstructure of EB–PVD TBCs*, in *26th Annual Conference on Composites, Advanced Ceramics, Materials, and Structures: B: Ceramic Engineering and Science Proceedings*. 2002. p. 353-360.

121. Zhang, D., *1 - Thermal barrier coatings prepared by electron beam physical vapor deposition (EB–PVD)*, in *Thermal Barrier Coatings*, H. Xu and H. Guo, Editors. 2011, Woodhead Publishing. p. 3-24.

122. Schulz, U., et al., *Review on advanced EB-PVD ceramic topcoats for TBC applications.* International Journal of Applied Ceramic Technology, 2004. **1**(4): p. 302-315.

123. Johnson, C.A., et al., *Relationships between residual stress, microstructure and mechanical properties of electron beam–physical vapor deposition thermal barrier coatings.* Surface and Coatings Technology, 1998. **108-109**: p. 80-85.

124. Gao, L.H., et al., *Deposition mechanisms of yttria-stabilized zirconia coatings during plasma spray physical vapor deposition.* Ceramics International, 2016. **42**(4): p. 5530-5536.

125. Hospach, A., et al., *Columnar-Structured Thermal Barrier Coatings (TBCs) by Thin Film Low-Pressure Plasma Spraying (LPPS-TF).* Journal of Thermal Spray Technology, 2011. **20**(1-2): p. 116-120.

126. Rezanka, S., G. Mauer, and R. Vassen, *Improved Thermal Cycling Durability of Thermal Barrier Coatings Manufactured by PS-PVD.* Journal of Thermal Spray Technology, 2014. **23**(1-2): p. 182-189.

127. He, W., et al., *Advanced crystallographic study of the columnar growth of YZS coatings produced by PS-PVD.* Journal of the European Ceramic Society, 2018. **38**(5): p. 2449-2453.

128. Mauer, G., A. Hospach, and R. Vassen, *Process development and coating characteristics of plasma spray-PVD.* Surface & Coatings Technology, 2013. **220**: p. 219-224.

129. Chen, Q.Y., et al., *Microstructure of YSZ Coatings Deposited by PS-PVD Using 45kW Shrouded Plasma Torch.* Materials and Manufacturing Processes, 2016. **31**(9): p. 1183-1191.

130. VanEvery, K., et al., *Column Formation in Suspension Plasma-Sprayed Coatings and Resultant Thermal Properties.* Journal of Thermal Spray Technology, 2011. **20**(4): p. 817-828.

131. Delbos, C., et al., *Phenomena Involved in Suspension Plasma Spraying Part 2: Zirconia Particle Treatment and Coating Formation.* Plasma Chemistry and Plasma Processing, 2006. **26**(4): p. 393-414.

132. Fazilleau, J., et al., *Phenomena involved in suspension plasma spraying part 1: Suspension injection and behavior.* Plasma Chemistry and Plasma Processing, 2006. **26**(4): p. 371-391.

133. Kassner, H., et al., *Application of Suspension Plasma Spraying (SPS) for Manufacture of Ceramic Coatings.* Journal of Thermal Spray Technology, 2008. **17**(1): p. 115-123.

134. Guignard, A., et al., *Deposition and Characteristics of Submicrometer-Structured Thermal Barrier Coatings by Suspension Plasma Spraying.* Journal of Thermal Spray Technology, 2012. **21**(3-4): p. 416-424.

135. Ganvir, A., et al., *Comparative study of suspension plasma sprayed and suspension high velocity oxy -fuel sprayed YSZ thermal barrier coatings.* Surface and Coatings Technology, 2015. **268**: p. 70-76.

136. Curry, N., et al., *Influence of bond coat surface roughness on the structure of axial suspension plasma spray thermal barrier coatings — Thermal and lifetime performance.* Surface and Coatings Technology, 2015. **268**: p. 15-23.

137. Bernard, B., et al., *Columnar suspension plasma sprayed coating microstructural control for thermal barrier coating application.* Journal of the European Ceramic Society, 2016. **36**(4): p. 1081-1089.

138. Curry, N., et al., *Thermal Conductivity Analysis and Lifetime Testing of Suspension Plasma-Sprayed Thermal Barrier Coatings.* Coatings, 2014. **4**(3): p. 630-650.

139. Kumar, R., et al., *Influence of microstructure on the durability of gadolinium zirconate thermal barrier coatings using APS & SPPS processes.* Surface & Coatings Technology, 2018. **337**: p. 117-125.

140. Su, Y.J., et al., *Thermal Conductivity, Phase Stability, and Oxidation Resistance of Y3Al5O12 (YAG)/Y2O3–ZrO2 (YSZ) Thermal-Barrier Coatings.* Oxidation of Metals, 2004. **61**(3): p. 253-271.

141. Kilo, M., et al., *Oxygen diffusion in yttria stabilised zirconia—experimental results and molecular dynamics calculations.* Phys. Chem. Chem. Phys., 2003. **5**(11): p. 2219-2224.

142. Miller, R.A., J.L. Smialek, and R.G. Garlick. *Phase Stability in Plasma-sprayed, Partially Stabilized Zirconia-Yttria*. in *Advances in Ceramics*. 1981. Columbus, OH: The American Ceramic Society.

143. Li, L., N. Hitchman, and J. Knapp, *Failure of Thermal Barrier Coatings Subjected to CMAS Attack.* Journal of Thermal Spray Technology, 2010. **19**(1): p. 148-155.

144. Bai, M., et al., *Microstructure and phase stability of suspension high velocity oxy-fuel sprayed yttria stabilised zirconia coatings from aqueous and ethanol based suspensions.* Journal of the European Ceramic Society, 2018. **38**(4): p. 1878-1887.

145. Kumar, R., et al., *Low Thermal Conductivity Yttrium Aluminum Garnet Thermal Barrier Coatings Made by the Solution Precursor Plasma Spray: Part I-Processing and Properties.* Journal of Thermal Spray Technology, 2018. **27**(5): p. 781-793.

146. Padture, N.P. and P.G. Klemens, *Low thermal conductivity in garnets.* Journal of the American Ceramic Society, 1997. **80**(4): p. 1018-1020.

147. Abell, J.S., et al., *An investigation of phase stability in the Y2O3-Al2O3 system.* Journal of Materials Science, 1974. **9**(4): p. 527-537.

148. Weyant, C.M. and K.T. Faber, *Processing-microstructure relationships for plasma-sprayed yttrium aluminum garnet.* Surface & Coatings Technology, 2008. **202**(24): p. 6081-6089.

149. Parukuttyamma, S.D., et al., *Yttrium aluminum garnet (YAG) films through a precursor plasma spraying technique.* Journal of the American Ceramic Society, 2001. **84**(8): p. 1906-1908.

150. Wu, Y.Q., J. Du, and K.L. Choy, *Novel deposition of columnar Y3Al5O12 coatings by electrostatic spray-assisted vapor deposition.* Journal of the American Ceramic Society, 2006. **89**(1): p. 385-387.

151. Gu, L., et al., *Phase stability of plasma sprayed YAG–YSZ composite beads/coatings at high temperature.* Journal of the European Ceramic Society, 2013. **33**(15): p. 3325-3333.

152. Kumar, R., et al., *CMAS behavior of yttrium aluminum garnet (YAG) and yttria-stabilized zirconia (YSZ) thermal barrier coatings.* Surface and Coatings Technology, 2017. **327**: p. 126-138.

153. Ravichandran, K.S., et al., *Thermal conductivity of plasma-sprayed monolithic and multilayer coatings of alumina and yttria-stabilized zirconia.* Journal of the American Ceramic Society, 1999. **82**(3): p. 673-682.

154. Taylor, R.E., *Thermal conductivity determinations of thermal barrier coatings.* Materials Science and Engineering: A, 1998. **245**(2): p. 160-167.

155. Pan, W., et al., *Low thermal conductivity oxides.* MRS Bulletin, 2012. **37**(10): p. 917-922.

156. Cernuschi, F., et al., *Thermo-physical properties of as deposited and aged thermal barrier coatings (TBC) for gas turbines: State-of-the art and advanced TBCs.* Journal of the European Ceramic Society, 2018. **38**(11): p. 3945-3961.

157. Bernard, B., et al., *Thermal insulation properties of YSZ coatings: Suspension Plasma Spraying (SPS) versus Electron Beam Physical Vapor Deposition (EB-PVD) and Atmospheric Plasma Spraying (APS).* Surface and Coatings Technology, 2017. **318**: p. 122-128.

158. Bernard, B., et al., *Effect of Suspension Plasma-Sprayed YSZ Columnar Microstructure and Bond Coat Surface Preparation on Thermal Barrier Coating Properties.* Journal of Thermal Spray Technology, 2017. **26**(6): p. 1025-1037.

159. Curry, N., et al., *Evaluation of the Lifetime and Thermal Conductivity of Dysprosia-Stabilized Thermal Barrier Coating Systems.* Journal of Thermal Spray Technology, 2013. **22**(6): p. 864-872.

160. Vaßen, R., et al., *Testing and evaluation of thermal-barrier coatings.* MRS Bulletin, 2012. **37**(10): p. 911-916.

161. Chen, Q.Y., et al., *Controlling grain size in columnar YSZ coating formation by droplet filtering assisted PS-PVD processing.* Rsc Advances, 2015. **5**(124): p. 102126-102133.

162. Dong, H., et al., *The influence of temperature gradient across YSZ on thermal cyclic lifetime of plasma-sprayed thermal barrier coatings.* Ceramics International, 2015. **41**(9): p. 11046-11056.

163. Gupta, M., et al., *Design of next generation thermal barrier coatings — Experiments and modelling.* Surface and Coatings Technology, 2013. **220**: p. 20-26.

164. Prabhu, R., *Synthesis and processing of nanocrystalline YAG (Yttrium Aluminium Garnet) ceramics*. 2015, Loughborough University: UK. p. 223.

165. Stetefeld, J., S.A. McKenna, and T.R. Patel, *Dynamic light scattering: a practical guide and applications in biomedical sciences.* Biophysical reviews, 2016. **8**(4): p. 409-427.

166. Fitzpatrick, L.E., *Encyclopedia of Materials Characterization*. Materials Characterization Series, ed. J. C. Richard Brundle and Charles A. Evans. 1992.

167. Ann Gan, J. and C.C. Berndt, *23 - Thermal spray forming of titanium and its alloys*, in *Titanium Powder Metallurgy*, M. Qian and F.H. Froes, Editors. 2015, Butterworth-Heinemann: Boston. p. 425-446.

168. Gougeon, P.M., C., *In-flight particle surface temperature measurement: Influence of the plasma light scattered by the particles.* Journal of Thermal Spray Technology, 1993. **2**(3): p. 229-233.

169. Salhi, Z., et al., *Influence of plasma light scattered by in-flight particle on the measured temperature by high speed pyrometry.* Infrared Physics & Technology, 2005. **46**(5): p. 394-399.

170. J.F. Bisson, et al., *Ensemble In-flight Particle Diagnostics under Thermal Spray Conditions*, in *Thermal Spray 2001: New Surfaces for a New Millenium*, K.A.K. Christopher C. Berndt, Erich F. Lugscheider, Editor. 2001, ASM International: Singapore. p. 705-714.

171. Giannuzzi, L.A. and F.A. Stevie, *A review of focused ion beam milling techniques for TEM specimen preparation.* Micron, 1999. **30**(3): p. 197-204.

172. Mayer, J., et al., *TEM Sample Preparation and FIB-Induced Damage.* MRS Bulletin, 2007. **32**(5): p. 400-407.

173. Marczewska, B. and K. Marczewski, *First Glass Electrode and its Creators F. Haber and Z. Klemensiewicz – On 100th Anniversary.* Zeitschrift Fur Physikalische Chemie-international Journal of Research in Physical Chemistry & Chemical Physics - Z PHYS CHEM, 2010. **224**: p. 795-799.

174. Fry, C.M.P., *Development of Magnesium-Based Multilayer PVD Coatings for Hydrogen Storage Applications*. 2013, The University of Nottingham: Nottingham.

175. Robert, E.D., L. Andreas, and S.O.E. John, *Rietveld Refinement*. 2019, Berlin, Boston: De Gruyter.

176. Fitzpatrick, L.E., *Encyclopedia of Materials Characterization*, ed. J. C. Richard Brundle and Charles A. Evans. 1992: Butterworth-Heinemann. 782.

177. Sahu, N. and S. Panigrahi, *Mathematical aspects of Rietveld refinement and crystal structure studies on PbTiO3 ceramics.* Bulletin of Materials Science, 2011. **34**(7): p. 1495-1500.

178. Scardi, P. and M. Leoni, *Whole powder pattern modelling.* Acta Crystallographica Section A, 2002. **58**(2): p. 190-200.

179. R. Zhou, R.L.S., *Structures and transformation mechanisms of the η, γ and θ transition aluminas.* Acta Crystallographica Section B, 1991. **47**(5): p. 617-630.

180. Repelin, Y. and E. Husson, *Etudes structurales d'alumines de transition. I-alumines gamma et delta.* Materials Research Bulletin, 1990. **25**(5): p. 611-621.

181. Bennett, T.D. and F. Yu, *A nondestructive technique for determining thermal properties of thermal barrier coatings.* Journal of Applied Physics, 2004. **97**(1): p. 013520.

182. Sun, J.G., *Thermal Conductivity Measurement for Thermal Barrier Coatings Based on One- and Two-Sided Thermal Imaging Methods.* Review of Progress in Quantitative Nondestructive Evaluation, Vols 29a and 29b, 2010. **1211**: p. 458-465.

183. Parker, W.J., et al., *Flash Method of Determining Thermal Diffusivity, Heat Capacity, and Thermal Conductivity.* Journal of Applied Physics, 1961. **32**(9): p. 1679-&.

184. Taylor, T.A., *Thermal-Properties and Microstructure of 2 Thermal Barrier Coatings.* Surface & Coatings Technology, 1992. **54**(1-3): p. 53-57.

185. Cowan, R.D., *Proposed Method of Measuring Thermal Diffusivity at High Temperatures.* Journal of Applied Physics, 1961. **32**(7): p. 1363-&.

186. Cowan, R.D., *Pulse Method of Measuring Thermal Diffusivity at High Temperatures.* Journal of Applied Physics, 1963. **34**(4): p. 926-&.

187. An, K., et al., *Microstructure, texture, and thermal conductivity of single-layer and multilayer thermal barrier coatings of Y2O3-stabilized ZrO2 and Al2O3 made by physical vapor deposition.* Journal of the American Ceramic Society, 1999. **82**(2): p. 399-406.

188. Charles, A.G.E.a.E.A., *Fracture toughness determinations by indentation.* Journal of the American Ceramic society, 1976. **59**(7-8): p. 371-372.

189. Oliver, W.C. and G.M. Pharr, *Measurement of hardness and elastic modulus by instrumented indentation: Advances in understanding and refinements to methodology.* Journal of Materials Research, 2011. **19**(1): p. 3-20.

190. Fischer-Cripps, A.C., *Nanoindentation*. Mechanical Engineering Series, ed. F.F. Ling. 2002, New York: Springer.

191. Zong, Z., et al., *Indentation size effects in the nano- and micro-hardness of fcc single crystal metals.* Materials Science and Engineering a-Structural Materials Properties Microstructure and Processing, 2006. **434**(1-2): p. 178-187.

192. Pabst, W., G. Tichá, and E. Gregorová, *Effective elastic properties of alumina-zirconia composite ceramics - Part 3. Calculation of elastic moduli of polycrystalline alumina and zirconia from monocrystal data.* Ceramics - Silikaty, 2004. **48**(2): p. 41-48.

193. Prevéy, P.S., *X-ray Diffraction Residual Stress Techniques.* Metals Handbook, 1986(513): p. 380-392.

194. Karadge, M., et al., *A comparison of strain measurements on an inertia friction weld using the ENGIN-X and SALSA neutron strain mapping instruments.* Residual Stresses Vii, 2006. **524-525**: p. 393-398.

195. Santisteban, J.R., et al., *ENGIN-X: a third-generation neutron strain scanner.* Journal of Applied Crystallography, 2006. **39**(6): p. 812-825.

196. Ahmed, R., et al., *Neutron diffraction residual strain measurements in post-treated thermal spray cermet coatings.* Materials Science and Engineering a-Structural Materials Properties Microstructure and Processing, 2008. **498**(1-2): p. 191-202.

197. Dye, D., et al., *The determination of the residual strains and stresses in a tungsten inert gas welded sheet of IN718 superalloy using neutron diffraction.* Journal of Strain Analysis for Engineering Design, 2000. **35**(4): p. 247-259.

198. Dieter, G.E., *Mechanical Metallurgy*. SI Metric Edition ed. McGraw-Hill Series in Materials Science and Engineering, ed. M.B.B.e. al. 1988, London: McGraw-Hill Book Company. 766.

199. Schajer, G.S., *Measurement of Non-Uniform Residual-Stresses Using the Hole-Drilling Method .1. Stress Calculation Procedures.* Journal of Engineering Materials and Technology-Transactions of the Asme, 1988. **110**(4): p. 338-343.

200. Ahmed, R., M.E. Fitzpatrick, and N.H. Faisal, *A comparison of neutron diffraction and hole-drilling residual strain measurements in thermally sprayed coatings.* Surface & Coatings Technology, 2012. **206**(19-20): p. 4180-4185.

201. Alburayt, A., W.P. Syam, and R. Leach, *Lateral scale calibration for focus variation microscopy.* Measurement Science and Technology, 2018. **29**(6): p. 065012.

202. Alburayt, A.I., *Calibration of focus variation microscopy for surface texture measurement*, in *Mechanical, Materials and Manufacturing*. 2019, Univeristy of Nottingham: Nottingham. p. 261.

203. Sudaprasert, T., *An investigation of microstructure and sliding wear in thermally sprayed WC-Co coatings*. 2002.

204. Rauch, J., et al., *Advances in High Velocity Suspension Flame Spraying (HVSFS).* Surface & Coatings Technology, 2009. **203**(15): p. 2131-2138.

205. Killinger, A., M. Kuhn, and R. Gadow, *High-Velocity Suspension Flame Spraying (HVSFS), a new approach for spraying nanoparticles with hypersonic speed.* Surface and Coatings Technology, 2006. **201**(5): p. 1922-1929.

206. Toma, F.L., et al., *Comparison of the Microstructural Characteristics and Electrical Properties of Thermally Sprayed Al2O3 Coatings from Aqueous Suspensions and Feedstock Powders.* Journal of Thermal Spray Technology, 2012. **21**(3-4): p. 480-488.

207. Don, M., *Henk G. Merkus and Gabriel M.H. Meesters " Production, Handling and Characterization of Particulate Materials " Springer International Publishing (Switzerland, 2016), pg. 528*, G.H. Merkus and M.H.G. Meesters, Editors. 2016. p. 528-528.

208. Morks, M.F., et al., *Splat microstructure of plasma sprayed cast iron with different chamber pressures.* Journal of Thermal Spray Technology, 2003. **12**(2): p. 282-289.

209. Jiang, S.S.a.X., *Splat formation and microstructure development during plasma spraying-deposition temperature effects.* 2001.

210. Pasandideh-Fard, M., et al., *Splat shapes in a thermal spray coating process: Simulations and experiments.* Journal of Thermal Spray Technology, 2002. **11**(2): p. 206-217.

211. Kang, C.W. and H.W. Ng, *Splat morphology and spreading behavior due to oblique impact of droplets onto substrates in plasma spray coating process.* Surface & Coatings Technology, 2006. **200**(18-19): p. 5462-5477.

212. Gadow, R., A. Killinger, and J. Rauch, *New results in High Velocity Suspension Flame Spraying (HVSFS).* Surface and Coatings Technology, 2008. **202**(18): p. 4329-4336.

213. Yang, Q., et al., *Sliding wear behavior and tribofilm formation of ceramics at high temperatures.* Surface and Coatings Technology, 2004. **184**(2): p. 270-277.

214. Murray, J.W., et al., *Microstructure and wear behaviour of powder and suspension hybrid Al2O3–YSZ coatings.* Ceramics International, 2018. **44**(7): p. 8498-8504.

215. Dhiman, R., A.G. McDonald, and S. Chandra, *Predicting splat morphology in a thermal spray process.* Surface & Coatings Technology, 2007. **201**(18): p. 7789-7801.

216. Chantikul, P., S.J. Bennison, and B.R. Lawn, *Role of Grain-Size in the Strength and R-Curve Properties of Alumina.* Journal of the American Ceramic Society, 1990. **73**(8): p. 2419-2427.

217. Hall, E.O., *Variation of Hardness of Metals with Grain Size.* Nature, 1954. **173**: p. 948.

218. Taha A., H.F., *Application of the Hall-Petch Relation to Microhardness Measurements on Al, Cu, Al-MD 105, and Al-Cu Alloys.* Physica Status Solidi (a), 1990. **119**(2): p. 455-462.

219. McPherson, R., *Formation of metastable phases in flame- and plasma-prepared alumina.* Journal of Materials Science, 1973. **8**(6): p. 851-858.

220. Van Santen, R.A., *The Ostwald step rule.* The Journal of Physical Chemistry, 1984. **88**(24): p. 5768-5769.

221. McHale, J.M., et al., *Surface Energies and Thermodynamic Phase Surface Energies and Thermodynamic Phase Stability in Nanocrystalline Aluminas.* 2010. **788**(1997): p. 788-792.

222. Metson, J., *Production of alumina*. 2010: Woodhead Publishing Limited.

223. Boumaza, A., et al., *Transition alumina phases induced by heat treatment of boehmite: An X-ray diffraction and infrared spectroscopy study.* Journal of Solid State Chemistry, 2009. **182**(5): p. 1171-1176.

224. Plummer, M., *The Formation of Metastable Aluminas at High Temperatures.* Journal of Applied Chemistry, 1958. **8**(1): p. 35-44.

225. Rooymans, H.P.R.a.C.J.M., *The Formation and Structure of Delta Alumina.* 1961.

226. Rong, J., et al., *Non-isothermal crystallization kinetics of Al2O3-YAG amorphous ceramic coating deposited via plasma spraying.* Journal of the American Ceramic Society, 2018. **101**(7): p. 2888-2900.

227. Wang, Y.G., et al., *Ordering of Octahedral Vacancies in Transition Aluminas.* Journal of the American Ceramic Society, 2005. **81**(6): p. 1655-1660.

228. Khorsand Zak, A., et al., *X-ray analysis of ZnO nanoparticles by Williamson–Hall and size–strain plot methods.* Solid State Sciences, 2011. **13**(1): p. 251-256.

229. Ungár, T., *Microstructural parameters from X-ray diffraction peak broadening.* Scripta Materialia, 2004. **51**(8): p. 777-781.

230. Thümmler, F. and W. Thomma, *The sintering process.* Metallurgical Reviews, 1967. **12**(1): p. 69-108.

231. Fang, Z.Z., et al., *Grain growth during sintering of nanosized particles.* Ceramic Transactions, 2010. **209**: p. 389-400.

232. Sahoo, P. and J.P. Davim, *Tribology of Ceramics and Ceramic Matrix Composites*, in *Tribology for Scientists and Engineers: From Basics to Advanced Concepts*, P.L. Menezes, et al., Editors. 2013, Springer New York: New York, NY. p. 211-231.

233. Bhushan, B., *Introduction to Tribology*. 2013, The Atrium, Southern Gate, Chichester, West Sussex, PO19 8SQ, UK: John Wiley & Sons, Ltd.

234. Chadha, S., R. Jefferson-Loveday, and T. Hussain, *Effect of nozzle geometry on the gas dynamics and evaporation rates of Suspension High Velocity Oxy Fuel (SHVOF) thermal spray: A numerical investigation.* Surface & Coatings Technology, 2019. **371**: p. 78-89.

235. Killinger, A., P. Müller, and R. Gadow, *What Do We Know, What are the Current Limitations of Suspension HVOF Spraying?* Journal of Thermal Spray Technology, 2015. **24**(7): p. 1130-1142.

236. Chadha, S., et al., *A Computational and Experimental Investigation into Radial Injection for Suspension High Velocity Oxy-Fuel (SHVOF) Thermal Spray.* Journal of Thermal Spray Technology, 2019. **28**(6): p. 1126-1145.

237. Dongmo, E., et al., *Modeling of Combustion as well as Heat, Mass, and Momentum Transfer During Thermal Spraying by HVOF and HVSFS.* Journal of Thermal Spray Technology, 2009. **18**(5): p. 896.

238. Rampon, R., C. Filiatre, and G. Bertrand, *Suspension plasma spraying of YPSZ coatings: Suspension atomization and injection.* Journal of Thermal Spray Technology, 2008. **17**(1): p. 105-114.

239. Coghe, A. and G.E. Cossali, *Quantitative optical techniques for dense sprays investigation: A survey.* Optics and Lasers in Engineering, 2012. **50**(1): p. 46-56.

240. Dai, Z. and G.M. Faeth, *Temporal properties of secondary drop breakup in the multimode breakup regime.* International Journal of Multiphase Flow, 2001. **27**(2): p. 217-236.

241. Bailey, J.E. and L. Rotherham, *The monoclinic-tetragonal transformation and associated twinning in thin films of zirconia.* Proceedings of the Royal Society of London. Series A. Mathematical and Physical Sciences, 1964. **279**(1378): p. 395-412.

242. Li, L., et al., *Suppression of crystallization during high velocity impact quenching of alumina droplets: Observations and characterization.* Materials Science and Engineering: A, 2007. **456**(1): p. 35-42.

243. Majumdar, D. and D. Chatterjee, *X-Ray Photoelectron Spectroscopic Studies on Yttria-Stabilized Zirconia and Its Surface Transformations.* Thin Solid Films, 1991. **206**(1-2): p. 349-354.

244. N. Patil, R. and E. C. Subbarao, *Monoclinic–tetragonal phase transition in zirconia: mechanism, pretransformation and coexistence*. Vol. 26. 1970. 535-542.

245. Matejicek, J., et al., *Quenching, thermal and residual stress in plasma sprayed deposits: NiCrAlY and YSZ coatings.* Acta Materialia, 1999. **47**(2): p. 607-617.

246. Parsard, G., G. Subhash, and P. Jannotti, *Amorphization-induced volume change and residual stresses in boron carbide.* Journal of the American Ceramic Society, 2018. **101**(6): p. 2606-2615.

247. AZoM. *Stainless Steel - Grade 304 (UNS S30400)*. 2001 [cited 2020 22 July 2020]; Available from: https://www.azom.com/article.aspx?ArticleID=965.

248. AZoM. *Alumina - Aluminium Oxide - Al2O3 - A Refractory Ceramic Oxide*. 2001 [cited 2020 22 July 2020]; Available from: https://www.azom.com/article.aspx?ArticleID=52.

249. AZoM. *Zirconia - ZrO2, Zirconium Dioxide*. [cited 2020 22 July 2020]; Available from: https://www.azom.com/properties.aspx?ArticleID=133.

250. Sang, Y., et al., *Yttrium aluminum garnet nanoparticles synthesized by nitrate decomposition and their low temperature densification behavior.* Journal of Alloys and Compounds, 2010. **490**(1): p. 459-462.

251. Ramanujam, P., et al., *A comparative study of the synthesis of nanocrystalline Yttrium Aluminium Garnet using sol-gel and co-precipitation methods.* Ceramics International, 2014. **40**(3): p. 4179-4186.

252. Sokolowski, P., et al., *Characterization of microstructure and thermal properties of YCSZ coatings obtained by suspension plasma spraying.* Surface & Coatings Technology, 2015. **268**: p. 147-152.

253. Kakade, M.B., S. Ramanathan, and P.V. Ravindran, *Yttrium aluminum garnet powders by nitrate decomposition and nitrate-urea solution combustion reactions - a comparative study.* Journal of Alloys and Compounds, 2003. **350**(1-2): p. 123-129.

254. Ramanathan, S., et al., *Processing and characterization of combustion synthesized YAG powders.* Ceramics International, 2003. **29**(5): p. 477-484.

255. Chen, D., E.H. Jordan, and M. Gell, *Effect of solution concentration on splat formation and coating microstructure using the solution precursor plasma spray process.* Surface & Coatings Technology, 2008. **202**(10): p. 2132-2138.

256. Carda, J., et al., *A Rietveld Study of the Cation Substitution between Uvarovite and Yttrium-Aluminum Synthetic Garnets, Obtained by Sol-Gel Method.* Crystal Research and Technology, 1994. **29**(3): p. 387-391.

257. Yamaguchi, O., K. Matui, and K. Shimizu, *Formation of YAIO3 with Garnet structure.* Ceramics International, 1985. **11**(3): p. 107-108.

258. Rodaev, V.V., et al., *Microstructure and Phase Composition of Yttria-Stabilized Zirconia Nanofibers Prepared by High-Temperature Calcination of Electrospun Zirconium Acetylacetonate/Yttrium Nitrate/Polyacrylonitrile Fibers.* Fibers, 2019. **7**(10): p. 82.

259. Liu, Y.Z., et al., *Microstructural evolution of the interface between NiCrAlY coating and superalloy during isothermal oxidation.* Materials & Design, 2015. **80**: p. 63-69.

260. Dong, H., et al., *Effect of TGO Thickness on Thermal Cyclic Lifetime and Failure Mode of Plasma- Sprayed TBCs.* Journal of the American Ceramic Society, 2014. **97**(4): p. 1226-1232.

261. Bodzenta, J., *Influence of order-disorder transition on thermal conductivity of solids.* Chaos Solitons & Fractals, 1999. **10**(12): p. 2087-2098.